Probing Micro-dynamics with Optical Tweezers: Pendula, Cell-stretching, and Thermodynamic Fluctuations

Christopher Joel Richards

Thesis submitted for the degree of

Doctor of Philosophy

Department of Physics and Astronomy

University College London

September 2017

Declaration

I, Christopher Joel Richards, confirm that the work presented in this thesis is my own. Where information has been derived from other sources, I confirm that this has been indicated in the thesis.

Christopher Joel Richards

Abstract

Optical tweezers are a powerful experimental tool, commonly utilised in microscopic experiments in a diverse cross-section of scientific fields, from biophysics to hydrodynamics of small systems, by enabling the exertion and measurement of forces that act in microscopic soft-matter systems. This thesis documents three experiments that probe the micro-dynamics of such systems.

First the theory of the mechanical phenomenon of the Kapitza pendulum is described: the unusual behaviour of the equilibrium of a pendulum whose point of suspension undergoes high frequency vertical oscillations. To go beyond this case, a Kapitza pendulum in the presence of significant damping is considered. Theoretical calculations are presented, revealing new regimes and positions of dynamic equilibrium. These are supported by Brownian motion simulations. A microscopic optical analogue of the damped Kapitza pendulum is realised using optical tweezers and the results of the theory and simulations are confirmed experimentally.

Next, the condition of diabetic retinopathy within sufferers of diabetes mellitus is discussed with reference to the deformability of red blood cells. A pilot study is conducted to assess the viability of investigating this correlation using optical tweezers with a healthy control group, a diabetic group, and a diabetic group with retinopathy. A dual optical tweezers set-up is utilised to stretch the cells

and calculate the extent of their deformability. The deformability of red blood cells from the diabetic groups is found to be significantly lower than that of the healthy control group.

Finally fluctuation theorems are considered: the asymmetry of the distributions of probabilities of observing forward and backward trajectories of micro-particles, and how this changes with the duration of the trajectories. Theoretical calculations are presented to find the fluctuation theorems for two methods of performing work on two hydrodynamically coupled particles. Simulations and trial experimental studies are performed to attempt to verify these calculations.

Publications

Peer-reviewed Journal Articles

R. Agrawal, T. Smart, J. Nobre-Cardoso, **C. J. Richards**, R. Bhatnagar, A. Tufail, D. Shima, P. H. Jones, C. Pavesio, 'Assessment of red blood cell deformability in type 2 diabetes mellitus and diabetic retinopathy by dual optical tweezers stretching technique', *Scientific Reports*, **6**, 15873 (2016)

C. J. Richards, T. Smart, P. H. Jones, D. Cubero, 'Kapitza's pendulum at the micrometre scale', *Submitted - awaiting review*

Conference Proceedings

P. H. Jones, T. Smart, **C. J. Richards**, D. Cubero, 'Optical Kapitza pendulum', *Proc. SPIE 9922, Optical Trapping and Optical Micromanipulation XIII*, 992202, (2016)

C. J. Richards, T. Smart, P. H. Jones, D. Cubero, 'Low frequency dynamical stabilisation in optical tweezers', *Proc. SPIE 9548, Optical Trapping and Optical Micromanipulation XII*, 954820, (2015)

T. Smart, **C. J. Richards**, X. Han, S. Siwiak-Jaszek, P. H. Jones, 'Correlated

fluctuations of optically trapped particles', *Proc. SPIE 9548, Optical Trapping and Optical Micromanipulation XII*, 954823, (2015)

T. Smart, **C. J. Richards**, R. Bhatnagar, C. Pavesio, R. Agrawal, P. H. Jones, 'A study of red blood cell deformability in diabetic retinopathy using optical tweezers', *Proc. SPIE 9548, Optical Trapping and Optical Micromanipulation XII*, 954825, (2015)

P. H. Jones, **C. J. Richards**, T. Smart, D. Cubero, 'Dynamical stabilisation in optical tweezers', *Proc. SPIE 9379, Complex Light and Optical Forces IX*, 93790L (2015)

Acknowledgements

There are a great many people to whom I owe a great deal for their assistance throughout the course of my Ph.D. It is because of the help offered to me by these people that the body of work in this thesis exists today. I would therefore like to take this opportunity to thank them.

Firstly I would like to thank Dr. Philip Jones for all that he has done as my supervisor; for piquing my interest and scientific curiosity with discussions on scientific topics both inside and outside the realm of study of this thesis, for freely sharing with me his time, knowledge, and expertise, for encouraging the pursuit of my ideas and methods and for guiding me through any setbacks.

I was fortunate during the course of my Ph.D. to be able to take part in exciting collaborations with researchers from other institutions. I would like to thank Professor David Cubero (University of Seville, Seville, Spain) for his theoretical assistance on the Kapitza Pendulum experiment. I would also like to thank Dr. Rupesh Agrawal (Tan Tock Seng Hospital, Singapore, and Moorfields Eye Hospital NHS Foundation Trust, London, U.K.) for sharing his haematological and ophthalmological knowledge, for pooling the people and resources together to initiate the red blood cell study in this thesis, and for overseeing the biochemical blood tests. For their roles in the same study I must also thank Rhythm Bhatnagar (Department of Mechanical Engineering, U.C.L, London,

U.K.) and João Nobre-Cardoso (Moorfields Eye Hospital NHS Foundation Trust, London, U.K.) for their assistance in delivering and separating the red blood cells. I would also like to thank Dr. Lívia Siman Gomes and Dr. Paula Magda da Silva Roma (Department of Physics, Federal University of Minas Gerais, Brazil) for providing the Matlab code for 3-D imaging of the red blood cells and for assisting me in understanding the images that needed to be taken and how they needed to be processed in order for this to work.

I would like to extend my warmest thanks to the other Ph.D. students in the U.C.L optical tweezers and magnetic tweezers groups: Thomas Smart, Johnny Nguyen, Nicholas Tidy, and Dario Conca, who have shared lab and office space with me for the last 3 years and have offered me their camaraderie and support throughout. Particularly special thanks go to Thomas who embarked upon these projects with me from day one under our shared funding, and with whom I have therefore spent thousands of hours in total working in the lab, pouring through formulae and indeed flying half-way around the world. I would also like to thank Dr. Alessandro Magazzù (Bilkent University, Ankara, Turkey) who joined us as a Ph.D. student on secondment for the first month of this Ph.D., for his friendship and for showing me the tricks of the trade in those early days.

I must also express my gratitude to the Leverhulme Trust and the UCL Impact Scheme for funding my research scholarship and travel to the SPIE 2015 conference.

Finally I would like to thank my family: my parents, for their inexhaustible love and support, and for teaching me to question and discover things; my brothers, for a life-time's worth of friendship, for sparking my interest in physics and for always believing in my abilities; and my partner, Mary, thank you for putting up with my living hundreds of miles away for 3 years yet offering nothing but your love, support, and understanding every step of the way, as you have always done.

Contents

List of Figures

List of Tables

Chapter 1

Introduction

This thesis will detail the experiments which have been undertaken during the course of the author's postgraduate research. Since all of these involve the use of optical tweezers, beginning with a brief introduction to this tool, and the history of its development, seems fitting.

1.1 Radiation Pressure

For over a century it has been known and proven both theoretically and experimentally that light is capable of exerting a force upon an object. This concept is known as 'radiation pressure', and is not limited to just the light that we can see, but extends to the whole spectrum of electromagnetic radiation. The notion of light exerting a force can be traced back as far as Johannes Kepler in the 1600s. During the course of his astronomical observations, Kepler found that a comet's tail would always be directed away from the sun. He postulated that this was due to a force or pressure being exerted upon it by the sunlight [1]. Indeed it is known now that Kepler's assertion was correct and that the direction of a comet's dust tail is caused by radiation pressure, whilst its ion tail (if one is present) is caused by solar wind [2].

Some significant time later, with his work in the latter half of the 19th century unifying electricity and magnetism, James Clerk Maxwell laid the theoretical groundwork for the phenomenon of radiation pressure [3, 4]. He correctly postulated that, when electromagnetic radiation (which has momentum) is incident upon a surface, a transfer of this momentum must ensue (as momentum must be conserved) because of the radiation being either reflected or absorbed. As a result of this transfer of momentum a 'pressure' is thus exerted in the direction of the incident radiation. It is from the conservation of momentum and the radiation force that optical trapping of particles, as seen in optical tweezers,

emerges.

After Maxwell had worked on the concept theoretically, the onus was on the scientific community to demonstrate it experimentally. This proved a very difficult task owing to the small size of the forces exerted. Nonetheless the concept was eventually demonstrated in experimental set-ups such as Nichols' radiometer in 1901 [5].

The question then arises of how to use this radiation pressure, this optical force, in order to do useful work - to move and manipulate objects. The main issue lies in the size of the optical force associated with this radiation pressure. It is very small compared to gravitational or frictional forces, and it is very small for the amount of power that is needed to produce it. A very bright light source would be key to practical manipulations with light.

Since the advent of the concept of lasers, and their first fully functioning demonstration by Maiman in 1960 [6], the possibilities for investigating radiation pressure and optical forces have greatly increased. This is owing to the high intensities attainable with, and great controllability of, lasers, thus making them useful for a wide range of applications.

1.2 Ashkin and Optical Trapping

Large numbers of experiments and theoretical works have investigated the pushing force of a laser beam via scattering of electromagnetic radiation by particles. Arguably the most noteworthy come from Arthur Ashkin, who within approximately 20 years of beginning work on micro-particle manipulation was able to successfully accelerate and trap a particle on the scale of a micron within an optical potential well using a single laser beam, and so demonstrated optical

tweezers as they are known today. What follows is a brief summary of the history of his contributions to the field [7].

Some 'back of the envelope' calculations of light reflecting from a mirror were what brought Ashkin to the field in 1969. The momentum of a single photon is given by $p = u/c = h\nu/c$ (where u is the energy of the photon, c the speed of the light, h Planck's constant, and ν is the frequency of the light), and so with an incident power of, P, directed at a mirrored surface then per second there will be $P/h\nu$ photons striking the mirror. Assuming a perfect mirror (and so reflection of all of these photons) then the gain in momentum, from the conservation of momentum, experienced by the mirror must be $2(P/h\nu)(h\nu/c) = 2P/c$. For a power of 1 W, Ashkin calculated that the maximum force that could be obtained from the light's momentum was 10 nN. Although this is a relatively small force compared to most daily macroscopic activities, Ashkin reasoned that if the laser light was focused down to a waist with a size comparable to that of a micro-particle it was directed at, then the low mass of the particle would mean that (assuming perfect reflection) the scattering forces upon the particle would produce an acceleration of $\sim 10g$, where g is acceleration due to gravity. This acceleration should produce notable, observable effects/motion when applied to the micro-particles in question [8].

Ashkin developed a simple experiment in order to look for this particle movement [9]. Using a fairly weakly focused Gaussian beam directed at a sample of latex spheres, and with only milliwatts of power, he was able to observe motion of the spheres in the direction of propagation of the beam - they were being pushed along its axis towards the edge of the sample. The velocity of the spheres in the beam was consistent with expectations based on rough force calculations, confirming that they were moving as a result of radiation pressure and the momentum imparted upon them by the beam.

In the course of this experiment Ashkin also discovered another effect. Not only were the spheres being pushed 'forwards' by the beam but those spheres located in the outer fringes of the beam were moving towards the high intensity centre of the Gaussian pattern at the axis of the beam, from whence they were then moving forwards as expected. This transverse (to the direction of beam propagation) force became known as the 'gradient force', since it arises as a result of the gradient in light intensity falling upon the sphere, the refraction of this light, and the associated momentum transfer [8, 9]. This behaviour can also be seen in a contrasting fashion in the case of spheres with low refractive indices, for example micro-bubbles within a solution. Here the direction of refraction is reversed and so the particles are pushed away from the greater intensity beam axis. Using specially shaped 'doughnut' beams to trap these bubbles and characterising such traps is an example of current research applying this effect [10].

With the knowledge of the scattering and gradient forces involved in this radiation pressure experiment, Ashkin was then able to move forward and create the first stable 3D optical trap. This was carried out using two such beams of the kind previously employed. This dual-beam set-up had two weakly focused diverging Gaussian beams directed towards each other along the same optical axis with their foci a small distance apart. Any neutral particle/sphere that diffused into the path of these two beams was then observed to be held at an equilibrium point between them [8, 9]. Displacement due to diffusion in the direction of propagation of either one of the beams causes a greater scattering force to be experienced from the opposite beam as the particle moves closer to its focus, and so the position of the sphere is corrected towards the middle of the two foci. Displacement away from the central axis of the beams results in a gradient force being felt from both beams and so corrective motion of the sphere

towards the beam's axis. It was the success of all of these experiments which led to the hypothesis that such trapping should be possible "...with atoms and molecules using laser light tuned to specific optical transitions", [9] something which has since been realised [11, 12].

The next leap forward in the development of optical trapping came in the form of the optical levitation trap in 1971. Here Ashkin employed a single beam, directed vertically upwards, to control and contain a single macroscopic particle in air against gravity. Again the beam has a focused Gaussian intensity pattern, and the particle sits just beyond its focus held there in balance between the two key forces of light scattering (radiation pressure) and gravity. If the particle descends along the optical axis due to gravity acting upon it, then it approaches the beam's waist and so experiences a greater scattering force pushing it back upwards. The reverse also holds true, in that, if the scattering force were to push the particle upwards along the beam's axis away from the waist and beyond its equilibrium point, this would quickly be rectified as the scattering force would drop off, and so the imbalance between the scattering force and gravity would grow larger and gravity would restore the particle back down to its equilibrium position. Throughout these movements the two balanced forces are complimented by the gradient force from the Gaussian beam, keeping the particle centred about the optical axis [13, 14]. The necessity of balancing the radiation pressure effect exerted against gravity limits the amount of optical scattering force that can be used with this set-up. With the trap established like this, it is possible to manipulate the particle in free space by moving the beam, and pairs of beams can be used to collide particles or build compound particles [15].

The invention of the single beam gradient force trap, or *'Optical tweezers'* as it is known today, came about shortly after this. It was achieved in a set-up originally designed and used for the trapping of atoms [11, 12], which was later applied to

dielectric spheres [16, 17]. The optical tweezers works using only a single Gaussian laser beam and strongly focussing it, usually through a microscope objective. In this way there is also a large gradient force present directed opposite to the direction of beam propagation, backwards along the beam's axis [8]. Unlike the levitation trap the optical tweezers trap does not need to be balanced against gravity. The limiting factor in the tweezers trap therefore is simply the power available from whichever laser is utilised for the trapping. Thus meaning that optical tweezers can provide confinement orders of magnitude stronger than levitation trapping, and so are useful tools in counteracting Brownian motion on the approximately micron scale.

It did not take long for optical tweezers, and the wider optical trapping, to develop into the very broad field it is today. Just a small number of the fields to have made use of these traps include: statistical physics and non-linear dynamics, microchemistry and spectroscopy, optical cooling, quantum computing and many more [7]. Key among these areas is how useful optical tweezers have become as a tool for studying soft matter and in particular biological cells. Very early after the development of optical tweezers Ashkin applied them to biological matter when he trapped the tobacco mosaic virus (TMV) [18]. He was able to trap and manipulate a TMV, although this did cause considerable optical damage in what he called 'opticution', death by light. This led to the idea of using a wavelength of laser light at which the absorption by many living cells and molecules rapidly decreases (near infra-red - 1064nm), immediately leading to far less damage to trapped biological matter [19]. For this reason this wavelength is still often employed in optical tweezers geometries today, and is used for the research carried out in this thesis. This ability to trap, manipulate and observe biological matter and its interactions on the single cell scale has become a very powerful tool for the study of biological matter.

1.3 Size Regimes in Optical Trapping

Within optical trapping and optical tweezers in particular the mechanism by which the trapping occurs, and the trapping force is obtained, can be explained with different levels of complexity depending upon the size regime occupied. This size regime refers to the relative sizes of the object being trapped (the characteristic dimension of a trapped sphere, α, is its radius), and the wavelength of the trapping light in a vacuum, λ_0. Two simplified models exist to describe the trapping in optical tweezers that correspond with regimes where the trapped object is much larger (ray optics - $\alpha \gg \lambda_0$), or much smaller (Rayleigh - $\alpha \ll \lambda_0$), than the wavelength of light used. The intermediate case where $\alpha \approx \lambda_0$ requires a more complete, complicated, and general treatment.

A common size parameter that is used to assess the validity of these simplifications involves the wavenumber, k_m, of the trapping light in the medium surrounding the particle [20].

$$k_m \alpha = \frac{2\pi n_m}{\lambda_0} \alpha, \tag{1.1}$$

where n_m is the refractive index of the same medium (and here λ_0 is the wavelength of the light in a vacuum). Using this parameter it can be seen that the ray optics model is valid when $k_m \alpha \gg 1$ and conversely that the Rayleigh regime approximation can be adopted when $k_m \alpha \ll 1$.

The limiting cases based upon this size relationship and the more general treatment will be discussed in this section.

1.3.1 The Ray Optics Regime

In the case where $\alpha \gg \lambda_0$ (that is, a particle size much larger than the wavelength of trapping light) then the trapping can be described via a simple ray optics model.

Electromagnetic radiation can be considered in the particle view as consisting of its quanta, photons. These quanta travel in the direction of the propagation of the radiation. The density of the energy flux of the radiation is equivalent to the number of photons that pass through a unit area in a unit time, multiplied by the energy of each photon. A photon in a vacuum has an associated energy of $u = hc/\lambda_0$, where h is the Planck constant and c the speed of light in a vacuum. Although this photon has no rest mass, it does have an associated momentum, $\boldsymbol{p} = (u/c)\hat{\boldsymbol{u}} = (h/\lambda_0)\hat{\boldsymbol{u}}$, where $\hat{\boldsymbol{u}}$ is a unit vector in the direction in which the photon is travelling.

N.B. It is worth mentioning here, since the propagation, reflection, and transmission of light between various media is to be discussed that there is considerable debate over the form of the momentum of light in a medium. The two main competing formalisms are those of Minkowski [21] and Abraham [22], $p = nh/\lambda_0$, and $p = h/n\lambda_0$, respectively. The difference between the two arises from considerations of how the wavelength, and the speed, of a photon respectively change when in a medium of refractive index n. The Minkowski formalism will be adopted in this thesis when necessary, although the end result of the ray optics approximation detailed here will not be affected by the definition of the momentum chosen. Further discussion of these momenta will not be conducted here, however reviews of the topic and attempts at reconciling them and explaining contradictory experimental results have been made [23, 24].

The transportation of energy in electromagnetic radiation can then be thought of

via the perspective of rays which are perpendicular to the wavefront of an electromagnetic wave and so point in the direction of energy flow. These rays can be considered to be carrying N photons per second through a fixed point such that they have an associated power given by: $P = Nu$. If one of these rays travels perpendicular to a mirrored surface, and is incident upon this surface then it will be reflected backwards (see Figure 1.1). The momentum change involved will work just as for any elastic scattering problem in classical mechanics. That is, the energy of the ray will not have changed but its momentum will have reversed. The momentum imparted to the mirror for every photon collision must therefore, according to Newton's third law, be $2\boldsymbol{p}$. It follows that the change of momentum per unit time is $2N\boldsymbol{p}$. Using Newton's second law, $\boldsymbol{F} = d\boldsymbol{p}/dt$, it can therefore be said (via a small rearrangement of the above equations) that the force imparted upon the mirror due to the reflecting ray is:

$$\boldsymbol{F}_{\text{reflection}} = 2N\boldsymbol{p} = \frac{2P}{c}\hat{\boldsymbol{u}}. \tag{1.2}$$

These forces are small relative to common macroscopic forces that are encountered every day. This can be readily seen by considering that c is of the order 10^8, and that commercial laser pointers commonly have powers of $P \leq 1$ mW (continuous wave lasers used in research can be much more powerful than this, at several watts, but this is still not comparable to the order of magnitude of c). These forces are important however, and do become comparable to other forces when considering macroscopic and nanoscopic objects.

In real-world situations not everything is a perfect reflector, and not every light ray approaches every surface with normal incidence. Different materials possess different refractive indices, rays approach material boundaries at a continuous range of angles and are in part both transmitted and reflected when they do so.

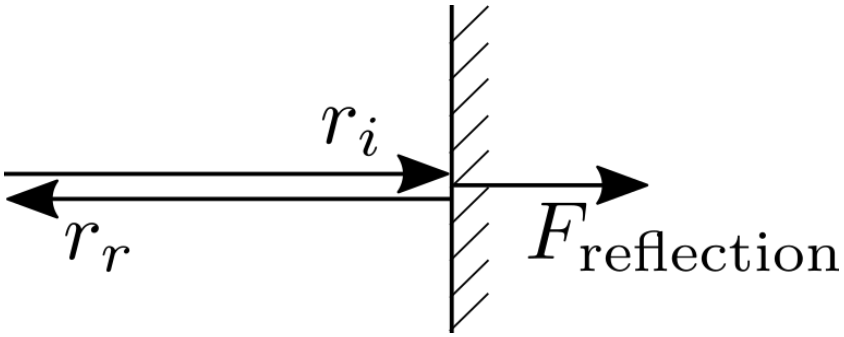

Figure 1.1: The reflection, r_r, of an incident light ray, r_i, normal to the surface of a mirror, and the resulting Force, $F_{\text{reflection}}$.

The above therefore represents the maximum force that could be generated from a ray incident upon a surface. The law of reflection governs the angle at which a light ray reflects from a flat interface between two media with different refractive indices, it is given by: [25]

$$\theta_i = \theta_r, \tag{1.3}$$

where θ_i (the angle of incidence) is the angle between the incident ray, r_i, and the normal to the point where it meets the interface, and θ_r (the angle of reflection) is the angle between this normal and the reflected ray, r_r. Snell's law governs the angle of transmission θ_t of rays that pass through this interface, and is given by: [25]

$$n_t \sin\theta_t = n_i \sin\theta_i, \tag{1.4}$$

where n_i and n_t are the refractive indices of the initial medium through which the ray is incident, and the final medium through which the ray is transmitted, respectively. An example of a ray, incident upon a planar interface between two media, being reflected and transmitted through these angles can be seen in Figure 1.2.

When a ray strikes an interface between media and is split into a reflected and a transmitted ray, so too will the incident power be split between these resultant

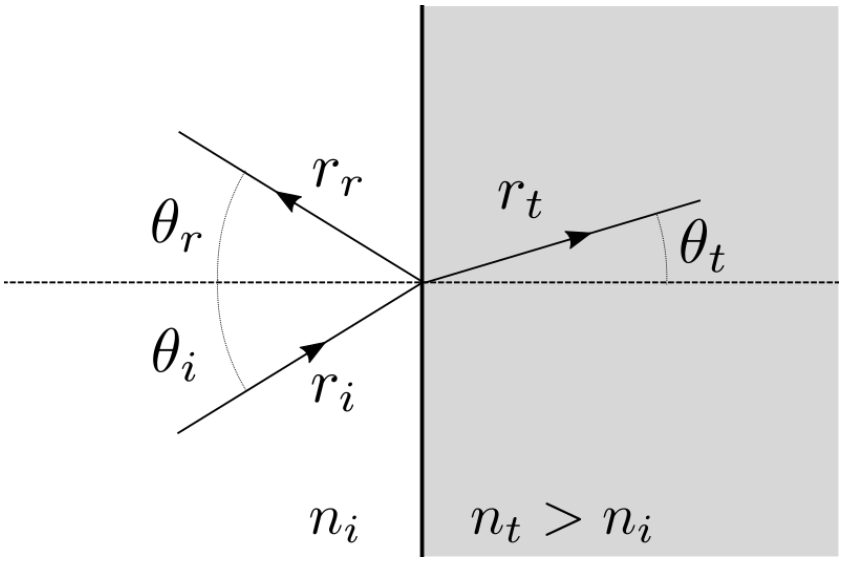

Figure 1.2: The reflection, r_r, and transmission r_t of an incident light ray, r_i, with angles θ_r, θ_t, and θ_i respectively to the normal of the interface between two media with refractive indices n_i and n_t.

rays. Generally speaking for most angles of incidence, the majority of the incident power will be transmitted. The sum of the power in the reflected and transmitted rays must be equal to the power in the incident ray, such that energy is conserved. The exact split of the incident power between these rays is given by the Fresnel equations, which give coefficients for transmitted and reflected intensity depending upon the polarisation of the incident light. These are derived from Maxwell's laws by requiring continuity of the tangential components of the electromagnetic fields across the interface [20]. The forms of the Fresnel relations are: [25]

$$\begin{aligned} R_s &= \left| \frac{n_i \cos\theta_i - n_t \cos\theta_t}{n_i \cos\theta_i + n_t \cos\theta_t} \right|^2, \\ T_s &= \frac{4 n_i n_t \cos\theta_i \cos\theta_t}{\left| n_i \cos\theta_i + n_t \cos\theta_t \right|^2}, \\ R_p &= \left| \frac{n_i \cos\theta_t - n_t \cos\theta_i}{n_i \cos\theta_t + n_t \cos\theta_i} \right|^2, \\ T_p &= \frac{4 n_i n_t \cos\theta_i \cos\theta_t}{\left| n_i \cos\theta_t + n_t \cos\theta_i \right|^2}, \end{aligned} \tag{1.5}$$

where T and R are the transmission and reflection intensity coefficients, respectively, and the subscripts s and p denote incident light with an electric field polarised normal to the plane of incidence and within the plane of incidence, respectively.

With an understanding of how a ray behaves when it reaches an interface, the simple case of a single ray incident upon a particle to be trapped can now be considered. Just as with the planar interface, the incident ray, r_i, will be split into a reflected ray, $r_{r,0}$, and a transmitted ray $r_{t,0}$. Unlike the single planar interface though, this transmitted ray will propagate forward through the particle until it strikes the opposite surface. At this surface it will be split again into reflected and transmitted rays ($r_{r,1}$ and $r_{t,2}$ respectively). A 2-D illustration of a few successive reflection and transmission events is shown in Figure 1.3. This process can occur an infinite number of times, however since most of the incident power is transmitted at each boundary, it is typically the case that almost all light has escaped from the particle within fewer than 10 events [20] (see Figure 1.5).

With the proper application of the tools introduced previously (the law of reflection, Snell's law, and the Fresnel equations) the total force on the particle can be calculated as:

$$\boldsymbol{F}_{ray} = \frac{n_i P_i}{c}\hat{\boldsymbol{r}}_i - \frac{n_i P_r}{c}\hat{\boldsymbol{r}}_{r,0} - \sum_{j=1}^{+\infty} \frac{n_i P_{t,j}}{c}\hat{\boldsymbol{r}}_{t,j}, \tag{1.6}$$

where the $\hat{\boldsymbol{r}}_i$, $\hat{\boldsymbol{r}}_{r,j}$, and $\hat{\boldsymbol{r}}_{t,j}$ are unit vectors in the direction of the incident ray and the j^{th} reflected and transmitted rays respectively. As the reflected and transmitted rays are all contained within the plane of incidence, the same can be said of the resulting force. This means that it is possible to split this force into components parallel to and perpendicular to the direction of the incident ray.

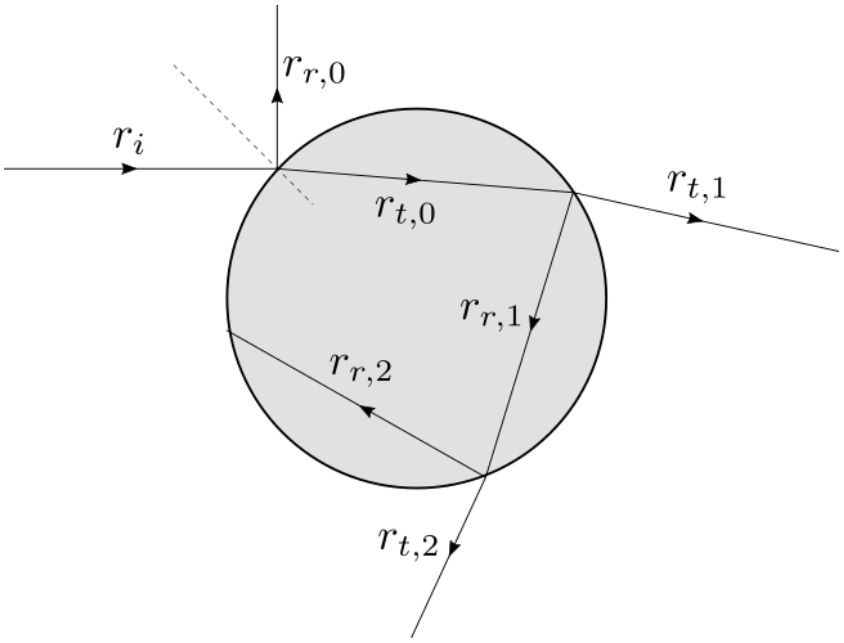

Figure 1.3: A 2-D illustration of a single incident ray, r_i, striking a dielectric sphere and being split into successive reflected, $r_{r,n}$, and transmitted, $r_{t,n}$, rays.

These are known as the scattering and gradient forces respectively. N.B. Only the 0^{th} order reflected and $j \geq 1$ order transmitted rays appear in Equation 1.6 and so the definition of momentum taken for light inside the sphere does not affect this calculation.

Whilst the way in which the forward scattering force comes about is fairly intuitive, the qualitative origin of the sideways, and indeed the 'backwards' (against propagation direction), gradient force that pulls a particle towards the centre of a laser beam of finite width is perhaps less obvious. This can be understood from a simple two ray model. Consider a sphere, placed slightly off axis in a Gaussian beam where two rays are incident upon it, symmetrically placed either side of the beam's propagation axis and propagating parallel to it. Both rays will be refracted and experience a direction change towards the opposite side of the sphere from which they were incident. Concordantly, both will transfer momentum to the sphere opposite to their change in direction - that is, forwards and towards the side of the sphere they initially struck. Since one

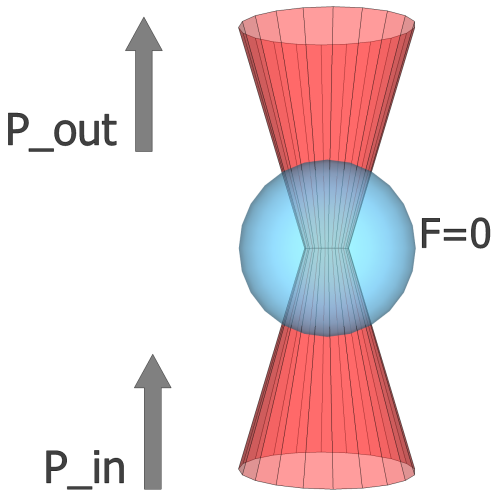

(a) A particle positioned at the beam's waist with no net force exerted.

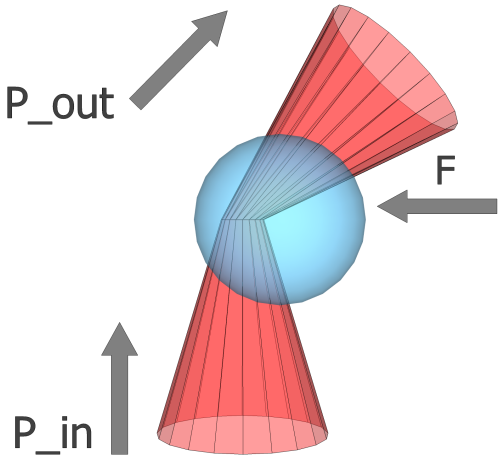

(b) A particle displaced laterally experiencing a lateral force directed towards the beam's waist.

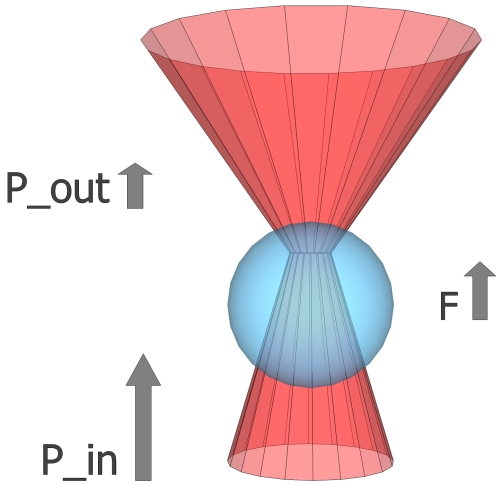

(c) A particle displaced axially from the waist experiencing an axial force directed towards the beam's waist.

Figure 1.4: Refraction of light rays striking a scattering sphere and demonstrating the optical forces that arise in the ray optics regime approach to optical tweezers.

ray must be closer to beam axis, and the beam is Gaussian, it will be the more intense of the two. This incident ray will therefore have the lager momentum, and so its refraction will exert a greater force upon the sphere, thus pulling it towards the beam axis. This is the origin of the gradient force. If incoming rays are at very large angles to the beam axis then they can actually have their direction changed by the refraction to have more of a component in the

forwards/propagation direction. When this occurs momentum in a backwards direction is transferred to the sphere. This is how the gradient force comes to counter the scattering force and stop the sphere from being pushed forwards. This balancing of the forward scattering, forward gradient, and backward gradient forces is why particles in optical tweezers will normally reside slightly beyond the beam waist.

The way optical tweezers function, in the ray optics regime, can be thought of as a large collection or set of these individual incident rays. This set of rays come from a single laser beam and are highly focussed, usually with a microscope objective lens. They will therefore converge from large angles towards some focal point. If a dielectric sphere is placed near to this focal point, then all of these rays will interact with the sphere through scattering events just as the single ray did in Figure 1.3. The optical force from each individual ray can be calculated as above, and all of their force contributions can be summed up in order to obtain the overall force that acts on the centre of mass of the sphere. It is found that for small displacements of the sphere's centre of mass from the focus of the lens it experiences a restoring force which is proportional to this displacement. This is the case for displacement in all three axes. Examples of this are illustrated in Figure 1.4.

In an optical tweezers set-up like this, it is the rays that are incident from very large angles that contribute most to trapping efficiency and most effectively transfer momentum to the particle (see Figure 1.5). It is therefore pertinent to have a large aperture radius, R_{ap}, and small focal length, f, on the microscope lens that is used, in order to obtain the highly convergent rays that strike the lens away from its centre and so have large angles of incidence towards the focus. Numerical aperture is a value often used to quantify this and is given by the relationship: $\mathrm{NA} = n_m(R_{\mathrm{ap}}/f)$, where n_m is the refractive index of the medium

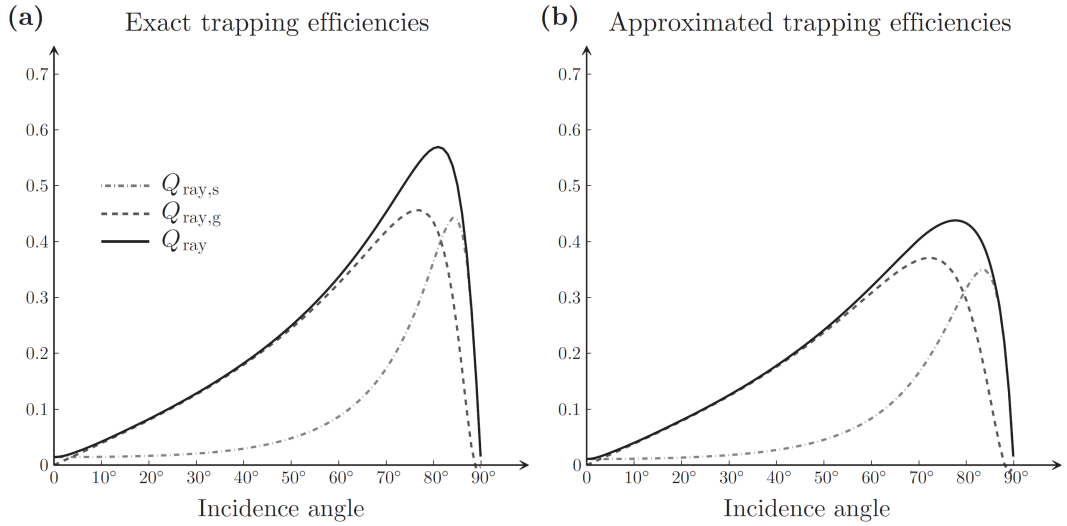

Figure 1.5: Trapping efficiencies for a glass ($n_p = 1.50$) spherical particle in water ($n_m = 1.33$) (a) taking into account all scattering events and (b) considering only the first two scattering events. The trapping efficiencies are dimensionless quantities derived from the optical gradient and scattering forces acting on the particle. They quantify how effectively momentum is transferred to the particle from the light ray. $Q_{ray,s}$ and $Q_{ray,g}$ are the efficiencies relating to the scattering force and the gradient force respectively. This figure is reprinted from *Optical Tweezers Principles and Applications*, P. H. Jones, O. M. Maragò, and G. Volpe, 1 ed. (Cambridge University Press, 2015), Chap. 2, pp. 28 under the freely granted permissions of Cambridge University Press for the reproduction of single figures.

in which the light is being focussed. A larger NA is therefore desirable. In the case of smaller apertures, the longitudinal confinement (along the propagation axis of the beam) is not as strong and may be insufficient to actually trap the particle. Along the same lines of reasoning, the importance of filling (typically experimentally just slightly overfilling) the aperture can be seen. If the, typically Gaussian, beam used has only a very small width then these high angle rays will not arise. It is only by filling the aperture that they do and that the longitudinal gradient force these rays create can be sufficiently large to overcome the scattering force in the propagation direction. This is why optical tweezers set-ups commonly slightly over fill the back aperture associated with their focussing lens, even though this will inevitably reduce the power of the trap somewhat since the edges of the beam will be lost as it passes through the aperture.

1.3.2 The Rayleigh Regime

In the event that $\alpha \ll \lambda_0$, this is the limiting case known as the Rayleigh regime/approximation and a electric point dipole model can be used to describe the force upon the sphere in the beam. Here the approach of Harada and Asakura will be followed [26].

Consider a sphere of radius α with dielectric constant ϵ_1, immersed in a medium with dielectric constant ϵ_2 and magnetic permeability μ_2. Assume a linearly polarised incident Gaussian beam operating in the fundamental mode with beam radius w_0 at its waist, propagating in the positive z-direction (ergo its electric field is oriented along the x-axis). Let O_G be the centre of the Gaussian beam waist and the origin of the coordinate system (x, y, z), and O_P the centre of a particle at position $\boldsymbol{r} = (x, y, z)$. Using a paraxial approximation to the scalar wave equation of a Gaussian beam to 0th order in the size parameter:

$$s = \frac{1}{kw_0} = \frac{\lambda_0}{2\pi w_0}, \tag{1.7}$$

where k is the wave number ($k = 2\pi/\lambda_0$), the following expression for the electric field vector at position $\boldsymbol{r}$ can be obtained [27, 28]:

$$\begin{aligned}
\boldsymbol{E}(\boldsymbol{r}) &= E(\boldsymbol{r})\ \hat{x} \\
&= E_0 \left(\frac{ikw_0^2}{ikw_0^2 + 2z} \right) \exp\left[-ikz\right] \dots \\
&\times \exp\left[-i \frac{2kz(x^2+y^2)}{(kw_0^2)^2 + (2z)^2} \right] \dots \\
&\times \exp\left[-\frac{(kw_0)^2(x^2+y^2)}{(kw_0^2)^2 + (2z)^2} \right] \hat{x},
\end{aligned} \tag{1.8}$$

where $\hat{x}$ is the unit vector in the direction of the electric field polarisation and E_0 is the electric field strength at O_G. The magnetic field vector then follows as:

$$\boldsymbol{H}(\boldsymbol{r}) = \hat{z} \times \frac{\boldsymbol{E}(\boldsymbol{r})}{Z_0} \approx n_2 \epsilon_0 c E(\boldsymbol{r})\ \hat{y} = H(\boldsymbol{r})\ \hat{y}, \tag{1.9}$$

where $\hat{y}$ and $\hat{z}$ are the unit vectors in the direction of the magnetic field and beam propagation respectively, $Z_0 = \sqrt{\frac{\mu_2}{\epsilon_2}} \approx 1/n_2\epsilon_0 c$ is the impedance of the medium for plane waves, n_2 is the refractive index of the medium, $c = 1/\sqrt{\epsilon_0 \mu_0}$ is the speed of light in a vacuum (ϵ_0 and μ_0 have their usual meanings of the permittivity and magnetic permeability in a vacuum). Also used in the above are $\epsilon_2 \approx \epsilon_0 n_2^2$ and $\mu_2 \approx \mu_0$ for a non-conducting and a non magnetic medium.

For a given space-time coordinate $(\boldsymbol{r}, t)$ the field vectors can be expressed as follows:

$$\begin{aligned} \boldsymbol{E}(\boldsymbol{r}, t) &= \mathrm{Re}[\boldsymbol{E}(\boldsymbol{r}) \exp(i\omega t)] \\ \boldsymbol{H}(\boldsymbol{r}, t) &= \mathrm{Re}[\boldsymbol{H}(\boldsymbol{r}) \exp(i\omega t)] \end{aligned} \tag{1.10}$$

where ω is the angular frequency of the light. The Poynting vector from its standard definition is:

$$\begin{aligned} \boldsymbol{S}(\boldsymbol{r}, t) &\equiv \boldsymbol{E}(\boldsymbol{r}, t) \times \boldsymbol{H}(\boldsymbol{r}, t) \\ &= \frac{1}{2}\mathrm{Re}[\boldsymbol{E}(\boldsymbol{r}) \times \boldsymbol{H}(\boldsymbol{r}) \exp(i2\omega t)] + \frac{1}{2}\mathrm{Re}[\boldsymbol{E}^*(\boldsymbol{r}) \times \boldsymbol{H}(\boldsymbol{r})], \end{aligned} \tag{1.11}$$

where here the complex amplitude nature of the fields has been taken into account to draw the following equivalence:

$$\boldsymbol{E}(\boldsymbol{r}, t) = \mathrm{Re}[\boldsymbol{E}(\boldsymbol{r}) \exp(i\omega t)] = \frac{1}{2}(\boldsymbol{E}(\boldsymbol{r}) \exp(i\omega t) + \boldsymbol{E}^*(\boldsymbol{r}) \exp(-i\omega t)).$$

Taking the time average of this instantaneous Poynting vector then gives the beam intensity or the irradiance as:

$$\begin{aligned}\boldsymbol{I}(\boldsymbol{r}) &\equiv \langle \boldsymbol{S}(\boldsymbol{r},t)\rangle \\ &= \frac{1}{T}\int_0^T \boldsymbol{S}(\boldsymbol{r},t)dt \\ &= \frac{1}{T}\int_0^T \left[\frac{1}{2}\mathrm{Re}[\boldsymbol{E}(\boldsymbol{r})\times\boldsymbol{H}^*(\boldsymbol{r})] + \frac{1}{2}\mathrm{Re}[\boldsymbol{E}(\boldsymbol{r})\times\boldsymbol{H}(\boldsymbol{r})\exp(2i\omega t)]\right] dt.\end{aligned}$$

The time average of the second term will equal 0, so we recover:

$$\begin{aligned}&= \frac{1}{2}\mathrm{Re}[\boldsymbol{E}(\boldsymbol{r})\times\boldsymbol{H}^*(\boldsymbol{r})] \\ &= \frac{n_2\epsilon_0 c}{2}|E(\boldsymbol{r})|^2\ \hat{z} = I(\boldsymbol{r})\ \hat{z},\end{aligned} \tag{1.12}$$

where:

$$I(\boldsymbol{r}) = \left(\frac{2P}{\pi w_0^2}\right)\frac{1}{1+(2\tilde{z})^2}\exp\left[-\frac{2(\tilde{x}^2+\tilde{y}^2)}{1+(2\tilde{z})^2}\right]. \tag{1.13}$$

P here represents the beam power $= \pi w_0^2 n_2\epsilon_0 c E_0^2/4$ and $\tilde{x},\tilde{y},\tilde{z}$ represent normalised spatial coordinates: $(\tilde{x},\tilde{y},\tilde{z}) = (x/w_0, y/w_0, z/w_0)$. As mentioned previously, the equations thus far depend on a zeroth order approach in size parameter s (Equation 1.7), so these remain fairly accurate providing $\lambda_0 \ll w_0$, i.e. $s \ll 1$. For more tightly focussed beams with narrower waists corrections of a higher order in s would be required. Investigations have been conducted in this vein with Gaussian beams for linearly polarised vector potentials [29] and relative errors calculated in the fields for Gaussian beams up to 5th order in s [30]. It was found that the zeroth order calculations have errors of $\sim 0.817\%$ for $s = 0.02$ i.e. $w_0 \simeq 8\lambda_0$, and $\sim 4.37\%$ for $s = 0.1$ i.e. $w_0 \simeq 1.6\lambda_0$ [30].

In the current regime being considered (where $\alpha \ll \lambda_0$) then the instantaneous electric field is uniform over the whole of the particle. The particle acts as if a

simple point dipole were at its centre with a dipole moment:

$$\begin{aligned}\boldsymbol{p}(\boldsymbol{r},t) &= 4\pi\epsilon_2\alpha^3\left(\frac{\epsilon_1-\epsilon_2}{\epsilon_1+2\epsilon_2}\right)\boldsymbol{E}(\boldsymbol{r},t)\\ &= 4\pi n_2^2\epsilon_0\alpha^3\left(\frac{m^2-1}{m^2+2}\right)\boldsymbol{E}(\boldsymbol{r},t),\end{aligned} \tag{1.14}$$

where m is the relative refractive index of the particle compared to the medium, $m = n1/n2$ [31, 32].

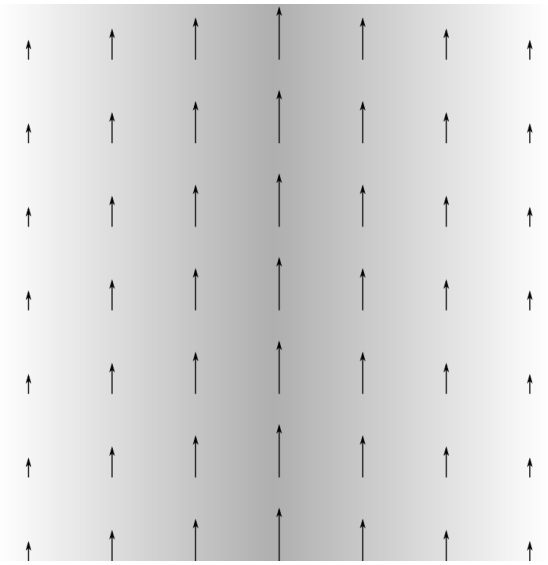

Figure 1.6: The optical scattering forces for a collimated Gaussian beam (propagating from the bottom of the image to the top) overlaid on top of the intensity profile of the beam.

As the electric field oscillates, the particle, acting as a point dipole, follows it in a synchronised fashion. Therefore, there is an oscillating electric dipole radiating scattered waves in all directions. This scattering means that the energy flux of the wave is changing in both direction and magnitude. There is an associated momentum transfer with these changes which is what we see as the scattering force exerted upon the particle. This scattering force is given by:

$$F_{\text{scat}} = \frac{C_{\text{Pr}}\langle\boldsymbol{S}(\boldsymbol{r},t)\rangle}{c/n_2} = \left(\frac{n_2}{c}\right)C_{\text{Pr}}\boldsymbol{I}(\boldsymbol{r})\ \hat{z}, \tag{1.15}$$

where C_{Pr} is the radiation pressure cross section of the particle. For small dielectric particles, like those being discussed here in the Rayleigh regime then the light is scattered isotropically and so the radiation pressure cross section is equal to the scattering cross section, C_{Scat}, that is:

$$C_{\mathrm{Pr}} = C_{\mathrm{Scat}} = \frac{8}{3}\pi(k\alpha)^4\alpha^2\left(\frac{m^2-1}{m^2+2}\right)^2. \tag{1.16}$$

By substituting this and Equation 1.13 into Equation 1.15, the scattering force in terms of the intensity distribution of the beam can be obtained (see Figure 1.6 for an illustration of this):

$$F_{\mathrm{scat}} = \left(\frac{n_2}{c}\right)\frac{8}{3}\pi(k\alpha)^4\alpha^2\left(\frac{m^2-1}{m^2+2}\right)^2\left(\frac{2P}{\pi w_0^2}\right)\frac{1}{1+(2\tilde{z})^2}\exp\left[-\frac{2(\tilde{x}^2+\tilde{y}^2)}{1+(2\tilde{z})^2}\right]\hat{z}. \tag{1.17}$$

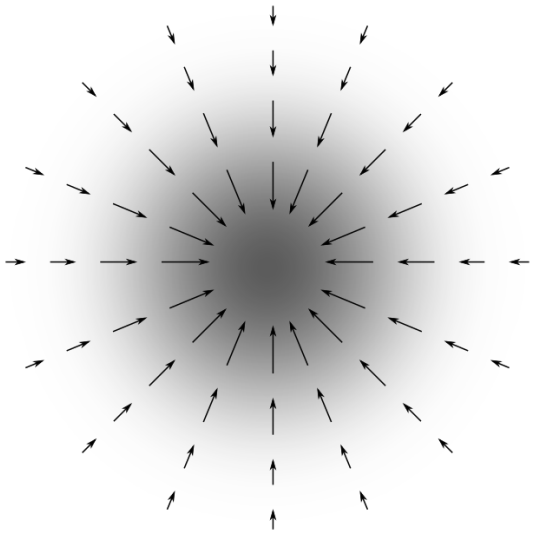

Figure 1.7: The optical gradient forces for a particle with a greater refractive index than the surrounding medium, overlaid on top of a Gaussian beam intensity distribution.

The scattering force is just one component, the other is the 'gradient force' due to the Lorentz force acting on the dipole, induced by the field. Using the dipole

moment, Equation 1.14 as an electrostatics analogue of the E-M wave, an instantaneous gradient force can be found as [31]:

$$\begin{aligned}\boldsymbol{F}_{\text{Grad}}(\boldsymbol{r},t) &= [\boldsymbol{p}(\boldsymbol{r},t)\cdot\nabla]\boldsymbol{E}(\boldsymbol{r},t)\\ &= 4\pi n_2^2\epsilon_0\alpha^3\left(\frac{m^2-1}{m^2+2}\right)\frac{1}{2}\nabla\boldsymbol{E}^2(\boldsymbol{r},t),\end{aligned} \tag{1.18}$$

where the vector identity $\nabla\boldsymbol{E}^2 = 2(\boldsymbol{E}\cdot\nabla)\boldsymbol{E} + 2\boldsymbol{E}\times(\nabla\times\boldsymbol{E})$ has been employed in conjunction with $\nabla\times\boldsymbol{E} = 0$ from Maxwell's equations. The steady-state/time-averaged version of this gradient force is given by:

$$\begin{aligned}\boldsymbol{F}_{\text{grad}}(\boldsymbol{r}) &= \langle\boldsymbol{F}_{\text{grad}}(\boldsymbol{r},t)\rangle\\ &= 4\pi n_2^2\epsilon_0\alpha^3\left(\frac{m^2-1}{m^2+2}\right)\frac{1}{2}\nabla\langle\boldsymbol{E}^2(\boldsymbol{r},t)\rangle,\\ &= \pi n_2^2\epsilon_0\alpha^3\left(\frac{m^2-1}{m^2+2}\right)\nabla|E(\boldsymbol{r})|^2,\\ &= \frac{2\pi n_2\alpha^3}{c}\left(\frac{m^2-1}{m^2+2}\right)\nabla I(\boldsymbol{r}),\end{aligned} \tag{1.19}$$

where $\langle\boldsymbol{E}^2(\boldsymbol{r},t)\rangle = \frac{1}{2}|E(\boldsymbol{r})|^2$ has been used as well as Equation 1.12. Finally, by substituting Equation 1.13 into Equation 1.19:

$$\begin{aligned}F_{\text{grad,x}} = &-\frac{2\pi n_2\alpha^3}{c}\left(\frac{m^2-1}{m^2+2}\right)\frac{4\tilde{x}/w_0}{1+(2\tilde{z})2}\\ &\times\left(\frac{P}{\pi w_0^2}\right)\frac{1}{1+(2\tilde{z})^2}\exp\left[-\frac{2(\tilde{x}^2+\tilde{y}^2)}{1+(2\tilde{z})^2}\right]\ \hat{x},\end{aligned} \tag{1.20}$$

$$\begin{aligned}F_{\text{grad,y}} = &-\frac{2\pi n_2\alpha^3}{c}\left(\frac{m^2-1}{m^2+2}\right)\frac{4\tilde{y}/w_0}{1+(2\tilde{z})2}\\ &\times\left(\frac{P}{\pi w_0^2}\right)\frac{1}{1+(2\tilde{z})^2}\exp\left[-\frac{2(\tilde{x}^2+\tilde{y}^2)}{1+(2\tilde{z})^2}\right]\ \hat{y}\end{aligned} \tag{1.21}$$

$$
\begin{aligned}
F_{\text{grad,z}} = &- \frac{2\pi n_2 \alpha^3}{c} \left(\frac{m^2 - 1}{m^2 + 2} \right) \frac{8\tilde{z}/(kw_0^2)}{1 + (2\tilde{z})2} \\
&\times \left[1 - \frac{2(\tilde{x}^2 + \tilde{y}^2)}{1 + (2\tilde{z})^2} \right] \\
&\times \left(\frac{P}{\pi w_0^2} \right) \frac{1}{1 + (2\tilde{z})^2} \exp \left[-\frac{2(\tilde{x}^2 + \tilde{y}^2)}{1 + (2\tilde{z})^2} \right] \hat{z},
\end{aligned}
\tag{1.22}
$$

three orthogonal components of the gradient force can be isolated, illustrating the 3-Dimensional nature of the restoring force towards the beam waist and contrasting with the scattering force seen in Equation 1.17 which acts only in the direction of beam propagation (see Figure 1.7 for an illustration of the gradient force). By visualising the combination of these two forces, the scattering force acting in the direction of the beam propagation (Figure 1.6), and the gradient force acting towards the beam waist (Figure 1.7), it can be understood how a particle in an optical trap in the Rayleigh regime comes to be held in 3-Dimensional space, just beyond the waist of the focussed beam in the propagation direction.

1.3.3 The General Case

Typically, neither of the respective criteria for the regimes/limiting scenarios discussed above is actually the case in an experimental setting. Whilst these two approaches have their merits then (providing an easily accessible and fairly visual qualitative explanation in the ray optics regime, and simplifying calculations to allow for quantitative predictions in the Rayleigh regime), neither describes the complete picture and so they do not allow for generalisation of the considered scenario to a range of different particle/light parameters, nor do they provide accurate qualitative predictions for these generalised scenarios.

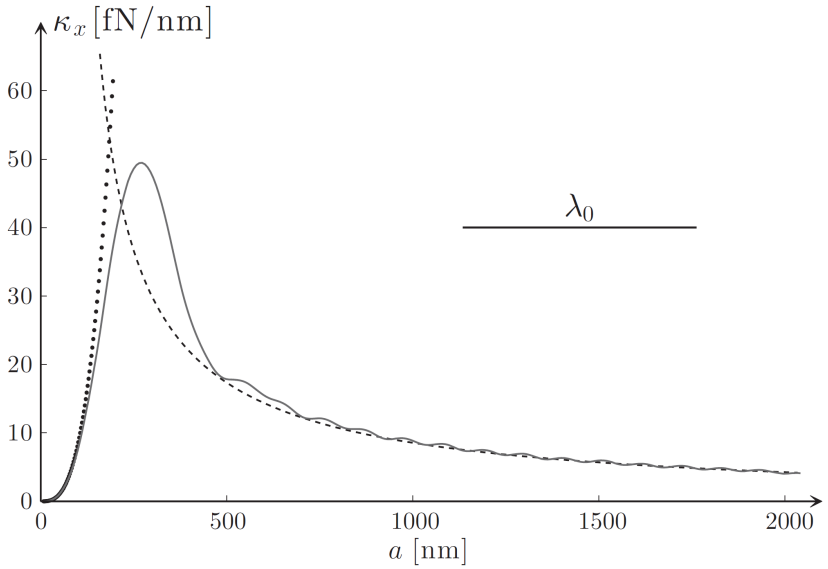

Figure 1.8: A comparison of transverse optical trap stiffness across trapping regime approximations. Here the trap is produced by a 10 mW laser beam of wavelength $\lambda_0 = 632$ nm focussed by a 1.20 NA objective onto a sphere of radius, a, with refractive index, $n_p = 1.50$, immersed in water ($n_m = 1.33$). The solid line represents the exact electromagnetic calculation. The dotted line shows the Rayleigh regime, point dipole approximation used for small particles. The dashed line shows the ray optics regime approximation used for large particles. This figure is reprinted from *Optical Tweezers Principles and Applications*, P. H. Jones, O. M. Maragò, and G. Volpe, 1 ed. (Cambridge University Press, 2015), Chap. 5, pp. 106 under the freely granted permissions of Cambridge University Press for the reproduction of single figures.

The much more common experimental case is an intermediate regime, wherein the size of the particle being trapped and the wavelength of the trapping light are approximately equal. As such the approximations of $\alpha \gg \lambda_0$ or $\alpha \ll \lambda_0$ used earlier break down and are no longer applicable. To accurately deal with this size regime requires a thorough and full treatment of the wave-optical modelling of the particle-light interaction based upon electromagnetic scattering theory.

This regime is invariably the one populated by the experiments in this thesis. However, obtaining precise expressions for the optical forces present is not the purpose of the experiments presented here, nor is it vital to understanding them or the significance of their results. As such, a full example treating the scattering theory in this regime will not be detailed here. Instead a brief description will

follow of the key stages that comprise an approach to this full treatment.

Taking the time average of the Maxwell Stress Tensor (MST - the stress tensor of the electromagnetic field, used to link the interaction between the electromagnetic forces and physical momentum in a system), and integrating its flux over a surface that bounds a given distribution of charges (a particle), it can be shown, recovers the force due to radiation pressure on the particle [20], i.e.

$$\boldsymbol{F}_{\text{rad}} = \oint_S \bar{\boldsymbol{T}}_M \cdot \hat{\boldsymbol{n}} dS. \tag{1.23}$$

where $\bar{\boldsymbol{T}}_M$ is the Maxwell stress tensor, S is the bounding surface, and $\hat{\boldsymbol{n}}$ is the unit vector normal to this. In order to find the radiation forces on a sphere evidently the MST must first be found, and in order to do this the electromagnetic fields incident upon and being scattered by the sphere must be determined. To begin finding the scattered fields, an electromagnetic field inside of a homogeneous medium with no free charges or currents (the field to be scattered) is considered in conjunction with Maxwell's equations [33], resulting in the 'Helmholtz equation' for the fields which is of the form:

$$(\nabla^2 + k_m^2) F(\boldsymbol{r}) = 0, \tag{1.24}$$

where ∇^2 is the Laplacian operator (the divergence of the gradient of a function) and k_m is the magnitude of the wave-vector in the medium. In order to solve this, typically it will be expressed in terms of spherical polar coordinates and the components in each direction shown via different variables, e.g.

$$F(r, \theta, \varphi) = R(r)\Theta(\theta)\Phi(\varphi)$$

. With some algebraic manipulation it is possible to separate out each of these

and arrive at three separate equations, each of which is expressed in terms of only one of the three coordinate directions/variables. Solutions to these are possible with varying degrees of complexity for the different coordinates: by utilising exponentials for the azimuthal coordinate, Legendre polynomials for the polar angle, and combinations of spherical Bessel/Neumann/Hankel functions for the radial distance. Finally these can be recombined to make general solutions for the Helmholtz equation of a couple of different forms depending upon whether the fields in question are finite at the origin (here Bessel functions are used), or whether a description of the radiation as the waves propagate towards infinity that doesn't diverge is required (utilising Hankel functions). Typically these are expressed with two sums whose indices correspond to the orders of Bessel/etc. functions utilised [20].

After calculating this general expression for the fields in the medium, it then must be considered how these fields will be scattered by the sphere. This is done by considering the incident, internal (inside the sphere) and scattered electromagnetic fields separately. These should each satisfy a vector Helmholtz equation in their respective media. Since the scattered field must satisfy a vector Helmholtz equation, then its separate components must satisfy a scalar Helmholtz equation. This means that the solution to the Helmholtz equation satisfying radiation propagating to infinity can be utilised to find an expression for this scattered component (this will utilise an amplitude term which will depend upon the direction of the incident radiation and the boundary conditions at the surface of the sphere), where for ease the incident field can be considered as a linearly polarised plane wave (as any electromagnetic field can be described as a superposition of plane waves). It is therefore possible to express the scattered field in terms of the incident field's amplitude and a function known as the normalised scattering amplitude. This process can be done for all of the

components of the vector scattering field yielding a complete scattering amplitude function showing the amplitude and direction of a scattered field based upon the incoming field [20].

In the simplest of cases, scattering a uniform plane wave of electromagnetic radiation from a homogeneous sphere, there has long existed a description that can be used to generate accurate predictions for arbitrary particle sizes and refractive indices known as 'Mie Scattering' or 'Mie Theory', which was laid out by Gustav Mie in 1908 [34]. Using the approach described above, as well as the scattered field it is possible to find the field within the sphere taking the Helmholtz solution that is regular at the origin. The boundary conditions require that the tangential components of the electromagnetic fields are continuous across the border of the sphere. Considering these conditions for the electric and magnetic fields and for the waves passing into and out of the sphere generates 4 equations, from which the the scattered field amplitudes and so the 'Mie Coefficients' which are the ratio of the scattered to incident amplitudes can be obtained.

It is quite commonly the case in optical trapping experiments that what is being trapped is not suitable for use with Mie Theory. Often the objects being trapped can be quite complex, especially when considering biological research and dealing with cells, organic molecules, viruses etc. These can be non-spherical, non-homogeneous, and come in a range of sizes from nanometres to micrometres, and so the assumptions made about the scatterer cease to be true and so regular Mie Theory is no longer suitable. In such cases more complete and complicated methods like the Transition matrix (T-Matrix) need to be utilised [20].

The T-Matrix utilises the linear nature of Maxwell's equations and the boundary conditions to express as a linear operator, $\mathbb{T}$, a transformation from the incident

electric field to the scattered electric field. i.e.

$$\boldsymbol{E}_s = \mathbb{T}\boldsymbol{E}_i \tag{1.25}$$

The T-matrix is found using a series of multipole expansions of the incident field and imposing boundary conditions at the surface of the spheres, it acts on the amplitude coefficients in these expansions in order to give the amplitudes for the scattered field. It was derived by Waterman in 1971 [35]. Computing the T-matrix can lead to complicated computational steps [36], however it is possible to follow formalisms that are more analytical and so lead to more efficient end computation [37].

The T-matrix in the case of a single homogeneous sphere of known refractive index and size will, as expected produce the same results as Mie theory. It offers a generalisation of this theory applicable to more complicated scattering objects. There are also other methods that can be employed to perform these calculations, such as Generalised Lorenz Mie Theory (GLMT) [38]. The two methods are essentially both generalisations to Mie theory, and although performed differently are equivalent [39].

So by finding the T-Matrix or employing GLMT, it is possible to find the total field (incident + scattering) and thus the MST, which can be used to find the optical force on the scatterer by integrating this over a sphere that contains the object.

1.4 Thesis Outline

This thesis presents the investigations made into the micro-dynamics and properties of 'soft-matter'. Soft-matter being materials which will undergo deformation or alteration as a result of thermal fluctuations in their surrounding media or similarly small external forces.

In Chapter 2, the phenomenon of the dynamical equilibrium of the macroscopic Kapitza pendulum is described. Full theoretical calculations are detailed from the introduction of the fast suspension point oscillations that characterise this pendulum, to the decomposition of its motion into fast and slow components, and the finding of an effective potential and resultant stability positions of the pendulum.

Chapter 3 seeks to go beyond the standard case of the Kapitza pendulum by explicitly considering an environment where the pendulum is subject to significant friction/damping. A theoretical analysis of this case is introduced and several regimes of dynamical equilibrium, which are dependent upon the relationships between the characteristic frequencies and parameters of the system, are identified and analysed for pendulum stability conditions. An example of modelling of the regimes in this damped Kapitza pendulum experiment is also presented for those cases where the parameters are experimentally achievable.

In Chapter 4, the theoretical work completed in the previous chapter is put into action. Details are given of the experimental optical set-up used, the calibration steps undertaken, and the methods of acquiring and processing data as a trapped silica sphere is used to realise a microscopic damped Kapitza pendulum. Results are presented from the identified regimes which were possible experimentally.

Chapter 5 concerns experiments performed on red blood cells (RBCs) to assess

and quantify their deformability in patients who exhibit a complication of diabetes known as diabetic retinopathy (DR), as compared to those who do not have the condition. A brief background on diabetes and DR is given before the experimental set-up and dual trap stretching optical tweezers method is given. Results of both blood tests and deformability measurements are presented. An initial, small scale, foray into 3-D defocusing microscopy of the RBCs is also made with a view to identifying morphological parameters that may differ in those of patients with DR.

Finally, Chapter 6 presents some initial investigations into fluctuation theorems (ratios of occurrence probability for instances of reversible forward and backward particle trajectories). This is done with a view to assessing these theorems for systems of coupled particles with some work done upon them. Methods of performing such work upon these systems are suggested, and theoretical calculations carried out for them. These are supplemented by simulations, and details of pilot experiments undertaken (from set-up through to calibration and results) are presented.

Chapter 2

The Kapitza Pendulum

As mentioned previously, this thesis comprises three areas of experimental research and study. The first of these concerns the stability of a microscopic analogue of a 'Kapitza pendulum'. A Kapitza pendulum is a classical, mechanical pendulum where the suspension point undergoes high frequency oscillations. This pendulum exists in a low damping environment (in air) and exhibits an unusual, inverted stability position.

The research in this thesis explores this Kapitza pendulum behaviour in a new environment with a much larger and more significant amount of damping. As will be seen in Chapter 3 this is realised by using an optical tweezers beam, scanned in a circle at high frequency in order to simulate the arc of a pendulum, to trap a silica bead under a microscope (in a fluid where the damping is large), whilst the movement of a microscope stage mimics the force of gravity and pushes the bead to one side of the ring, and a modulation of the centre of the scanning circle emulates the osciallations of the Kapitza pendulum. In order to explore the theoretical calculations behind this modification of Kapitza's pendulum (Chapter 3), and document the experiments performed on it (Chapter 4), an introduction to the theory and stability results of the *normal* Kapitza pendulum will be provided in this chapter.

2.1 Theory

It is an unusual feature of a rigid pendulum that, if the point of suspension (base) is subject to oscillations, its equilibrium position is not always directly downwards. If the base is driven at a sufficiently high frequency in the vertical direction (parallel to gravity), then it is possible for the pendulum to occupy a fully inverted stable equilibrium position, that is, pointing directly upwards. This was first observed and recorded in 1908 by Stephenson [40].

Pyotr Kapitza came to study this phenomenon of pendulum movement in 1951. His analysis explained the counter-intuitive behaviour by separating out the motion of the pendulum into fast and slow components, leading to an effective potential with a stable point emerging at the inverted position. [41, 42].

This subsection will work through a theoretical/mathematical approach to describing the motion of a Kapitza pendulum. Starting from simple expressions for the oscillating coordinates of a regular pendulum it will: describe how these are modified to introduce the high frequency base oscillations that typify a Kapitza pendulum; consider the energy in a system to build up an equation of motion; seek to separate this equation of motion into the slow and fast variables mentioned previously, before time averaging these to find an effective potential whose minimum can be found to predict stability positions for the pendulum.

2.1.1 The Simple Pendulum

Consider a rigid pendulum rod of length, L, fixed at the origin of a Cartesian coordinate system. Let this origin be placed a distance L above the ground such that when the pendulum hangs directly downwards it has no gravitational potential energy - obviously in real physical terms this would necessitate a pendulum bob that does not extend beyond the end of the rod, or a pendulum without a bob and all of the mass of the rod concentrated at its end, but this simplifies the set-up and makes it amenable to calculations . Let x be increasing to the right of the origin and y be increasing downwards below it, such that gravity, g (acceleration due to gravity), acts downwards in positive y. Finally let θ denote increasing anti-clockwise angular displacement of the pendulum from this downwards position.

Assuming some initial displacement of the pendulum, the x and y positions of its

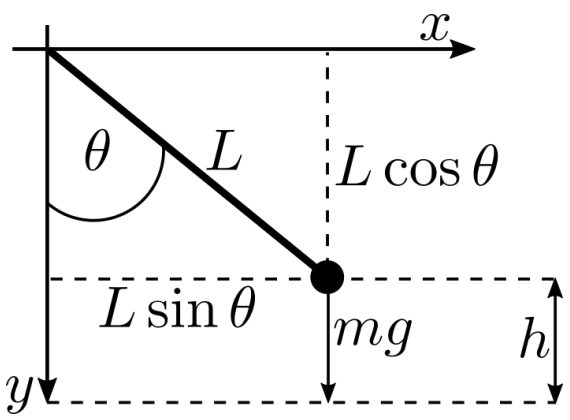

Figure 2.1: A simple pendulum.

end can be described as follows (Figure 2.1):

$$x = L\sin\theta, \qquad y = L\cos\theta. \tag{2.1}$$

The velocity of the end of the pendulum can then be found:

$$\dot{x} = \frac{d}{dt}L\sin\theta \quad = \frac{\partial}{\partial\theta}\frac{\partial\theta}{\partial t}L\sin\theta \quad = \dot{\theta}L\cos\theta \tag{2.2}$$

$$\dot{y} = \frac{d}{dt}L\cos\theta \quad = \frac{\partial}{\partial\theta}\frac{\partial\theta}{\partial t}L\cos\theta \quad = -\dot{\theta}L\sin\theta, \tag{2.3}$$

where $\dot{\theta}$ is introduced because the angle is a time-dependent coordinate, i.e. $\theta = \theta(t)$.

Well known classical mechanics equations can be used to consider the energy involved in the motion of this simple pendulum [43]. The kinetic energy, for

example, can be written as:

$$\begin{aligned} E_{\mathrm{k}} &= \frac{1}{2}mv^2 = \frac{1}{2}m(v_x^2 + v_y^2) = \frac{1}{2}m(\dot{x}^2 + \dot{y}^2) \\ \Rightarrow E_{\mathrm{k}} &= \frac{1}{2}m(\dot{\theta}^2 L^2 \cos^2\theta + \dot{\theta}^2 L^2 \sin^2\theta) \\ &= \frac{1}{2}m\dot{\theta}^2 L^2(\sin^2\theta + \cos^2\theta) \\ &= \frac{1}{2}m\dot{\theta}^2 L^2. \end{aligned} \tag{2.4}$$

Similarly the potential energy can be found using the classical equation:

$$\begin{aligned} E_{\mathrm{p}} &= mgh \\ &= mgL(1 - \cos\theta). \end{aligned} \tag{2.5}$$

With the energies in the system known it is possible to form the Lagrangian, $\mathcal{L}$. Lagrangian mechanics is an alternative approach to classical mechanics to the Newtonian method. Unlike Newtonian mechanics which considers the forces involved to build an equation of motion and plot the progression of a system, Lagrangian mechanics considers the energies of the system to develop its equations of motion. It is widely used when it is inconvenient to proceed with Newtonian mechanics, is ideal for systems involving constraint forces, and can sometimes simplify problems by allowing for simpler treatment of them in different coordinate systems. N.B. It is perfectly possible to progress with this problem from a classical Newtonian mechanics perspective, considering the forces and torque in the system. However, for the sake of simplicity, the explanation to follow will develop the Lagrangian and work from there.

The Lagrangian is given by [44]:

$$\begin{aligned}\mathcal{L} = E_{\mathrm{k}} - E_{\mathrm{p}} &= \frac{1}{2}m\dot{\theta}^2L^2 - mgL(1-\cos\theta) \\ &= mL\left(\frac{1}{2}\dot{\theta}^2L - g(1-\cos\theta)\right). \end{aligned} \tag{2.6}$$

It is now possible to use this Lagrangian to form the Euler-Lagrange equation. This is a second order differential equation also known as the characteristic equation or Euler's equation. Its solution is the equation of a curve known as a characteristic curve or an extremal. 'The integral $\int_a^b F(x, y, \acute{y})dx$, whose end points are fixed, is stationary for weak variations if y satisfies' the Euler-Lagrange equation [45].

Creating this equation with the pendulum angle, θ, will therefore mean that its solutions will lead to the stationary points or stable angles of the pendulum. The Euler-Lagrange equation can be written as [44]:

$$\frac{d}{dt}\left(\frac{\partial\mathcal{L}}{\partial\dot{\theta}}\right) = \frac{\partial\mathcal{L}}{\partial\theta}. \tag{2.7}$$

Breaking this down to find each of the derivatives yields:

$$\begin{aligned}\frac{\partial\mathcal{L}}{\partial\theta} &= \frac{\partial}{\partial\theta}\left[mL\left(\frac{1}{2}\dot{\theta}^2L - g(1-\cos\theta)\right)\right] \\ &= -mgL\sin\theta, \end{aligned} \tag{2.8}$$

$$\begin{aligned}\frac{\partial\mathcal{L}}{\partial\dot{\theta}} &= \frac{\partial}{\partial\dot{\theta}}\left[mL\left(\frac{1}{2}\dot{\theta}^2L - g(1-\cos\theta)\right)\right] \\ &= mL^2\dot{\theta}, \end{aligned} \tag{2.9}$$

and

$$\Rightarrow \frac{d}{dt}\left(\frac{\partial \mathcal{L}}{\partial \dot{\theta}}\right) = \frac{d}{dt}\left(mL^2\dot{\theta}\right) = mL^2\ddot{\theta}. \tag{2.10}$$

Finally, substituting the expressions from Equations 2.10 and 2.8 into Equation 2.7 leads to the result:

$$\begin{aligned} mL^2\ddot{\theta} &= -mgL\sin\theta \\ \Rightarrow \ddot{\theta} &= -\frac{g}{L}\sin\theta \\ &= -\Omega^2\sin\theta, \end{aligned} \tag{2.11}$$

where $\Omega = \sqrt{\frac{g}{L}}$ is the natural oscillation frequency of the pendulum [43],thus recovering the well known differential equation detailing the motion of a simple pendulum.

To more easily obtain a solution to this equation, it is typically treated with the assumption that $\theta \ll 1$, such that the small-angle approximation can be used to say that $\sin\theta \approx \theta$. This yields the equation: $\ddot{\theta} = -\Omega^2\theta$, which is analogous to the familiar form of a harmonic oscillator, e.g. $F = -kx$, where k is some spring constant. Assuming the pendulum is at its position of largest displacement (θ_0) at time 0, $\theta(0) = \theta_0$, and that it is at rest at this time, $\dot{\theta}(0) = 0$, then the solution for the simple pendulum motion is as follows:

$$\theta(t) = \theta_0\cos(\Omega t) \qquad \theta_0 \ll 1. \tag{2.12}$$

2.1.2 Introducing Oscillations - the Kapitza Pendulum

Now that the case of a simple pendulum has been outlined, the oscillations of the pendulum base can be introduced to adapt this to the case of the Kapitza

pendulum.

Let the point of suspension of the pendulum be oscillated in a vertical, y, direction such that the motion of this suspension point can be described by [46]:

$$y_{\mathrm{s}} = a\sin(\omega t), \tag{2.13}$$

where a is the magnitude of the oscillation, and ω its frequency.

The new x and y coordinates of the pendulum can now be considered, bearing this base motion in mind. They become:

$$x = L\sin\theta \tag{2.14}$$

$$y = L\cos\theta + a\sin(\omega t). \tag{2.15}$$

The x velocity is therefore no different to the simple pendulum and remains: $\dot{x} = \dot{\theta}L\cos\theta$. The y direction velocity however takes on a different form:

$$\begin{aligned}\dot{y} &= \frac{\partial}{\partial t}\left(L\cos\theta + a\sin(\omega t)\right)\\ &= -\dot{\theta}L\sin\theta + a\omega\cos(\omega t).\end{aligned} \tag{2.16}$$

Following the same steps as for the simple pendulum case, the kinetic energy is now:

$$\begin{aligned}E_{\mathrm{k}} &= \frac{1}{2}mv^2\\ &= \frac{1}{2}m\left((\dot{\theta}L\cos\theta)^2 + (-\dot{\theta}L\sin\theta + a\omega\cos(\omega t))^2\right)\\ &= \frac{1}{2}m\left(\dot{\theta}^2L^2\cos^2\theta + \dot{\theta}^2L^2\sin^2\theta - 2\dot{\theta}La\omega\sin\theta\cos(\omega t) + a^2\omega^2\cos^2(\omega t)\right)\\ &= \frac{1}{2}m\left(L^2\dot{\theta}^2 - 2aL\omega\dot{\theta}\sin\theta\cos(\omega t) + a^2\omega^2\cos^2(\omega t)\right),\end{aligned} \tag{2.17}$$

and the potential energy can be calculated as:

$$\begin{aligned} E_{\mathrm{p}} &= mgh \\ &= mg(L-y) \\ &= mgL\left(1-\cos\theta-\frac{a}{L}\sin\left(\omega t\right)\right). \end{aligned} \tag{2.18}$$

Reconstructing the Lagrangian for these new energies yields:

$$\begin{aligned} \mathcal{L} &= E_{\mathrm{k}} - E_{\mathrm{p}} \\ &= \frac{1}{2}m\left(L^2\dot{\theta}^2 - 2aL\omega\dot{\theta}\sin\theta\cos\left(\omega t\right) + a^2\omega^2\cos^2\left(\omega t\right)\right)\ldots \\ &\quad \ldots - mgL\left(1-\cos\theta-\frac{a}{L}\sin\left(\omega t\right)\right) \end{aligned} \tag{2.19}$$

Remembering the Euler-Lagrange equation (Equation 2.7) the derivatives this involves can now be tackled with the newly found form of the Lagrangian. The results of these are as follows:

$$\frac{\partial\mathcal{L}}{\partial\theta} = mL\left(-a\omega\dot{\theta}\cos\theta\cos\left(\omega t\right) - g\sin\theta\right), \tag{2.20}$$

$$\frac{\partial\mathcal{L}}{\partial\dot{\theta}} = mL\left(L\dot{\theta} - a\omega\sin\theta\cos\left(\omega t\right)\right), \tag{2.21}$$

and finally,

$$\begin{aligned} \frac{d}{dt}\left(\frac{\partial\mathcal{L}}{\partial\dot{\theta}}\right) &= \frac{d}{dt}mL\left(L\dot{\theta} - a\omega\sin\theta\cos\left(\omega t\right)\right) \\ &= mL\left(L\ddot{\theta} + a\omega^2\sin\theta\sin\left(\omega t\right) - a\omega\dot{\theta}\cos\theta\cos\left(\omega t\right)\right). \end{aligned} \tag{2.22}$$

Equations 2.22 and 2.20 can now be substituted in to the Euler-Lagrange

equation to give:

$$mL\left(L\ddot{\theta} + a\omega^2 \sin\theta \sin(\omega t) - a\omega\dot{\theta}\cos\theta\cos(\omega t)\right) = mL\left(-a\omega\dot{\theta}\cos\theta\cos(\omega t) - g\sin\theta\right), \quad (2.23)$$

from which the last terms on both sides can be cancelled as well as the factor mL from all terms, leaving the following:

$$\begin{aligned} L\ddot{\theta} + a\omega^2 \sin\theta \sin(\omega t) &= -g\sin\theta \\ \Rightarrow \ddot{\theta} &= \frac{1}{L}\left(-g\sin\theta - a\omega^2 \sin\theta \sin(\omega t)\right) \\ \Rightarrow \ddot{\theta} &= -\sin\theta\left(\Omega^2 + \frac{a}{L}\omega^2 \sin(\omega t)\right). \end{aligned} \quad (2.24)$$

It is reassuring to note at this point the consistency of this result with the one found earlier for the simple pendulum. That is, in the event that the amplitude of the pendulum base modulations is set to nil, $a = 0$, then the second term in the bracket on the right hand side of this equation becomes 0, and so the original equation of motion found for the simple pendulum (Equation 2.11) is recovered.

Visual inspection of this result suggests that it is not easily soluble. For this reason Kapitza's famous separation of motions technique will now be employed in order to progress further.

2.1.3 Separation of Motions

When Kapitza arrived at this impasse of the hard to solve equation of motion for the angle of a pendulum with an oscillating base, he forged a technique which would foster the field of vibrational mechanics [47–49]. This technique was based upon a logical analysis of the motion of the pendulum; the consideration that its

motion, as Kapitza saw it, owed its behaviour to two things: 1) the slow/smooth motion of the swinging similar to that seen in a regular pendulum, 2) the fast/rapid small vibrations of the base. These two motions have a compound effect on the pendulum. By attempting to separate them and their effects out from the general angle, θ, that has been dealt with so far, Kapitza found it was possible to form an 'effective potential'. This potential could be used to describe the slow motion of the pendulum [41, 50]. This is the more crucial of the two motions to be able to chronicle, as it will lead to the stability positions of the pendulum. This is evident if thought is given to this motion. Without the rapid vibrations this slow motion would just behave as a regular pendulum and exhibit a downwards stability position. With the modulations of the fast vibrations it is this slow motion which changes and exhibits the shift to the new dynamic stabilisation position at the top of the pendulum arc.

Landau and Lifshitz, in their classic mechanics text, touch on this method for the inverted pendulum [51]. Considering their approach, and the angular variable so far dealt with as being made up of a fast and a slow component, it can be rewritten in the following manner:

$$\theta(t) = \tilde{\theta}(t) + \xi(t), \tag{2.25}$$

where $\tilde{\theta}(t)$ is the smooth or slow motion, typical for the oscillations of a rigid pendulum travelling around its arc, and $\xi(t)$ is the fast/rapid motion associated with the small vibrations of the base of the pendulum. From here it is assumed that, true to its description, the *slow* motion is such that $\tilde{\theta}(t)$ changes negligibly over the time scale of an oscillation of the fast motion. That is, it is assumed constant on this time scale compared to $\xi(t)$ and the motion of the pendulum base; and the vibration frequency is far greater than the natural pendulum

oscillation frequency, $\omega \gg \Omega$.[1]

This can be substituted into the equation of motion found for the Kapitza pendulum (Equation 2.24) to re-express it in terms of the newly defined components:

$$\ddot{\tilde{\theta}} + \ddot{\xi} = -\sin(\tilde{\theta} + \xi)(\Omega^2 + \frac{a}{L}\omega^2 \sin(\omega t)). \tag{2.26}$$

It is possible at this point to make use of the additive trigonometric identity:

$$\sin(A + B) = \sin A \cos B + \cos A \sin B$$

to give:

$$\ddot{\tilde{\theta}} + \ddot{\xi} = -(\sin\tilde{\theta}\cos\xi + \cos\tilde{\theta}\sin\xi)(\Omega^2 + \frac{a}{L}\omega^2 \sin(\omega t)). \tag{2.27}$$

ξ represents the angular coordinate resulting from the fast modulation. As mentioned above this is a relatively small oscillation and so it can be assumed that this relates to a very small angular change from one extent of the vibration to the other, $\pm a$. Therefore small angle approximations:

$$\sin\xi \approx \xi, \qquad \cos\xi \approx 1 - \frac{\xi^2}{2} \approx 1, \quad (\text{for } \xi \ll 1), \tag{2.28}$$

[1] Although the pendulum's motion is considered in the limit of a large driving frequency as per this inequality, the pendulum is still considered completely rigid compared to the driving. More information on this can be found amongst the regimes in Chapter 3.

can be employed for this coordinate, yielding the following:

$$\begin{aligned}\ddot{\tilde{\theta}} + \ddot{\xi} &= -(\sin\tilde{\theta} + \xi\cos\tilde{\theta})(\Omega^2 + \frac{a}{L}\omega^2\sin(\omega t)) \\ &= -\left(\Omega^2\sin\tilde{\theta} + \frac{a}{L}\omega^2\sin(\omega t)\sin\tilde{\theta} + \xi\Omega^2\cos\tilde{\theta} + \xi\frac{a}{L}\omega^2\sin(\omega t)\cos\tilde{\theta}\right).\end{aligned} \tag{2.29}$$

The component whose solution is of most interest, and the one for which the generation of an effective potential is the goal, is the slow, $\tilde{\theta}$, motion. To that end the next step in this process will be to try to find an expression for the fast motion, ξ, such that this can be substituted into Equation 2.29 to leave an expression for just the slow motion. Considering Equation 2.29, it can be noted that this involves both oscillatory and smooth terms which must be separately equal. For the oscillating terms we can put:

$$\ddot{\xi} = -\frac{a}{L}\omega^2\sin(\omega t)\sin\tilde{\theta} - \Omega^2\sin\tilde{\theta}, \tag{2.30}$$

where these terms are grouped together because the other terms on the right hand side of Equation 2.29 contain the small factor ξ and are therefore of a higher order of smallness (but the derivative $\ddot{\xi}$ is proportional to the large quantity ω and so is not small like them) [51].

From here a trial solution for this non-homogeneous differential equation is attempted. Since an equation for the quickly varying coordinate, ξ, due to the fast oscillations, ω, is desired, a trial solution of the following form is made:

$$\xi_{ts} = C\sin(\omega t) + D\cos(\omega t), \tag{2.31}$$

where C and D are simply constants to be found. The differentials of this trial

solution then look as follows:

$$\dot{\xi}_{ts} = C\omega\cos(\omega t) - D\omega\sin(\omega t) \tag{2.32}$$

$$\ddot{\xi}_{ts} = -C\omega^2\sin(\omega t) - D\omega^2\cos(\omega t). \tag{2.33}$$

Substituting these back into the differential equation (Equation 2.30) then gives the following:

$$-C\omega^2\sin(\omega t) - D\omega^2\cos(\omega t) = -\frac{a}{L}\omega^2\sin\tilde{\theta}\sin(\omega t) - \Omega^2\sin\tilde{\theta} \tag{2.34}$$

From this it is immediately visible that D must equal zero. Rearranging the above expressions for C yields:

$$C = \frac{a}{L}\sin\tilde{\theta} + \frac{\Omega^2}{\omega^2}\frac{\sin\tilde{\theta}}{\sin(\omega t)}, \tag{2.35}$$

and the particular solution for this differential equation becomes:

$$\xi = C\sin(\omega t) = \frac{a}{L}\sin\tilde{\theta}\sin(\omega t) + \frac{\Omega^2}{\omega^2}\sin\tilde{\theta}. \tag{2.36}$$

It is possible to perform a reasonable further simplification of this expression by remembering the condition that $\omega \gg \Omega$. Using this inequality, the above can easily be seen to resolve to:

$$\xi = \frac{a}{L}\sin\tilde{\theta}\sin(\omega t). \tag{2.37}$$

2.1.4 Effective Potential and Stability Positions

With this equation for the fast vibratory motion deduced, the next step in understanding the motion of the Kapitza pendulum is to find the effective potential of the system. Minima in such a potential will point directly to the stable positions/angles in the set-up.

To do this an equation of motion for the slowly evolving component is needed. Remembering that $\xi(t)$ corresponds to the position change from the small fast oscillations, its mean value, and the average value of these sinusoidal oscillations over this fast time period, will therefore be zero. The function $\tilde{\theta}(t)$ changes only slightly in this time. A time average, denoted by angled brackets, can therefore be considered and it can be said that the smooth motion can be described as $\langle\theta\rangle = \tilde{\theta}(t)$. Consider the right hand side of Equation 2.29, after substituting in for ξ from Equation 2.37:

$$-\left(\Omega^2 \sin\tilde{\theta} + \frac{a}{L}\omega^2 \sin\omega t \sin\tilde{\theta} + \frac{a}{L}\Omega^2 \sin\tilde{\theta}\cos\tilde{\theta}\sin(\omega t) + \left(\frac{a}{L}\right)^2 \omega^2 \sin\tilde{\theta}\cos\tilde{\theta}\sin^2(\omega t)\right). \quad (2.38)$$

As mentioned above,any terms with a single power of the fast sinusoidal oscillations, $\sin(\omega t)$, will become zero. In the single case where this term is raised to the power of 2, we make use of the trigonometric relation: $\langle\sin^2(\phi)\rangle = 0.5$. In this way we can obtain an equation of motion for the slowly varying term as follows:

$$\ddot{\tilde{\theta}} = -\Omega^2 \sin\tilde{\theta} - \frac{1}{2}\left(\frac{a}{L}\right)^2 \omega^2 \sin\tilde{\theta}\cos\tilde{\theta}. \quad (2.39)$$

This expression, now written solely in terms of the $\tilde{\theta}$, and without a ξ term, can

be re-written in a differential form, which will lend itself perfectly to finding an effective potential.

$$\langle \ddot{\tilde{\theta}} \rangle = \frac{\partial}{\partial \tilde{\theta}} \left[\Omega^2 \cos \tilde{\theta} + \frac{1}{4} \left(\frac{a}{L} \right)^2 \omega^2 \cos^2 (\tilde{\theta}) \right] \tag{2.40}$$

This is directly comparable to the general equation for the motion of an object in a potential, U: $\ddot{y} = -\frac{1}{m} \frac{\partial U}{\partial y}$. Therefore it is simple to see that the effective potential for the slow motion of such a Kapitza pendulum is given by:

$$U_{\text{eff}} = -m \left(\Omega^2 \cos \tilde{\theta} + \frac{1}{4} \left(\frac{a}{L} \right)^2 \omega^2 \cos^2 (\tilde{\theta}) \right). \tag{2.41}$$

It is worthy of discussion at this juncture why this is referred to as an effective potential. This equation, via the time averaging and separation of variables that have been conducted, provides a simplified picture of the motion of the pendulum. The true potential energy of the pendulum at any given moment would depend only upon gravity and the pendulum's height and mass. This method of describing the motion of the pendulum smooths and corrals it into behaving as if its potential was that written above. It is treating the two motions that have been separated out, and acts as if the fast motion gives some constant energy contribution towards the potential. Indeed this has been seen from the time averaging of it in the second component of U_{eff} above.

With the effective potential established, it can be put to work to help analyse the stability of the Kapitza pendulum. Systems normally seek to minimise their potential energy as long as it is possible to do so. A ball at the top of a steep hill will roll down it - unless there is some force/object preventing it from doing so (both such scenarios will be shown in this Kapitza pendulum analysis before this chapter is through). And so, by minimising this effective potential and finding

the corresponding angles of these minima it is possible to find where the pendulum will stabilise. Taking the derivative of this effective potential is the first step to finding the minimum angles. This is set to zero and rearranged to reveal the turning points of the equation:

$$\frac{\partial U_{\text{eff}}}{\partial \tilde{\theta}} = m\left(\Omega^2 \sin\tilde{\theta} + \frac{1}{2}\left(\frac{a}{L}\right)^2 \omega^2 \cos\tilde{\theta}\sin\tilde{\theta}\right) = 0 \tag{2.42}$$

$$\Rightarrow m\sin\tilde{\theta}\left(\Omega^2 + \frac{1}{2}\left(\frac{a}{L}\right)^2 \omega^2 \cos\tilde{\theta}\right) = 0. \tag{2.43}$$

Immediately the first turning point of $\tilde{\theta} = 0$ is obvious from the $\sin\tilde{\theta}$ term. This position is a minimum and corresponds to the typical downwards stability position of any simple pendulum. In addition to this a sine will also provide a minimum at $\tilde{\theta} = \pi$. This corresponds to the upwards, inverted, stability position unique to the Kapitza pendulum and occurs provided a certain criterion is met by the parameters of the set up. This criterion can be ascertained by analysis of the other turning points (N.B. these turning points are maxima, not potential minima and so not stable positions. This will be shown more clearly in the derivation to come and in the stability plots which follow). These turning points are located at angles which cause the bracket in Equation 2.43 to equal zero, in other words when:

$$\cos\tilde{\theta} = -2\left(\frac{\Omega}{\omega}\right)^2\left(\frac{L}{a}\right)^2. \tag{2.44}$$

Requiring that this yields a real and physical angle with no complex parts to it, allows for the imposition of a condition on the right hand side of this equation, namely:

$$2\left(\frac{\Omega}{\omega}\right)^2\left(\frac{L}{a}\right)^2 \leq 1, \tag{2.45}$$

which after minor manipulation can be rearranged into a condition on any one of the experimental parameters: pendulum length, vibration frequency, and

vibration amplitude, relative to the others $\left(\text{E.g. } \omega \geq \sqrt{2}\Omega \left(\frac{a}{L}\right)^{-1}\right)$. Perhaps the most useful and general possibility to consider here is an overall inverted stability parameter, say $\beta = \left(\frac{\omega}{\Omega}\right)\left(\frac{a}{L}\right)$ [52]. This is a dimensionless quantity, which has useful ratios of the frequencies and lengths in the system, and must satisfy the following inequality in order for inverted stability to be seen:

$$\beta \geq \sqrt{2}. \tag{2.46}$$

Such turning points are maxima, and emerge when the above conditions are met. It is then that peaks emerge in the potential energy landscape and a minimum is established between them corresponding to the inverted vertical stability position at $\tilde{\theta} = \pi$. Indeed this can be confirmed if the second derivative of the effective potential is considered.

$$\frac{\partial^2 U_{\text{eff}}}{\partial \tilde{\theta}^2} = m\left(\Omega^2 \cos\tilde{\theta} + \frac{1}{2}\left(\frac{a}{L}\right)^2 \omega^2 \cos 2\tilde{\theta}\right) \tag{2.47}$$

The sign of a second derivative at a turning point indicates whether there is a maximum or a minimum present (a negative sign indicates a maximum and vice versa). Therefore by requiring that $\tilde{\theta} = \pi$ corresponds to a minimum we insist that the second derivative of U_{eff} at this point is greater than or equal to zero (since being equal to zero does not alone indicate a maximum or minimum turning point but can be present in either case). i.e.

$$\begin{aligned} \frac{\partial^2 U_{\text{eff}}(\pi)}{\partial \tilde{\theta}^2} &\geq 0 \\ \Rightarrow m\left(\Omega^2 \cos\pi + \frac{1}{2}\left(\frac{a}{L}\right)^2 \omega^2 \cos 2\pi\right) &\geq 0 \\ \Rightarrow m\left(-\Omega^2 + \frac{1}{2}\left(\frac{a}{L}\right)^2 \omega^2\right) &\geq 0. \end{aligned} \tag{2.48}$$

From which, only a very small rearrangement is needed to once again arrive back at the threshold condition of Equation 2.46.

It is perhaps easiest at this point to consider an example experiment and some typical values of all of these parameters in order to better illustrate these two cases and the inverted stability. Consider the following parameter values:

$$g = 9.81 \text{ ms}^{-2}, \qquad L = 1 \text{ m}, \qquad a = 0.1 \text{ m}, \qquad m = 1 \text{ kg},$$

with ω the variable to be altered. Immediately it is possible to compute the threshold value of frequency modulation for inverted stabilisation to occur: $\omega = \sqrt{2}\Omega(L/a) \approx 44 \text{ Hz} \approx 2\pi \times 7 \text{ Hz}$.

First then ω is set to a value well below this threshold, $\sim 2\pi \times 1.6$ Hz. At this value $\beta \approx 0.32$, well below the $\sqrt{2}$ criteria quoted above, and so it is expected that the inverted stability position will not emerge and the pendulum will behave just as a simple pendulum, it will only stabilise downwards. Plotting the effective potential over the full $\tilde{\theta} = 0 \rightarrow 2\pi$ range of travel (with the inverted vertical position $\tilde{\theta} = \pi$ in the middle) can provide a check and an illustration of this.

Figure 2.2 confirms this. It shows a single peak at $\tilde{\theta} = \pi$. This peak signifies a high potential energy here, with nothing to stop a pendulum occupying this position from leaving it to fall back to the downwards stability position. Of course here $\frac{\partial U}{\partial \tilde{\theta}} = 0$, so this is actually an astable point, meaning it is theoretically possible for a perfectly balanced pendulum to be stable at this point, but any small perturbation would disturb this stability. This is just like the ball on a hill analogy mentioned earlier. This is a simple hill with no walls or objects, and a ball placed on top of it would roll away from this peak.

Now consider ω set to a value just above threshold, say $\sim 2\pi \times 8$ Hz. At this value $\beta \approx 1.60$. The potential energy for this driving frequency can be seen in

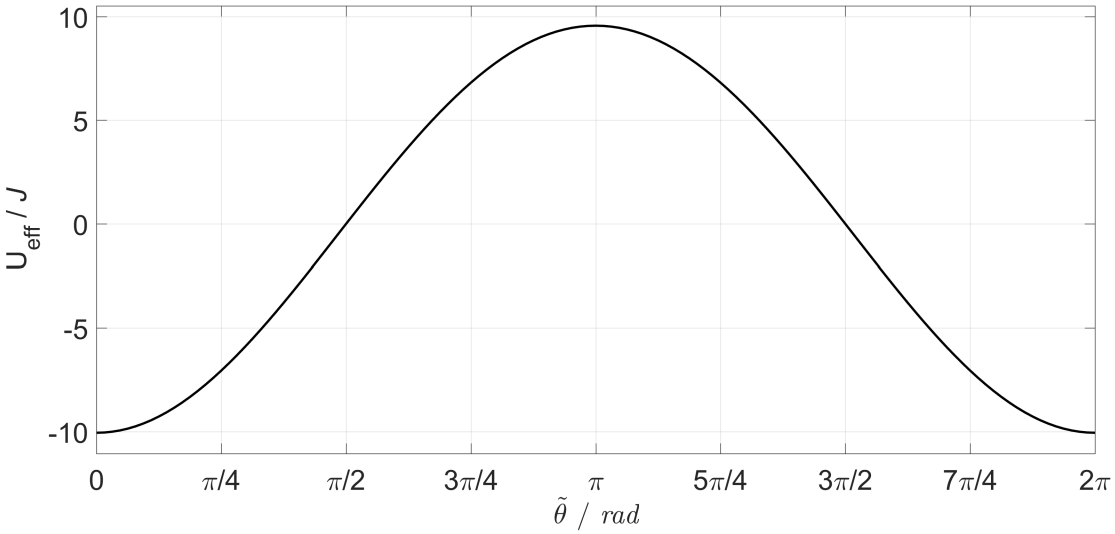

Figure 2.2: The effective potential for a Kapitza pendulum with sub threshold driving ($\omega = 2\pi \times 1.6$ Hz, $\beta = 0.32$)

Figure 2.3.

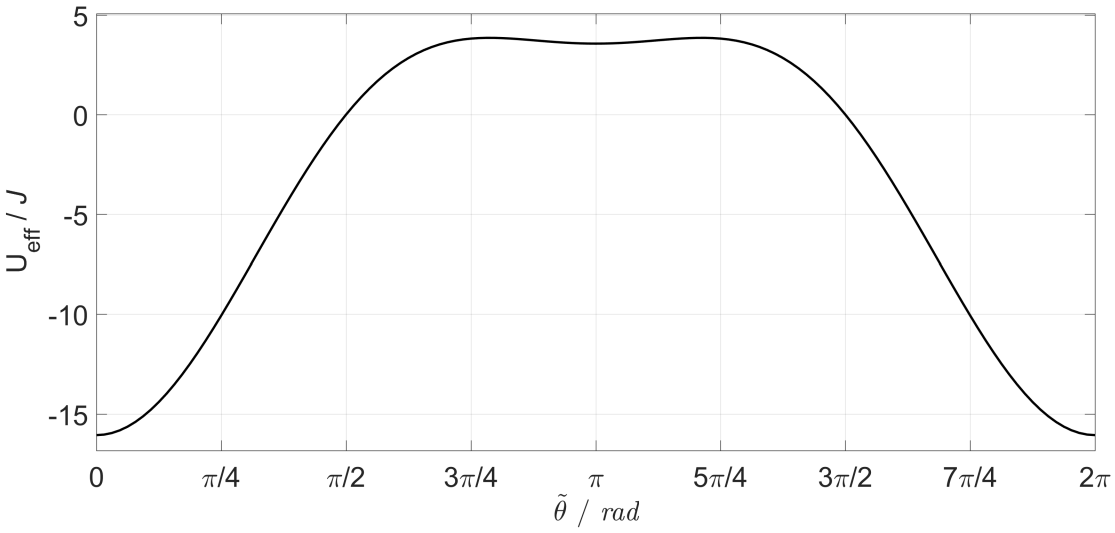

Figure 2.3: The effective potential for a Kapitza pendulum with base driving at just above threshold frequency ($\omega = 2\pi \times 8$ Hz, $\beta = 1.60$)

Here it is seen that the two maxima mentioned above have started to emerge, and between them the minimum at $\tilde{\theta} = \pi$. These are the first signs of the stability of the vertical/inverted position of the Kapitza pendulum. At this point it is a fairly weakly stable position and the maxima either side of it are not relatively very large. Thus it would only take a small push from some outside

source to make the pendulum move beyond these, at which point it would fall back down to a conventional downwards stability position.

Finally consider $\omega \approx 2\pi \times 16$ Hz. Now $\beta \approx 3.2$, a value well in excess of $\sqrt{2}$, and so very strong stabilisation at the inverted position would be expected. The potential can be seen in Figure 2.4.

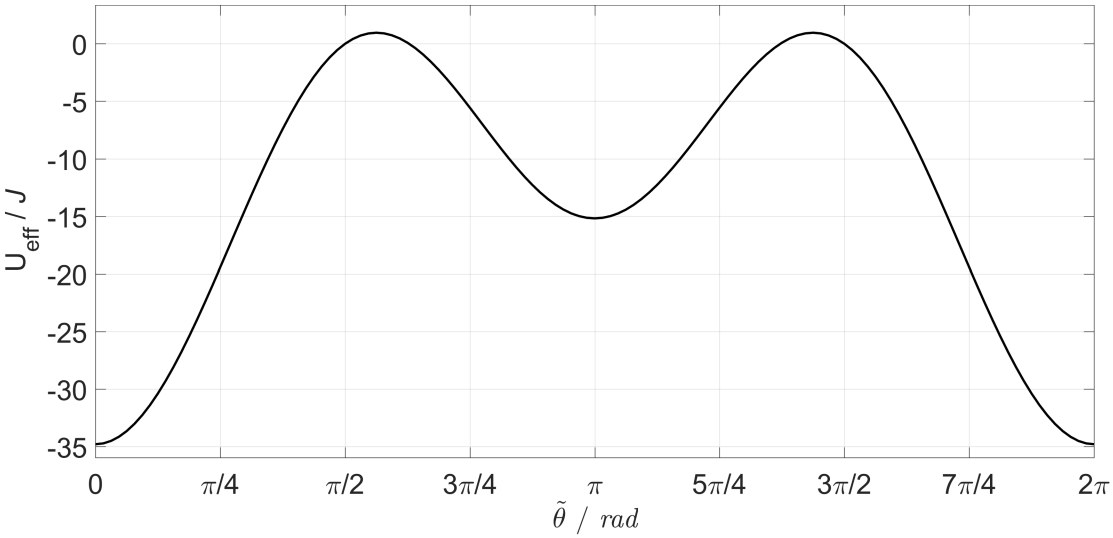

Figure 2.4: The effective potential for a Kapitza pendulum with base driving far above threshold frequency ($\omega = 2\pi \times 16$ Hz, $\beta = 3.2$)

Now the two maxima points either side of the inverted stability position are well established. They are far larger potential barriers with a deep potential well between them, and would require far more external energy to overcome and force the pendulum out of the inverted stability position. This now can be compared to a ball on a hill in the inverted stability position, only this time it sits in a small depression with walls either side of it, requiring energy to be contributed to lift the ball over the walls such that it can run back down the hill.

It has been demonstrated theoretically then, that when a sufficiently rapid and large oscillation is introduced to the base of a pendulum it is possible to create a new, counter-intuitive stability position of the pendulum which is oriented vertically upwards. It has been shown that via separation of this pendulum's

motion into fast and slow components, and the obtaining of an effective potential, it is possible to generalise this motion and predict for what parameter space it will occur, and how strongly the pendulum will stabilise.

2.2 Recent Literature Review

The legacy of Kapitza's investigation of this phenomenon, and the development of his separation of motions technique, has been substantial. As mentioned earlier in this chapter, it fostered a new subject area in physics, namely vibrational mechanics [47–49]. That is, the description and study of the effect of vibrations/periodic oscillations upon non-linear systems. This is a field of study which has applications across large areas, and scales of physics. It can be applied to macroscopic areas (as shown by Kapitza's pendulum), where, for example, it can help to describe the behaviour of granular media in vibrating vessels [53]. But vibrational mechanics also has applications on microscopic and nanoscopic scales in areas such as Brownian motors [54], atomic physics [55–58], and biophysics [59, 60].

Kapitza pendulum-style stability effects have also been suggested for application to a reactor [61]. Here there is a desirable intermediate state between all of an introduced mixture being used up (hot regime) and it passing through the reactor almost without transformation (cold regime). It is suggested that high frequency perturbations may bring about stability in this state. Indeed, it is even possible to find the application of Kapitza pendulum-like time scale separations outside of physics, in the completely different field of economics, and markets reaching new equilibria [62]. Moving back to areas more relevant to the studies in this thesis though, many investigations undertaken since Kapitza's work have sought not to apply vibrational mechanics to different disciplines and fields, but

to look further at his pendulum. Numerous authors make the connection between the equation of motion of a Kapitza pendulum, when linearising it about the equilibrium points, and the canonical form of the Mathieu equation: $y'' + \delta y' + (\alpha - \beta \sin \tau)y = 0$ (where y' denotes the time derivative of y), an equation already extensively applied in many fields of physics, and well studied for its stability characteristics [63]. Such approaches suggest that the averaging method applied by Kapitza may be limiting with regards to understanding certain areas of the stability map of such an open-loop control system [63]. Others have used techniques to look in more detail at the motion of the pendulum and found that the inverted stability position is not 'perfect', in the sense that it is not a stationary equilibrium position, but rather that small oscillations around the vertical position are seen [64]. Studies have been conducted into these oscillations, and indeed into widening the range of parameters and precision with which stability can be explained and predicted. Sub-harmonic and parametric resonances in the system have been linked to the lower and upper stability positions respectively, and it has also been demonstrated that by forcing the amplitude of the oscillations to ever larger values it is possible to make the pendulum destabilise in the upper position and enter a 'flutter' mode, whereby it exhibits oscillations about the vertical at half the drive frequency [46, 65–67].

In general, the investigations mentioned in the above paragraph kept the Kapitza pendulum experiment they were studying fundamentally the same. They analysed the motion in more depth, perhaps with different methods, or they stretched parameters such as the vibration amplitude and frequency to see how extremes of these changed the stability of the pendulum. There have however been numerous scientific enquiries made into systems very similar to the standard Kapitza pendulum, but with small changes introduced. The first group

of these, those with arguably the smallest changes made to the basic system, are those that maintain the open-loop control philosophy. What is meant by open-loop control here is a fixed input vibration/oscillation, one which is not modified according to the output (the pendulum's position and behaviour) through some sort of feedback system. Experiments of this nature have introduced changes such as: horizontal driving [52], investigating the modes that this yields, the lack of vertical stability but rich hanging configuration; differently shaped oscillations (rectangular not sinusoidal) [68], showing that these can achieve inverted stability at lower frequency driving than would otherwise be needed; or an extra oscillation by way of a vibrating surface upon which the pendulum sits [69], showing that this too yields a greater region of stability parameters and that the pendulum exhibits a 'beating' phenomenon.

The next group then must be the studies which change the Kapitza pendulum by making it a closed-loop experiment, adding some sort of feedback to the oscillations. It has been shown that a feedback term can be added that vanishes in the inverted position to restore normal Kapitza pendulum behaviour, but is sufficiently strong when the pendulum is in its downwards position to cause this to become unstable and the pendulum to actually swing up to its inverted state [70]. In addition the oscillations around the non-perfect upwards stability position mentioned earlier have been 'tamed' and made periodic and stable by use of feedback [71]. Then there are those who have built upon this closed-loop idea and the control it allows by investigating coupled pendula [72], even chains of coupled Kapitza pendula [73], and have shown that these extra excitations can be used to tame the chaos in these scenarios and make them dynamically stable.

Bridging the gap from coupled oscillators to analogues of the Kapitza pendulum, there are studies such as that of Lisovskii and Mansvetova [74] where the physics of the pendulum have been investigated via the analogue of single or a pair of

coupled compass arrows in an oscillating magnetic field, and the existence of two dynamically stabilised equilibrium states has been found in the coupled example. Striking a chord with the experiments documented in this thesis there are links drawn between the Kapitza pendulum and light trapping. It has been used as an analogy for the dynamically induced stabilisation of two-level atomic motion due to slight misalignment of the light fields of optical molasses [75]. Finally, discussions have been made of treating the dynamics of a solid placed in a vessel of fluid using the averaging methods seen [76]. Here an analogy has been drawn between the classical pendulum and a submerged spherical solid undergoing vibrations, a sort of hydrodynamic version of the Kapitza pendulum. These last examples are worthy of note in relation to the experiment within this thesis where an analogy for the Kapitza pendulum will be seen using both optical trapping and oscillations through a fluid. However the results presented herein will exhibit substantially different Kapitza pendulum-like stability to those already seen and the typical inverted positions.

It is clear then that the stability of Kapitza-like pendula, and the created field of vibrational mechanics, generate significant interest to this day, are applied successfully to a broad range of subject areas, and have complexities about them in given situations which are still being discovered.

Chapter 3

Beyond the Kapitza Pendulum - Theory

Until this point, almost all of the literature referenced that discusses a Kapitza pendulum-type setup has done so with a surrounding medium of air. At the very least they have considered the case of an under-damped pendulum, where the inverted stability position is observed. Indeed, as Carbo *et al.* [77] highlight, whilst the standard Kapitza pendulum has received much attention, the damped case has been studied far less extensively, with no apparent attempt at an experimental study except their own. What attention the damped case has received has sometimes produced seemingly contradictory ideas; with Leiber and Risken [78] and Bartucelli *et al.* [79] stating that dissipation has a destabilising effect on the inverted stability position, whilst Blackburn *et al.* [65] argued that 'finite damping enhances the stability of the inverted state'.

The exact experimental apparatus and set-up for this research will be covered in detail in the following chapter. However it is useful and will help with visualising the problem to give an idea of the layout of the experimental system now, at the beginning of these novel calculations and their simulations.

The experiment is a microscopic analogue of the Kapitza pendulum, in an environment with large damping. A silica bead, immersed in water (which provides the damping), is trapped using an optical tweezers. The beam path will encounter two computer controlled galvanometer mirrors which will be used to scan the trapping spot in a circle. This will be performed at high speed, such that the bead will see a solid ring of trap. This trapping ring provides the microscopic analogue for the circle of positions that a pendulum could occupy (imagine for comparison at this point, a rigid pendulum without gravity, free to move around in a circle in response to the smallest impulse). Then the computer controlled stage on which the microscope slide is mounted will be translated in one direction (sideways, to the right, in positive x, in the case of the experiment in this thesis). This translation will cause a translation of the water surrounding

the bead, and this will exert a force upon the bead and cause it to also move in the direction of stage translation. This provides the analogue of gravity in the experiment, forcing the bead to one side of the ring. Finally, the centre of the ring will be oscillated (as in the Kapitza pendulum) by simply moving the centre of the scanned circle via different voltage outputs to the galvanometer mirrors. It is hoped that this description will provide insight into what is being attempted in the following calculations and simulations.

3.1 Objectives

It is still felt that the theoretical conclusions the above studies reached, and the nature of the experiment undertaken, can be expanded upon and made more general to define more clearly the behaviour of a pendulum with periodic driving in the presence of damping. This study, therefore, seeks to go beyond the typical idealisations of the standard case, by explicitly considering the finite stiffness of the pendulum and an over-damped case, as well as a dissipative interaction with the surrounding medium. These regimes of damping will be analysed theoretically to determine the properties of their stability. These predictions will be tested using Brownian motion simulations and, finally, the scenarios will be realised experimentally on a microscopic scale with an analogue of the Kapitza pendulum featuring an immersed colloidal particle trapped using optical tweezers, and the experimental results will be compared with those from theory and simulation.

3.2 Contributions

The research in this theoretical, and the following experimental pendulum chapters was collaborative. In order to clarify my personal contribution to this work, I will outline here the individuals involved with this project and the areas in which they worked. David Cubero (University of Seville) worked on the theoretical calculations up to the effective potential. The analysis of this effective potential for the experimental stability positions and range of relevant parameters was performed by myself and my Ph.D. colleague, Thomas Smart (University College London). Thomas and I performed all of the experiments and acquired the data together, collaboratively. Where our contributions differ is that Thomas worked on the simulations of our experiment, to attempt to confirm the possibility of achieving novel stabilisation; whilst I wrote Labview and MATLAB software to achieve synchronised control of the galvanometer mirrors, microscope stage, and video recording, as well as to track the particles in the resulting videos and analyse their movement to deduce final stability positions and other properties which will be discussed in the experimental chapter.

3.3 Theoretical Calculations

To study the different dynamical regimes inherent in a vibrating pendulum set-up, it is first necessary to have an analytical model of such a pendulum with a finite stiffness and in the presence of dissipation. The theoretical work in Chapter 2 can be built upon and this dissipation incorporated, by considering a two-dimensional pendulum system with a single particle of mass, m, governed by equations of motion of the form:

$$
\begin{aligned}
m\ddot{x}(t) &= -\gamma\dot{x}(t) - \frac{\partial U}{\partial x}(x(t), y(t) - y_s(t)) + \zeta_x(t) \\
m\ddot{y}(t) &= -\gamma\dot{y}(t) - \frac{\partial U}{\partial y}(x(t), y(t) - y_s(t)) - F + \zeta_y(t),
\end{aligned} \tag{3.1}
$$

where γ is the viscous drag coefficient (and the form of the viscous damping is given by Stokes' Law [80], i.e. $\gamma = 6\pi\eta\alpha$, where η is the dynamic viscosity of the medium surrounding), $U(x(t), y(t))$ the annular pendulum potential, and F the pendulum confining force (weight in the case of a typical pendulum). The terms $\zeta_x(t)$ and $\zeta y(t)$ correspond to multivariate Gaussian noise used to account for the Brownian interactions of the colloidal particle with the surrounding fluid. Therefore these random forces have zero mean, $\langle\zeta_x(t)\rangle = \langle\zeta_y(t)\rangle = 0$, are uncorrelated with particle position, i.e. $\langle\zeta_x(t)x(t)\rangle = \langle\zeta_y(t)y(t)\rangle = 0$, and fluctuate much faster than the particle position, i.e $\langle\zeta_x(t)\zeta_x(t+\tau)\rangle = 2S\delta(\tau)$, where $2S$ is the intensity of the noise and the $\delta(\tau)$ is a Kronecker delta where the second argument is set to 0, such that $\delta = 1$ if $\tau = 0$, but $\delta = 0$ otherwise. S is given by $S = \gamma k_B T$ where k_B is the Boltzmann constant and T is the absolute temperature. As such these forces could be re-written as $\zeta_x(t) = \sqrt{2S}W(t)$ where $W(t)$ represents white noise (zero mean, unitary variance and time independent) [20]. These random forces will not alter the outcome of the theoretical analysis presented, and so beyond this point will be omitted, but have been included here for completeness of cataloguing the experiment. Similarly to Equation 2.13 the movement of the suspension point of the pendulum can be written as:

$$
y_s(t) = -a\cos(\omega t + \varphi_0), \tag{3.2}
$$

where a is the amplitude of the oscillations, ω their frequency, and here φ_0 has been introduced to denote the phase of the oscillations too.

To flesh out this analytical model a form for the potential, $U(x(t), y(t))$ is needed to emulate the radial confinement of the pendulum. The following quartic model is considered:

$$U(x(t), y(t)) = \frac{U_0}{L^4}(x(t)^2 + y(t)^2)(x(t)^2 + y(t)^2 - 2L^2). \tag{3.3}$$

This is a relatively simple form that encompasses the significant features of a pendulum of length L for some $U_0 > 0$. It also lends itself well to being manipulated for calculations. It can be seen that this form is well suited to modelling the basics of the pendulum by assigning values to L and U_0 and plotting this potential over a domain (Figure 3.1).

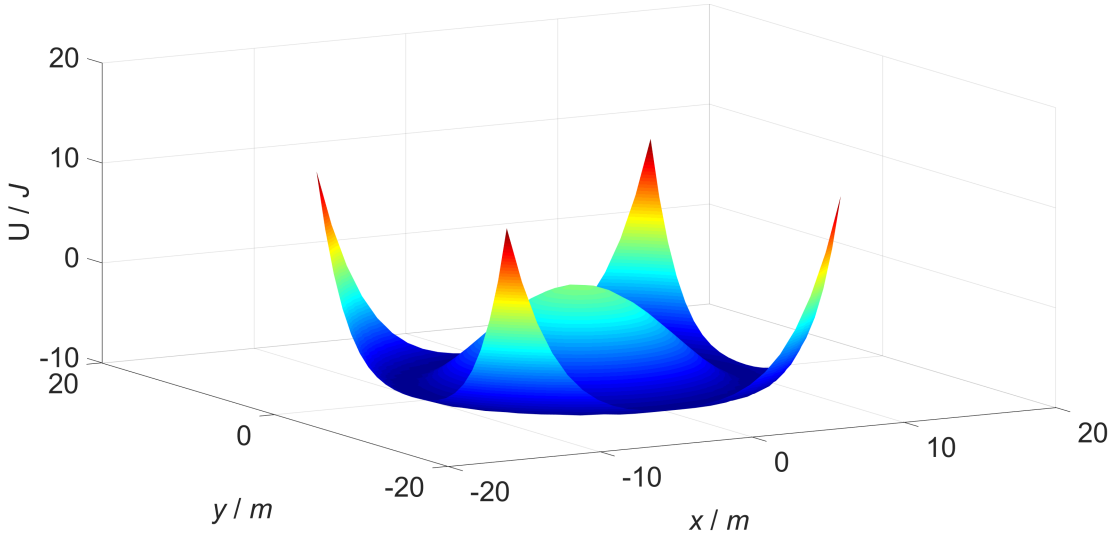

Figure 3.1: The landscape of a quartic potential energy expression for a pendulum, ($U_0 = 10$J, $L = 10$m). The colours correspond to the magnitude of U, from dark blue being smallest to dark red being largest.

This landscape shows steeply banked corners of potential with a well surrounding a central hill. It is therefore expected that a particle placed randomly in this landscape would move towards a minimum in this potential and so occupy a

position with radial coordinate L, in much the same way that a pendulum without gravity would be expected to occupy some position along its arc with no particular angular preference.

A useful analytical result for a property of this pendulum potential can be discovered by expanding it for small deviations about its minimum, L. It simplifies the expansion greatly (as it need only be an expansion of one variable not two) to substitute $x(t)$ and $y(t)$ with a radial coordinate variable, i.e. $r^2(t) = x^2(t) + y^2(t)$. N.B. This is not the bold $\boldsymbol{r} = (x, y, z)$ seen earlier, it is simply the radial coordinate. This substitution gives:

$$U(r(t)) = \frac{U_0}{L^4}(r^4(t) - 2r^2(t)L^2). \tag{3.4}$$

A Taylor expansion [81] is a standard tool used to approximate a function, $f(x)$, at some point, b, as follows:

$$f(x) = \sum_{n=0}^{\infty} \frac{f^{(n)}(b)}{n!}(x-b)^n, \tag{3.5}$$

with different orders of the summation taken depending upon the level of error tolerable in the approximation. Using this to second order to approximate the pendulum potential about L gives:

$$U(r(t)) \approx -U_0 + \frac{1}{2}\left(\frac{8U_0}{L^2}\right)(r(t) - L)^2. \tag{3.6}$$

This (discounting the potential offset U_0) is very similar to the form of the potential energy in a simple harmonic oscillator with a given spring constant, k,

and displacement, d, from its central position [43]:

$$E_{\mathrm{p}}(d) = \frac{1}{2}kd^2. \tag{3.7}$$

Direct comparison of Equations 3.6 and 3.7 suggests then that the spring constant equivalent in the pendulum potential is the term: $8U_0/L^2$. Using this in conjunction with the expression for the angular frequency of a simple harmonic oscillator [43], $\omega_0 = \sqrt{k/m}$ (where m is the mass of the oscillator), yields the following for the pendulum potential:

$$\omega_0 = \left(\frac{8U_0}{mL^2}\right)^{1/2}. \tag{3.8}$$

This quantity will be referred to as the proper frequency of this pendulum potential. It gives a measure of the rigidity of the pendulum. This insight can be explained qualitatively by the notion that this is the frequency of radial oscillations of the mass around the pendulum length. Just as a typical (mass on a spring oscillator) angular frequency is derived from a spring constant, k, which informs how strongly the mass is pulled back to a central position; this proper frequency is derived from the spring constant equivalent for the potential which informs how strongly the radial coordinate of the mass is restored to L. It follows that the pendulum will therefore be a truly rigid pendulum in the limit $\omega_0 \to \infty$.

A simple pendulum's natural oscillation frequency is given by, $\Omega = \sqrt{g/L}$ [43], but a more general expression suitable for any confining force is: $\Omega = \sqrt{F/mL}$. It can therefore be said that 'pendulum-like' behaviour and properties can be maintained in the system as long as: $\omega_0 \gg \Omega$. That is, the frequency describing how quickly the radial coordinate of the mass restores to the length L (proper frequency) is far greater, and so this happens on a much quicker time scale, than

that of the frequency of the natural oscillations of the pendulum.

What follows in this Section 3.3 is an analysis of the stability of this analytical pendulum model in different regimes of driving and friction.

3.3.1 A Dominant Driving Frequency

In the first instance, a very high frequency vibration of the point of suspension of the pendulum is considered. Let this driving frequency be sufficiently large that it is much larger than any other frequency of the system. Mathematically this can be expressed by taking the limit that $\omega \to \infty$, without changing the other parameters of the system. This is a significant departure from the standard Kapitza pendulum of Chapter 2, wherein the pendulum is immediately considered to be completely rigid. Such rigidity implies $\omega_0 \to \infty$, and certainly mandates that $\omega_0 \gg \omega$. Now the inequality $\omega \gg \omega_0$ holds, and what follows is an analysis of this case to find where the pendulum is stable.

Identifying the Effective Potential

It follows from the high frequency driving that the coordinates of the pendulum's mass will change on a much slower time scale than its base is being driven. As seen previously in Chapter 2, there is now a slow and a much faster motion in the system. This time, though, the resulting stability will be decidedly different. The time and phase dependence of the fast motion can be eliminated from the equation of motion by averaging. This averaging can be done by integration with a time interval of a period of the high frequency driving. This will yield an effective potential, analysis of which will deliver the stability positions of the pendulum in this regime. In the time period being averaged over, the coordinates $x(t)$ and $y(t)$ do not change appreciably. i.e. these can now be treated as

constants on this time scale such that:

$$\begin{aligned} x(t) &\to x \\ y(t) \to y \quad \Rightarrow \quad (y(t) - y_s(t)) &\to (y - y_s(t)). \end{aligned} \tag{3.9}$$

To begin this process of averaging, the y coordinate of the quartic potential (Equation 3.3) must first be modified to $(y - y_s(t))$ in order to reflect that this system has an oscillating base. This yields :

$$U(x, y - y_s(t)) = \frac{U_0}{L^4}\left(x^2 + (y - y_s(t))^2\right)\left(x^2 + (y - y_s(t))^2 - 2L^2\right). \tag{3.10}$$

Expanding and simplifying gives the following expression for this potential:

$$\begin{aligned} U(x, y - y_s(t)) = \frac{U_0}{L^4}\Big[& x^4 + (y - y_s(t))^4 + 2x^2(y - y_s(t))^2 \\ & - 2x^2L^2 - 2(y - y_s(t))^2L^2\Big]. \end{aligned} \tag{3.11}$$

The oscillations can then be accounted for and an effective potential for the driving dominated regime determined from the time average of this expression as follows:

$$U_{\text{eff,DD}}(x, y) = \langle U(x, y - y_s(t))\rangle = \frac{1}{T}\int_0^T U(x, y - y_s(t))dt, \tag{3.12}$$

where T is the period of the high frequency driving. The integration for the averaging of this expression is not too daunting as it is only the terms with

$(y - y_s(t))$ in Equation 3.11 that have this fast time period dependence, and of these there are only two kinds. First there is:

$$\begin{aligned}\langle (y - y_s(t))^2 \rangle &= \langle y^2 - 2yy_s(t) + y_s(t)^2 \rangle \\ &= \langle y^2 + 2ya\cos(\omega t + \varphi_0) + a^2\cos^2(\omega t + \varphi_0)^2 \rangle, \end{aligned} \tag{3.13}$$

where the expression for $y_s(t)$ from Equation 3.2 has been substituted in. Finding this time average is then just a simple matter of using some standard results for the integration of a cosine function, namely:

$$\langle \cos^n(\phi) \rangle = \frac{1}{2\pi}\int_0^{2\pi} \cos^n(\phi) d\phi = 0, \quad \text{for all odd } n, \text{ and,} \tag{3.14}$$

$$\langle \cos^2(\phi) \rangle = \frac{1}{2\pi}\int_0^{2\pi} \cos^2(\phi) d\phi = \frac{1}{2}, \tag{3.15}$$

where ϕ indicates a phase in the cosine functions and integrates over 2π for one complete cycle. Using these in Equation 3.13 yields:

$$\langle (y - y_s(t))^2 \rangle = y^2 + \frac{a^2}{2}. \tag{3.16}$$

The second of the fast time scale dependent terms in Equation 3.11 is:

$$\begin{aligned}\langle (y - y_s(t))^4 \rangle &= \langle (y^2 - 2yy_s(t) + y_s(t)^2)(y^2 - 2yy_s(t) + y_s(t)^2) \rangle \\ &= \langle y^4 - 4y^3 y_s(t) + 6y^2 y_s^2(t) - 4y y_s^3(t) + y_s^4(t) \rangle. \end{aligned}$$

It has already been shown that odd powered $y_s(t)$ terms will average to 0 and that $y_s^2(t) = 1/2$, therefore this only leaves the term with the 4^{th} power in the expression above to be calculated. Another standard result is:

$$\langle \cos^4(\phi) \rangle = \frac{1}{2\pi} \int_0^{2\pi} \cos^4(\phi) d\phi = \frac{3}{8}. \tag{3.17}$$

Therefore this second fast time scale dependent term for the effective potential can be written:

$$\langle (y - y_s(t))^4 \rangle = y^4 + 3y^2a^2 + \frac{3}{8}a^4. \tag{3.18}$$

These time averages found via integration can now be incorporated into finding an expression for $U_{\text{eff,DD}}(x, y)$. Inserting the expanded form of $U(x, y - y_s(t))$ from Equation 3.11 into the expression for the effective potential, $U_{\text{eff,DD}}(x, y)$ (Equation 3.12), and substituting in the time averaged solutions for $(y - y_s(t))^2$ and $(y - y_s(t))^4$ from Equations 3.16 and 3.18 respectively gives:

$$\begin{aligned} U_{\text{eff,DD}}(x, y) = \frac{U_0}{L^4} \Bigg[& x^4 + y^4 + 3y^2a^2 + \frac{3}{8}a^4 + 2x^2y^2 \\ & + x^2a^2 - 2x^2L^2 - 2y^2L^2 + a^2L^2 \Bigg]. \end{aligned} \tag{3.19}$$

After some rearrangement and factorisation this can be re-expressed as:

$$U_{\text{eff,DD}}(x, y) = \frac{U_0}{L^4} \left[(x^2 + y^2)(x^2 + y^2 - 2L^2) + a^2(x^2 + 3y^2 + \frac{3}{8}a^2 - L^2) \right]. \tag{3.20}$$

This is a useful factorised form because it is clear to see that the first two terms in this expression are then equivalent to the original quartic potential that was the starting point of these calculations. The expression above can therefore be re-written as:

$$U_{\text{eff,DD}}(x,y) = U(x,y) + \frac{1}{8}m\omega_0^2\left(\frac{a}{L}\right)^2\left[(x^2+3y^2) + \left(\frac{3}{8}a^2 - L^2\right)\right], \qquad (3.21)$$

where the proper frequency ω_0 has been pulled out as being a multiplier of the non-original potential terms. As happened in Chapter 2, the form of this equation allows for a check of internal consistency. Namely, all of the non-original potential terms to the right of this equation are multiplied by a^2; which means that were the amplitude of the vibrations decreased to 0 (eliminating them entirely), then this expression would reduce to simply being the original quartic potential. If this were the case, then the stability position would be the same as for a pendulum without a vibrating base, directly downwards, as would be expected. And so, there is an important logical consistency to this equation. The question now becomes one of at what point, with what driving amplitude, will this cease to be the case? When will the pendulum stabilise away from the typical downwards position as the driving amplitude is ramped up?

Analysing the Effective Potential for Stability

The equations of motion can be expressed by incorporating the effective potential deduced for this high frequency driving:

$$m\ddot{x} = -\gamma\dot{x} - \frac{\partial U_{\text{eff,DD}}(x,y)}{\partial x}$$
$$m\ddot{y} = -\gamma\dot{y} - \frac{\partial U_{\text{eff,DD}}(x,y)}{\partial y} - F. \tag{3.22}$$

In order to find when the stability position of the pendulum within this regime changes, the minimum of the conservative, position dependent forces in Equation 3.22 must be found. This corresponds to finding the solutions to the following pair of simulataneous equations:

$$-\frac{\partial U_{\text{eff,DD}}(x,y)}{\partial x} = 0 \tag{3.23}$$
$$-\frac{\partial U_{\text{eff,DD}}(x,y)}{\partial y} - F = 0. \tag{3.24}$$

The first obvious step to solving these equations is finding the partial derivatives of $U_{\text{eff,DD}}$. Using the fully expanded form of the potential in Equation 3.19, it can be seen that:

$$\begin{aligned}\frac{\partial U_{\text{eff,DD}}(x,y)}{\partial x} &= \frac{U_0}{L^4}\left[4x^3 + 4xy^2 + 2xa^2 - 4xL^2\right] \\ &= 2\frac{U_0}{L^4}x\left[a^2 + 2(x^2 + y^2 - L^2)\right],\end{aligned} \tag{3.25}$$

and similarly

$$\frac{\partial U_{\text{eff,DD}}(x,y)}{\partial x} = \frac{U_0}{L^4}\left[4y^3 + 6ya^2 4x^2 y - 4yL^2\right]$$
$$= 2\frac{U_0}{L^4}x\left[3a^2 + 2(x^2 + y^2 - L^2)\right], \tag{3.26}$$

which, when substituted back into the simultaneous equations, gives:

$$-2\frac{U_0}{L^4}x\left[a^2 + 2(x^2 + y^2 - L^2)\right] = 0 \tag{3.27}$$
$$-2\frac{U_0}{L^4}y\left[3a^2 + 2(x^2 + y^2 - L^2)\right] - F = 0. \tag{3.28}$$

Rearranging Equation 3.28 yields:

$$2y^2 = 2L^2 - 2x^2 - 3a^2 - \frac{FL^4}{2U_0 y}, \tag{3.29}$$

which can be substituted directly into Equation 3.27, where many terms then cancel out, to give:

$$-2\frac{U_0}{L^4}x\left[-2a^2 - \frac{FL^4}{2U_0 y}\right] = 0. \tag{3.30}$$

The model has been set up such that U_0 and L are non-zero. Therefore this expression can be true either if $x = 0$ or if the expression in the brackets comes to 0. Taking the former case would not provide any information about the stability of the system relative to the driving amplitude and would likely be indicative of normal pendulum stability at $(0, -L)$. Therefore the case of the bracket equalling 0 will be analysed to provide more detail of the system. Isolating and rearranging this leads to the following expression for the y coordinate stability position:

$$-2a^2 - \frac{FL^4}{2U_0 y} \tag{3.31}$$

$$\Rightarrow y = -\frac{FL^4}{4U_0 a^2}. \tag{3.32}$$

Substituting this back into Equation 3.28:

$$-2\frac{U_0}{L^4}\left(-\frac{FL^4}{4U_0a^2}\right)\left[3a^2 + 2(x^2 + \left(-\frac{FL^4}{4U_0a^2}\right)^2 - L^2)\right] - F = 0, \tag{3.33}$$

then rearranging for x gives:

$$x = \pm L\sqrt{1 - \frac{1}{2}\left(\frac{a}{L}\right)^2 - \left(\frac{FL^3}{4U_0a^2}\right)^2}. \tag{3.34}$$

Using the definitions of ω_0 and Ω, the solutions for x and y can be expressed more usefully in terms of the relative driving amplitude and the ratio of proper to natural oscillation frequency:

$$x = \pm L\sqrt{1 - \frac{1}{2}\left(\frac{a}{L}\right)^2 - 4\frac{\left(\frac{\Omega}{\omega_0}\right)^4}{\left(\frac{a}{L}\right)^4}} \tag{3.35}$$

$$y = -2L\frac{\left(\frac{\Omega}{\omega_0}\right)^2}{\left(\frac{a}{L}\right)^2}. \tag{3.36}$$

Now that these solutions have been obtained it is possible to analyse when and if the pendulum will begin to stabilise away from the typical downward position. This will be done by analysing its stability as the driving amplitude, a, is increased. Threshold values of this driving amplitude, a_1 and a_2 (or the relative

threshold amplitudes, a_1/L and a_2/L), at which the pendulum's stability behaviour changes between different regimes will now be derived.

It is known that the downwards position will be stable if $a/L = 0$, i.e. there is no high frequency driving. The question is, at what point, as a/L is increased, will this stability break down? This can be determined by stipulating in the simultaneous equation solutions that $y = -L$ (the downwards stability position). Applying this condition and rearranging for a/L yields:

$$\frac{a_1}{L} \approx \sqrt{2}\frac{\Omega}{\omega_0}. \tag{3.37}$$

The assumption of pendulum-like behaviour corresponded with the assumption that $\omega_0 \gg \Omega$, i.e. that the pendulum rigidity was sufficiently greater than the natural oscillation frequency. With this condition holding true, it must be the case that $\Omega/\omega_0 \ll 1$. Bearing this in mind and substituting this value for a_1/L into Equation 3.35 confirms that $x = 0$ is the corresponding x coordinate for this stability point. So the downwards stability position, $(0, -L)$, remains stable for driving amplitudes in the range $0 \leq a \leq a_1$.

As a increases beyond this value a_1, the stability position of the pendulum will conform to the Equations 3.35 and 3.36, but this time won't collapse nicely to the very simple form and values of the downwards stability position. A representation of these stability positions can be seen in Figure 3.2. The question then becomes: is there some upper value of driving amplitude at which these equations reduce down again to give some new simple stability values? And if so what are these values? Indeed this is the case, and the driving amplitude necessary can be picked out by inspection of Equations 3.35 and 3.36. These equations give the stable positions of the pendulum provided that: $a_1 < a < a_2$, where $a_2/L \approx \sqrt{2}$.

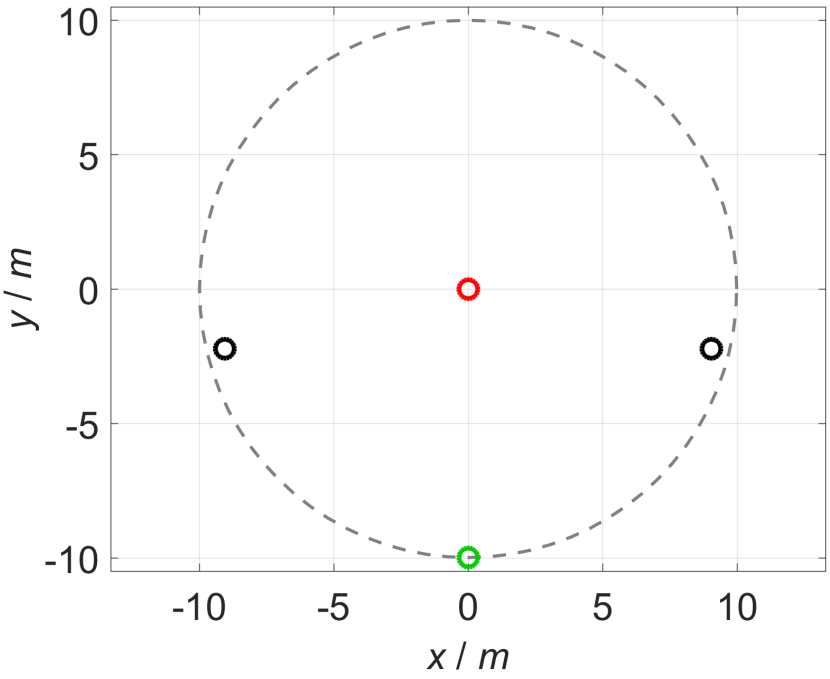

Figure 3.2: A representation of the stability positions of a pendulum with different base driving amplitudes. The standard downwards position (green circle) with $a < a_1$, the dominant driving frequency regime (black circles) for the condition $a_1 < a < a_2$, with $L = 10$ m, $a/L = 0.3$, and $\omega_0/\Omega = 10$, and a breakdown of the pendulum arc entirely when $a > a_2$ (red circle).

For driving amplitudes larger than this, $a_2 < a$, then it can be shown by substituting a_2 into these equations, and remembering that $\Omega/\omega_0 \ll 1$, that there is only one stability point. This point is found at approximately the pendulum's centre, $(0, 0)$. This may, at first, seem an odd result. This is, after all, nowhere near the typical arc of the pendulum. However, at this point the amplitude of the driving has increased to be $\sqrt{2}L$, nearly half as large again as the radius of the original pendulum arc. With such a large amplitude of driving, occuring at such a high relative frequency, it would not be the case that the pendulum would stay along its original arc.

It is worth noting at this point that, although non-typical stabilisation has been calculated, none of the three stability cases mentioned above correspond to the inverted stability which is characteristic of the Kapitza pendulum. In order to

witness that effect, a different regime featuring a very rigid pendulum is needed, one with a proper frequency which greatly exceeds the driving frequency.

3.3.2 Introducing High Friction

To go beyond these cases this dominant driving frequency is now scaled back and no longer considered in the limit $\omega \to \infty$. A regime with a rigid pendulum with respect to the driving (as was the case in the standard Kapitza pendulum) is once again considered, that is:

$$\omega_0 \gg \omega. \tag{3.38}$$

This time though, unlike in Chapter 2, friction is present. This causes some interesting new stability cases to emerge from the pendulum, as shown in the following analysis.

To begin with, the presence of large friction means that the condition of a rigid pendulum in Equation 3.38 is no longer sufficient to ensure observation of the Kapitza effect of inverted stabilisation. This is most easily explained qualitatively.

Assume all other parameters remain constant, while the friction coefficient γ is gradually increased. This friction from the surrounding medium opposes the motion of the pendulum. As such, an increasing γ will cause the pendulum's motion to become increasingly slower, and so will increase the system's response time, meaning that it takes longer and longer for the pendulum to reach its equilibrium positions. If γ continues to increase, and the system continues to slow, then the pendulum may never reach the inverted position; and for large enough friction coefficients, the response time of the system will drop to being

much slower than the driving frequency ω. In such a case it is irrelevant to attaining inverted stability, whether or not $\omega_0 \gg \omega$, because it has been rendered impossible by the large friction in the system. At which time, the pendulum can be said to have effectively been forced back into the dominant driving frequency regime once more.

Taking this train of thought further, quantitative consideration of this over-damped case proffers a significant result. If the friction is sufficiently large, then it can be said that the inertial terms, $m(\ddot{x}, \ddot{y})$, in Equation 3.1 are negligible compared to the magnitude of the friction forces, $-m\gamma'(\dot{x}, \dot{y})$. A new term, γ' has been introduced here to denote a mass-normalised friction coefficient, i.e. $\gamma' = \gamma/m$. This is introduced for convenience of notation and will be used heavily hereafter. It is a particularly convenient term since γ' has dimensions of frequency which makes it amenable to comparison with the other frequencies in the system (the proper, natural, and driving frequencies). The value of γ' relative to these frequencies, it will be shown, is very significant for determining the behaviour of the pendulum. Consideration of the over-damped case renders the equation of motion a first order differential equation:

$$m\gamma'\dot{y}(t) = -\frac{\partial U}{\partial y}\left(x(t), y(t) - y_s(t)\right) - F. \tag{3.39}$$

Substituting in from Equation 3.3 for U, differentiating this, dividing through by the friction, γ', and re-expressing the coefficient of the first term on the right in terms of the proper frequency yields the result:

$$m\dot{y} = \left(\frac{\omega_0^2}{\gamma'}\right)\left(\frac{m}{2L^2}\right)\left(y(t) - y_s(t)\right)\left(x(t)^2 + \left(y(t) - y_s(t)\right)^2 - L^2\right) - \frac{F}{\gamma'}. \tag{3.40}$$

From this, the characteristic time-scale for the relaxation of the pendulum length, τ_0 can be seen (by comparison to, for example, a first order rate equation) to be given by the ratio: $\tau_0^{-1} = \omega_0^2/\gamma'$. Inspection of Equation 3.40 shows that this is the largest intrinsic frequency in this system. The condition, therefore, for the driving frequency in this term to once again become dominant in the system has changed from the previous, weakly damped, case of $\omega \gg \omega_0$ to now being:

$$\omega \gg \frac{\omega_0^2}{\gamma'}, \tag{3.41}$$

in the over-damped case. This then, is how a large enough friction can render irrelevant the rigidity of a system relative to its driving frequency when it comes to attaining a Kapitza-like inverted stability position.

3.3.3 A Rigid Pendulum With Friction

Unfortunately, all that considering a rigid pendulum with respect to the driving in the previous section achieved was to bring back the case of the driving dominated pendulum, albeit via a different method. To get back to the goal of finally moving beyond this dominant driving, the following steps must be taken. A reduced modulation frequency, ω, is still considered such that the driving dominated regime is avoided in terms of the driving frequency at least. The truly rigid pendulum limit of $\omega_0 \to \infty$ must be considered, but with the caveat that γ'/ω_0 is kept constant (a constant which can be zero), such that this friction does not escalate again in the same manner, and the weakly damped regime can be maintained. This limit implies that $\omega \ll \omega_0$ (as was the case previously for the standard Kapitza pendulum). By maintaining both this moderate amount of

friction and driving frequency it is possible to access the regime where:

$$\omega \ll \frac{\omega_0^2}{\gamma'}. \tag{3.42}$$

That is, the driving frequency is now smaller than the characteristic time scale for the relaxation of the pendulum length. This could be rewritten as: $\frac{\gamma'}{\omega_0} \ll \frac{\omega_0}{\omega}$, to show how this inequality is easily satisfied, with γ'/ω_0 on the left hand side now being kept a constant, as $\omega_0 \to \infty$. Or indeed this could be rearranged as a condition on the friction in the experiment being much smaller than the size of the rigidity relative to the driving: $\gamma' \ll \frac{\omega_0^2}{\omega}$. In this case the expressions for threshold amplitude and stable angle can no longer be approximated into forms that only include the pendulum frequencies Ω and ω [82]. The friction coefficient must also be included as will be seen below.

Changing to a Polar Coordinate System

It is convenient at this point, to change the coordinate system from a Cartesian to a polar system. This will make significant results about the system more immediately obvious, as angles of equilibrium are of the primary interest and this system gives a whole coordinate for them. Let these coordinates be defined relative to the pendulum's base as follows:

$$x(t) = r(t)\sin\phi(t), \tag{3.43}$$

$$y(t) = -r(t)\cos\phi(t) + y_s(t), \tag{3.44}$$

where again the non-bold r corresponds to the radial coordinate. N.B. From this

point onwards, unless otherwise stated, the time dependencies will be omitted in the interests of saving time and eliminating unnecessary bulk in the display of the equations. The time derivatives of these are therefore given by:

$$\frac{\partial x}{\partial t} = \dot{r}\sin\phi + r\dot{\phi}\cos\phi, \tag{3.45}$$

$$\frac{\partial y}{\partial t} = -\dot{r}\cos\phi + r\dot{\phi}\sin\phi + \dot{y}_s, \tag{3.46}$$

$$\frac{\partial^2 x}{\partial t} = \ddot{r}\sin\phi + 2\dot{r}\dot{\phi}\cos\phi + r\ddot{\phi}\cos\phi - r\dot{\phi}^2\sin\phi, \tag{3.47}$$

$$\frac{\partial^2 y}{\partial t} = -\ddot{r}\cos\phi + 2\dot{r}\dot{\phi}\sin\phi + r\ddot{\phi}\sin\phi + r\dot{\phi}^2\cos\phi + \ddot{y}_s. \tag{3.48}$$

Substituting these time derivatives into the equations of motion, Equation 3.1, and utilising the differentiated form of the pendulum potential and re-expression of coefficients seen in Equation 3.40 gives the following two equations:

$$\begin{aligned} m\Big(\ddot{r}\sin\phi + 2\dot{r}\dot{\phi}\cos\phi + r\ddot{\phi}\cos\phi - r\dot{\phi}^2\sin\phi\Big) \\ = -m\gamma'\big(\dot{r}\sin\phi + r\dot{\phi}\cos\phi\big) - \frac{m\omega_0^2}{2L^2}\big(r\sin\phi\big)\big(r^2 - L^2\big), \end{aligned} \tag{3.49}$$

$$\begin{aligned} m\Big(-\ddot{r}\cos\phi + 2\dot{r}\dot{\phi}\sin\phi + r\ddot{\phi}\sin\phi + r\dot{\phi}^2\cos\phi + \ddot{y}_s\Big) \\ = -m\gamma'\big(-\dot{r}\cos\phi + r\dot{\phi}\sin\phi + \dot{y}_s\big) - \frac{m\omega_0^2}{2L^2}\big(-r\cos\phi\big)\big(r^2 - L^2\big) - F. \end{aligned} \tag{3.50}$$

If these are labelled as equations A and B respectively, then calculating:

$$(A\cos\phi + B\sin\phi) \qquad \text{and} \qquad (A\sin\phi - B\cos\phi)$$

leads (after significant cancelling of equivalent terms) to the following results respectively:

$$m\Big(r\ddot{\phi} + 2\dot{r}\dot{\phi} + \ddot{y_s}\sin\phi\Big) = -m\gamma'\big(r\dot{\phi} + \dot{y_s}\sin\phi\big) - F\sin\phi \tag{3.51}$$

$$m\Big(\ddot{r} - r\dot{\phi}^2 - \ddot{y_s}\cos\phi\Big) = -m\gamma'\big(\dot{r} - \dot{y_s}\cos\phi\big) - \frac{m\omega_0^2}{2L^2}r\big(r^2 - L^2\big) + F\cos\phi \tag{3.52}$$

Deriving an Equation of Motion for the Angular Coordinate

With these equations of motion re-expressed in a polar coordinate system, it is more easily possible to immediately simplify these with an approximation. The simplification in mind can be applied to the potential term (the penultimate term) in Equation 3.52. Let $f(r) = -\frac{m\omega_0^2}{2L^2}r\big(r^2 - L^2\big)$. A Taylor series expansion about the value $r = L$ (the length of the pendulum/radius of the pendulum's arc) to a few terms would then look as follows:

$$f(r)|_{r=L} \approx f(L) + f'(L)(r - L) + \frac{f''(L)}{2!}(r - L)^2. \tag{3.53}$$

This pendulum is currently being considered in the limit $\omega_0 \to \infty$, i.e. it is a rigid pendulum. Certainly, its proper frequency is much greater than its natural frequency ($\Omega/\omega_0 \ll 1$), thus it is very stiff compared to the time frame of any natural oscillations or position relaxations. With these limits and inequalities in mind it is a natural and reasonable assumption to make that any deviation of the radial coordinate from the pendulum length is very small indeed, i.e.
$dr = (r - L) \ll 1$. With this property established, it can be seen that any orders of the Taylor expansion in Equation 3.53 above the second/linear term will very

quickly tend towards 0. The result $f(L) = 0$ can very quickly be seen. So all that is left to do before using this approximation is to find the derivate of $f(r)$.

$$f'(r) = \frac{\partial}{\partial r}\left(-\frac{m\omega_0^2}{2L^2}r\big(r^2 - L^2\big)\right) = -\frac{m\omega_0^2}{2L^2}\big(3r^2 - L^2\big) \tag{3.54}$$

Substituting into this $r = L$ gives $f'(L) = -m\omega_0^2$. Therefore the equation of motion 3.52 with this linear approximation to the potential is:

$$m\left(\ddot{r} - r\dot{\phi}^2 - \ddot{y}s\cos\phi\right) = -m\gamma'\big(\dot{r} - \dot{y}_s\cos\phi\big) - m\omega_0^2(r - L) + F\cos\phi \tag{3.55}$$

It is a fairly fast procedure to extract from this equation an expression for just the radial coordinate $r(t)$. Expanding and rearranging gives the following:

$$m\omega_0^2(r - L) - m\gamma'\dot{y}_s\cos\phi - m\ddot{y}_s\cos\phi + m\ddot{r} = mr\dot{\phi}^2 + F\cos\phi - m\gamma'\dot{r}. \tag{3.56}$$

Inspection of the right hand side of Equation 3.56 shows that all of the terms present make up one side of an equation of motion in the radial direction. There is a centripetal force term, $mr\dot{\phi}^2$, a gravitational/confining force term, $F\cos\phi$, and a viscous/friction/damping force term, $m\gamma'\dot{r}$. These terms can thus be equated to the final, inertia style term on the left hand side of the equation, leading to all four terms being cancelled out. This therefore leaves:

$$m\omega_0^2(r - L) - m\gamma'\dot{y}_s\cos\phi - m\ddot{y}_s\cos\phi = 0, \tag{3.57}$$

which after a small rearrangement yields an expression for the radial coordinate;

which will either experience fast oscillations around its equilibrium length, L (weakly damped), or a rapid decay to it (over-damped):

$$r(t) = L + \frac{\ddot{y}_s \cos\phi + \gamma' \dot{y}_s \cos\phi}{\omega_0^2}. \tag{3.58}$$

With this equation for the radial coordinate isolated, it is possible to use this to obtain an equation of motion for the angular coordinate. This can be done by substituting this Equation 3.58 back into Equation 3.51:

$$\begin{aligned} m\Bigg[\ddot{\phi}\bigg(L + \frac{1}{\omega_0^2}\big(\ddot{y}_s\cos\phi + \gamma'\dot{y}_s\cos\phi\big)\bigg) + 2\dot{\phi}\frac{\partial}{\partial t}\bigg(L + \frac{1}{\omega_0^2}\big(\ddot{y}_s\cos\phi + \gamma'\dot{y}_s\cos\phi\big)\bigg) \\ + \ddot{y}_s\sin\phi\Bigg] = -m\gamma'\Bigg[\dot{\phi}\bigg(L + \frac{1}{\omega_0^2}\big(\ddot{y}_s\cos\phi + \gamma'\dot{y}_s\cos\phi\big)\bigg) + \dot{y}_s\sin\phi\Bigg] - F\sin\phi. \end{aligned} \tag{3.59}$$

Before seeking to expand this out any further it pays to once more be mindful of the 'rigid pendulum' scenario, i.e. the limit $\omega_0 \to \infty$, and that $\gamma'/\omega_0 = \text{constant}$. Bearing these in mind, all terms with a divisor of ω_0^2 vanish, with the exception of one, which has a numerator of γ'^2. After eliminating these terms and rearranging, the equation of motion for the angular coordinate is found to be:

$$mL\ddot{\phi} = -m\gamma'\left(L\dot{\phi} + \dot{y}_s\sin\phi\right) - \left(F + m\ddot{y}_s\right)\sin\phi - m\left(\frac{\gamma'}{\omega_0}\right)^2 \dot{y}_s\dot{\phi}\cos\phi. \tag{3.60}$$

It is once again reassuring to note the similarities between this and previous results, and to make internal checks of consistency. This equation makes more general Kapitza's original result, seen previously in Equation 2.24 (Section 2.1.2),

by adding to it. Comparison of the two, for example, shows that the second bracket on the right of Equation 3.60 is equivalent to the right hand side of that original equation (where the mL factor has been divided through and the natural frequency, Ω, has been used). With this new expression, moderate friction coefficients are accommodated in the range $0 < \gamma' \ll \omega_0^2/\omega$. Above this intermediate regime when large frictions occur, it is already known that the regime where driving begins to dominate is reached, as discussed previously.

As mentioned at the beginning of this chapter, although there is far less literature than for the un-damped case, others have previously considered a Kapitza pendulum in the presence of dissipation. At this point, with the above result establised these are reconsidered. The previous studies [65, 77, 79] considered an equation of motion like the one above but neglect the final term in Equation 3.60. This is as expected with an infinitely rigid pendulum ($\omega_0 = \infty$), rather than a pendulum that is rigid, but has a finite stiffness as is the case here. However they also omit the term proportional to $\dot{y}_s \sin\phi$, which takes into account the vertical vibrations of the base of the pendulum and arises because the damping force is proportional to the velocity of the pendulum relative to the medium. In the one study where it was mentioned earlier that an experiment was enacted [77], this term is absent because the damping does not originate from a surrounding fluid, but rather from a specially designed magnetic braking system used in the experiment.

Identifying an Effective Potential

Now that an equation of motion for ϕ has been found, the job of separating this out into fast and slow components can be done, just as it was for the standard case in Chapter 2, in order to facilitate finding the effective potential of the pendulum in this scenario. Before beginning this, a division through by the

coefficients of $\ddot{\phi}$ is performed to simplify the equation and reintroduce the natural frequency, ($\Omega^2 = F/mL$):

$$\ddot{\phi} = -\gamma'\left(\dot{\phi} + \frac{\dot{y_s}}{L}\sin\phi\right) - \left(\Omega^2 + \frac{\ddot{y_s}}{L}\right)\sin\phi - \left(\frac{\gamma'}{\omega_0}\right)^2\frac{\dot{y_s}}{L}\dot{\phi}\cos\phi. \tag{3.61}$$

First let the angle, ϕ, consist of the sum of a slow variable, $\tilde{\phi}$, and a fast variable, ξ:

$$\phi = \tilde{\phi} + \xi, \tag{3.62}$$

where $\xi = -(y_s/L)\sin\tilde{\phi}$. Operating under the assumption that ξ is a small angular deviation, then the small angle approximations given in Equation 2.28 are once more applicable here. Since time derivatives of both ξ and y_s will come to be used in this derivation, both are defined here first:

$$y_s = -a\cos(\omega t + \phi_0), \quad \dot{y_s} = a\omega\sin(\omega t + \phi_0), \quad \ddot{y_s} = a\omega^2\cos(\omega t + \phi_0), \tag{3.63}$$

and

$$\begin{aligned}\xi &= \frac{a}{L}\sin\tilde{\phi}\cos(\omega t + \phi_0),\\ \dot{\xi} &= -\frac{a}{L}\omega\sin\tilde{\phi}\sin(\omega t + \phi_0) + \frac{a}{L}\dot{\tilde{\phi}}\cos\tilde{\phi}\cos(\omega t + \phi_0).\end{aligned} \tag{3.64}$$

In addition to this, a reminder of and expansion of the following results from Equations 3.14 and 3.15 will be helpful in this section of calculations when averaging over the fast driving is performed:

$$\langle \cos(\omega t + \phi_0) \rangle = 0 \qquad \langle \sin(\omega t + \phi_0) \rangle = 0 \tag{3.65}$$

$$\langle \cos^2(\omega t + \phi_0) \rangle = \frac{1}{2} \qquad \langle \sin^2(\omega t + \phi_0) \rangle = \frac{1}{2} \tag{3.66}$$

$$\langle \cos^2(\omega t + \phi_0) \sin(\omega t + \phi_0) \rangle = 0 \qquad \langle \cos(\omega t + \phi_0) \sin^2(\omega t + \phi_0) \rangle = 0 \tag{3.67}$$

$$\langle \cos(\omega t + \phi_0) \sin(\omega t + \phi_0) \rangle = 0 \tag{3.68}$$

To make the calculation easier to perform and to display, Equation 3.61 will be dealt with in three parts, A, B, and C, according to each of the three groups of terms present ($\ddot{\phi} = A + B + C$). First there is:

$$\begin{aligned} A &= -\gamma' \left(\dot{\phi} + \frac{\dot{y_s}}{L} \sin\phi \right) \\ &= -\gamma' \left(\dot{\tilde{\phi}} + \dot{\xi} + \frac{a\omega}{L} \sin(\omega t + \phi_0) \big(\sin\tilde{\phi} + \xi \cos\tilde{\phi} \big) \right) \\ &= -\gamma' \left(\dot{\tilde{\phi}} - \frac{a}{L}\omega \sin\tilde{\phi} \sin(\omega t + \phi_0) + \frac{a}{L} \dot{\tilde{\phi}} \cos\tilde{\phi} \cos(\omega t + \phi_0) \right. \\ &\qquad \left. + \frac{a}{L}\omega \sin(\omega t + \phi_0) \big(\sin\tilde{\phi} + \xi \cos\tilde{\phi} \big) \right). \end{aligned}$$

Using the trigonometric averages above to average over the fast driving for expression A, it can be seen that all but one of the terms vanish:

$$\langle A \rangle = -\gamma' \dot{\tilde{\phi}}. \tag{3.69}$$

Now part B is tackled:

$$\begin{aligned} B &= -\left(\Omega^2 + \frac{\ddot{y_s}}{L}\right)\sin\phi \\ &= -\left(\Omega^2 + \frac{a}{L}\omega^2\cos\left(\omega t + \phi_0\right)\right)\left(\sin\tilde{\phi} + \xi\cos\tilde{\phi}\right) \\ &= -\left(\Omega^2 + \frac{a}{L}\omega^2\cos\left(\omega t + \phi_0\right)\right)\left(\sin\tilde{\phi} + \frac{a}{L}\sin\tilde{\phi}\cos\tilde{\phi}\cos\left(\omega t + \phi_0\right)\right). \end{aligned}$$

Fully expanding these brackets out is not necessary, as it can be seen by inspection that after applying the trigonometric averages, the only terms which will endure will look as follows:

$$\langle B\rangle = -\Omega^2\sin\tilde{\phi} - \frac{1}{2}\left(\frac{a}{L}\right)^2\omega^2\sin\tilde{\phi}\cos\tilde{\phi}. \tag{3.70}$$

For the final step before recombining all three parts, expression C must be tackled.

$$\begin{aligned} C &= -\left(\frac{\gamma'}{\omega_0}\right)^2\frac{\dot{y_s}}{L}\dot{\phi}\cos\phi \\ &= -\left(\frac{\gamma'}{\omega_0}\right)^2\frac{a}{L}\omega\sin\left(\omega t + \phi_0\right)\left(\cos\tilde{\phi} - \xi\sin\tilde{\phi}\right)\left(\dot{\tilde{\phi}} + \dot{\xi}\right) \\ &= -\left(\frac{\gamma'}{\omega_0}\right)^2\frac{a}{L}\omega\sin\left(\omega t + \phi_0\right)\left(\cos\tilde{\phi} - \frac{a}{L}\sin^2\tilde{\phi}\cos\left(\omega t + \phi_0\right)\right)\ldots \\ &\qquad \ldots\times\left(\dot{\tilde{\phi}} - \frac{a}{L}\omega\sin\tilde{\phi}\sin\left(\omega t + \phi_0\right) + \frac{a}{L}\dot{\tilde{\phi}}\cos\tilde{\phi}\cos\left(\omega t + \phi_0\right)\right) \end{aligned}$$

Although a little more difficult this time it can once again be seen by inspection (or by expanding out the brackets) that all but one of these terms will average

out leaving only:

$$\langle C \rangle = \frac{1}{2}\left(\frac{\gamma'}{\omega_0}\right)^2 \left(\frac{a}{L}\right)^2 \omega^2 \sin\tilde{\phi}\cos\tilde{\phi}. \tag{3.71}$$

All three parts can now be recombined to give an expression for the acceleration of the slow component:

$$\begin{aligned} \Rightarrow \ddot{\phi} &= \ddot{\tilde{\phi}} + \ddot{\xi} \quad = A + B + C \\ \Rightarrow \langle\ddot{\phi}\rangle &= \langle\ddot{\tilde{\phi}} + \ddot{\xi}\rangle = \langle A + B + C\rangle \\ \Rightarrow \langle\ddot{\phi}\rangle &= \langle\ddot{\tilde{\phi}}\rangle + \langle\ddot{\xi}\rangle = \langle A\rangle + \langle B\rangle + \langle C\rangle, \end{aligned}$$

N.B. It has not been explicitly stated but it can be seen relatively trivially that all terms in $\ddot{\xi}$ would feature either $\cos(\omega t + \phi_0)$ or $\sin(\omega t + \phi_0)$ to a single power, thus this term would, after time averaging over the fast driving, become 0. Therefore using the results from Equations 3.69, 3.70, and 3.71:

$$\begin{aligned} \langle\ddot{\tilde{\phi}}\rangle &= -\gamma'\dot{\tilde{\phi}} - \Omega^2 \sin\tilde{\phi} - \frac{1}{2}\left(\frac{a}{L}\right)^2 \omega^2 \sin\tilde{\phi}\cos\tilde{\phi} + \frac{1}{2}\left(\frac{\gamma'}{\omega_0}\right)^2 \left(\frac{a}{L}\right)^2 \omega^2 \sin\tilde{\phi}\cos\tilde{\phi} \\ \langle\ddot{\tilde{\phi}}\rangle &= -\gamma'\dot{\tilde{\phi}} - \Omega^2 \sin\tilde{\phi} - \frac{1}{2}\left(\frac{a}{L}\right)^2 \omega^2 \sin\tilde{\phi}\cos\tilde{\phi}\left(1 - \left(\frac{\gamma'}{\omega_0}\right)^2\right) \\ \langle\ddot{\tilde{\phi}}\rangle &= -\gamma'\dot{\tilde{\phi}} - \Omega^2\left(\sin\tilde{\phi} + \frac{1}{4}\left(\frac{a}{L}\right)^2 \left(\frac{\omega}{\Omega}\right)^2 \left(1 - \left(\frac{\gamma'}{\omega_0}\right)^2\right)\sin 2\tilde{\phi}\right) \\ \langle\ddot{\tilde{\phi}}\rangle &= -\gamma'\dot{\tilde{\phi}} - \Omega^2\left(\sin\tilde{\phi} + \frac{\Lambda}{2}\sin 2\tilde{\phi}\right), \end{aligned} \tag{3.72}$$

where:

$$\Lambda = \frac{1}{2}\left(\frac{a}{L}\right)^2\left(\frac{\omega}{\Omega}\right)^2\left(1-\left(\frac{\gamma'}{\omega_0}\right)^2\right). \tag{3.73}$$

Therefore, by inserting a mass term and comparing this to an equation of motion featuring a differential of a potential:

$$\begin{aligned} m\ddot{\tilde{\phi}} &= -m\gamma'\dot{\tilde{\phi}} - m\Omega^2\left(\sin\tilde{\phi} + \frac{\Lambda}{2}\sin 2\tilde{\phi}\right) \\ m\ddot{\tilde{\phi}} &= -m\gamma'\dot{\tilde{\phi}} - \frac{dU_{\text{eff,F}}(\tilde{\phi})}{d\tilde{\phi}}, \end{aligned} \tag{3.74}$$

where $U_{\text{eff,F}}$ is the effective potential in this regime with moderate friction, it can be seen that:

$$\begin{aligned} \frac{dU_{\text{eff,F}}(\tilde{\phi})}{d\tilde{\phi}} &= m\Omega^2\left(\sin\tilde{\phi} + \frac{\Lambda}{2}\sin 2\tilde{\phi}\right) \\ \Rightarrow U_{\text{eff,F}}(\tilde{\phi}) &= -m\Omega^2\left(\cos\tilde{\phi} + \frac{\Lambda}{4}\cos 2\tilde{\phi}\right). \end{aligned} \tag{3.75}$$

Locating the Stable Equilibrium Positions

With this effective potential, $U_{\text{eff,F}}(\tilde{\phi})$ calculated, it can now be analysed in order to determine the location of the stable equilibrium positions for this system of a finitely rigid pendulum with damping (but not over-damped); and to determine how these positions change whilst a key system parameter, the friction coefficient, is varied. Perhaps the easiest way to do this, is to observe a plot of the effective potential as the dimensionless variable Λ, (which contains the

friction coefficient, γ'), is altered. The multiplicative constants, $m\Omega^2$, will have no effect on the angular position of the stable points, merely how strong the stabilisation is. Therefore, for the sake of simplicity, the expression that will be plotted is: $f(\tilde{\phi}) = U_{\text{eff,F}}(\tilde{\phi})/(m\Omega^2)$.

What emerges from this analysis is that there are three distinct regimes of stability depending upon the value of Λ, and so ultimately γ'. The first of these is seen when:

$$\Lambda > 1, \tag{3.76}$$

which has a potential energy landscape as seen in Figure 3.3, plotted for $\Lambda = 2.5$.

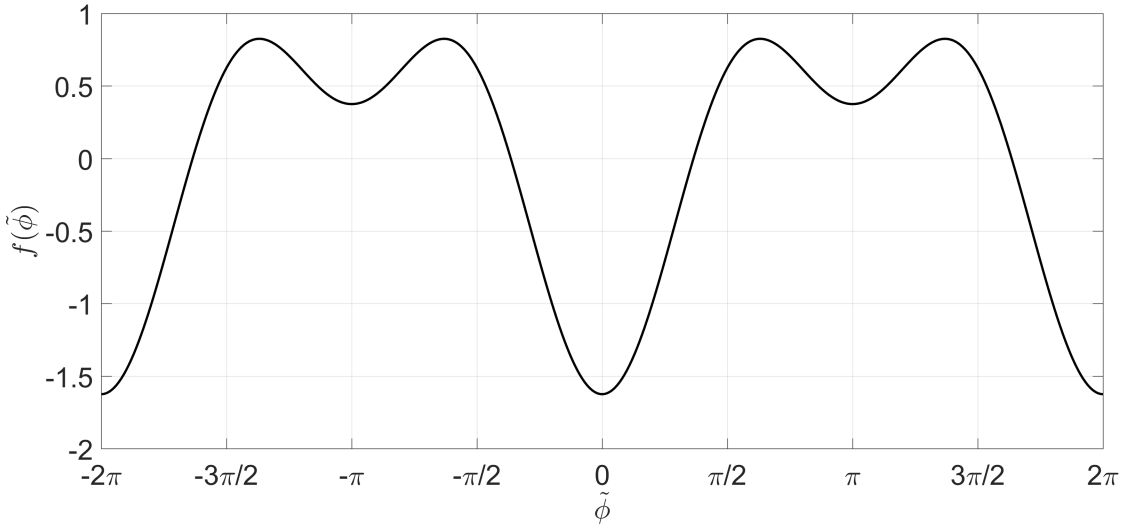

Figure 3.3: The form of the angular potential energy of the damped, finitely rigid, pendulum with dimensionless parameter $\Lambda = 2.5$.

Figure 3.3 has been plotted from $\tilde{\phi} = -2\pi \to 2\pi$. A full circle, of course, only needs a range of 2π; but plotting the angle in this way allows for both sides of potential troughs to be seen without any breaks, and so stability positions to be more easily identified and appreciated. It is found that when $\Lambda > 1$, the Kapitza effect is seen once again. That is, the inverted position at the top of the

pendulum becomes stable (as evidenced by the trough at $\tilde{\phi} = \pm\pi$. This is of course in addition to the standard downwards position still being stable.

If Λ is decreased further into the range:

$$-1 < \Lambda < 1, \tag{3.77}$$

then another new stability behaviour exists as seen in Figure 3.4, plotted for $\Lambda = 0$.

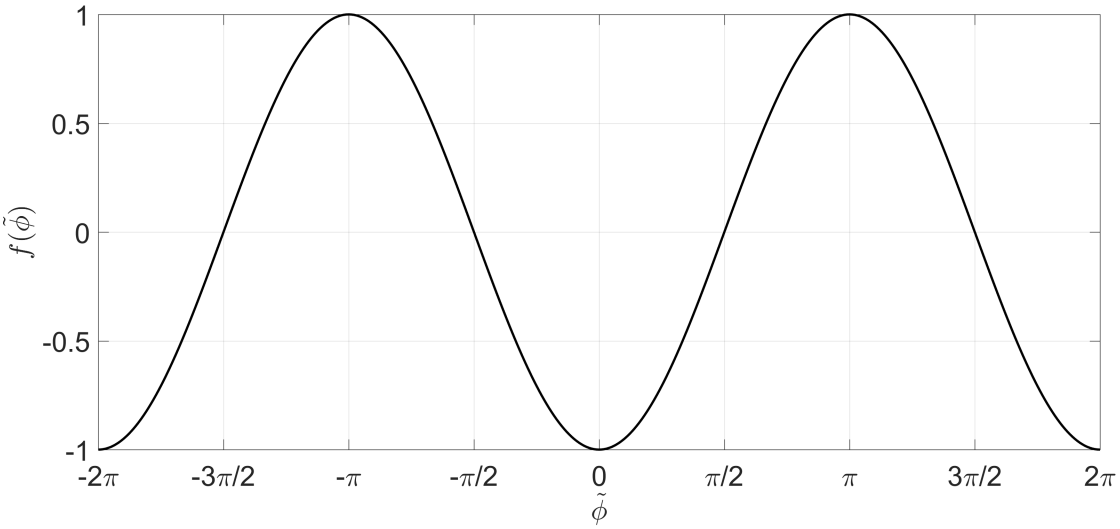

Figure 3.4: The form of the angular potential energy of the damped, finitely rigid, pendulum with dimensionless parameter $\Lambda = 0$.

Figure 3.4 shows that when inequality $-1 < \Lambda < 1$ is satisfied there is only one stable equilibrium position for the pendulum. This corresponds with the standard, vertically downwards, stability position of an unperturbed pendulum.

Finally, decreasing Λ even further into the region:

$$\Lambda < -1, \tag{3.78}$$

leads to an interesting development in the potential energy landscape as shown

in Figure 3.5, plotted for $\Lambda = -2.5$.

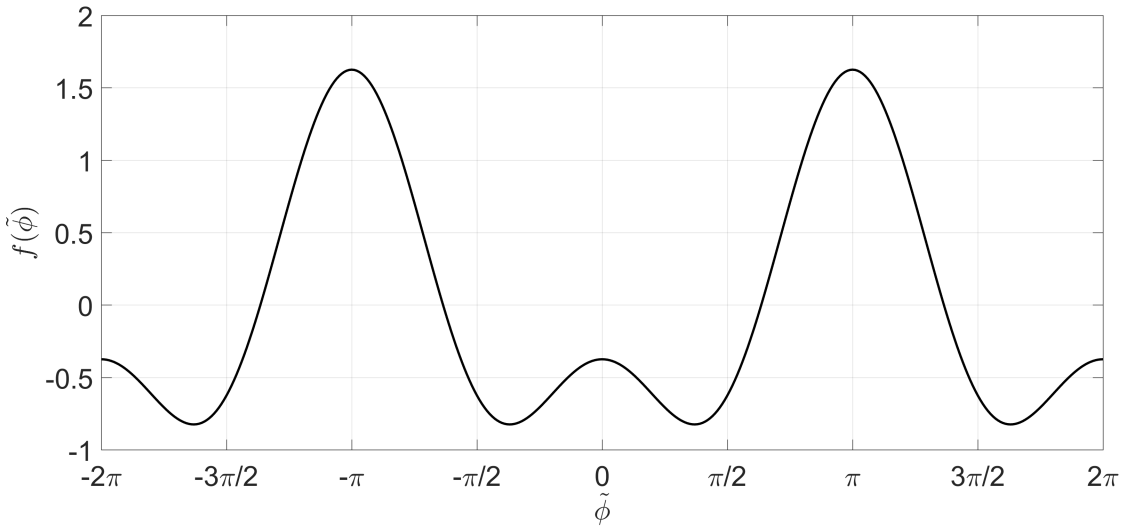

Figure 3.5: The form of the angular potential energy of the damped, finitely rigid, pendulum with dimensionless parameter $\Lambda = -2.5$.

Here in Figure 3.5 it is seen that not only is the inverted position not a stable equilibrium point, but the bottom position also is no longer stable. It has undergone a bifurcation into two separate points around the bottom position.

Analysis for γ' and Parameter Conditions

Knowing these stability positions, and the requirements on Λ to attain them, allows for quick analysis of the values of the friction coefficient, γ' that will be required in each case. The key values of the dimensionless parameter are $\Lambda = \pm 1$. The two values of γ' needed to satisfy these can quickly be calculated:

$$\Lambda = \frac{1}{2}\left(\frac{a}{L}\right)^2\left(\frac{\omega}{\Omega}\right)^2\left(1 - \left(\frac{\gamma'}{\omega_0}\right)^2\right) = \pm 1$$

therefore giving:

$$\gamma'_{1,2} = \omega_0 \sqrt{1 \mp 2 \left(\frac{\omega}{\Omega}\right)^{-2} \left(\frac{a}{L}\right)^{-2}}. \tag{3.79}$$

The condition therefore for inverted, Kapitza effect, stability to be seen is: $0 < \gamma' < \gamma'_1$. The lower limit here can be introduced because it is known that γ' is a positive friction coefficient. To that same end, because γ' is a real valued coefficient, the expression for γ'_1 in Equation 3.79 shows that for this inverted solution to exist, it is a requirement that $(a/L)^2 > 2(\Omega/\omega)^2$. This gives a condition for inverted stability based upon the relative amplitude of the driving modulation. The square root in this equation must therefore evaluate to a fractional result, and so for γ' to remain satisfying this inequality it can be seen that $\gamma' < \omega_0$ is also a necessary condition to be fulfilled in order to see inverted stability.

The condition for standard stability at $-1 < \Lambda < 1$ can very simply be seen from the results of Equation 3.79 to transfer to the friction coefficient as: $\gamma'_1 < \gamma' < \gamma'_2$. To go beyond this into the bifurcated regime it is necessary that: $\gamma'_2 < \gamma'$. To find the angular coordinates of these points, the differentiated form of the effective potential found earlier can be set equal to zero and manipulated.

$$\begin{aligned} \frac{dU_{\mathrm{eff,F}}(\tilde{\phi})}{d\tilde{\phi}} = m\Omega^2 \left(\sin\tilde{\phi} + \frac{\Lambda}{2} \sin 2\tilde{\phi} \right) &= 0 \\ \sin\tilde{\phi} + \frac{\Lambda}{2} 2 \sin\tilde{\phi} \cos\tilde{\phi} &= 0 \\ \sin\tilde{\phi} \left(1 + \Lambda \cos\tilde{\phi} \right) &= 0 \end{aligned} \tag{3.80}$$

Analysing when $\sin\tilde{\phi} = 0$ will only yield the standard and inverted stability positions at $\tilde{\phi} = (0, \pi)$ respectively. Therefore the bracket is looked at in more depth.

$$\begin{aligned} 1 + \Lambda\cos\tilde{\phi}_1 &= 0 \\ \cos\tilde{\phi}_1 &= -\frac{1}{\Lambda} \\ \tilde{\phi}_1 &= \arccos\left(-\frac{1}{\Lambda}\right) \end{aligned} \tag{3.81}$$

Thus the angular values of the bifurcated bottom stability position case associated with $\gamma_2' < \gamma'$ are $\tilde{\phi} = \pm\tilde{\phi}_1$. Similarly to what was done for the inverted case, the condition $\gamma_2' < \gamma'$ can be re-expressed with just a small rearrangement to give a condition for seeing these bifurcated stability points in terms of the relative amplitude of the driving modulation: $\left(\frac{a}{L}\right)^2 > 2\left(\frac{\Omega}{\omega}\right)^2\left(\frac{\gamma'^2}{\omega_0^2} - 1\right)^{-1}$.

These two, non $\tilde{\phi} = 0$, stability positions are somewhat reminiscent of the equilibrium angles seen in the driving dominated regime in Equations 3.35 and3.36. It is even possible, without too much algebra, to convert these expression into polar coordinates and find the similar looking result:

$$\phi_{1,\mathrm{DD}} = \arccos\left(2\left(\frac{\Omega}{\omega_0}\right)^2\left(\frac{a}{L}\right)^{-2}\left(1 - \frac{1}{2}\left(\frac{a}{L}\right)^2\right)^{-1/2}\right). \tag{3.82}$$

There is however an important distinction to be made between these two cases. In the former, driving dominated case, the limit $\gamma' \gg \omega_0^2/\omega$ enabled the expressions for the stability angles to be approximated by forms that only included the pendulum frequencies, Ω and ω_0. Physically, in this limit, the relaxation time of the pendulum in the potential was longer than the period of

the driving modulation, such that it only experienced the time-average of the potential. Outside of this limit though and in the latter case ($\gamma' \ll \omega_0^2/\omega$), the relaxation time of the pendulum is now shorter than the period of the modulation, so that the particle is sensitive to the movement of the potential during its relaxation towards equilibrium. The stable angle necessarily, therefore, depends on the modulation frequency, ω, and also the friction coefficient, γ' [83]. As such, this regime of varying stabilisation angle with friction coefficient and driving frequency will henceforth be labelled as the *Friction Filter* regime. N.B. the very low frequency driving limit is not considered as it can be reasoned that for a slow enough driving the pendulum would stabilise at the bottom as normal and just bob up and down in this place directly following the sinusoidal motion of the driving.

3.3.4 Summary Of Pendulum Stability Regimes

Many regimes and positions of stability for a Kapitza pendulum have been identified and explained in this thesis so far. In the interest of clarity, these will be briefly summarised here.

A Standard Pendulum

A standard rigid pendulum, not undergoing any vibrational modulation of its base, has one stable equilibrium position, at the bottom of its travel. Here rigidity is meant as $\omega_0 = \infty$; however finite but large rigidity of $\omega_0 \to \infty$ is sufficient as this implies the important condition that will endure throughout all regimes, $\omega_0 \gg \Omega$ (the rigidity associated proper frequency is far larger than the natural frequency of the pendulum). The vertically upwards position exists as a turning point under mathematical analysis but is not a stable equilibrium point -

if a pendulum were perfectly balanced here, any small perturbation would knock it back down to the bottom position.

A Kapitza Pendulum

Next, oscillatory modulation of the base of the pendulum was introduced to make a Kapitza pendulum. The frequency of this modulation is considered to be very large, in the limit $\omega \to \infty$ (implying $\omega \gg \Omega$), however it is key that the pendulum must still be rigid compared to this driving: $\omega_0 \gg \omega$. In this instance there are two possibilities for stability. These depend on the dimensionless parameter that was shown, $\beta = \left(\frac{a}{L}\right)\left(\frac{\omega}{\Omega}\right)$. For $\beta < \sqrt{2}$ only the bottom position is stable, as with a conventional pendulum. For $\beta \geq \sqrt{2}$ the inverted vertical position also becomes stable.

A Kapitza Pendulum With Friction

Finally, friction was introduced to the system. First very high frequency driving was considered, where $\omega \to \infty$ and was the largest characteristic frequency in the system (i.e. $\omega \gg \omega_0$). Here a driving dominated regime is entered where three cases were possible:

1. The bottom position was still stable assuming $0 \leq a < a_1$, (where $\frac{a_1}{L} \approx \sqrt{2}\frac{\Omega}{\omega_0}$).
2. In the interval $a_1 < a < a_2$ (where $a_2 \approx \sqrt{2}L$) there were only two stable equilibrium positions given by Equations 3.35 and 3.36, neither of which was the bottom or inverted positions.
3. Increasing the driving amplitude further into the range $a_2 < a$ saw a breakdown of the pendulum's arc and a stability position near

$(x, y) = (0, 0)$.

The driving frequency was then lowered and varying the amount of the introduced friction was considered. It was found that, with a large enough friction it was possible to force the system back into the driving dominated regime. This was the case even if now $\omega \ll \omega_0$. The new condition for entering this regime then became $\gamma' \gg \frac{\omega_0^2}{\omega}$.

To avoid this regime, γ' was considered fixed relative to ω_0 and the pendulum rigid (finitely) once again. Using this new criterion of $\gamma' \ll \frac{\omega_0^2}{\omega}$, the stability of the pendulum was seen to split into three cases. Using the $\gamma'_{1,2}$ expressions in Equation 3.79, the following was found:

1. For $0 < \gamma' < \gamma'_1$, with $(a/L)^2 > 2(\Omega/\omega)^2$ and $\gamma' < \omega_0$, a Kapitza effect of inverted stability is seen.

2. For $\gamma'_1 < \gamma' < \gamma'_2$ the only stable equilibrium point is the standard bottom position.

3. For $\gamma'_2 < \gamma'$ the bottom position bifurcates and the two positions given by $\tilde{\phi} = \pm\tilde{\phi_1}$, where $\tilde{\phi_1}$ is shown in Equation 3.81, become stable. These stability angles are driving frequency and friction coefficient dependent.

In an attempt to clarify, a parameter space diagram of these stability regimes is shown in Figure 3.6, for a range of proper frequency normalised driving frequencies and friction coefficients. N.B. As many of the conditions are inequalities there is generally a smoother transition between regions than Figure 3.6 suggests, but this gives a rough guide as to how the regimes are traversed.

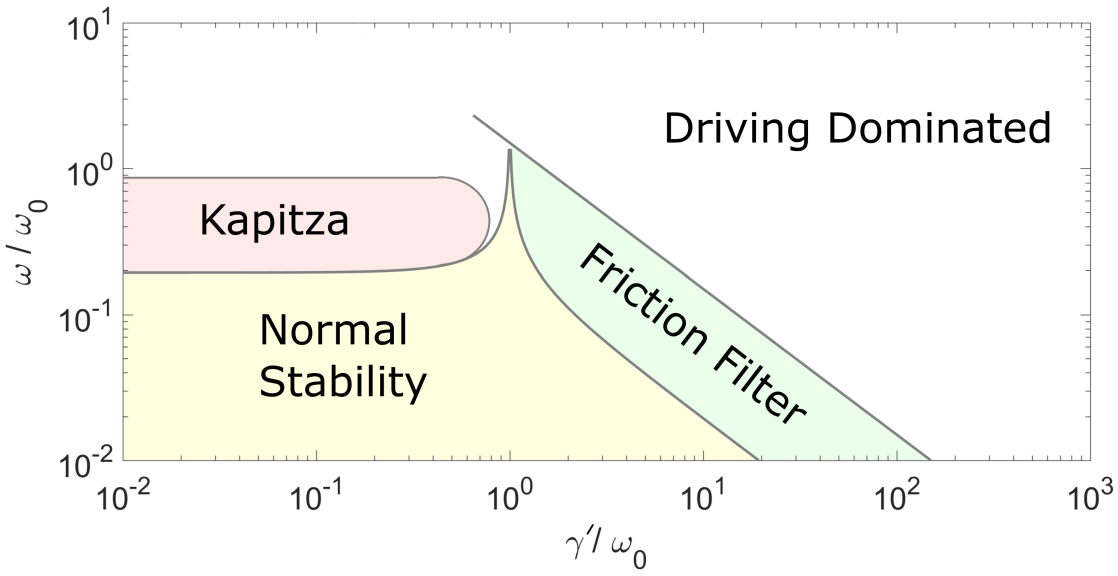

Figure 3.6: A parameter space diagram showing the different regimes of stability in a damped driven pendulum, with $\omega_0/\Omega = 100$ and $a/L = 0.0732$.

3.4 Simulations

To verify and complement these analytical results, before experimentation was commenced, simulations of a Brownian particle in an oscillating pendulum potential were carried out.

A full specification of the experimental set-up will be provided in the following section, however for the purposes of these simulations it is noted here that the experiment was conducted using an optical tweezers apparatus and trapped a silica micro-sphere for use as the pendulum's bob. This is a significant point to raise as, for a particle of this size in a suspension of water, the Reynolds number will be very small. Reynolds number is a quantity used to try to predict patterns of what will occur in different situations of fluid flow. It is the ratio of the inertial forces to the viscous forces present [84]. One of the simplest ways to express this ratio for the Reynolds number, Re, is: $Re = \rho\alpha v/\eta$, where ρ is the fluid density ($\rho \approx 10^3$ kgm^{-3} for water at room temperature), α is the characteristic dimension of the immersed object, v is the velocity with which it

moves through the fluid, and η is the dynamic viscosity ($\eta \approx 10^{-3}$ Pas for water at room temperature) . The silica beads in question are in the order of a micrometre in size, and will be moving relative to the fluid at approximately a micrometre a second. So it is very quickly possible to see that the Re will be in the order 10^{-6} depending on exactly the size and velocity of the object. For a human swimming through water it is estimated that $Re \approx 10^4$ and for a small fish $Re \approx 10^2$ [85], so it is clear that relative to these things, the domain of low Reynolds number has well and truly been entered by the size parameters of the experiment. For such low values of Re, it can be said that the viscous forces dominate, and the inertial forces become negligible [85].

In this regime then, the inertial term in the equation of motion for the pendulum can be omitted, and the finite difference method of Volpe and Volpe [86] can be employed to perform the necessary simulations. This method considers the Einstein-Ornstein-Uhlenbeck theory of Brownian motion describing a bead in a harmonic potential with the Langevin equation [87, 88] (a stochastic differential equation describing the Brownian motion of a particle in a fluid):

$$m\ddot{x}(t) = -\gamma\dot{x}(t) - \kappa x(t) + \sqrt{2k_{\mathrm{B}}T\gamma}W(t), \tag{3.83}$$

or, when the inertial forces are considered negiligible:

$$\dot{x}(t) = \frac{1}{\gamma}\left(-\kappa x(t) + \sqrt{2k_{\mathrm{B}}T\gamma}W(t)\right), \tag{3.84}$$

where $W(t)$ is a white noise term. A standard approach to a finite difference simulation of an ordinary differential equation (ODE) is then taken. That is, a continuously evolving solution, $x(t)$, to the ODE is approximated by many

individual x_i, the solutions to a corresponding finite difference equation at discrete small time intervals $t_i = i\Delta t$. With a small enough Δt then $x_i \approx x(t_i)$. Such finite difference equations are generated by the following substitutions in the ODE: $x(t) \to x_i$, $\dot{x_i} \to (x_i - x_{i-1})/\Delta t$ (the acceleration term's substitution is not given here as it has already been mentioned that this will be omitted). The resulting expression is then rearranged for x_i and this is solved recursively for each time step using the values of the previous x_{i-1} solutions.

The white noise term, $W(t)$, in this Equation 3.83 has properties of mean, variance, and time independence as already catalogued in Section 3.3. Due to these properties, and its discontinuity, the white noise cannot be approximated by its instantaneous value at some time t_i as this will not be well defined. To treat the white noise $W(t)$ within a finite difference method, a discrete sequence of random numbers W_i is needed. These must have zero mean and satisfy the condition: $\langle (W_i \Delta t)^2 \rangle / dt = 1$, so that they have a variance $1/\Delta t$. In practice, this is fairly easy to implement. Most programming languages are able to generate sets of Gaussian random numbers w_i, it is then simply a case of scaling these to give the appropriate variance, i.e. $W_i = w_i/\sqrt{\Delta t}$.

After dropping the inertial term, the finite difference equation obtained for these simulations then looks as follows [89]:

$$x_i = x_{i-1} + \frac{1}{\gamma}\left(\boldsymbol{F}_{\mathrm{Opt},i-1} + \sqrt{\frac{2k_{\mathrm{B}}T\gamma}{\Delta t}}w_i\right)\Delta t + \frac{\boldsymbol{F}}{\gamma}\Delta t, \tag{3.85}$$

where $\boldsymbol{F} = (F_x, F_y)$ is a constant force acting on the pendulum, realised practically with a constant fluid flow of velocity v, such that $\boldsymbol{F}/\gamma = (v_x, v_y)$. The force $\boldsymbol{F}_{\mathrm{Opt}}$ represents the optical confining force from the tweezers setup. This is assumed proportional to radial displacements of the particle from the pendulum length, L, from an instantaneous circle centre position: $y_{c,i} = (a/L)\sin(i\omega\Delta t)$.

As an optical tweezers utilises a Gaussian beam this force is calculated as: $\boldsymbol{F}_{\mathrm{Opt}} = -\nabla \boldsymbol{U}_{\mathrm{Opt}}$, where U_{Opt} describes a circularly symmetric potential, Gaussian in radial coordinate r, and centred on $r = L$. The $2k_{\mathrm{B}}T$ term comes from the Equipartition Theorem, wherein the energy associated with each harmonic degree of freedom is $0.5k_{\mathrm{B}}T$ for a system at thermodynamic equilibrium at absolute temperature T. Here this comes to $2k_{\mathrm{B}}T$, as a harmonic oscillator has a kinetic and a potential degree of freedom for every coordinate dimension, and a two-dimensional pendulum is being considered [20]. This potential can be seen in Figure 3.7a. Figures 3.7b and 3.7c show the resulting force in the x and y directions respectively. It can be seen from these that there are components pushing left/right and up/down in each direction respectively to hold the particle fixed at the pendulum radius L (here set at $L = 8$ μm). Full details of the experimental apparatus and design will be provided in the following section.

Simulations were performed and are shown here for parameter values comparable to those possible and utilised in the experimental setup. By ensuring that parameters in the simulations suited the inequality: $\gamma' \gg \omega_0^2/\omega$, it was possible to explore the driving dominated, high frequency regime. Figure 3.8 shows an exploration of two possible outcomes in this regime, and has the property here that $\gamma' / \left(\frac{\omega_0^2}{\omega}\right) \approx 50$. Figures 3.8a and 3.8b represent the case where: $a < a_1$; such that standard, downwards stabilisation is seen (here $a/a_1 \approx 0.9$). Figures 3.8c and 3.8d display the case: $a_1 < a < a_2$, where only one possible stabilisation point was found. In this instance, $a/a_1 \approx 2.6$, and $a/a_2 \approx 0.2$, and the stabilisation angle predicted by the theoretical calculations was $\phi \approx 1.4$ rad.

Finally, by ensuring that the parameters of the equation corresponded with the inequality $\gamma' \leq \omega_0^2/\omega$ it was possible to explore the rigid pendulum with friction regime, where neither the driving or the damping are dominant as seen in the previous case. Figure 3.9 shows an exploration of two of the possible outcomes

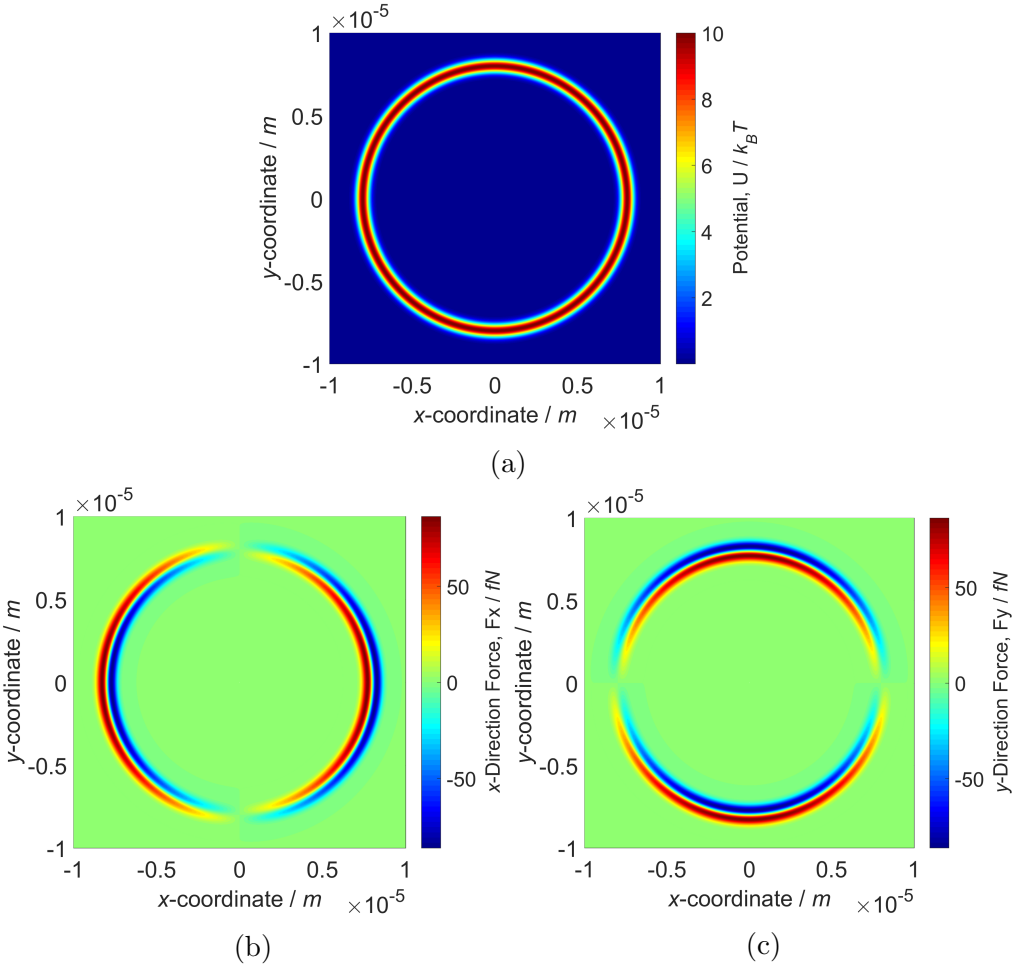

Figure 3.7: The origin of the optical trapping force term in the Brownian motion simulations. a) The Gaussian optical potential centred about $r = L$. b) and c) The force in the x and y directions respectively, derived by finding the gradient of the optical trapping potential.

from this regime. In the case of the simulations shown, it is the case that $\gamma'/\left(\frac{\omega_0^2}{\omega}\right) \approx 0.2$. The Figures 3.9a and 3.9b show the case where: $\gamma_1' < \gamma' < \gamma_2'$; such that standard, downwards, stability is expected (here $\gamma'/\gamma_2' \approx 0.2$). Figures 3.9c and 3.9d display the case where a bifurcation of this bottom stability position is seen (i.e. $\gamma_2' < \gamma'$, the friction filter regime). In this instance: $\gamma'/\gamma_2' \approx 1.8$, giving an expected stability position of $\phi \approx \pm 1.3$ rad.

These simulations of two sub-regimes of each of the two main regimes demonstrate very good agreement with the theoretical predictions. They show

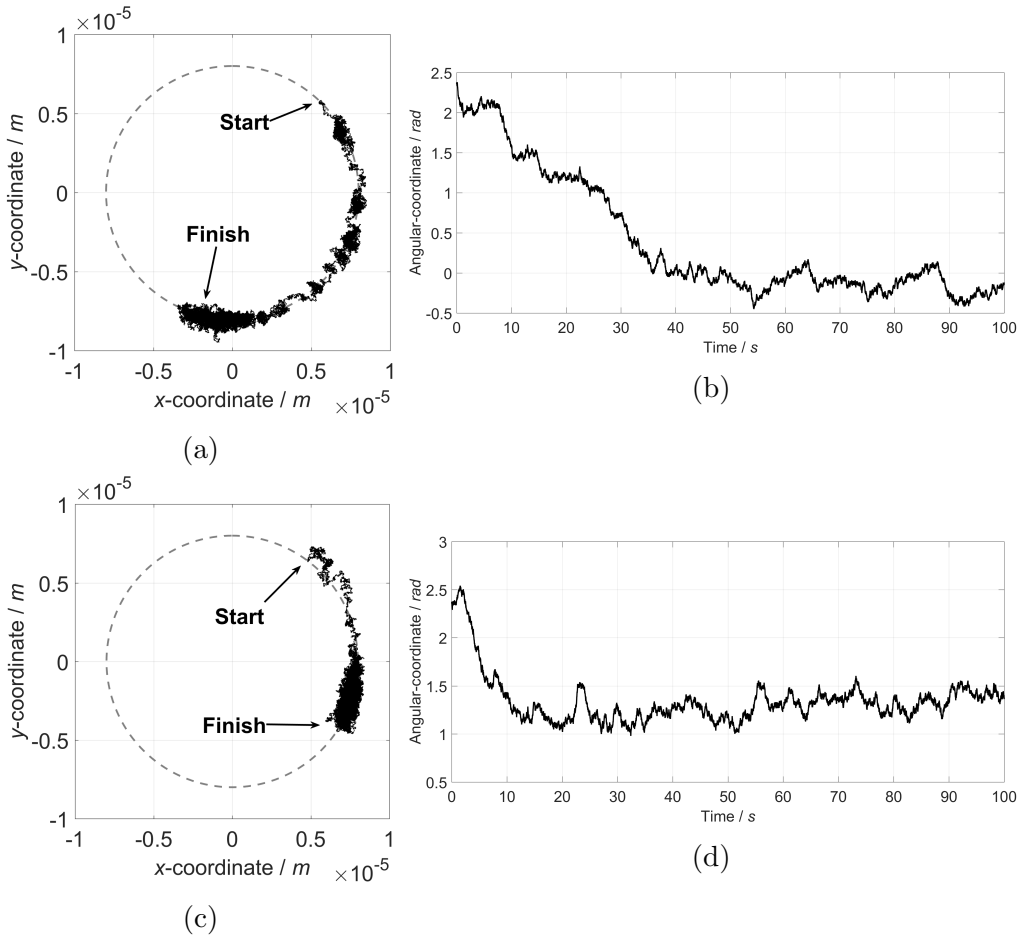

Figure 3.8: Equilibrium stability simulations in the driving dominated regime of a pendulum subject to a confining force (gravity) acting vertically downwards, in $-y$, and undergoing base oscillations parallel to this force. a) An x-y plot of coordinates from a simulation in the $0 < a < a_1$ regime, overlaid on the circle of potential centred at $(x, y) = (0, 0)$. b) An angle vs time plot of this simulation, showing the particle stabilising at its expected downwards position. c) An x-y plot of coordinates from a simulation in the $a_1 < a < a_2$ regime. d) An angle vs time plot of this simulation, showing agreement with the predicted stability position of $\phi \approx 1.4$ rad.

that in the ranges specified by the analytical inequalities derived, the stability behaviour of the pendulum is as expected (be that standard downwards or some alternate stability position). They also show that for these alternate stability positions; the quantified theoretical predictions made about the exact angle of stability expected, seem to be accurate, as good agreement is seen between these and the final equilibrium angles of the simulations in these regimes.

There are regimes mentioned in the analytical work of section 3.3 that are

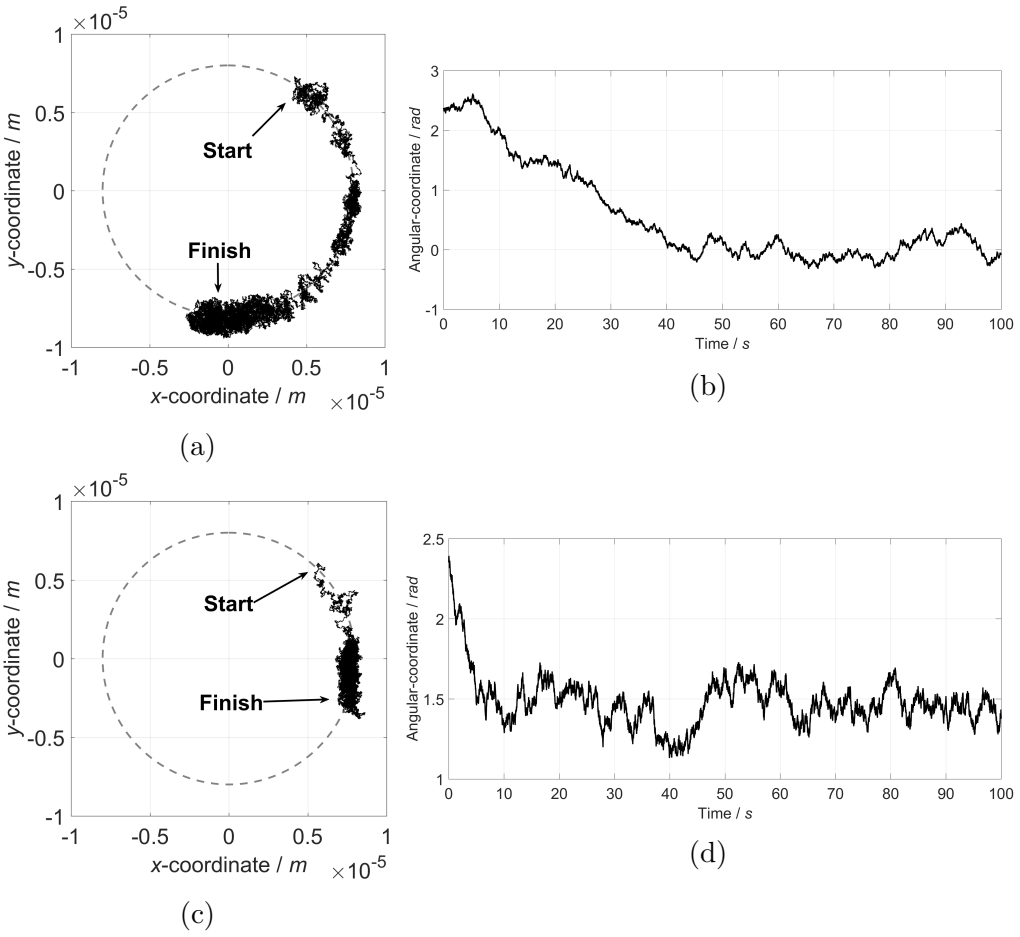

Figure 3.9: Equilibrium stability simulations in the 'rigid pendulum with friction' regime of a pendulum subject to a confining force (gravity) acting vertically downwards, in $-y$, and undergoing base oscillations parallel to this force. a) An x-y plot of coordinates from a simulation in the $\gamma_1' < \gamma' < \gamma_2'$ regime, overlaid on the circle of potential centred at $(x, y) = (0, 0)$. b) An angle vs time plot of this simulation, showing the particle stabilising at its expected downards position. c) An x-y plot of coordinates from a simulation in the $\gamma_2' < \gamma'$, friction filter, regime. d) An angle vs time plot of this simulation, showing agreement with the predicted stability position of $\phi \approx 1.3$ rad.

omitted in these simulations. The first is the $a_2 < a$ regime of the driving dominated setup. This is because it was shown that in this case the pendulum behaviour breaks down almost completely, and because the modulations are so large the pendulum comes to rest somewhere near $(x, y) = (0, 0)$. As the pendulum is no longer following its arc exhibiting interesting stability along it, this case was omitted. The other is in the lower driving frequency regime where $\gamma' < \gamma_1'$. This was omitted because, in the case of our experiment and its

achievable parameters, it would not be possible to enter this regime of inverted/Kapitza stabilisation (as will be seen in the following section).

Chapter 4

Beyond the Kapitza Pendulum - Experiment

4.1 Experimental Set-up

In order to test the results of the simulations and the predictions of the analytical theory, a microscopic analogue of a Kapitza-like pendulum was realised using an optical tweezers experiment. The optical tweezers is built around a Zeiss Axiovert 200 inverted fluorescence microscope using a $\times 100$, NA = 1.3 oil immersion objective lens. The trapping laser beam is derived from a single mode Nd:YAG laser with maximum output power of 3 W. The path of the trapping beam includes a pair of galvanometer scanning mirrors [90] in a plane made conjugate to the back aperture of the objective by a pair of lenses which also serve to increase the beam diameter to slightly overfill the aperture. The galvanometer mirrors can thus steer the location of the beam waist in two dimensions in the focal plane of the objective. Control of the scanning mirrors, and thus of the focal spot position, is performed via a National Instruments Labview interface in conjunction with Matlab. The microscope is also equipped with a Mad City Labs three-axis nano-positioning stage which is used to apply a controlled fluid drag to the trapped particle. Light from the microscope's lamp is transmitted through a slide and enters the objective lens before being extracted via a dichroic mirror and arriving at a ThorLabs CMOS camera used to visualise the experiment. A schematic of the experimental apparatus is shown in Figure 4.1.

The arc of the pendulum is realised in this microscopic analogue as a ring-shaped optical potential well. This is created by using the galvanometer mirrors to rapidly scan the waist of the laser beam in a circle of a given radius, $L \approx 8$ μm. This is done at a high frequency, $f_{\text{scan}} = 1.2$ kHz, such that a trapped particle (acting as the pendulum bob in this experiment) experiences a time-averaged potential approximating a quasi-rigid pendulum. The particles used are 1.5 μm diameter silica microspheres (Kisker Biotech). The external force of gravity in a

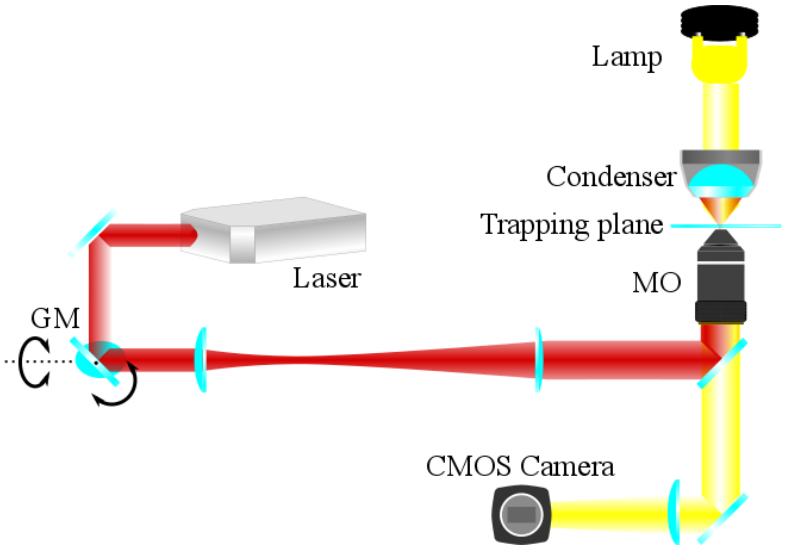

Figure 4.1: Experimental set-up for the optical pendulum. The laser beam is directed via orthogonally-mounted steerable galvanometer mirrors (GM) and expanded in a telescope before being injected into the microscope objective (MO). The black arrows indicate the rotations of the galvanometer mirrors. The experiment is imaged using the CMOS camera, movie from which is used for digital video microscopy particle tracking and analysis.

regular pendulum is mimicked by subjecting the trapped particle to a viscous drag force. This is achieved by translating the nano-positioning stage at a controlled speed, typically in the range $0 < v_x < 2$ μms^{-1} for a duration of up to 50 s. This speed, along with the radius of the ring of potential contribute to the pendulum's natural oscillation frequency as: $\Omega = \sqrt{F/ml} = \sqrt{\gamma' v/L}$. It is important to note and remember that the pendulum is strongly damped and so does not undergo angular oscillations at this frequency. Nonetheless Ω is still an important factor as it contributes to the thresholds found analytically for the dynamical stabilisation angle in both the driving dominated and the friction filter regimes discussed previously. Finally, to complete the microscopic analogue of the Kapitza pendulum, the centre of the ring of potential (equivalent to the base of the macroscopic pendulum) was oscillated at frequencies of up to $\omega = 2\pi \times (500$ Hz). This was done simply by translating the centre coordinate of the circle being driven by the galvanometer mirrors. The modulation frequency,

ω, is written in this fashion ($2\pi \times (f$ Hz)) to facilitate easy reading of the normal frequency the mirrors were driven at via user inputs into MATLAB scripts. Since there are many inequalities that govern the behaviour of the pendulum (as Chapter 3 has detailed), the other angular frequencies of the system will also be written in this way to aid easy comparison of them. Unlike gravity in the macroscopic pendulum, the stage can be translated and the fluid drag can act in either positive or negative, x or y, directions. This force therefore needn't necessarily be applied in a negative y direction. Indeed, in this experiment, the fluid flow was executed in a positive x direction, and so the modulations were applied to the x associated galvanometer mirror accordingly.

4.2 Method

4.2.1 Slide Preparation

The microscope slides housing the immersed silica micro-particles were prepared as follows. 20 ml of distilled water was mixed with 2 μl of the 1.5 μm silica spheres in a large conical bottomed tube, making a $1/10^4$ dilution. 100 μl of the surfactant Triton-X was also added to this solution to prevent the particles from sticking to each other or the surface of the glass cover slip. Calling this solution 'A', it was further diluted to at a ratio of 1:19 A:water to fill a small conical bottomed 1 mL centrifuge tube with the solution that would eventually go into the slides. This further dilution of A was done as regularly as was needed, usually decided by monitoring the accumulation of foreign bodies on the slide (bacteria etc.), seen when searching the slides for particles under the microscope. The microscope slides used had a single depression with a volume of approximately 80 μL. Therefore 80 μL of the diluted solution was pipetted into

this depression to completely fill it and a cover slip (No. 1.5, thickness $160 - 190$ μm) slid over the top of this. Finally the cover slip was secured in place using commercial nail polish to adhere its edges to the slide.

4.2.2 Video Tracking

The position of the particle around the pendulum potential was tracked using video microscopy. Video was recorded at a typical frame rate of 40 fps using the CMOS camera for up to 100 s over an area of approximately 24 μm $\times$ 24 μm. A custom written (in Matlab) particle tracking algorithm was used to track the position of the centre-of-mass of the particle. This thresholded the recorded images and tracked the mean location of the bright centre of mass of the particle (the centroid). An example of the results of the video tracking output is shown in Figure 4.2 for a trapping circle that was not undergoing base modulation, but with fluid drag still applied.

It is noted here that, due to the averaging in the centroid calculation, this is a technique which can achieve sub-pixel resolution, typically of the order of about a tenth of the pixel size (approximately 5 nm in the case of this experiment) [20]. Faster and more accurate methods of particle tracking in optical tweezers do exist; such as interferometry using photodetectors and light from a detection laser being scattered from trapped particles. Due to the nature of this experiment though (the large arc of potential around which a particle might possibly move) this method is not suitable here.

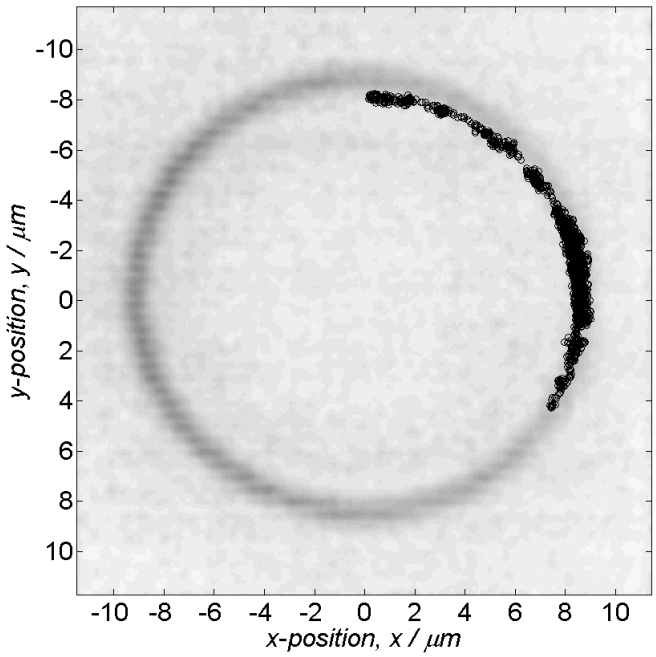

Figure 4.2: An example of the output from the custom written Matlab tracking script. The particle's tracked position is shown for an experimental run with no modulation of the centre of the potential and with a fluid flow of $v_x = 1$ μms^{-1}. The tracked coordinates are overlaid on an image (to the same scale) of a reflection of the scanning laser beam from the microscope slide's cover slip.

4.2.3 Calibration

Pixel Size

The first calibration step performed in this experiment was assessing the relative size of the pixels in the images captured and relating this to some real-world micrometre value. This was done using a reference stage graticule (National Physical Laboratory) [91]. This is a chrome-on-glass microscope slide with four testing areas comprising different shapes and sizes of squares and spots. The Root-2 array of spots, increasing in diameter from 3 μm to 48 μm, was used to calibrate the pixel size. An example of one of these can be seen in Figure 4.3a.

An image of each spot was acquired and these were analysed in Matlab. The dark spots were picked out from the light background and their diameter in

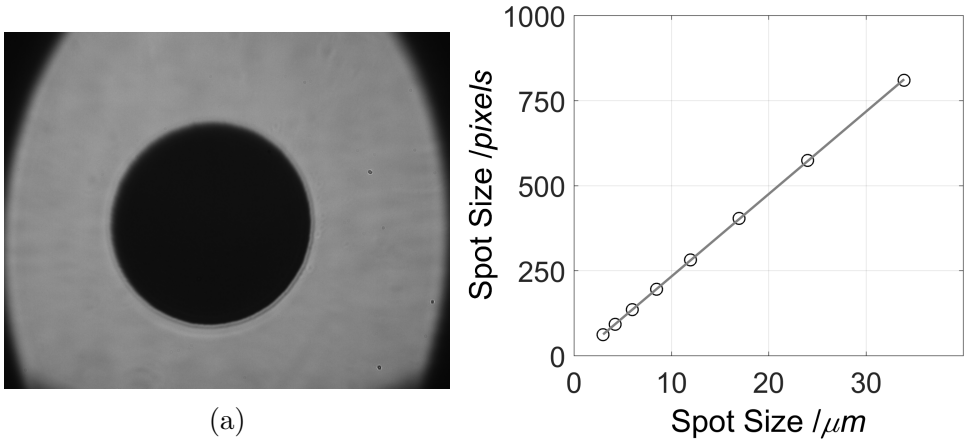

(a) (b)

Figure 4.3: a) A 24 μm diameter reference graticule spot imaged with a 100× objective lens. b) A plot of the spot size in pixels vs. μm. The linear fit used to obtain the pixels-to-microns conversion factor of $p = (413 \pm 3) \times 10^{-4}$ μmpix^{-1} has been added.

pixels in the images was found. The spot sizes in both unit systems, pixels and micrometres, were plotted against each other and a line of best fit drawn up such that its gradient could be used as a conversion factor (see Figure 4.3b). The result of this calibration was a pixels-to-microns conversion value of $p = (413 \pm 3) \times 10^{-4}$ μmpix^{-1} (where the error has been taken from the 95% confidence bounds of the fit). This is approximately 25 pixels per micron.

Galvanometer Mirrors

The next calibration step undertaken was to assess the performance of the galvanometer mirrors. First, a Matlab script was written to interface with a National Instruments Data Acquisition (NI-DAQ) board. Two output channels from the NI-DAQ were used to control the x and y galvanometer mirrors independently. This was tested by trapping a silica particle and driving the mirrors with a slow, 2 Hz, sine and cosine signal respectively (the expected result being a circle traced out by the trapped particle). The values transmitted to steer galvanometer mirrors are voltages and not micrometres, so a convenient

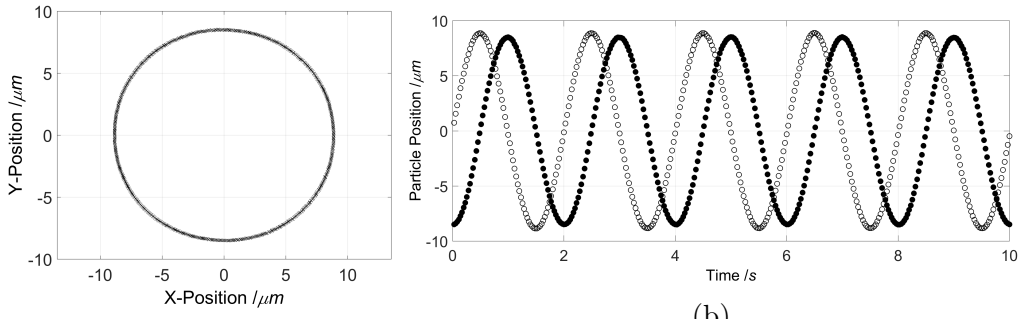

(a) (b)

Figure 4.4: The results of initial tests of the galvanometer mirrors as they scan a 2 Hz circle of radius $L \approx 8.2$ μm whilst trapping a silica particle. a) An x-y tracked particle coordinate plot. b) The x (open circles) and y (filled circles) particle coordinates plotted against time, showing the 2 Hz period expected and the slight disparity in the amplitudes of the two waves.

value which created a circle with a radius of roughly a few times the diameter of the particles was selected. This was an outputted radial voltage value of $V_r = 0.2$ V to each of the mirrors, which corresponded to an actual circle radius of $L \approx 8.2$ μm. The Thorlabs UC480 camera software was used to observe the particle and verify that this was the case. Video was recorded from the camera and tracked in Matlab. As seen in Figure 4.4 the results obtained from this experiment were very much as expected. The particle did indeed trace out a circle and the frequency of the individual coordinate traces matched the 2 Hz that was outputted to the mirrors. However as can be seen in Figure 4.4b there did appear to be a slight discrepancy in the x and y oscillation amplitudes suggesting this was not perfectly circular. More will be written on this later.

Higher frequency mirror scanning was then attempted, to place the particle in the desired time averaged ring of potential, rather than have it simply be dragged slowly around a circular track. A frequency of $f_{\text{scan}} = 1.2$ kHz was selected as this was within the operational parameters of the galvanometer mirrors, fast enough to present a time averaged ring to the particle, and crucially much larger than any other frequency that would be outputted to the system

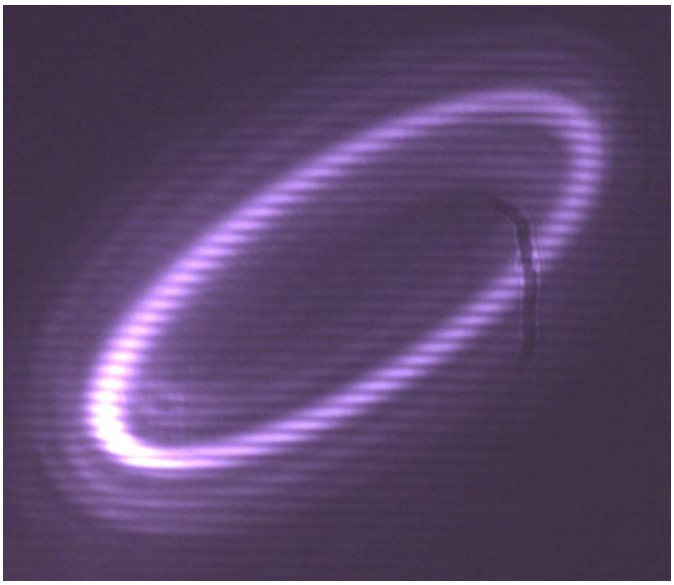

Figure 4.5: The reflection of the Nd:YAG laser from the cover slip whilst scanning the galvanometer mirrors at 1200 Hz. Prior to amplitude and phase corrections being applied an ellipse was seen.

(the modulation applied never exceeded 500 Hz). Initial tests of imaging reflections of the trapping laser from the cover slip showed an elliptical trap, rather than the expected circle (see Figure 4.5). This suggested that there was a significant phase shift occurring between the two mirrors when driving them at this high frequency, and possibly an amplitude variation too.

A quick initial test with very coarse steps revealed that a phase correction of approximately $\varphi_0 = -0.8$ rad applied to the x galvanometer mirror was needed to correct for this. Then smaller more regular steps of phase change values between -0.7 and -1.0 rad were applied, and the resulting cover slip reflection images were saved. An ellipse fitting regime was used to analyse these and the lengths of the major and minor axes were identified. These axes' lengths as a function of the phase correction applied were then plotted together on the same graph (see Figure 4.6a). Their lines of best fit were found and the point of intersection of the two lines was used to obtain the final phase correction value applied to the x galvanometer mirror when driving at $f_{\text{scan}} = 1.2$ kHz. The value

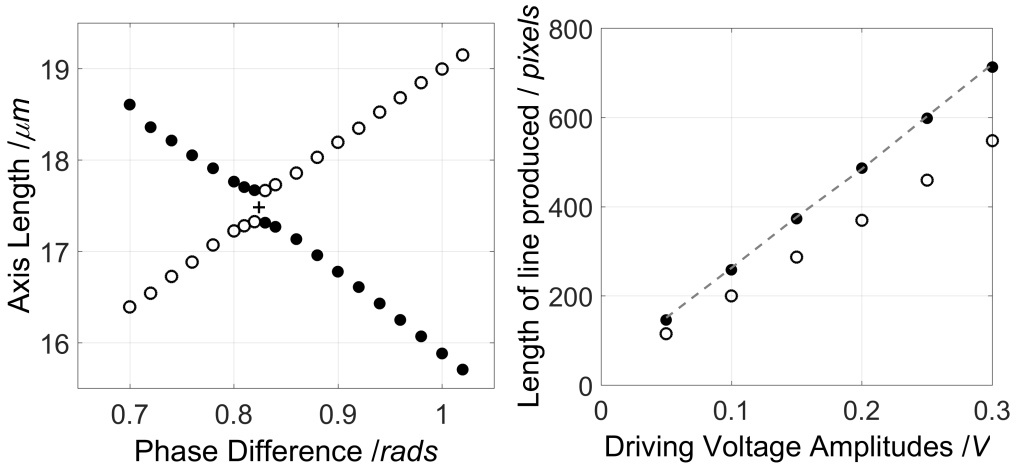

(a) (b)

Figure 4.6: Filled circles and open circles denote the x and y directions respectively. a) Ellipse axes lengths observed when scanning the galvanometer mirrors at $f_{\text{scan}} = 1.2$ kHz. The central cross indicates the $\varphi_0 = -0.8241$ rad overlap position. b) Trapping laser reflected line lengths recorded in response to varying galvanometer mirror driving voltages. The dashed line corresponds to the y-direction line lengths multiplied by the 1.3122 amplitude correction factor found, showing how this overlaps with the x line lengths.

found was $\varphi_0 = -0.8241$ rad.

The amplitude response of the two mirrors at this scanning frequency was then assessed. Straight lines were drawn in the x and y directions respectively by only driving one of the mirrors at a time with a range of different NI-DAQ output driving voltages, whilst the other mirror remained fixed. Cover slip reflections were once again recorded and were analysed to determined the length of each of the lines seen. These were plotted together (as seen in Figure 4.6b), and lines of best fit were found for each direction. The gradients of these lines showed that the x-direction galvanometer mirror's movement was 1.3122 times larger than that of the y-direction for a given voltage ouput from the NI-DAQ. This amplitude correction factor was therefore applied to the y galvanometer mirror from then onwards to ensure an equal amplitude of driving in both directions. After applying both phase and amplitude corrections the trapping laser reflection was once again imaged and it was confirmed (via ellipse fitting again) that this

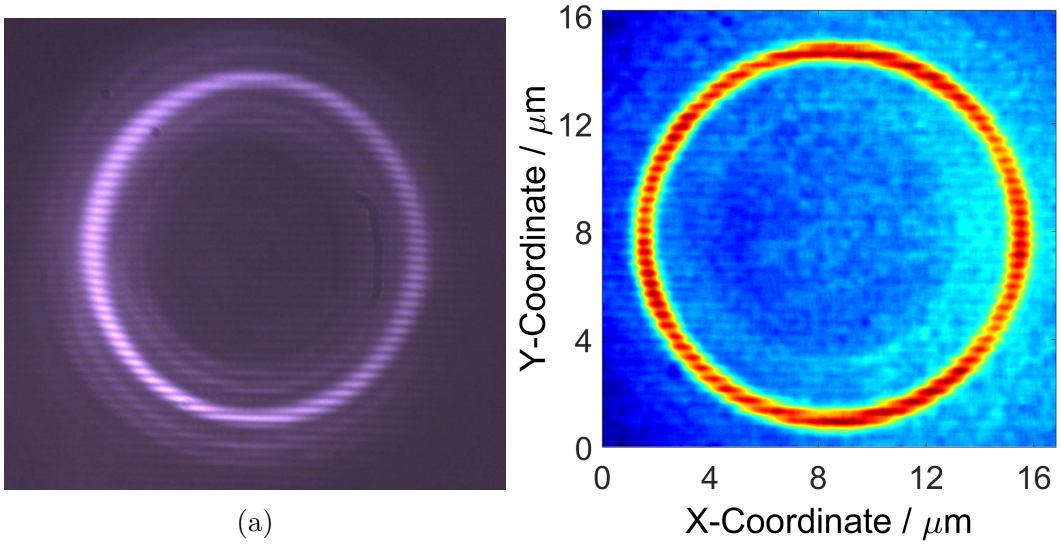

(a) (b)

Figure 4.7: a) The circular reflection of the Nd:YAG laser from the cover slip whilst scanning the galvanometer mirrors at 1200 Hz, after applying amplitude and phase corrections. b) A scaled colour image of the realigned trapping potential showing the even intensity around the circle.

time the trace was indeed circular. Figure 4.7a shows the result of these efforts.

It was also noted that the reflection from the cover slip of the trapping laser appeared brighter in certain locations on screen than others. It was postulated that this was probably due to some small alignment issue in the imaging path once the light leaves the microscope. Nonetheless, to try to negate any effect this may have, the trapping circle was realigned and repositioned using steering mirrors in the optical path such that the intensity of the reflection around the trapping circle was as even as possible. This balancing of the intensity around the ring was confirmed by looking at the intensity values in the image in MATLAB. The intensity balanced trap is seen using scaled colours in MATLAB in Figure 4.7b.

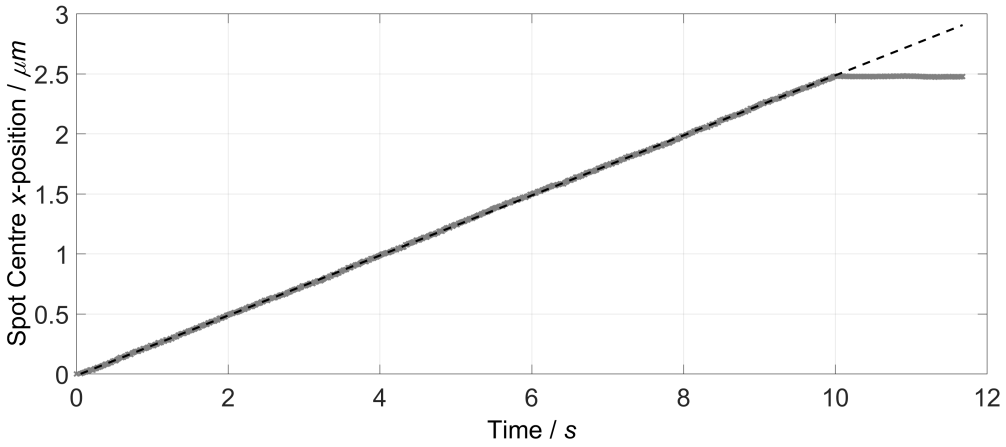

Figure 4.8: The x-coordinate of the centre of mass of a reference graticule spot plotted against time as it is translated at $v_x = 0.25$ μms^{-1} for $t = 10$ s. The dashed line is a linear fit to this data, the gradient of which confirmed the desired speed was achieved (although this is obvious by inspection).

Nano-positioning Stage

The Mad City Labs 3-directional microscope stage came with Labview software and functions with routines for specifying a distance and speed of desired translation. These were tested for accuracy by once more using the reference graticule. The stage was translated at a desired speed, and the motion of one of the Root-2 spots was recorded. Tracking the centre of mass of this spot in the direction of translation and performing a linear fit to this confirmed that the stage was behaving as expected. The results of performing this calibration with a translation speed of $v_x = 0.25$ μms^{-1} for a duration of $t = 10$ s can be seen in Figure 4.8. It was confirmed that the stage does indeed move accurately with the expected speed.

Pendulum Potential Radial Stiffness

The final calibration step was one of the most crucial, due to the information it would yield about the parameter space and limitations of the experiment. This step was identifying the radial spring constant (κ_r), or stiffness, of the circular

pendulum potential.

This was done by allowing a 1.5 μm sphere to diffuse freely around the optical potential, without hindrance from any fluid drag or modulation of the pendulum circle's centre, whilst recording it with as large a frame rate as possible. This is akin to having a 2D macroscopic pendulum in an environment without gravity, where it would just float around its arc (although with significantly greater Brownian effects imparted on it from the surrounding water molecules and more friction to contend with). Several videos of this were taken, beginning at equally spaced locations around the potential. This process was then repeated multiple times. The tracked particle position from these videos demonstrated that the particle did not preferentially travel in one direction (and so was not dragged by the scanning laser), and that it did not preferentially reside in any one location around the trap.

There are a number of ways this data could have been used in order to find κ_r. One method employed involved characterising the landscape of the optical potential energy. The tracked x and y positions had a circle fitted to them and were converted to radial and angular components. Being the component of interest for finding the stiffness, the radial coordinates were analysed and a histogram of the fluctuations in the radial position of the particle is shown in Figure 4.9a. This particular histogram is derived from a total number of video frames of the order of $N = 3 \times 10^4$, and comprises data from 12 different videos with 4 starting positions of the particle around the potential. From this histogram the radius of the circular potential (the length of the pendulum) was found to be $L = 8.2021$ μm, with a standard error on the mean of $\mathrm{SE}_{\bar{L}} = 0.8$ nm.

The histogram of radial position fluctuations then allows for the reconstruction of the pendulum potential energy landscape $U(r)$. Using the Maxwell Boltzmann distribution, (because the particle is in thermal equilibrium with the fluid

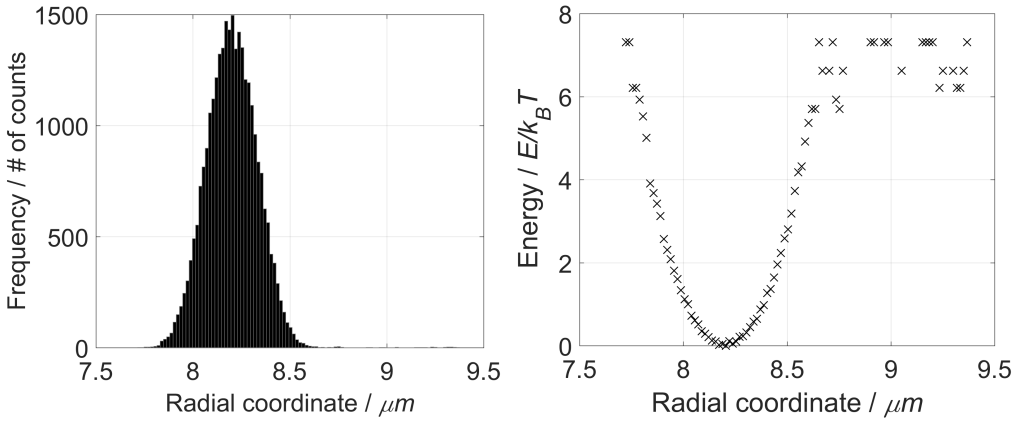

(a) (b)

Figure 4.9: a) Histogram of the radial positions for a 1.5 μm diameter micro-sphere in the circular optical potential. The mean radius found was $L \approx 8.2$ μm. b) The radial position distribution converted into the potential energy landscape for the optical potential.

molecules around it) the equilibrium probability density of the particle occupying a given radius r from the centre of the potential can be expressed as [20]:

$$P(r) = P(r)_0 \exp\left(-\frac{U(r)}{k_{\mathrm{B}}T}\right), \tag{4.1}$$

where $P(r)_0$ is a normalisation factor (the inverse of the partition function: $P(r)_0 = Z^{-1}$). Therefore by taking the logarithm of the frequency in the histogram, it is possible to solve for $U(r)$ and obtain the shape of the potential energy landscape as:

$$\frac{U(r)}{k_{\mathrm{B}}T} = -\ln\left(P(r)\right) + U_0, \tag{4.2}$$

where here the potential energy is expressed in terms of $k_{\mathrm{B}}T$, and U_0 is a constant.

To a first approximation the potential of an optical trap is harmonic and of the

form:

$$U(r) = \frac{1}{2}\kappa_r(r - r_{\mathrm{eq}})^2, \tag{4.3}$$

where r_{eq} is the equilibrium position of the trap. Indeed, it can be seen from Figure 4.9b that the potential does appear to have a quadratic shape to it (excepting the few larger radius points, where it is possible that in one of the collated videos the particle was lost from the trap). The validity of this approximation can be confirmed by inserting this harmonic approximation into the probability distribution (Equation 4.1), yielding:

$$P(r) = P(r)_0 \exp\left(-\frac{\kappa_r(r - r_{\mathrm{eq}})^2}{2k_{\mathrm{B}}T}\right); \tag{4.4}$$

and fitting with an equation of a similar form:

$$P(r) = A \exp\left(-\left(\frac{(r - B)}{C}\right)^2\right), \tag{4.5}$$

to the points that make up the histogram. This fit can be seen in Figure 4.10a, at which point it is possible to follow one of two paths to find κ_r. Either the constant, C, in the above fit form can be compared with the analytical form in Equation 4.4 and a small rearrangement made to identify the spring constant. Effectively the same step, since the harmonic approximation is valid, is to fit the form of the harmonic potential (Equation 4.3) directly to the energy landscape, with fit parameters for the spring constant and equilibrium position. Figure 4.10b shows an example of this fit, where the outlying large radius data points were omitted in the fitting process. Alternatively it is possible to use a method based on the equipartition theorem (see Section 3.4), namely that a system in

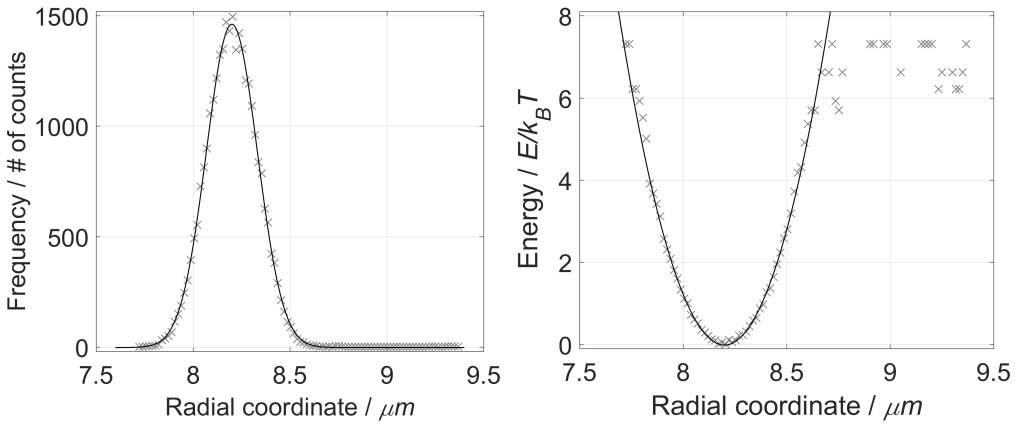

(a) (b)

Figure 4.10: a) The points that make up the radial coordinate histogram, with a Gaussian fit of the form seen in Equation 4.5. b) The potential energy landscape seen previously, with an quadratic fit of the form of the harmonic potential seen in Equation 4.3.

thermodynamic equilibrium at temperature T has an associated potential energy of $\frac{1}{2}k_{\mathrm{B}}T$ in every coordinate direction. Considering the radial coordinate therefore gives: $\langle U(r)\rangle = \frac{1}{2}\kappa_r\langle(r - r_{\mathrm{eq}})^2\rangle = \frac{1}{2}k_{\mathrm{B}}T$, where a time average is employed. As the probability distribution is Gaussian, practically for a series of independent samples r_n with $n = 1,...,N$ taken at times t_n, the equilibrium position and variance can be estimated as:

$$r_{\mathrm{eq}} = \frac{1}{N}\sum_{n=1}^{N} r_n \qquad \text{and} \qquad \sigma_{\mathrm{r}}^2 = \frac{1}{\mathrm{N}}\sum_{\mathrm{n}=1}^{\mathrm{N}} \left(\mathrm{r_n} - \mathrm{r_{eq}}\right)^2, \tag{4.6}$$

and the trap stiffness can be estimated as:

$$\kappa_r = \frac{k_{\mathrm{B}}T}{\sigma_r^2}. \tag{4.7}$$

All three radial stiffness values given by these approaches are in agreement, and give a value for this particular case which is encompassed within $\kappa_r = 0.23 \pm 0.01$ pNμm^{-1}.

Another method of establishing the radial stiffness of the trap that was employed

was to perform power spectrum analysis. This method is generally regarded as very reliable and has a couple of notable advantages. For one, it does not rely upon the assumption of a harmonic potential seen previously. In addition to this it works in the frequency domain, which makes it useful for identifying and removing noise from a system, which can appear as clear peaks in a power spectral density plot [20]. Following the approach of Berg-Sørensen and Flyvbjerg [20, 92], a one-dimensional Langevin equation, similar to that seen in Equation 3.84, is considered:

$$\dot{r}(t) + 2\pi f_{c,r} r(t) = \sqrt{2D} W_r(t), \tag{4.8}$$

where D is the diffusion coefficient given by: $D = k_{\mathrm{B}}T/\gamma$, and the corner frequency has been introduced:

$$f_{c,r} = \frac{\kappa_r}{2\pi\gamma}. \tag{4.9}$$

Taking the Fourier transform of Equation 4.8 gives:

$$2\pi(f_{c,r} - if)\hat{R}(f) = \sqrt{2D}\hat{W}(f), \tag{4.10}$$

where $\hat{R}(f)$ and $\hat{W}(f)$ are the Fourier transforms of $r(t)$ and $W_r(t)$ respectively. Taking the square modulus of this expression gives the power spectral density (PSD) of the particle's motion, a breakdown into frequency components of the distribution of power present:

$$P_r(f) = |\hat{R}(f)|^2 = \frac{D/(2\pi^2)}{f_{c,r}^2 + f^2}, \tag{4.11}$$

where $|\hat{W}(f)|^2 \equiv 1$ since the white noise has unitary power and is not correlated in time. In a practical, experimental sense, $r(t)$ will be logged with some sampling frequency f_s for a duration T_s. What will be obtained is therefore $r_j = r(t_j)$, where $j = 1, ...,\mathrm{N}$, $t_j = j\Delta t$, and $\Delta t = 1/f_s$. The finite difference equation for r_j becomes:

$$r_{j+1} = (1 - 2\pi f_{c,r}\Delta t)r_j + \sqrt{2D\Delta t}w_{j,r}, \tag{4.12}$$

where, as expected, $w_{j,r}$ are Gaussian distributed independent random numbers. From Equation 4.12 the discrete Fourier transform is calculated as:

$$\hat{R}_k = \Delta t \sum_{j=1}^{N} \exp^{i2\pi f_k t_j} r_j = \Delta t \sum_{j=1}^{N} \exp^{i2\pi jk/N} r_j, \tag{4.13}$$

where here $f_k = k/T_s$, $k = -N/2 + 1, ...,\mathrm{N}/2$. This discrete case is a good approximation to the continuous Fourier transform as long as $|f_k| \ll f_s$. From Equations 4.13 and 4.12 comes the following:

$$\exp^{i2\pi k/N} \hat{R}_k = (1 - 2\pi f_{c,r}\Delta t)\hat{R}_k + \sqrt{2D\Delta t}\hat{W}_{k,r}. \tag{4.14}$$

A simplification can be applied to this in the form of the approximation $\exp^{i2\pi k/N} \approx 1 + i2\pi k/N$ for $k \ll N$ (or $|f_k| \ll f_s$), and the observation that $k/N = f_k\Delta t$. The form of the experimental power spectrum after this simplification is:

$$P_k = \frac{|\hat{R}_k|^2}{\sqrt{T_s}} = \frac{D/(2\pi^2\Delta t)}{f_{c,r}^2 + f_k^2}|\hat{W}_{k,r}|^2. \tag{4.15}$$

Since the $w_{j,r}$ are independent random numbers from a Gaussian distribution

with zero mean and unit variance, the real and imaginary components of $\hat{W}_{k,r}$ must also be independent Gaussian random numbers. Therefore the $|\hat{W}_{k,r}|^2$ will be exponentially distributed independent positive random numbers. Expected values therefore are:

$$\langle P_k \rangle = \frac{D/(2\pi^2 \Delta t)}{f_{c,r}^2 + f_k^2}, \tag{4.16}$$

with standard deviations given by:

$$\sigma(P_k) = \langle P_k \rangle. \tag{4.17}$$

To perform a least squares fitting of an experimentally determined power spectrum (given by Equation 4.15) to the theoretical form (Equation 4.11); the data points must be statistically independent, and they must be drawn from a Gaussian or normal distribution. The former condition of independence is satisfied by the experimental power spectrum, but not the latter. P_k is exponentially distributed, rather than normally. There are two quick ways to circumvent this problem. These rely on the central limit theorem that the mean of a large number of iterates of independent random variables will tend towards being normally distributed [81]. This can be achieved either by repeating experiments and averaging the P_k values, or by compressing/blocking the data. This involves taking 'blocks' of consecutive data points and averaging them to produce single points. With a large enough number of repeats or a large enough number of blocked data points, the resulting averages have a Gaussian distribution.

Figure 4.11a shows a PSD plot for a single video of a silica micro-sphere diffusing around the optical potential ring. Block averages with an exponentially

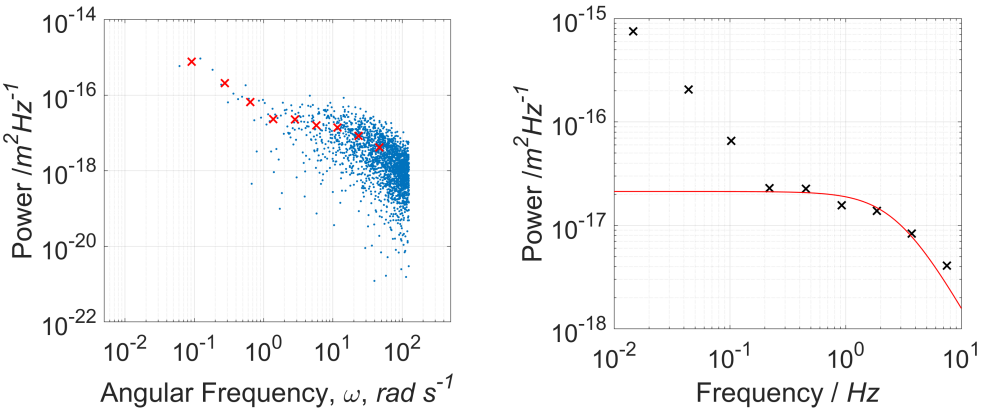

(a) (b)

Figure 4.11: a) The power spectral density plot for the tracked data from a silica microsphere diffusing around a ring of optical potential. Red crosses denote the exponentially increasing size block averages that were calculated. b) Fitting (red line) performed on the block averages (black crosses) with Equation 4.18 to enable finding the radial spring constant, here $\kappa_r = 0.22$ pNμm^{-1}.

increasing number of constituent points have been calculated and are seen marked on this plot by crosses. It is evident from the increase in the PSD to the left of this plot that some low frequency noise was present during this recording. This low frequency data was treated as anomalous, and fitting to the block averages above an angular frequency of $\omega = 1$ rads^{-1} was performed with a Lorentzian-type equation of the form:

$$P = \frac{A}{B + f^2}, \tag{4.18}$$

where A and B were parameters to be fitted, such that B represents the square of the corner frequency. Such exponential blocking does not yield a large amount of high frequency data in order to allow for confident fitting. However this is performed here in the interest of having evenly spaced points to display well on a logarithmic plot. Additionally, it can be useful to use larger blocks for the higher frequency data as this can reduce the sensitivity to high frequency noise. It is also noted that this is a single video and that as well as blocking, averaging

across several videos is performed. Regardless, Figure 4.11b shows this fit overlaid on the block averages. The corner frequency yielded by this fit was manipulated using Equation 4.9, and the radial spring constant found to be, $\kappa_r = 0.22$ pNμm^{-1}, a value which is in good agreement with those found previously.

Many more methods of analysing the trap and finding this spring constant exist, such as autocorrelation analysis and mean squared displacement analysis. However both a fast and a very reliable method have been detailed, and produce good agreement, therefore these other methods will not be employed and described here. Further information on them can be found in Jones *et al.* [20]

4.2.4 Acquiring Data

Beyond the slide preparation (used and detailed previously as it was a necessity in completing some calibration steps) and the calibration steps themselves, there was very little by way of method in this experiment to document when it came to acquiring the videos/data. This is because a Labview VI (virtual instrument) was written in order to perform most of the steps in the process of taking data (see Figure 4.12).

Once a slide had been prepared and placed on the microscope stage, an individual silica particle was found and if necessary manoeuvred such that it was isolated from other particles and would not come into contact with them as the stage began to move. Steering positions for the galvanometer mirrors were generated as a large array in Matlab, encompassing both the scanning movements and the centre modulation of the optical potential. These were then loaded into the VI where several parameters for the experiment and data taking were then specified. These included: the area of interest (AOI) over which to

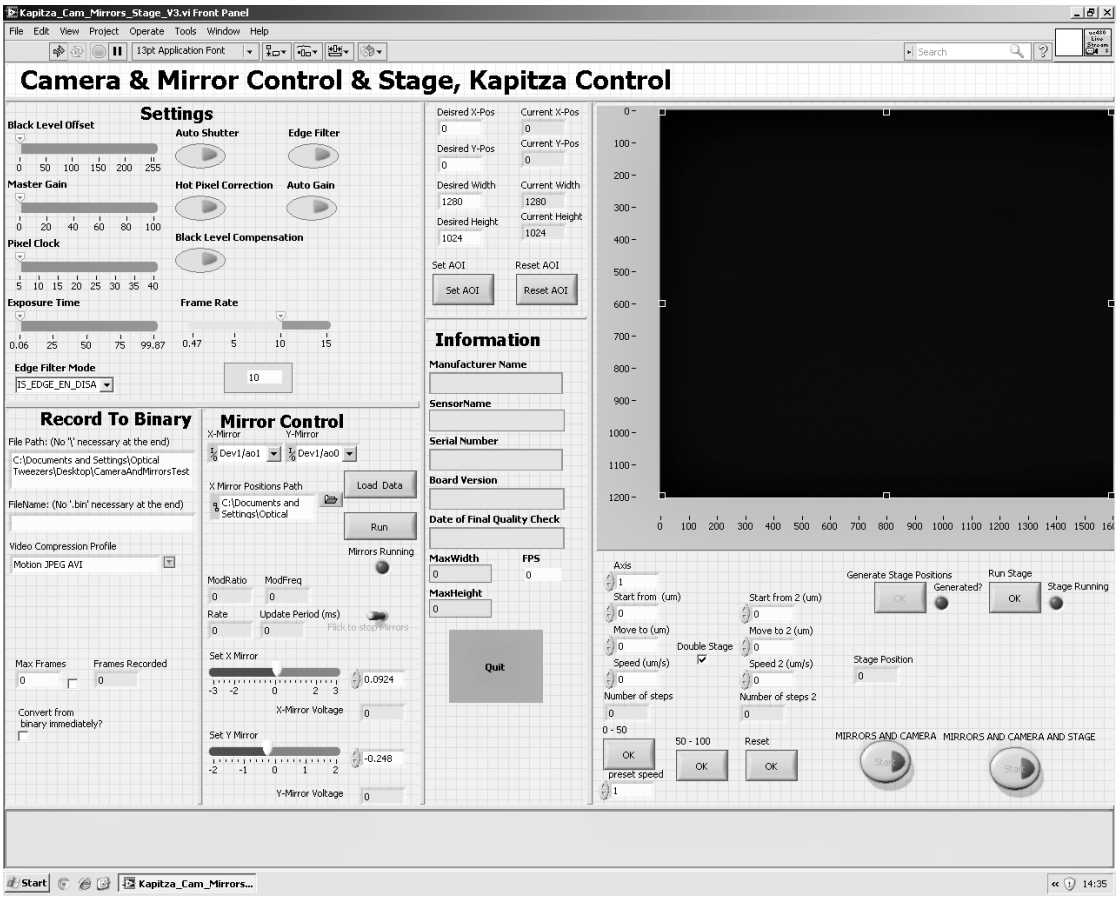

Figure 4.12: A screen-shot of the Labview VI written to automatically control the nano-positioning stage, galvanometer mirrors, and camera recording for the Kapitza pendulum analogue experiment.

record the video, the frame rate of the video, brightness (exposure, gain etc.) settings for the video recording, the location to save all of the recorded data, and the speed and distance over which to move the stage. Once started the Labview VI would automatically and simultaneously begin scanning the optical potential with modulation, moving the stage, and recording the video data, before saving this out after the stage movement was completed. Several repeat runs were taken for all parameter settings that were utilised.

4.2.5 Processing Data

Once the videos had been acquired they were then processed as follows. The particles were tracked, and their positions converted to radial and angular coordinates as described previously. Any videos where an irregular event had occurred such as a foreign body entering the AOI, the particle being pushed axially out of the trap, the particle being lost from the trap, or the tracking performing poorly, were rejected at this stage, if they had not been already. The angular coordinate of the tracked particle was then plotted against time and, since the position of an overdamped particle in a harmonic potential relaxes exponentially towards equilibrium, an exponential of the form:

$$\phi = (\phi_f - \phi_i)\left(1 - \exp^{-\phi/\tau}\right) + \phi_i, \tag{4.19}$$

was fitted to the trajectory; where ϕ_f and ϕ_i denote the final (stabilisation) and initial angles respectively, and τ is the exponential rise time. In addition to this, due to the occasionally fluctuating nature of a particle once at equilibrium, the mean angle occupied by the particle once the ϕ_f value had been reached was also calculated and recorded.

4.3 Results

4.3.1 Characteristic Frequencies and Potential Regimes

After the radial spring constant was established in the calibration stages of the experiment, all of the characteristic frequencies of the system could be calculated and the achievable regimes identified. The proper frequency of the system follows: $\omega_0 = \sqrt{\kappa_r/m}$. With the available laser power it was found that the

Property Name -	Symbolic Variable -	Frequency $2\pi \times (f$ Hz)
Mass-normalised Friction Coefficient	γ'	$423,000$
Proper Frequency	ω_0	$< 2,400$
Driving Frequency	ω	< 500
Natural Frequency	Ω	< 125

Table 4.1: Characteristic frequencies of the microscopic experimental pendulum analogue.

proper frequency was approximately limited to $\omega_0 < 2\pi \times (2.4$ kHz). The stage was driven no faster than 2 μms^{-1} (and usually slightly slower than this), giving a natural frequency, $\Omega = \sqrt{\gamma' v/L}$, of approximately $\Omega < 2\pi \times (125$ Hz). The mass-normalised friction coefficient is given by $\gamma' = 6\pi\eta r/m \approx 2\pi \times (423$ kHz). Finally the driving frequency is a controlled parameter in the experiment. In order to keep this significantly different from the scanning frequency of the circle, it was never operated at frequencies above $\omega = 2\pi \times (500$ Hz). For clarity these are tabulated (See Table 4.1).

It is immediately evident from this table that Ω is much smaller than any other characteristic frequency in the system. This was a condition that was assumed early on in the theoretical work in order to maintain 'pendulum-like' properties of being much stiffer and the modulations happening far faster than the natural oscillation frequency of the pendulum. This assumption was therefore justified and correct.

Closer inspection reveals that, due to the comparatively large value of the friction coefficient, γ', the driving dominated regime is very easily achievable. The condition for this was $\gamma' \gg \omega_0^2/\omega$. Values of driving well below the upper used limit of $\omega = 2\pi \times (500$ Hz) can satisfy this. The much harder task is leaving this regime and entering the rigid pendulum with friction/friction filter regime. This can only be achieved by drastically lowering the driving frequency. With typical trap stiffness and stage speed values, $k_r = 0.5$ pNμm^{-1} and $v = 1$ μms^{-1}, it is

required that $\omega < 2\pi \times (6\text{ Hz})$ in order to leave the driving dominated regime.

4.3.2 Driving Dominated Regime Results

Hereafter the angular notation shall be such that a position of 0 rad corresponds to a particle lying on the right hand side of the circle, on what would be the x axis if conventional Cartesian axes were to be drawn from the centre of the trapping circle, this is in the same positive x direction as the fluid flow and so the standard stability position. The angle shall increase clockwise in the bottom half of the trap and decrease in the top half, such that a particle at the top of the circle, on an imaginary y axis, occupies a radial coordinate of $-\pi/2$ rad. Particles are typically held fixed at an angular position of approximately $\phi = -\pi/2$ rad (or even just beyond this at $\phi = -6\pi/8$ rad if they are expected to stabilise near the top of the circle) before scanning of the trap and recording of the video is started, such that they have an opportunity to travel to their stability position.

The first regime that was explored experimentally was the driving dominated regime, since this was by far the easiest to reside in. Of particular interest was the range where $a_1 < a < a_2$, since this is when abnormal stability around the arc is predicted. Initially the proper frequency was set at $\omega_0 = 2\pi \times (806\text{ Hz})$. The trap centre was modulated at $\omega = 2\pi \times (500\text{ Hz})$, and the stage was translated in the positive x direction at $v_x = 1\ \mu\text{ms}^{-1}$ for 40 seconds.

Quick trial runs of the experiment confirmed that the particle seemed to be behaving as expected, resting first in standard and then novel stabilisation positions as the modulation amplitude was ramped up. This can be seen in Figure 4.13 where a particle's motion in each of three scenarios (no modulation, below threshold modulation, above threshold modulation) has been overlaid upon an image of the trap. Figure 4.14 shows a typical angle vs time trace of two

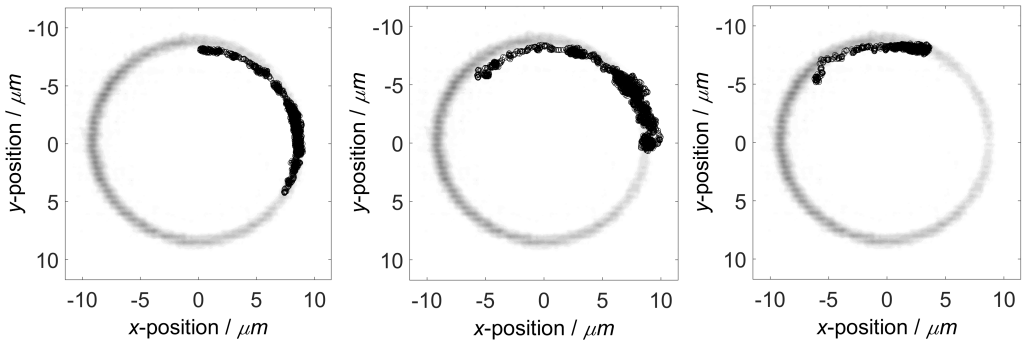

Figure 4.13: Trajectory of particles in the optical pendulum potential with three differing amplitudes of pendulum centre modulation. a) No modulation ($a/L = 0$), exhibiting normal stability. b) Below threshold modulation ($a/L = 0.12$), where the particle still exhibits normal stabilty. c) Above threshold modulation ($a/L = 0.3$), where the particle now stabilises nearly $\pi/2$ rad from the traditional stability position.

particles' trajectories, one with no modulation and one with a large modulation of $a/L = 0.3$.

After this confirmation that the experiment seemed practical and viable, a more thorough approach was taken. In this driving dominated regime, the pendulum stability position was predicted insensitive to changes in friction and driving frequency, but not the relative amplitude of the driving. The modulation amplitude was therefore varied systematically from $a/L = 0$, to $a/L = 0.5$, in increments of 0.02. The predicted threshold for stabilisation away from the conventional downwards position (the right of the circle in this microscopic analogue) was $a_{\mathrm{thr}}/L = 0.159 \pm 0.002$. It was observed that experiments run with no, or below threshold, modulation behaved as expected and progressed consistently to a $\phi = 0$ rad position where they then stabilised, exhibiting only random Brownian motion thereafter. As the modulation amplitude was increased to the point of threshold and beyond this no longer held true. The particles behaved very much as expected, leaving the $a < a_1$ case and progressing into the realm of non-standard stability where $a_1 < a < a_2$. Their angular stability position quickly jumped to approximately $\phi = -\pi/3$ rad, where it continued to

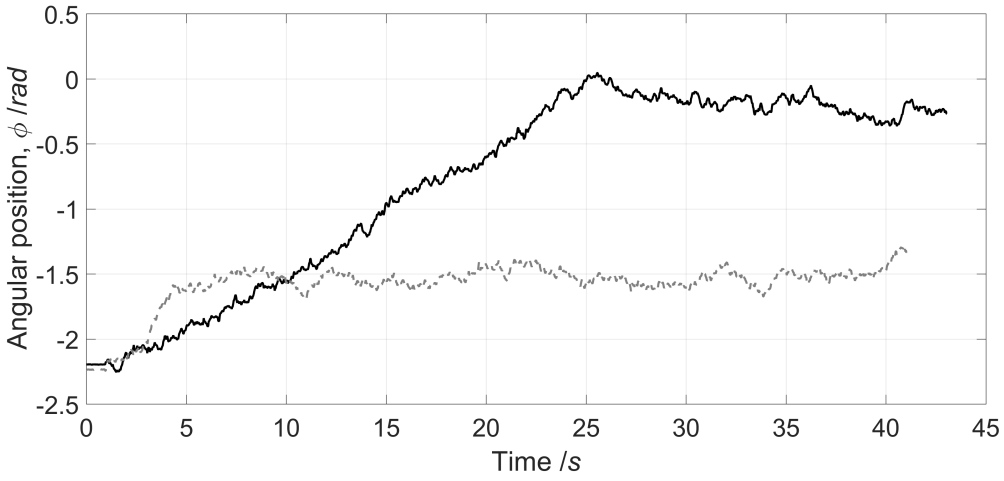

Figure 4.14: A comparison of two angle vs time traces for a particle trapped in the microscopic pendulum. The black solid line shows the trajectory and eventual stability of a particle in a trap which is not being modulated. The grey dashed line shows the greatly altered trajectory and stability position of a particle in a trap undergoing modulation with a large amplitude ($a/L = 0.3$).

evolve with increasing driving amplitude and reached a plateau at approximately $\phi = -\pi/2$ rad. At least three repeats were taken for each a/L value used and the results were averaged, the resulting plot of the progression of the equilibrium stability angle as the relative amplitude modulation is increased can be seen in Figure 4.15, where the error bars have been taken from the 95% confidence intervals of the least squared fitting.

Experimental, simulated, and analytical results all show the evolution of the equilibrium position that tends towards some saturation value, and as expected the pendulum never reaches a fully inverted position. In particular the experimental data agrees well with the theoretical value for the threshold amplitude for non-standard stabilisation. The three data sets show reasonable levels of agreement with each other as the modulation amplitude is increased and above threshold driving is achieved. Observed deviations may arise due to a combination of the randomness of the Brownian motion in conjunction with the possibility of slight anharmonicity of the relatively shallow optical potential (stronger optical tweezing is possible experimentally but with the galvanometer

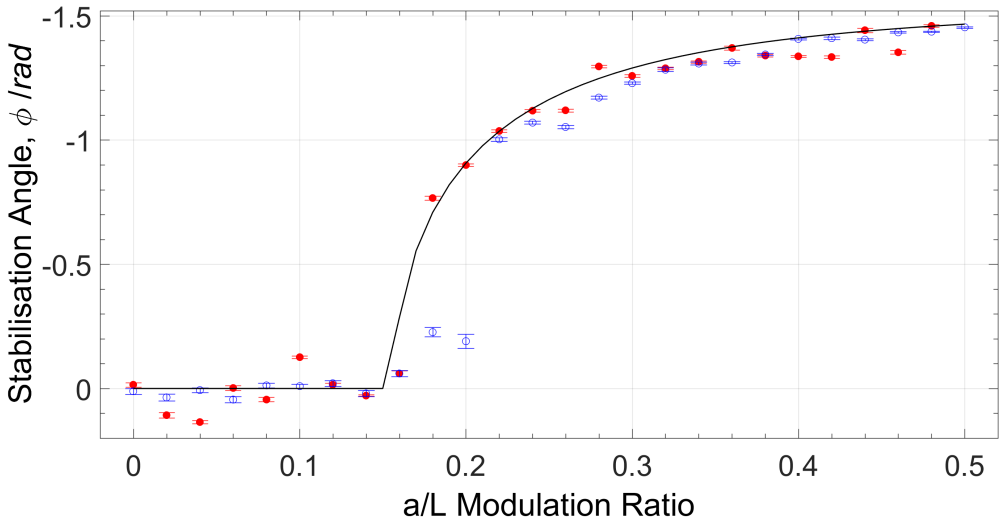

Figure 4.15: Equilibrium angular positions of a particle in the modulated optical pendulum trap. The solid line represents theoretical positions based on Section 2.1. Open blue circles show the result of Brownian motion simulations based on Section 3.4. The experimental data is shown as filled red circles. The parameters used for this experiment were: $\omega_0 = 2\pi \times (806\text{ Hz})$, $\omega = 500$ Hz, and $V_x = 1.0\ \mu\text{ms}^{-1}$.

scanning the trap strength was lessened, and it was found that higher optical powers caused an axial exit of the particle from the potential).

After completing this experimental work an attempt was made to shift the appearance of this plot, i.e. to change the location of the threshold driving amplitude. Analysis of the equation for the angular stability position in this regime (Equation 3.82) suggested that the easiest way to do this was to alter the proper frequency ω_0 of the pendulum by changing the laser power and so strength of the trap. This was increased to $\omega_0 = 2\pi \times (1.274\text{ kHz})$, giving a new predicted amplitude threshold for non-standard stabilisation of $a_{\text{thr}}/L = 0.087 \pm 0.002$ (the stage speed was also reduced to $v_x = 0.75\ \mu\text{ms}^{-1}$ to ensure the particle remained in the trap). The experiment was then run again for the same range of modulation amplitudes. A comparison of the two sets of results can be seen in Figure 4.16.

This shows that there is reasonably good agreement between the analytical line and the experimental data for this new strength of trap, again this is particularly

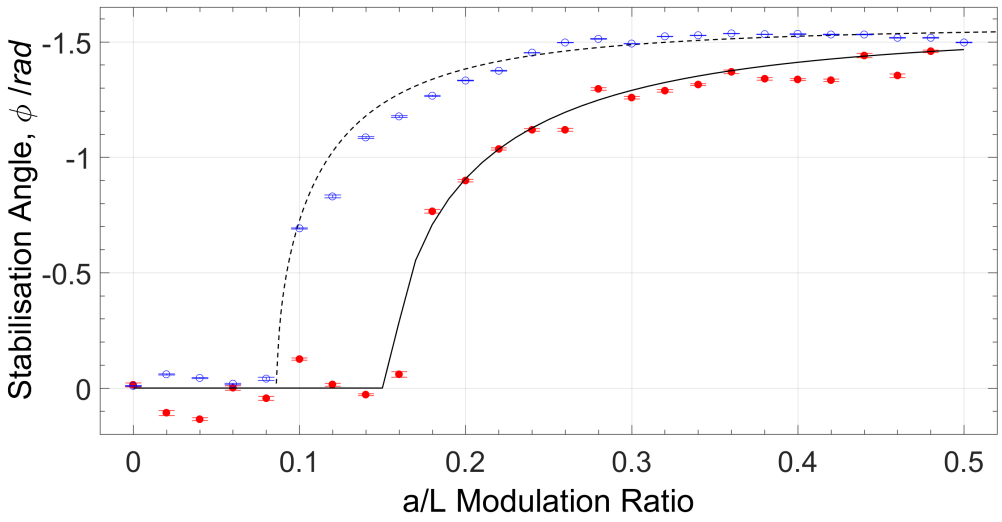

Figure 4.16: Equilibrium angular positions of a particle in the modulated optical pendulum trap for two different trapping strengths. The solid line and filled red circles show the analytical and experimental results respectively for a pendulum with: $\omega_0 = 2\pi\times(806\text{ Hz})$, $\omega = 500$ Hz, and $V_x = 1.0\ \mu\text{ms}^{-1}$. The dashed line and open blue circles show the analytical and experimental results respectively for a pendulum with: $\omega_0 = 2\pi \times (1.274\text{ kHz})$, $\omega = 500$ Hz, and $V_x = 0.75\ \mu\text{ms}^{-1}$.

true when it comes to identifying the threshold amplitude. It can be seen that changing the trapping strength via the proper frequency did indeed have the expected effect of shifting the amplitude threshold, to a lower value. The particle more quickly stabilised away from the standard position as the relative amplitude modulation was increased, and reached a slightly higher plateau for its equilibrium stability angle.

As Equation 3.82 shows, in this driving dominated regime, the stabilisation angle of the particle should not depend on the frequency of the driving. In an attempt to verify this, frequencies of two different size orders were used whilst all other parameters were kept the same. The two frequencies selected were:
$\omega = 2\pi \times (500\text{ Hz})$, and $\omega = 2\pi \times (50\text{ Hz})$. Due to tweaks in the experimental set-up that had been made, the proper frequency was marginally different to previous values. This experiment was conducted with a proper frequency of:
$\omega_0 = 2\pi \times (1.07\text{ kHz})$, yielding a threshold amplitude of $a_{\text{thr}}/L = 0.119 \pm 0.002$.

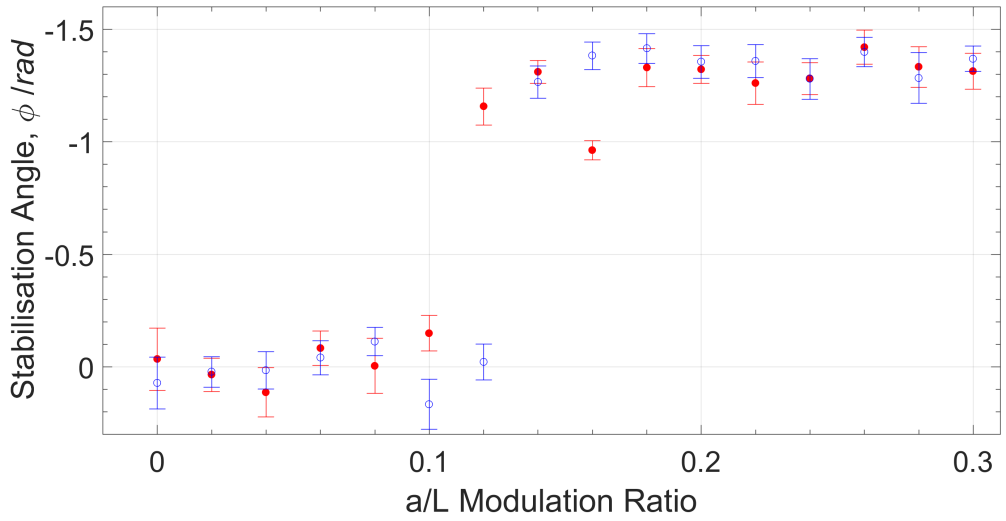

Figure 4.17: Equilibrium angular positions of a particle in the modulated optical pendulum trap for two different modulation frequencies. The filled red circles show experimental results for a pendulum with modulation frequency: $\omega = 2\pi \times (500\text{ Hz})$. The open blue circles show experimental results for a pendulum with modulation frequency $\omega = 2\pi \times (50\text{ Hz})$.

It can be seen from Figure 4.17 that generally, this theoretical expectation was witnessed experimentally. There is very good agreement between the two frequencies both below threshold and around the plateau region for the higher amplitude modulation ratios. This agreement worsens for the 'transition' region of $0.1 \leq a/L \leq 0.2$ where the equilibrium angle rises from $\phi = 0$ rad to its plateau value of $\phi \approx \pi/2$ rad. This is likely due to two factors. Firstly it was found in this experiment, particularly when dealing with lower frequencies like the $\omega = 2\pi \times (50\text{ Hz})$ here and those lower still in the following results section, that around this transition region it was harder to achieve stabilisation. Particles were more likely to exit the trap in this range than they were for higher or lower amplitude modulation ratios. At lower frequencies of modulation the particle is more likely to be dragged to and fro rather than seeing a fast average of the trap movement. As the modulation amplitude increases, the physical speed at which the trap centre is moving left and right must increase to maintain the same frequency of modulation. It is likely the case therefore that this region is where

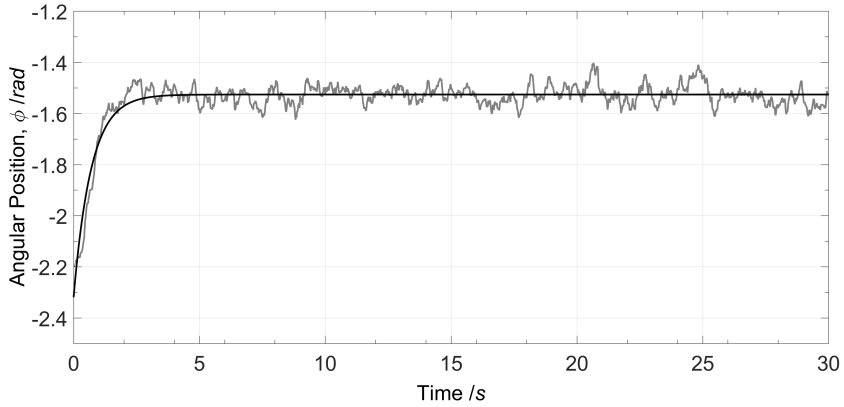

Figure 4.18: An example of the exponential fitting performed on the particles' angular trajectories in order to obtain their final stabilisation angles; shown for a video where $\omega = 2\pi \times 500$ Hz and $a/L = 0.34$. The grey line represents the particle's angular position, and the black line represents the fit made, of the form shown in Equation 4.19.

the particle changes from being dragged to experiencing an instant averaged potential picture. So it may be that the particle is dragged in one direction, then lost from the trap briefly as it moves the other way, until it returns to this point in its oscillation. It is conceivable that if this occurs Brownian kicks may move the particle away from a position where it can be recaptured from the trap, and so it is lost this way. Certainly that appeared to be the case. Secondly, this comparison was done quickly, with a much smaller data set than the previous graphs (as evidenced by the lower upper limit of the modulation ratio and the larger error bars on each of the points). So individual videos where the particle is lost or strays more from a typical stabilisation position will have much more of an effect and produce more anomalous points such as those seen in this region.

To extract as much information as possible from the tracked data and angles, the rise time of the exponential fitting was also analysed. The dynamics of the motion of the particle towards its new equilibrium position give information about the local curvature of the potential, i.e the spring constant [93]. An example of one of these fittings can be seen in Figure 4.18.

The rise times of the exponentials were averaged and compared for the increasing

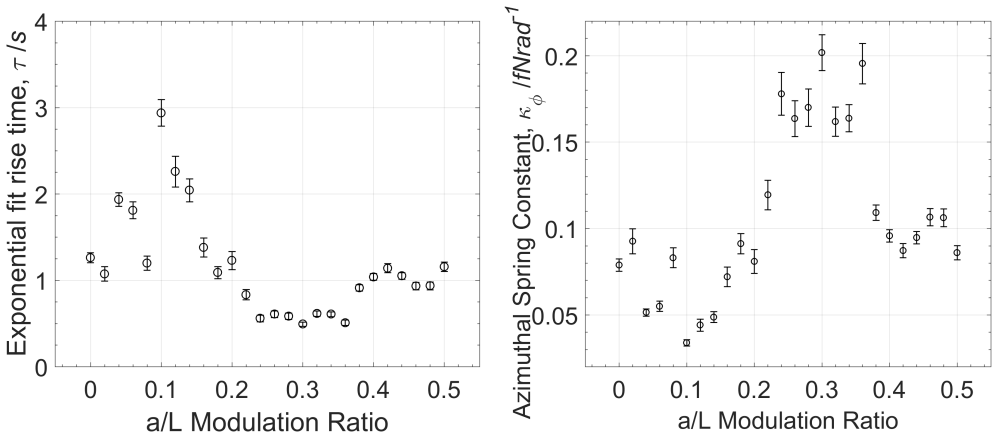

(a) (b)

Figure 4.19: a) The mean rise times from the exponentials fitted to the angular trajectories of particles in the optical pendulum, plotted against the amplitude modulation ratios. b) Azimuthal spring constants extracted from these rise times, again plotted against the amplitude modulation ratios.

amplitude modulation ratios. The expected trend was that an initial small increase in rise time would be seen as a/L was increased, since the effective potential is shallower and so the particle may sample more of the anharmonic part of the trap here. Then a sharp decrease was expected beyond threshold as the alternate stability position comes into existence and there is a deeper potential and stronger trap for the particle to fall into here. Just as with the stabilisation angles, this was expected to plateau eventually. The data set with $a_{\mathrm{thr}}/L = 0.087$ was used to check this and the results are shown in Figure 4.19a. These seem to agree reasonably well with what was predicted. There is a small increase as threshold is approached and then a sudden drop thereafter. The plateau region is not as well defined as it could be, with a slight increase from $a/L = 0.38$ and upwards, but this is not a large increase and it still stays relatively flat compared to the value at threshold.

Next these rise times were used to calculate the azimuthal, or angular, spring constant. The characteristic time for the relaxation of the angular position, i.e. the rise time τ, in the fitted evolution of $\phi(t)$, is related to the spring constant for

angular displacements by: $\kappa_\phi = L\gamma/\tau$. The intuitive expectation for this plot was (and not simply because the formula contains the inverse of the rise time) that at low a/L values the spring constant would be small, and would decrease towards the threshold a/L value. This was expected due to the angular fluctuations seen at low modulation ratios during the experiment, and the slight straying of the experimental points from $\phi = 0$ rad below threshold in Figure 4.15. An increase in κ_ϕ was expected for higher amplitude modulation ratios as the particles' angles fluctuated less for these during experiments and hugged the predicted line more tightly in the same figure. The angular spring constants found via this method are shown in Figure 4.19b.

The plot confirms these expectations. Below threshold there is a general slight decrease in κ_ϕ although a lot of variation here masks this slightly. Then above threshold the angular stiffness increases greatly with a/L. This figure does however suggest that the slight increase in rise times seen for $a/L = 0.38$ and above seen previously has more of a significant effect here, as no plateau is seen but rather a drop in the spring constant at these modulation values. It is not immediately clear why this change should occur, and so more investigation and further experimentation is warranted here.

This behaviour can also be qualitatively observed in the extent of the fluctuations of the angular trajectories, since it is also the case that: $\kappa_\phi = k_\mathrm{B}T/L\sigma_\phi^2$ by equipartition of energy. It should be noted however that in the region of the threshold the anharmonicity of the effective potential is significant since, in a Taylor expansion of the effective potential around $\phi = \phi_\mathrm{eq}$ (the equilibrium angle) the quadratic term is zero. For this reason, exact agreement for the magnitudes of the angular spring constant determined by this method is not found, but similar behavior in the limits of low and high modulation (where the potential anharmonicity is less significant) is observed. Most notably though,

the confining potential in the dynamically stabilized case is generally stronger than the unmodulated pendulum.

4.3.3 Friction Filter Regime Results

After testing the driving dominated regime, the experiment was moved on to the case where neither friction nor the driving were limiting the stabilisation behaviour, the 'rigid pendulum with friction' regime. As mentioned at the beginning of this results section, due to the very large friction coefficient (relative to the other frequencies in the system) it was very difficult to enter this regime and required a significant lowering of the driving frequency.

An initial exploratory investigation into this regime was conducted using amplitude modulation for the independent variable again. This was in order to quickly establish that non-standard stabilisation and stability angle evolution was being seen. In this instance a driving frequency of $\omega = 2\pi \times (1\text{Hz})$ was selected. Experimentation revealed that in order to keep the particle in the trap in this regime, both a lower stage translation speed and a lower laser power were required. The stage speed used was $v_x = 0.5\ \mu\text{ms}^{-1}$. The lower laser power resulted in a radial spring constant of $\kappa_r = 0.08\ \text{pN}\mu\text{m}^{-1}$, which gave a pendulum proper frequency of $\omega_0 = 2\pi \times (658\ \text{Hz})$, giving a threshold modulation amplitude of $a_{\text{thr}}/L = 0.141 \pm 0.002$. It can then be seen that this satisfies the condition for leaving the driving dominated regime since, $\gamma' = 2\pi \times 423$ kHz, and so now $\omega_0^2/\omega \gg \gamma'$. This slower stage speed meant that a longer period of stage translation was needed in order to achieve standard stabilisation. These videos therefore take place over twice as long as the previous set, approximately 80 s.

Experiments were conducted again in a systematic fashion of raising the amplitude of the driving modulation, although this time only up to a value of

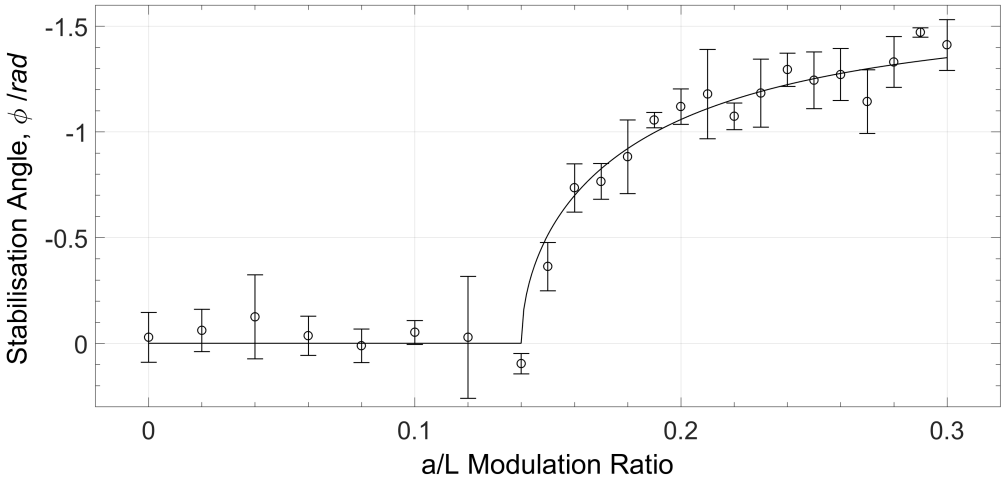

Figure 4.20: Equilibrium angular positions for a particle in the modulated optical pendulum trap in the friction filter regime. The solid line represents theoretical positions based on Section 2.1.

$a/L = 0.3$ since it was observed during experimentation that a transition was occurring and the particle was approaching its plateau stability value already at this modulation size. The results are reported in Figure 4.20.

The experimental data and theoretical predictions are in excellent agreement both for the predicted threshold modulation amplitude and for the equilibrium angle across the range of modulation amplitudes tested. Above threshold there is a continuous evolution of the stabilisation angle tending towards a plateau value of $\phi = \pi/2$ at large modulation amplitudes. Inverted stability is not seen, as was expected, because the necessary condition that $\gamma' < \omega_0$ (as mentioned in Section 3.3.3) is not true here and was not achievable in this experiment.

The exponential rise times in this experiment were also analysed, and from these the angular stiffness (azimuthal spring constant) was extracted.

These were generally as expected and looked much as they did for the previous regime. Figure 4.21a shows the mean exponential rise times for each ratio. Once again these generally rise by a small amount towards threshold and have dropped to much shorter times thereafter. In this instance though there is not the

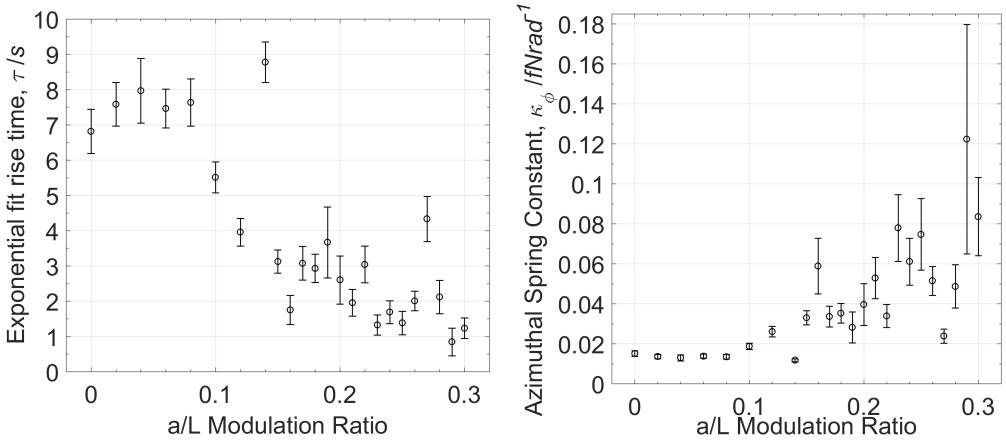

(a) (b)

Figure 4.21: a) The mean rise times from the exponentials fitted to the angular trajectories of particles in the optical pendulum in the friction filter regime, plotted against the amplitude modulation ratios. b) Azimuthal spring constants extracted from these rise times, plotted against the amplitude modulation ratios.

unexpected rise towards the higher a/L values, but there is also less of a plateau. Both of these could be because this experiment was only run to $a/L = 0.3$ and so there is less higher modulation amplitude data than for the previous experiments. Figure 4.21b shows the derived angular spring constants. These exhibit the expected low value and slight decreasing trend towards threshold where the potential is shallower and the particle experiences more of an anharmonic trap, and then a large increase in the angular stiffness above threshold is seen. Encouragingly, this plot doesn't have the drop at larger modulation amplitudes seen in the previous section, although this could once again be simply because fewer large a/L values were used for this experiment.

As was mentioned in Section 3.3.3; the significant difference between the angular stabilisation of this regime, compared to the driving dominated regime, is that the equilibrium angle is now additionally dependent upon both the driving frequency, ω, and the friction coefficient, γ'. It therefore seemed pertinent to go beyond the current exploratory initial method of varying a/L, and to vary these parameters and check that the results agree with the theory for these dependent

variables too. Changing the friction coefficient, γ' would have been difficult. The most obvious way to do so would be to change the medium surrounding the particles, the water. However a lower friction coefficient than the water would be desirable, since γ' is already large compared to the characteristic frequencies in the system and so already makes it hard to enter the friction filter regime. There are few liquids with lower dynamic viscosities (and so friction coefficients) than water, and fewer still which would be suitable. Certain alcohols, methanol for example, possess a low friction coefficient at room temperature. These were not readily available in the laboratory in the quantities needed to dilute the solutions. They also come with their own problems, they are hazardous in various ways and must be properly disposed of. Also, they would not be compatible with the commercial nail varnish used to glue down the cover slips (methanol etc. would simply dissolve this). Therefore consideration was given to the evolution of the stabilisation angle as a function of the modulation frequency, ω, instead.

For these experiments the amplitude modulation ratio was kept at $a/L = 0.25$. Suitable ranges of trapping strength and stage driving speed were identified in order to maintain the conditions for the friction filter regime ($\gamma' \ll \omega_0^2/\omega$ and $\gamma_2' < \gamma$) whilst shifting the appearance of the plots and changing the threshold driving frequency, as was done previously for the driving amplitude in Figure 4.16. The trapping strengths ranged from: $\kappa_r = (0.47 \rightarrow 1.02)$ pNμm^{-1}, whilst the stage driving speeds were all in the range: $v_x = (0.46 \rightarrow 1.00)$ μms^{-1}. The modulation frequency was gradually increased from $\omega = 2\pi \times (0 \rightarrow 10$ Hz). All other parameters were held fixed, as before. The experimental results can be seen in Figure 4.22

From this plot it can immediately be seen that changing the trapping strengths had the desired and expected effect of shifting the threshold frequency. Rather than quoting the trapping strength (κ_r) or the proper frequency which depends

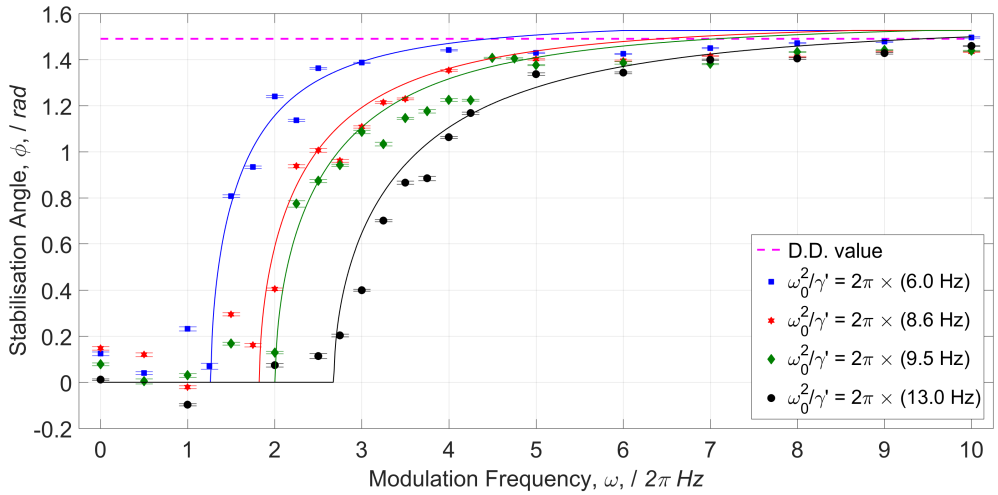

Figure 4.22: Equilibrium angular positions for a particle in the modulated optical pendulum trap in the friction filter regime, as a function of the modulation frequency, ω. Solid lines represent theoretically predicted positions for the same coloured data sets based on Section 2.1. The dashed line represents the driving dominated regime value over these frequencies.

upon this (ω_0) in the legend for each case, the decision has been taken to show the quantity ω_0^2/γ'. Firstly, this has a factor of κ_r in its numerator (via the ω_0^2 term) and so is directly proportional to the trapping strength anyway, making it easy to immediately identify which direction a stronger or weaker trap shifts the threshold frequency. Secondly, this quantity is a rearrangement of the driving dominated/rigid pendulum with friction regime condition ($\gamma' \ll \omega_0^2/\omega$) for ω. This makes it very easy to see where all 4 sets of data fall below the driving dominated regime, as it gives a very quick upper frequency limit for remaining in the rigid pendulum with friction regime which can be compared to the values on the x-axis.

The plot shows that there was good agreement between the experiments and theoretical predictions. The stability angles of all four trapping strengths increase around their predicted threshold values, and all of them show a gradual evolution of the stability angle towards a plateau at $\phi = \pi/2$ that agree well with the predicted curves. The plot also features a reference line displaying the

driving dominated regime stability position across these driving frequencies - naturally, in order to enter this regime at these low frequencies the trapping strength and stage speed had to be altered for the purposes of this theoretical stability line. This line serves to make the point that with modulation frequency as the independent variable, the stability angle behaves very differently in the driving dominated regime (where it remains constant) as compared to how it behaves in the friction filter regime (where it slowly evolves towards a plateau value which is approximately equal to the driving dominated regime value). Indeed the steady evolution of the stability angle behaviour is seen in this plot; where it initially varies greatly at low frequency driving in the friction filter regime, and then as these curves begin to enter the high frequency regime it becomes independent of the modulation frequency.

4.3.4 Dynamics Direct Comparison

It is interesting, with both low and high frequency modulation results acquired, to do a direct comparison of the dynamics of the particles. Figure 4.23 shows a side-by-side comparison of a typical trajectory in both regimes, for a similar modulation amplitude, a/L.

In both cases the particle is seen to stabilise away from the standard position, however it can be seen in Figure 4.23a that in the low frequency regime, the particle oscillates about the equilibrium angle, in an elastic rod fashion, as well as undergoing Brownian motion. It is dragged by the modulating potential before it fully relaxes into its equilibrium position. Contrastingly, in the high frequency regime (Figure 4.23b), this oscillation is strongly damped, as for a (quasi)rigid pendulum rod. The particle quickly assumes its position at the expected stabilisation angle, undergoing small Brownian motion around it.

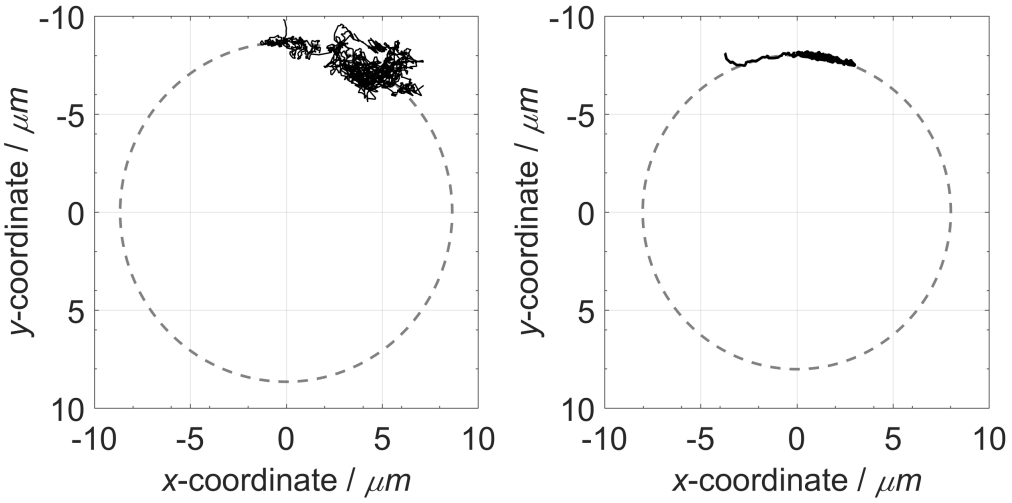

Figure 4.23: Experimental trajectories for particles in an optical pendulum potential. a) A particle trapped in the low frequency, friction filter regime, displaying radial oscillations about its stabilisation angle. Here $a/L = 0.21$. b) A particle trapped in the high frequency, driving dominated regime, where these oscillations are strongly damped ($a/L = 0.22$).

Analysis of the power spectra of the particles' radial coordinate in the two regimes illustrates this well, see Figure 4.24.

In the low frequency regime, Figure 4.24a, a large peak is clearly seen near $\omega = 2\pi \times (1\text{ Hz})$, thus indicating radial oscillations of the particle at the driving frequency. No such peak is seen in Figure 4.24b, the high frequency regime, where the driving frequency is $\omega = 2\pi \times (500\text{ Hz})$, greatly in excess of the time resolution of the camera used. Observing these power spectra adds a new clarity to the threshold condition for switching regimes. The low frequency regime's power spectrum exhibits a peak very close to the corner frequency, whereas the high frequency regime's modulation is much greater than it, and cannot be observed in this power spectrum due to the frame rate attainable with the camera used. Here the power spectrum shows a particle that is insensitive to this high frequency, the trap acting as a low-pass filter, and only showcases the Lorentzian component from the radial confinement of the particle.

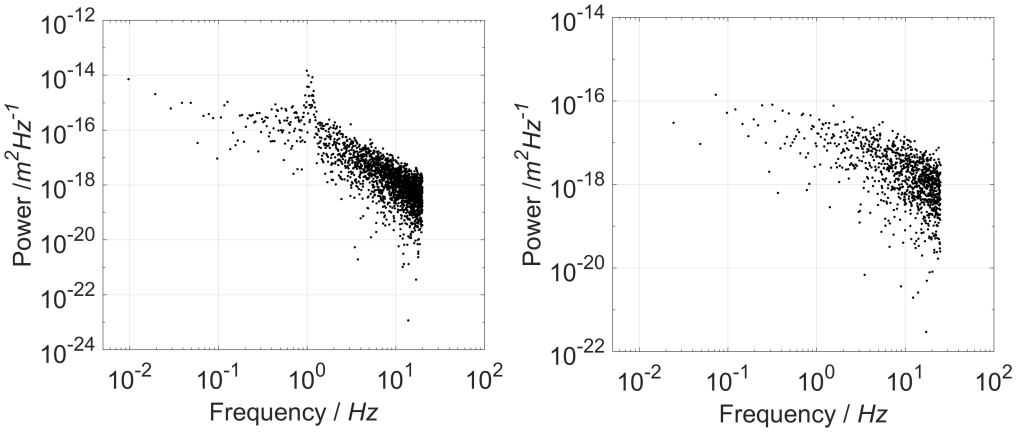

(a) (b)

Figure 4.24: Experimental power spectra of the radial coordinate of a particle in an optical pendulum potential. a) In the low frequency, friction filter regime, where the trap is modulated at $\omega = 2\pi \times (1\text{ Hz})$, very close to the corner frequency and visible as a large peak in the plot. b) In the high frequency, driving dominated regime, where the trap is modulated at $\omega = 2\pi \times (500\text{ Hz})$, a value much higher than both the corner frequency and the time resolution of the camera used.

4.4 Summary and Outlook

4.4.1 Summary

In this chapter Kapitza's pendulum has been revisited, using a very different environment to that in which it was originally described.

A pendulum of finite stiffness, in a regime where damping is no longer negligible, has been considered, and a comprehensive theory has been presented describing the dynamics and behaviour of this strongly overdamped pendulum throughout a range of modulation frequencies.

It has been shown that at high driving frequencies, or with very large friction, the pendulum will enter what has been termed a 'driving dominated' regime. Similarly to Kapitza's theory, analysis of this high frequency regime showed that dynamical stabilisation at angles away from $\phi = 0$ rad was possible, given a sufficiently large amplitude modulation of the pendulum. Thereafter the

stabilisation angle of the pendulum would be dependent upon the modulation amplitude and the characteristic natural and proper frequencies of the system. Unlike the underdamped pendulum of Kapitza though, this would not achieve a fully inverted stability position.

Low driving frequencies were also considered for a finitely rigid, finitely damped pendulum. Again in this instance, it was demonstrated theoretically that dynamical stabilisation away from a standard equilibrium position should be possible. Here though it was seen that this stabilisation was additionally dependent upon the driving frequency and the friction present in the system, hence this was termed the 'friction filter' regime. It was shown that the behaviour within the friction filter regime split again into three distinct regimes which, with the correct combination of the above parameters, would yield stabilisation at angles ranging from the standard $\phi = 0$ rads right through to the inverted $\phi = \pi$ rads.

Brownian motion simulations of both the low and high frequency regimes were completed, using a finite difference method of simulating the differential equations, in order to complement the theoretical calculations. These were employed with realistic experimental parameters where possible, and were in good agreement with the predictions of the theory. They therefore served not only to bolster confidence in the theoretical analysis but also to confirm the viability of this experiment practically.

This pendulum was realised experimentally using a microscopic silica particle held fixed in an optical tweezers set-up. The trapping laser was scanned in a circle to emulate a pendulum arc, the centre of which was modulated to provide the driving seen in the Kapitza pendulum. Gravity was then accounted for by way of a fluid drag force, created by translating the microscope stage, thus completing the optical microscopic analogue of the Kapitza pendulum.

Experimental results generally agreed very well with both theory and simulations. Non-zero stabilisation was seen in both regimes for above threshold amplitude modulation of the pendulum potential. The parameter space possible experimentally was such that the inverted pendulum sub-regime was not achievable. Both regimes showed continuous evolution of the stabilisation angle towards a plateau in the horizontal position, as would be expected from substitution of the correct parameters into the theoretical equations (and as backed up by simulations). The particles' dynamics in the high frequency regime were comparable to those of a pendulum with a quasi-rigid rod, exhibiting quick relaxation to the trapping potential radius at the correct stabilisation angle. The low frequency behaviour was much more akin to an elastic rod, with radial oscillations about the angular coordinate and a peak in the power spectrum at approximately the corner frequency.

The low frequency, friction filter regime was explored experimentally by varying the modulation frequency of the pendulum. An evolution of the stabilisation angle as a function of this frequency was achieved when driving at a fixed amplitude. Moreover different trapping strengths were tested and these were found to shift the modulation frequency threshold for non-standard stabilisation. The experimental data showed good agreement with the theoretical predictions, both on the threshold frequencies and the stability angles above this frequency. It was seen in all trapping strengths that a transition was made from low frequency, where the stabilisation angle varied and was sensitive to the driving frequency and friction conditions, to the high frequency where it was stable and indifferent to these.

4.4.2 Outlook

Dynamics of colloidal systems are typically strongly overdamped, with large friction present. This experiment has demonstrated a pendulum regime where different friction coefficients yield different equilibrium angles. Different sized particles have different friction coefficients. It is therefore expected that understanding the dynamics of a particle across these regimes will enable opto-fluidic manipulations of colloidal particles in applications involving; for example, filtering of particulate material depending on size and so the value of the friction coefficient, and may possibly be applied to macroscopic pendula. This could add new possibilities to existing sorting techniques such as extended optical landscapes [94] or Brownian ratchets [95–97].

A potential and interesting future experiment using this set-up would be to attempt such filtering or sorting. To see if, by modulating at a given frequency and amplitude, and/or by finding a suitable low viscosity fluid for the immersing medium, different angles of stability could reliably be obtained for different sized particles, and this could be used to sort them based upon their size or perhaps also their density/mass.

Chapter 5

Red Blood Cell Deformability in Diabetic Retinopathy

This chapter departs from the Kapitza pendulum and catalogues the second main area of experimental study undertaken during this Ph.D. This second section of original research ventures into the landscape of biophysics. It will deal with erythrocytes, red blood cells (RBCs), in particular their deformability. The details of a pilot study, conducted with a view to assessing the RBC deformability in diabetic test groups, will be documented.

5.1 Background

5.1.1 Diabetes Mellitus

Diabetes Mellitus (DM) or more commonly, diabetes, is a metabolic disease. Its occurrence is due either to the pancreas producing an insufficient amount of insulin, or the body not responding correctly to the insulin produced and using it ineffectively (Types 1 and 2 respectively) [98]. Insulin is a hormone that affects the metabolism by promoting the absorption and storage of glucose from the blood into body cells (fat, liver, and skeletal muscle) by converting it into glycogen [99]. As such, insulin helps to regulate the body's blood sugar levels. A lack of insulin can therefore lead to an excess of glucose in the blood and so high blood sugar levels, known as hyperglycaemia. Chronic hyperglycaemia is the defining characteristic of DM.

Diabetes, and the potentially associated chronic hyperglycaemia, greatly increases the risk of long-term complications. These generally relate to damage to blood vessels. This can be on the macroscopic level, with macrovascular diseases commonly associated with atherosclerosis (thickening of artery walls due to the accumulation of leukocytes, white blood cells (WBCs) [100]) such as stroke, coronary artery disease and peripheral vascular disease [101]. It can also

be on the microscopic level. Microscopic complications include: diabetic neuropathy (damage to the nerves due to inadequate blood flow, resulting in a number of symptoms such as numbess and pain), diabetic nephropathy (damage to the kidneys that can result in chronic kidney disease and require dialysis or a kidney transplant) [102], and most significantly here, diabetic retinopathy(DR).

5.1.2 Diabetic Retinopathy

In the early stages of DR, known as non-proliferative diabetic retinopathy (NPDR), there are little to no symptoms, and patients may not see any reduction in the clarity of their vision. NPDR progress via hyperglycaemic damage to the microvasculature of the retina. The high blood glucose levels characteristic of hyperglycaemia can cause the endothelial cells (those lining the inside surface of a blood vessel) to take up more glucose than normal. They form more proteins on their surface than usual and cause a thickening and weakening of the membrane that separates the blood vessel from the connective tissue around it. With this thinning of the blood vessels can come the formation of microaneurysms (small blood filled bulges in the walls of the vessels). In the early stages of NPDR, the only way to detect the condition is by the presence of these microaneurysms when fundus photography is used (a special kind of photography that utilises a microscope to image the back of the eye, the fundus, allowing for inspection of the retina, optic nerve head, and macula) [103]. In a small percentage of patients, these swollen and damaged blood vessels can leak RBCs and serous fluid onto a small part of the retina called the macula (a central part of the retina with many cones that enable clear colour vision in the centre of the field of view) [104]. This leaked fluid can cause swelling, obscuring the path of the light to the retina, and causes a loss of vision via blurred and distorted images, which is known as macular oedema [105, 106].

Progression of the condition (further thinning of the vessels, glucose uptake and membrane thickening) can lead to vascular occlusions, in which vessels become blocked and blood flow through them is ceased. This in turn leads to retinal ischaemia, a restriction of the oxygen and glucose needed to keep the cells of the retina alive [107, 108]. It is then possible for proliferative diabetic retinopathy (PDR) to develop. In response to the ischaemia, and the lack of oxygenated blood flow, new blood vessels begin to proliferate and grow both along the retina and in the vitreous humor (the gel that sits between the retina and the back of the lens). These new vessels are fragile, and can bleed into the vitreous, clouding and obscuring a patient's vision. If left untreated this can lead to the formation of scar tissue, retinal detachment, and ultimately blindness [109].

In 2014, the number of adults with diabetes worldwide was 422 million [110]. A 2012 analysis into the prevalence of DR, based on pooled data from over 20,000 individuals with diabetes worldwide, found that approximately one third of people with diabetes have signs of diabetic retinopathy, and that a third of these have potentially vision threatening retinopathy [111]. In many countries DR is the most common cause of preventable blindness amongst the working-age population (20-74 years) [107, 112]. In the U.S.A. for example, it is estimated that 40% and 86% of people with types 1 and 2 diabetes respectively have diabetic retinopathy [113, 114]. Encouragingly though, research has suggested that a large proportion of new cases could be reduced with vigilant monitoring of the eyes and proper treatment [115].

Three major treatments exist for DR [115], and even those with advanced DR have a high probability of keeping vision if treatment is begun before severe retinal damage has occurred. The first of these treatment methods is laser surgery. Various methods exist depending upon the the patient's specific DR manifestation. These include: destroying or coagulating the new vasculature,

causing low intensity burns in an area around the macula to help clear the oedema, and deliberately creating a large number of small burns in the retina to reduce its oxygen demand and so the ischaemia [116]. Caution is advised with laser treatment due to the damage to/loss of retinal tissue. The second major treatment method comes in the form of intravitreal injections. This can either be of corticosteroids, which help to decrease the macular oedema and improve vision, which are not permanent and so must be re-administered every 3 months. Alternatively, this can be multiple doses of an injection of anti-VEGF drugs (VEGF - vascular endothelial growth factor, is a protein that stimulates vasculogenesis, blood vessel formation by production of endothelial cells) [117, 118]. The final treatment method, vitrectomy, is used when there is already a clouding of the vitreous humour due to blood leaking from new vasculature. This involves the partial or complete removal of the vitreous humour, usually to be replaced with a clear saline solution [119, 120].

With the narrowing of the vascular system discussed above, it is necessary that RBCs have a degree of flexibility or deformability in order to maintain sufficient blood flow in the microcirculation to prevent this occlusion [121, 122]. In the microcirculation, the diameter of blood vessels is typically in the range of 2 to 10 μm, whilst the average RBC diameter is approximately 8 μm. It is crucial therefore that RBCs are deformable under applied stress to enable them to pass through these vessels and supply glucose and oxygenated blood to the surrounding tissue [123–126].

5.2 Literature Review

There are many different techniques that have been utilised to quantify the deformability of RBCs, some of which are: *in vivo* imaging (in rats), cell transit

analyser - filtration techniques, the use of glass capillaries and micro fluidics, and ektacytometers (analysis based on detection of laser diffraction by an RBC) [127–131].

As mentioned in Chapter 1; optical tweezers, operating at a wavelength (1064 nm) at which optical absorption in living cells is low, have become a powerful tool for observation and manipulation of biological matter on a single cell scale [18, 19]. Optical tweezers have in fact already been used to trap RBCs and assess some of their properties such as shape-recovery, cell deformability and cell membrane shear modulus [132–134]. Novel laser techniques of assessing RBC properties have also been realised, including using two non-focussed counter-propagating beams to make an 'optical stretcher', and a multiple trap tweezers set-up [134, 135].

Optical forces are typically applied to these cells in one of two ways. Microbeads can be attached to the cells and then used as handles, trapped by the optical tweezers [136]. Alternatively the simpler method of trapping the cell directly with the laser can be used. This has been employed to measure the transverse stretch of an RBC by jumping the trap at high frequency between two positions [137].

It is known that RBC deformability can be affected by many factors linked to diabetes (hyperglycaemic/insulin levels, platelet aggregation and the shape of the cells) [138, 139]. Indeed, impaired deformability of RBCs has previously been linked in studies to DM and also to diabetic nephropathy (kidney disease) [140–142]. Less clear and studied is the link between RBC deformability and retinal vascular disorders, particularly compared to the deformability of patients with T2DM (type 2 diabetes mellitus) but without DR. Additionally no studies could be found researching the initial length and morphology of RBCs as a factor in cell deformability. Where an investigation into RBC deformability in DR does exist [128], it has been carried out using the above mentioned filtration

techniques. These rely on the passage of RBCs through micropores in a polycarbonate filter. Although this allows for a large number of cells to be measured in a short space of time, it has a 2% total sampling error as cells can be haemolysed (ruptured) giving possible incorrect results [143]. In an optical tweezers experiment, cells can be individually selected and ensured healthy, taking more time but rendering negligible this source of sampling error.

5.3 Objectives

The main aim of this research is to collaborate with Dr. Rupesh Agrawal of Moorfields Eye Hospital to conduct a pilot study to investigate RBC deformability in a patient group with DR, using a dual-trap optical tweezers apparatus. Patients with T2DM, and a healthy control group, will also be included in the study in order to provide a comparison of the acquired deformability data.

A subsidiary aim is to assess potential factors (morphological and chemical) that may alter the RBC deformability in the DR cohort compared to the healthy control group and those with T2DM.

5.4 Contributions

As before, I will take this opportunity to make clear the contributions of myself, and the others involved in this red blood cell research. Rupesh Agrawal (Institute of Ophthalmology, University College London) was the lead clinical contributor on this project. In addition to pooling the relevant personnel from different institutions/departments and obtaining ethical permission to enable the

study to progress, he was responsible for acquiring the blood samples from the patient volunteers and having this blood centrifuged, as well as having the blood/chemical tests performed . Rhythm Bhatnagar (University College London, Engineering Department) transported the samples to the Physics department and demonstrated to myself and Thomas Smart (University College London) the procedure for preparing the microscope slides with dilutions of the blood samples. After establishing the experimental procedure to be used and inserting optical elements into the beam path to split the trapping beam in two, Thomas and myself performed the stretching experiments together. I worked to implement the 3D-defocussing microscopy code in MATLAB and acquire the experimental images for these in order to try to obtain morphological properties of the cell. Thomas made modifications to the tracking code written for previous chapters to track the red blood cells throughout the videos of the stretching procedures. The raw data of stretched and un-stretched lengths for all of the cycles was then sent to João Nobre-Cardoso who performed the statistical tests to find the significance of the stretching lengths.

5.5 Experiment

5.5.1 Ethics and Study Groups

All the research was performed as per the ethical principles of the Declaration of Helsinki [144]. Ethics board approval was obtained. The study was approved by Coventry and Warwick NRES Committee, West Midlands (REC ref: 14/WM/1038). The study was conducted between August 2014 and July 2015.

Five patients with T2DM without DR (DM - study group 1) (mean age: 51.6 years, 3 (60%) males, and seven patients with T2DM and associated mild non

proliferative diabetic retinopathy (DR - study group 2) (mean age: 54.7 years, 4 (50%) male) were recruited for the study. Additionally, eight age and gender matched control subjects were recruited (control group) (mean age: 52.4 years, 5 (71%) males). Informed consent was obtained from all participants and details of their demographics and personal history were recorded on a pre-coded data information sheet [122].

5.5.2 Experimental Set-Up

The experimental set-up for this RBC deformability study is broadly speaking the same as that seen and documented previously in Section 4.1. The trapping laser, galvanometer mirrors, microscope, objective lens, and camera are all identical to those used before.

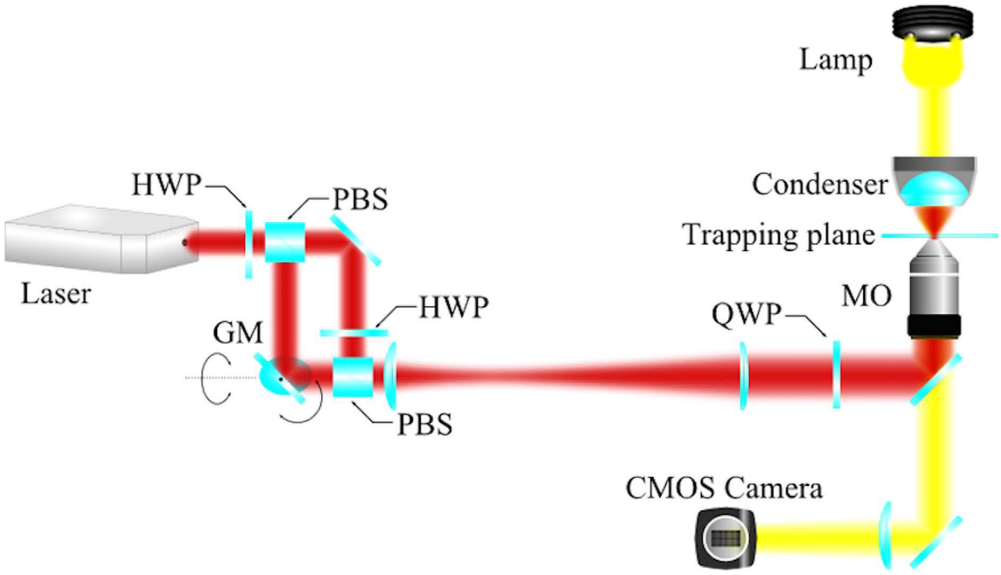

Figure 5.1: Experimental set-up for the RBC deformability experiment. The laser is split into two beams, such that one can be steered relative to the other. The two beams are also given opposite handed circular polarisations by a quarter wave plate to avoid interference effects. The black arrows indicate the rotations of the galvanometer mirrors [109].

The primary differences in the set-up can be found in the beam path of the

trapping laser (see Figure 5.1). Here it can be seen that extra optic elements have been added when compared to Figure 4.1. A polarising beam splitter (PBS) cube has been used in order to split the incident laser into two orthogonally polarised (vertically and horizontally) components. This is accompanied by a half wave plate (HWP) used to rotate the plane of polarisation of the laser light before it hits the PBS. The combination of these two elements enables tuning of the proportions of light being transmitted and reflected, and so adjustment of the relative power of the two separated beams.

One of these beams then propagates to the galvanometer mirrors such that it can be steered relative to the other beam which acts as a fixed optical trap in this experiment. The fixed beam must be directed through another HWP such that when both beams arrive at the second PBS it is reflected rather than transmitted (the steerable beam has its polarisation state changed by the two reflections from the galvanometer mirrors, hence its behaviour change at this PBS compared to the first one). The beams are recombined at this PBS and in addition to the system of telescoping lenses seen previously, they pass through a quarter wave plate (QWP) to finally give two nearly co-propagating beams with orthogonal circular polarisations, such that interference effects between them are avoided.

5.5.3 Method

Blood Collection

Blood samples were collected from study participants at Moorfields Eye Hospital using a vacutainer (BD) and collection needles (21G 1 inch, sleeve wall: thin) from the antecubital vein with interruption of the venous flow. All samples were collected at noon, prior to lunch being eaten, and in a seated position to avoid any potential confounders secondary to time and posture [145]. 20ml of the

collected blood was used to conduct tests, under the direction of Dr. Agrawal at Moorfields Eye Hospital NHS Foundation Trust, including: full blood count, renal function, liver function, random blood glucose, glycosylated haemoglobin, and more (see Agrawal *et al.* [122] for full details) .

4 ml of RBCs were separated out from the samples by a centrifuge and collected in a spray-coated k2-EDTA (plastic) BD vacutainer tube with BD hemogard closure for assessment of RBC deformability via optical tweezers. This was then transported from the hospital to the Department of Physics and Astronomy at University College London in a labelled bio-box, kept at a temperature of around 4 °C. Total transfer time of the blood from the phlebotomist room to the research laboratory was 30-45 minutes.

Slide Preparation

Latex gloves were worn by all persons handling the RBCs and preparing microscope slides. All equipment used for preparation of the RBCs (including microscope slides, cover slips, and microcentrifuge tubes) were cleaned with isopropyl alcohol (IPA) and washed with phosphate buffered saline solution (PBS) before being used. The RBC samples were diluted with PBS at a ratio of 1 mL of PBS to 1 μL of RBCs and with 1% bovine serum albumin (BSA) to prevent RBC aggregation and adhesion to the slide. 100 μL of this diluted RBC suspension was then pipetted into the well of a microscope slide before being sealed beneath a No. 1.5 cover slip (as used previously for the Kapitza experiment) [109]. Following this slide preparation, the cells were subjected to a visual inspection under the microscope. This was to confirm the overall healthy appearance of the cells, as well as a satisfactory concentration of RBCs (not so concentrated that there was risk of additional RBCs entering the traps when stretching was underway), and fewer than 5% echinocytes per slide (cells that

have an abnormal cell membrane characterized by many small, evenly spaced thorny projections [146]).

Calibration

Prior to trapping the RBCs, a calibration procedure was carried out in order to ensure the two optical traps were evenly balanced. A spherical particle (1.5 μm silica) was used for this. The particle was held fixed in each trap, whilst the other was blocked. Its motion was recorded and tracked in order to obtain a trapping spring constant in both x and y directions. This was done for both traps, and for a range of HWP settings. The results for the two traps were then compared and the waveplate adjusted accordingly to make the strength of both traps as similar as possible in both directions.

After this balancing, RBC trapping was attempted. Initially the foci of the two beams were controlled such that their separation was less than the diameter of a RBC. Upon entering the traps, cells that were initially laying flat (such that they appeared mostly round under the microscope) adopted a side-on orientation to the angle of viewing, meaning their biconcave shape could be more clearly seen. This orientation is due to the RBCs rotating such that as much cell volume as possible is placed within the traps, see Figure 5.2.

By lowering the microscope stage it was possible to move cells away from the cover slip. They were then held fixed in the two traps and videos were taken such that their Brownian fluctuations could be recorded. The frames of the resulting videos were analysed in order to identify the centre-of-mass (COM) position of the RBCs. Using the equipartition method explained in Section 4.2.3 the trapping strengths in the x (parallel to the line joining the two traps) and y (perpendicular to the line joining the two traps) directions respectively were

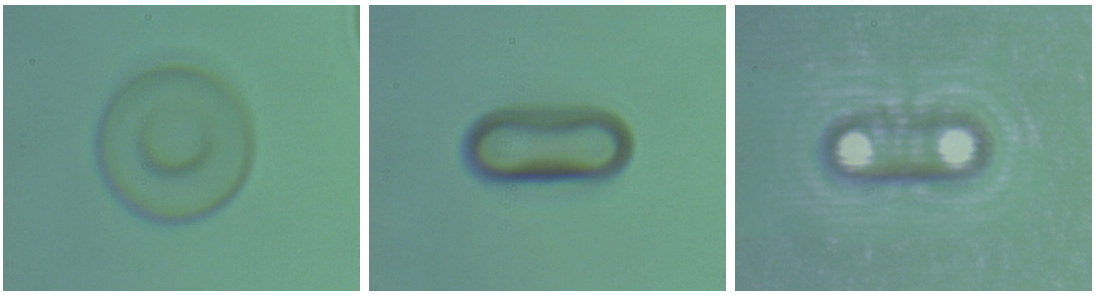

(a) (b) (c)

Figure 5.2: An example of the re-orientation of a RBC in response to the dual trap optical tweezers. a) An un-trapped RBC seen in a 'flat' orientation through the microscope. b) A RBC trapped by the optical tweezers, seen adopting a side-on orientation. c) The same trapped RBC with the laser spot reflections made visible.

found to be: $\kappa_x = k_{\mathrm{B}}T/\sigma^2(x) = 2.7$ pNμm^{-1}, and

$\kappa_y = k_{\mathrm{B}}T/\sigma^2(y) = 5.9$ pNμm^{-1}. These values are an order of magnitude larger than those seen in the Kapitza experiment, this is unsurprising though since here the trap is not scanning in a circle at high frequency.

Video Tracking

Video of this experiment was recorded using the CMOS camera mentioned previously at frame rates of up to 40 fps and with an AOI sufficiently large to accommodate the RBC and the area it would stretch into. Once video microscopy images had been acquired the image analysis and cell COM location was once again completed and extracted with a custom written Matlab script. Frames were converted into grayscale images and noise removal filtering was applied. These were then thresholded to convert them into binary images. These images would contain a white region, corresponding to the cross-section of the cell as viewed under the microscope, upon a black background. The co-ordinates of the boundary of the cell could then be extracted from these binary images, and from this the orientation of the cell deduced. This was a critical step since it was often seen that upon relaxation of the cell, where it was only confined by one

trap, the cell would rotate freely about this trap and so its orientation along the stretching axis was not maintained. The binary image was then rotated such that its major axis was aligned with the x direction and its length and COM location were calculated [109].

Cell Stretching Protocol

Since it has already been shown that direct optical trapping is capable of deforming RBCs to a measurable extent [137], and this technique is simpler than attaching microbead handles, this was the technique utilised for this study.

Cells were initially held fixed by the two optical traps which were separated by a horizontal distance of 5.06 ± 0.01 μm. The cells were then stretched by increasing the trap separation. This was done by moving the galvanometer mirrors to steer the right hand trap in the positive x direction. The trap was moved at a speed of $v_x = 0.47$ μms^{-1} for 3 seconds such that the final separation distance of the two traps was 6.48 ± 0.01 μm. The steerable trap was then quickly jumped to a very large separation (more than twice the cell length) of 24.30 μm, where it was held for 1 second to allow the cell to relax to its initial length. It was during this relaxation phase that the cell was sometimes observed rotating about the single fixed trap. Re-capture of the cell by both traps was then ensured by jumping the steerable trap to a very small separation distance of 2.08 μm, which was then gradually increased to the initial separation distance of 5.06 μm over the next second, i.e. with a speed of $v_x = 2.98$ μms^{-1}. An example of this RBC stretching can be seen in Figure 5.3.

If 10 repetitions of the above stretching routine are defined as one stretching cycle, then each individual cell was subjected to 3 stretching cycles, with each of the cycles recorded in a separate video. An identical stretching protocol was

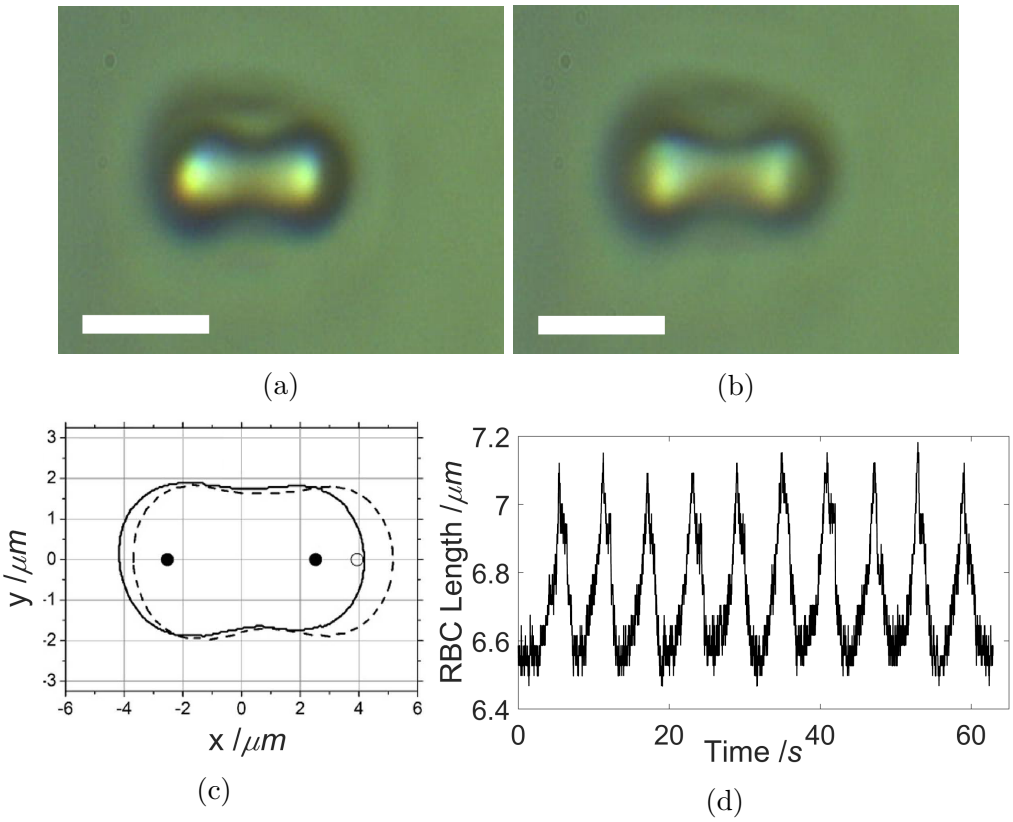

Figure 5.3: An example of a RBC held in the dual trap optical tweezers in both a) unstretched, and b) stretched states (white scale bars represent 5 μm). c) An example difference between the stretched (dashed line) and unstretched (solid line) cell boundaries with positions of the traps indicated. d) A typical cell length against time plot for one stretching cycle.

applied to all of the selected cells from all of the test groups, be they patients with DR, T2DM, or healthy control patients. For each sample stretching was attempted on 10 randomly selected cells. Cells were on average held in the traps for approximately 3.5 minutes. Every effort was made to complete the stretching as quickly as possible for each cell so as not to risk damaging them by prolonged exposure to the beams. Before any data was acquired it was verified that for the optical power used there were no observable changes to the properties of the cells if they were trapped for several times the length of a typical stretching experiment. No direct temperature measurements were taken during the experiment to see what heating had occured, however the following can be considered. The spot size in these experiments was diffraction limited. The

objective numerical aperture, NA = 1.3, and light wavelength, $\lambda = 1064$ nm, yield a smallest possible laser spot diameter, d, of approximately $d = 0.41$ μm. Power measurements taken immediately after the objective yielded a background corrected trapping power of $P = 5.0$ mW. Combining these two gives a worst/largest case possible power density of 3.8 MW/cm. A simulation study by Krasnikov *et al.* exists in the literature that models irradiation of red blood cells via light of the same wavelength used here over a range of power densities which encompasses those used in this experiment [147]. This study simplifies the red blood cell to a spherical shape composed entirely of haemoglobin and considers the absorption and scattering coefficients of the haemoglobin and the surrounding water. It is found that depending upon the exact value taken for the absorption coefficient of the haemoglobin, of which there is a small range reported in the literature, the temperature increase of the RBC from its initial temperature of 20 °C (the same as that of the surrounding water and the laboratory) can be anywhere in the range of $7 - 15$ °C. This represents a final temperature range of $27 - 35$ °C [147]. A study of several markers of erythrocyte (red blood cell) damage has been conducted by using a water bath to heat the red blood cells to temperatures ranging from room temperature up to 57 °C [148]. This study reports that there were no significant changes to any of these markers when the cells were heated to 35 °C, the upper end of the range of temperatures that might have been reached by the heating in our experiment, going by the simulation study of Krasnikov *et al.*

Despite this, it was seen during this verification that after long periods of being held in the optical trap some irreversible change occurred in the cells which meant that it was no longer possible to trap them. It is suggested that this may be due to damage to the cell membrane caused by prolonged exposure to the very large power densities the laser was delivering. Damage to this membrane

may affect the scattering and refraction of the light as it affects the barrier between two mediums, and this may be the cause for trapping failing. Why should this occur when the above studies suggest that the heating and range of temperatures reached in our experiment should not cause significant changes to observable markers of the cell's health? The simulation study of Krasnikov *et al.* makes several simplifications about the shape and internal contents of the cell, which will not be the case in our experiment. Moreover it highlights just how dependent the heating is on small changes in the absorption coefficient of the haemoglobin. Errors in these reported coefficients, a difference in the cell shape and make-up, and tolerances in our power measurements could all lead to larger heating than is estimated based on the above study, which could lead to cell changes and the lack of trapping seen.

Statistical Measures

Various formulae exist and are proposed in the literature as measures of RBC deformability, including such quantities as shear modulus or Young's modulus [133]. For this study, a relatively straightforward fractional elongation measure, here referred to as the deformability index, DI, was used:

$$DI = \frac{L_{max} - L_0}{L_0}, \tag{5.1}$$

where L_{max} and L_0 correspond to the stretched and unstretched lengths of the RBC respectively.

Correlation between the control group and the study group of the blood tests undertaken was tested for using either Fisher's exact test or a χ^2 test [149, 150]. A Wilcoxon signed rank test and t-test were applied to analyse the difference in means for L_0, L_{max}, and DI between the volunteer groups [151]. Bivariate

regression analysis was performed, using DI as the dependent variable. Any variables that showed significant association with DI in this analysis were included in a multivariate analysis model. Results were considered statistically significant when $p < 0.05$. The data was analysed using Stata SE, version 13.0 (Stata Corp, College Station, TX, USA) [122].

5.6 Results

5.6.1 Blood Test Results

Results from the routine blood, liver function, renal function etc. tests for the control and DR groups were compared by Dr. Agrawal and can be seen in Table 5.1. Blood from the T2DM study group did not show any statistically significant differences for the tested haematological or biochemical parameters when compared to the DR study group. As might be expected of diabetes patients, these two groups both showed raised random blood glucose (RBG) and glycosylated haemoglobin (HbA1C) levels. Additionally alkaline phosphatase (ALP), total protein, and globulin levels were also elevated in the DR group, although not necessarily out of a normally expected range. By contrast mean corpuscular volume (MCV) and mean corpuscular haemoglobin (MCH) were reduced in the DR study group compared to the control group. These are a measure of the average volume of an RBC and the average mass of haemoglobin per red blood cell in a sample of blood respectively. Although comparatively low, again these were not yet outside of a normally expected range.

Haematological/Biochemical variables	Normal range (units)	Controls (SD, 95% CI)	Patients (SD, 95%CI)	pvalue (t-test
Hemoglobin (Hb)	13.0 - 17.0(g/dL)	14.27(1.64,12.90 - 15.64)	13.34(1.80, 11.67 - 15.01)	0.31
Hematocrit (Hct)	37 - 50%	42.12(0.04, 0.38 - 0.45)	39.47(0.04, 0.35 - 0.43)	0.27
Red blood cell count (RBC)	4.40 - 5.80(x10^12/L)	4.8(0.51, 4.37 - 5.22)	4.71(0.45, 4.51 - 5.01)	0.74
Mean corpuscular volume (MCV)	80 - 99(fL)	**87.81(2.81, 85.45 - 90.16)**	**83.48(3.22, 80.50 - 86.47)**	**0.01**
Mean corpuscular hemoglobin (MCH)	26.0 - 33.5(pg)	**29.68(1.04, 28.81 - 30.56)**	**27.84(1.82, 26.15 - 29.52)**	**0.02**
Mean corpuscular hemoglobin concentration (MCHC)	30.0 - 35.0(g/dL)	29.90(10,72, 20.94 - 38.87)	36.63(11.84, 32.53 - 34.72)	0.38
RBC distribution width (RDW)	11.5 - 15.0	13.58(1.48, 12.34 - 14.82)	13.65(1.37, 12.41 - 14.90)	0.92
Platelet count (PC)	150 - 400(x10^9/L)	270.5(76.63, 206.42 - 334.57)	317.57(69.54, 253.25 - 381.8)	0.23
Mean platelet volume (MPV)	7 - 13(fL)	10.73(1.41, 9.55 - 11.91)	10.88(0.77, 10.17 - 11.60)	0.81
White blood cell count (WBC)	3.0 - 10.0(x10^9/L)	7.07(1.63, 5.71 - 8.44)	7.79(1.25, 6.64 - 8.95)	0.36
Neutrophils	2.0 - 7.5(x10^9/L)	3.67(1.00, 2.83 - 4.51)	4.40(0.68, 3.76 - 5.03)	0.12
Lymphocytes	1.2 - 3.65(x10^9/L)	2.45(0.86, 1.73 - 3.18)	2.55(0.71, 1.89 - 3.21)	0.82
Monocytes	0.2 - 1.0(x10^9/L)	4.32(1.4, 3.11 - 5.53)	4.71(1.95, 2.90 - 6.52)	0.66
Eosinophils	0.0 - 0.4(x10^9/L)	3.5(0.9, 2.7 - 4.2)	3.14(0.2, 0.12 - 0.50)	0.66
Basophils	0.0 - 0.1(x10^9/L)	3.28(1.81, 1.77 - 4.80)	3.4(3.6, 0.67 - 6.73)	0.94
Erythrocyte sedimentation rate (ESR)	1 - 20(mm/hr)	7.87(6.26, 2.63 - 13.11)	21.14(28.81, - 5.50 - 47.78)	0.22
Sodium (Na)	135 - 145(mmol/L)	142.62(2.26,140.73 - 144.51)	140(3.60, 136.66 - 143.33)	0.11
Potassium (K)	3.5 - 5.1(mmol/L)	4.46(0.36, 4.15 - 4.76)	4.77(0.18, 4.32 - 5.22)	0.18
Chloride (Cl)	98 - 107(mmol/L)	102.37(1.76, 100.89 - 103.85)	99.85(2.47, 97.56 - 102.14)	0.04
Bicarbonate	22 - 29(mmol/L)	23.62(2.50, 21.53 - 25.71)	24.14(2.11, 22.18 - 26.09)	0.67
Urea	1.7 - 8.3(mmol/L)	4.61(1.59, 3.28 - 5.94)	6.31(2.90, 3.62 - 8.99)	0.17
Creatinine	66 - 112(mmol/L)	83(24.85, 62.22 - 103.77)	92.71(22.42, 71.97 - 113.45)	0.44
Bilirubin	0 - 20(umol/L)	5.375(2.77, 3.05 - 7.69)	6(3.10, 3.12 - 8.87)	0.69
Alkaline phosphatase (ALP)	40 - 129(IU/L)	**64(12.4,53.51 - 74.48)**	**89.71(18.10, 72.96 - 106.46)**	**<0.001**
Aspartate aminotransferase (AST)	0 - 37(IU/L)	22.62(5.65, 17.89 - 27.35)	23.71(15.25, 9.61 - 37.81)	0.85
Alanine transaminase (ALT)	10 - 50(IU/L)	23.12(10.80, 14.09 - 32.15)	37.71(23.68, 15.81 - 59.61)	0.14
Protein	63 - 83(g/L)	**67.37(3.50, 64.44, 70.30)**	**73.28(3.77, 69.79 - 76.77)**	**0.007**
Albumin	34 - 50(g/L)	43.62(2.77, 41.30 - 45.94)	43.57(3.35, 40.46 - 46.67)	0.97
Globulin	19 - 35(g/L)	**23.75(2.54, 21.61 - 25.88)**	**29.71(1.88, 27.96 - 31.46)**	**<0.001**
C-reactive protein (CRP)	0 - 5.0(mg/L)	2.18(2.33, 0.23 - 4.14)	2.12(2.34, 0.04 - 4.29)	0.962
Random blood glucose (RBG)	3.9 - 6.9(mmol/L)	**4.91(0.40, 4.58 - 5.24)**	**10.04(3.67, 6.64 - 13.43)**	**0.001**
Glycosylated hemoglobin (HbA1C)	4.5 - 6.0%	**5.82(0.34, 5.54 - 6.11)**	**9.77(2.64, 6.17 - 9.15)**	**0.001**
Triglycerides (TG)	0.0 - 2.2(mmol/L)	1.62(0.98, 0.80 - 2.44)	2.31(2.10, 0.36 - 4.26)	0.42
Cholesterol	2.3 - 4.9(mmol/L)	4.93(1.18, 3.94 - 5.93)	4.47(1.18, 3.94 - 5.93)	0.38
High density lipoprotein (HDL)	0.9 - 1.5(mmol/L)	1.34(0.31, 1.05 - 1.63)	1.17(0.29, 1.08 - 1.42)	0.29
Low density lipoprotein (LDL)	0 - 3.0(mmol/L)	2.82(0.84, 2.12 - 3.52)	2.76(0.72, 2.00 - 3.53)	0.89
Angiotensin converting enzyme (ACE)	8 - 52 Units/liter	35.87(11.63, 26.15 - 45.60)	31(26.41, 6.56 - 55.43)	0.64
Fibrinogen	2 - 4 (g/L)	3(0.59, 2.50 - 3.5)	3.12(0.89, 2.29 - 3.95)	0.74

Table 5.1: Haematological and Biochemical test results for the control and study (DR) groups.

5.6.2 Deformability Results

The stretching protocol was successfully applied to the cells of all control groups. Observations (as mentioned already in the method section) included the occasional rotation of cells during the relaxation part of the cycle (accounted for under image analysis by orientation determination and subsequent image rotation). The cells overall looked healthy, were in optimal concentration, and upon visual inspection there were less that 5% echniocytes present in the slides. These were easy to identify due to the cell-by-cell nature of the stretching, and so did not affect the deformability assessment of the cells.

The mean initial cell length at the beginning of each stretching cycle for the control group was: $L_{0-C} = 8.45 \pm 0.01$ μm (mean±standard error on mean). For the T2DM and DR groups respectively this value was:
$L_{0-T2DM} = 8.67 \pm 0.02$ μm, and $L_{0-DR} = 8.82 \pm 0.01$ μm. Using a Wilcoxon signed rank test on the DR and control data gives a p-value of < 0.001, thus advocating the rejection of the null hypothesis of zero median for the difference between the sets of data at a 5% significance level. The mean final, stretched cell length for each cycle of the control group was: $L_{max-C} = 9.04 \pm 0.01$ μm. For the DM and DR groups respectively this was: $L_{max-DM} = 9.23 \pm 0.02$ μm, and $L_{max-DR} = 9.39 \pm 0.01$ μm ($p < 0.001$). Using these values to compute the mean deformability index, DI, for each of the three groups respectively gave the following: $DI_C = 0.0703 \pm 0.0008$, $DI_{DM} = 0.065 \pm 0.001$, and $DI_{DR} = 0.0645 \pm 0.001$, again with $p < 0.001$. Plots of the initial and final lengths of all three volunteer groups can be seen in Figure 5.4. The mean values can also be seen in a tabulated form (Table 5.2).

A kernel density estimation (KDE) was undertaken to estimate a probability density function (pdf) for the deformability index. The formula for a KDE of a

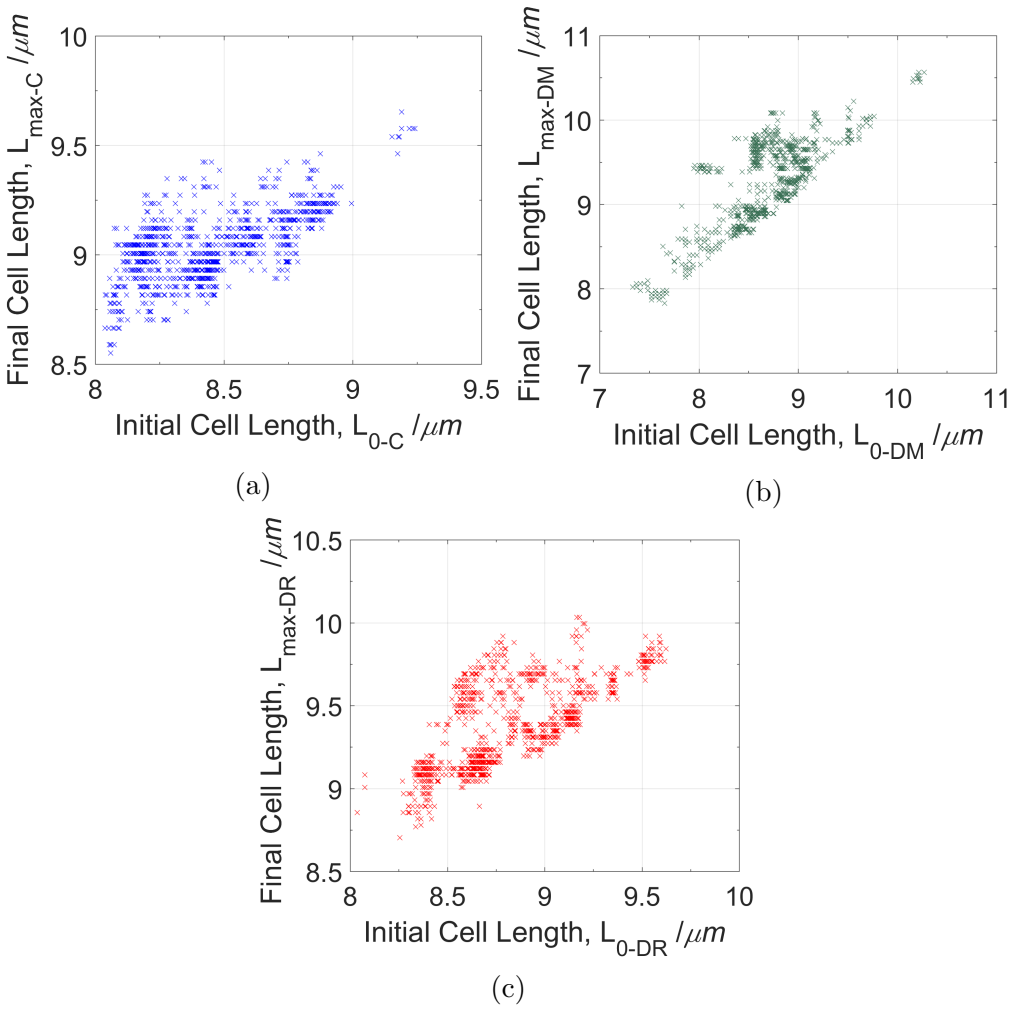

Figure 5.4: Plots of final, stretched RBC length (L_{max}) against initial, unstretched RBC length (L_0) in the dual trap optical tweezers deformability experiment for a) the control group, b) the DM group, c) the DR group.

	Number of Cell Stretches	$\bar{L}_0 \pm \sigma_{\bar{L}_0}$ (range) , μm	$\bar{L}_{max} \pm \sigma_{\bar{L}_{max}}$ (range) , μm	$\bar{DI} \pm \sigma_{\bar{DI}}$ (95% C.I.)
Control Group	925	8.45 ± 0.01 $(8.04 - 9.24)$	9.04 ± 0.01 $(8.55 - 9.65)$	0.0703 ± 0.0008 $(0.0687 - 0.0719)$
DM Group	925	8.67 ± 0.02 $(7.33 - 10.27)$	9.23 ± 0.02 $(7.83 - 10.56)$	0.065 ± 0.001 $(0.063 - 0.068)$
DR Group	923	8.82 ± 0.01 $(8.04 - 9.62)$	9.39 ± 0.01 $(8.7 - 10.03)$	0.0645 ± 0.001 $(0.0627 - 0.0664)$
p-value	-	< 0.001	< 0.001	< 0.001

Table 5.2: Initial and final stretched lengths alongside the deformability index for all 3 volunteer groups of the RBC deformability study.

random variable, x, is given by:

$$\hat{f}_h(x) = \frac{1}{nh} \sum_{i=1}^{n} K\left(\frac{x - x_i}{h}\right), \tag{5.2}$$

where the x_i are independent and identically distributed, K is the kernel, h is a smoothing parameter (the bandwidth), and n is the number of data points. A variety of kernel functions exist and are commonly employed. Here the Epanechnikov kernel is used since it is optimal in a mean square error sense [152]. The choice of bandwidth is important. If the bandwidth is too small then the pdf will be undersmoothed, possessing unwanted spikes and artefacts from the data. Conversely if it is too large then the pdf will be oversmoothed, and may not include important structural features. The mean integrated squared error (MISE) is a criterion used commonly in order to optimise this value. This uses derivatives of the unknown pdf function so cannot be used explicitly, but data based methods to calculate it exist [153]. There is, however, an approximation that can be used to give the optimal choice for h, assuming the underlying data is Gaussian [154]:

$$h = \left(\frac{4\sigma^5}{3n}\right)^{\frac{1}{5}}, \tag{5.3}$$

where σ is the standard deviation of the sample. Kernel density estimate plots for the deformability index of the three groups studied can be seen in Figure 5.5. A small decrease in the DI can be seen for the two groups with diabetes compared to the control group by the shift of their peaks to lower values.

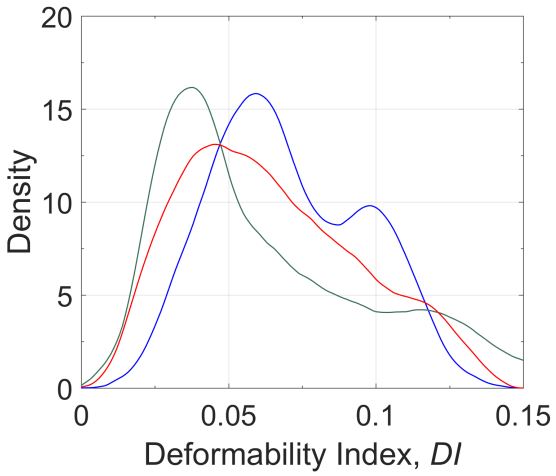

Figure 5.5: Kernel density estimate plots showing an estimated probability density function for the deformability index in the three volunteer groups. The blue line represents the control group, the green line the DM group, and the red line the DR group.

5.6.3 Further Analysis

Bivariate regression analysis was undertaken, using DI as a dependent variable, in order to evaluate the significance of the levels of the biochemical factors in the blood towards the deformability. It was found that none of the haematological or biochemical factors correlated significantly with the deformability index. However, results from the stretching experiments suggested a significant negative correlation between the deformability index and the initial cell size for the control and DR groups (Pearson's R^2 correlation coefficient for the control and DR groups respectively: 0.64, 0.40, $p < 0.001$ for both). Plots of the deformability index against initial cell length for these groups can be seen in Figure 5.6.

In response to this correlation, further analysis was done on the biochemical parameters in order to ascertain any significant effect on the initial cell size. Under simple bivariate analysis serum potassium, RBG, HbA1C, and MCH appeared to have a statistically significant influence on this initial cell size, see Table 5.3. Further testing under a multivariate model, however, suggested that this was not the case for any of these factors.

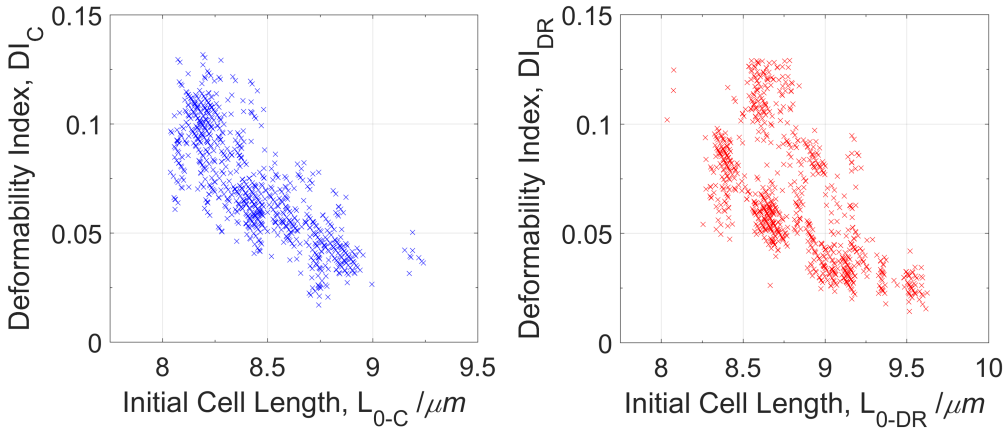

(a) (b)

Figure 5.6: Plots of deformability index (DI) against initial, unstretched RBC length (L_0) in the dual trap optical tweezers deformability experiment showing significant negative correlation for a) the control group, and b) the DR group.

	R^2	95% C.I.	p-value
Potassium	0.334	$0.047 - 0.565$	0.024
Random blood glucose	0.424	$0.012 - 0.071$	0.008
HbA1C	0.406	$0.019 - 0.096$	0.006
MCH	0.274	$-0.14 \rightarrow -0.001$	0.045

Table 5.3: Regression analysis of haematological and biochemical factors affecting the initial cell size (MCH - Mean corpuscle haemoglobin, HbA1C - glyosylated haemoglobin) [122].

5.6.4 Discussion

The results of this study are similar to those pre-existing in the literature [140, 142, 155, 156]. The RBC deformability index of patients with DR and T2DM was found to be significantly reduced when compared to a control group. Additionally there was a significant difference in both the initial and final cell sizes, as well as the deformability index between the DM and DR groups. The mean DI of the DR group was found to be significantly smaller than that of the DM group.

The haematological and biochemical factors tested for did not appear to have a significant correlation with a reduced deformability index. It was seen however

that the initial cell size correlated negatively with DI, as well as being significantly larger for those patients with diabetes than for the control group. This suggests some metabolic factor inherent to diabetes that can affect RBC cell size, and through this deformability. The biochemical factors were tested therefore for correlation with the initial cell size. Initial analysis suggested MCH (average mass of haemoglobin per red blood cell) was correlated with this cell size increase, suggesting some change in the intra-cytoplasmic viscosity (the viscosity of the material within the cell) which lead to swollen RBCs. Additionally both HbA1C and RBG were also linked to this increased cell size initially, suggesting the association of impaired glycaemic control with osmotically swollen RBCs [122]. Upon further multivariate analysis however these parameters were no longer found to be significant.

Limited studies exist on DI in DR, and to the best knowledge of the author no studies exist reporting the comparative size of the cell at the baseline in patients with T2DM, nor using a two beam optical tweezers apparatus in order to assess the deformability of RBCs in T2DM (although as mentioned previously, studies of this exist using alternative methods) [143]. Diamantopoulos *et al.* used a filtration technique in order to assess a deformability index of patients with DR in 1987 [128]. They tested 69 patients with diabetes and 40 healthy controls and found a reduction in the DI which was proportional to the severity of DR. They postulated diffuse metabolic disturbance as a cause of this. Additional meaningful studies related to this one include: that of Shin *et al.* [131] who showed a reduced elongation index in DM patients, demonstrated a negative correlation between this index and levels of glycosylated haemoglobin, and saw a significant reduction in this index for patients with diabetic nephropathy and retinopathy; and that of Keymel *et al.*, who analysed this index in patients with DM and coronary artery disease, and found similar significant reductions in

deformability, as well as a negative effect of plasma glucose concentration on this index. The results of this study appear to agree well then with these others. RDW, a measure of the range of RBC volume variation has previously been linked to diabetes-associated complications [157], but was not found to be significantly associated with DI in this study. This could perhaps be due to the relatively small sample size present.

Based on the results of this study and the above literature, it is postulated that increased blood glucose/glycosylation and oxidative stress result in altered cell morphology, leading to swollen RBCs with impaired deformability [122, 158].

5.7 3-D Defocussing Microscopy Imaging

In addition to the optical tweezers stretching, three-dimensional imaging using defocussing microscopy (3DDM) was also attempted in this study. This was performed in order to try to obtain as much information as possible about the morphology of the RBCs. This technique facilitates the generation of a complete, 3-D, reconstruction of the surface membrane of the cell, and therefore enables the calculation of properties of the cell such as its volume, surface area, and sphericity index.

This technique works in standard bright-field microscopy. When defocussing a microscope, a phase difference between diffracted and transmitted (zeroth order) orders of light from an object accrues. By taking images of a cell in two focal planes, contrast intensity measurements can be obtained for them, from which information about the phase of the optical electric field can be extracted, and therefore the height profile of the object reconstructed. The work of Roma *et al.*, who use Fresnel diffraction theory and the formalism of propagation of the angular spectrum [159, 160] to propagate the light's electric field throughout the

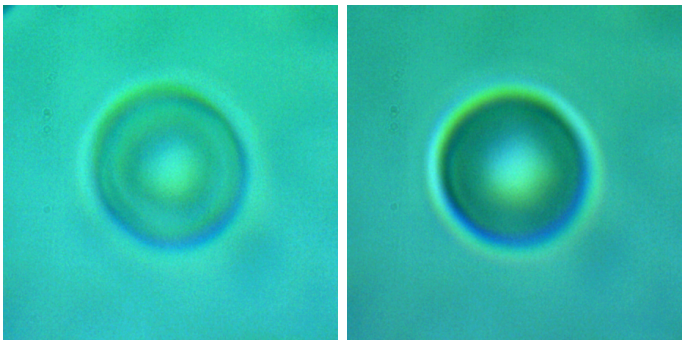

(a) (b)

Figure 5.7: Example images of a RBC used for 3DDM, captured at heights of a) 0 μm and b) 2 μm relative to the cell centre.

defocussed microscope, is used here in order to obtain these images [161]. Roma *et al.* (Universidade Federal de Minas Gerais, Brazil) kindly provided a Matlab script to perform the necessary calculations for reconstruction of the cell surface.

A selection of five different RBCs on which to perform 3DDM was made from the blood samples at random from cells that had a healthy appearance. The location of the plane of the centre of the cells was first determined by finding where the edges of the cell appeared in sharpest focus, and so where there was the least shadow/outline to be seen around the cell (N.B. cells imaged with 3DDM are not held by the optical trap, so do not adopt a side-on orientation). This position was confirmed by observation of the variation in intensity across the image of the cell in the camera software; which was to the best by-eye approximation, minimised simultaneously for all three colour channels acquired from the CMOS camera. Once a candidate RBC was selected, three images of the cell at heights -2, 0, and 2 μm relative to the cell centre were captured [109] (see Figure 5.7). These images then went through several processing stages. They were first cropped to a square that was centred upon the cell, before being subjected to a shading correction routine in the ImageJ software package to compensate for any fluctuations in the background intensity of the image. They were then scaled/binned into a 64×64 array and converted to grayscale. This step was

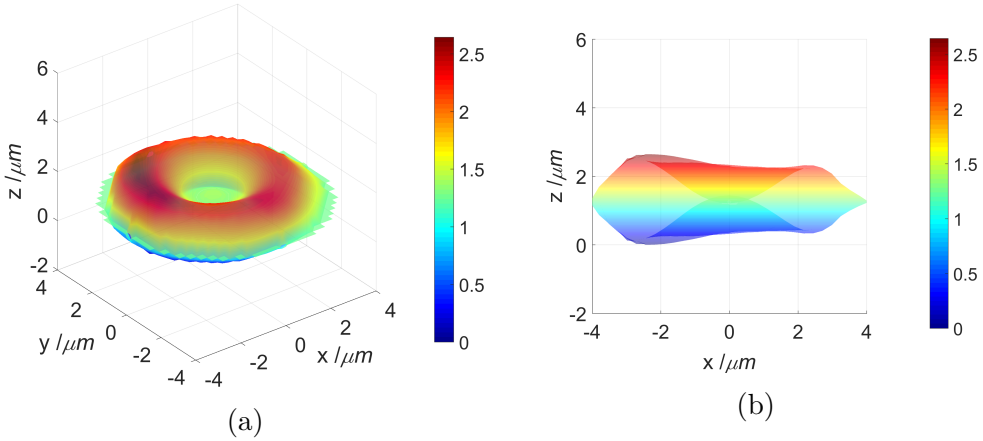

Figure 5.8: An example result of the 3DDM process. Here a red blood cell is seen a) an elevated and rotated position such that the 3-D nature of the reconstruction can be appreciated, and b) a side-on, $x - z$ view such that the cross-section of the cell can be seen and the expected biconcave shape of the cell identified. The colours indicate the height of the cell, as seen in μm on the colour bar.

performed due to the exponential scaling of time taken to process the data as the image size increases, and the limitations in processing power and memory available. Finally the image data was then used in the algorithm of Roma *et al.* An example image of a reconstructed cell can be seen in Figure 5.8.

Unfortunately, due to the time taken to perfect the technique of acquiring these images (which required correspondence with the Brazilian team), and the small size of the test groups in this study, few 3D cell images of a high quality were obtained. Of those that were obtained, there was insufficient evidence to suggest any significant correlation between any of the morphological parameters obtained and the deformability index of the cell. Whether this is because there is no correlation, or simply because of a lack of data remains to be seen.

5.8 Summary and Outlook

5.8.1 Summary

In this chapter, the deformability of red blood cells has been investigated as a factor linked to the onset of diabetic retinopathy.

A study has been undertaken, using the novel set-up of a dual beam optical tweezers, in order to assess RBC DI. This study involved three volunteer groups: a healthy control group, a group with type 2 diabetes mellitus without diabetic retinopathy, and a group with type 2 diabetes mellitus with diabetic retinopathy. RBCs were rotated and fixed in place by the optical tweezer beams. One beam was then slowly translated to apply a stretching force to the cells. This was repeated 30 times in total over three sessions, for up to 10 individual cells from each blood sample, whilst the whole process was recorded with a CMOS camera. An extra 5 cells from each sample were selected, and images of them captured at different height planes relative to their centres, in order to attempt to recreate a 3-D profile of their surfaces. In addition to the RBC stretching, a range of standard blood tests were conducted to identify the levels of various haematological and biochemical factors in the blood.

The experimental videos were processed in Matlab to obtain the cells' orientations and, after re-orienting, their lengths. These were recorded at the beginning (unstretched) and end (stretched) of each stretching cycle. These values were then used to calculate the fractional elongation of the cells, the deformability index. The cell height images were also processed, cropping and scaling them, and eliminating background noise, in order to obtain their 3-D surfaces.

It was found that the mean deformability index of the two diabetes groups was

significantly lower than that of the control group, and that the DR group was the lowest of these. No haematological factors were found to be correlated with this reduction. It was reported for the first time in this study that there appears to be a correlation between the baseline cell size and the reduced deformability index, suggesting an inverse relationship between the two. Haematological factors were therefore analysed in conjunction with this baseline cell size and initial analysis suggested some correlation with potassium, RBG, HBA1c, and MCH, however further multivariate analysis seemed to disagree with this. A link between increased blood glucose and oxidative stress with decreased RBC deformability and so DR is postulated here.

5.8.2 Outlook

A large weakness in this study is its small sample size, which was limited by the number of patients presenting and willing to participate. Indeed, this was the reason why little was gained from the 3DDM investigations. Nonetheless, it has demonstrated the validity of the dual beam optical tweezers technique for RBC deformability measurements.

It is hoped therefore that future experimentation will be possible, using this technique with larger study cohorts. Based upon the results of this pilot study, this could help to establish more strongly an association between severity of DR in T2DM and the deformability of red blood cells, along with haematological factors and rheology of the blood. Such a larger study would also be able to collect more data from the 3DDM method. This data could lead to the discovery of some association between the morphological properties of RBCs (volume, surface area, sphericity) and their deformability. In turn this may yield a new line of investigation and study for DR, and indeed other diseases of the

microvasculature since neither this nor the dual tweezers stretching are limited to investigations of just DR.

Chapter 6

Fluctuation Theorems and Coupled Particles

This chapter documents the third and final section of original research undertaken. It concerns the field of thermodynamics, but is not without its implications for the world of microbiology. It deals with the fluctuations of optically trapped particles and the irreversibility of these movements. It considers hydrodynamically coupled particles as a model system, and the entropy produced when a small amount of work is done on it. Simulations and experiments have been undertaken to explore this and are documented herein.

6.1 Background

Thermodynamics is the field of physics which seeks to explain the relationship and the transfer between heat/thermal energy and other forms of energy, and in so doing make predictions about systems and their equilibrium states. The second law of thermodynamics, in its many re-statements involving the flow of heat in a body, or the conversion of work into heat, gives us the 'arrow of time'. This is the one-way direction in which time must flow. It arises from the notion that in isolated systems heat does not flow from colder to hotter areas, or in another re-statement of the law, that the entropy of a thermally isolated system must not decrease ($dS \geq 0$) [162].

6.1.1 Fluctuation Theorems

Random thermal fluctuations occur in systems of all sizes. In macroscopic systems the effects of these fluctuations are relatively small, and the behaviour of the system is generally speaking predictable and reproducible. As the size of a system decreases however, these fluctuations become much more significant. For microscopic systems they can begin to dominate and often lead to observable

deviations from the system's average behaviour. For example, if the work done over an operating cycle of a machine is comparable to its thermal energy per degree of freedom, then on short time scales it might run in reverse [163]. Components, such as actuators, are already being built on the nano-scale and could one day become part of motors in this size regime [164]. Such motors would be highly susceptible to thermal fluctuations, potentially running backwards by taking in thermal energy from their environment and converting this into useful work. Many microscopic molecular machines do already exist in cells, and they are capable of carrying out biological functions. One such example is kinesin, which facilitates many cellular tasks (such as DNA replication) by carrying protein cargoes along microtubules [165]. These molecular motors, over time and on average, must not violate the second law of thermodynamics. They do occasionally run backwards however, converting heat/thermal fluctuations from their surroundings into useful mechanical work or chemical energy [163, 166].

These quirks of nano-scale motors would, in larger systems, be described as violations of the second law of thermodynamics. It was Josef Loschmidt in 1876 who first questioned the second law derivation from Newton's laws. He pointed out that the equations of motion are time reversible, i.e. for every positive/forward trajectory that satisfies them, there is a negative/backward anti-trajectory that will also satisfy them, therefore questioning how the irreversible macroscopic equations (as per the second law) arise from the reversible microscopic equations [167, 168].

In the 1990s Evans *et al.* proposed a new formalism to tackle this issue which they referred to as fluctuation theorems (FTs) [169, 170]. These FTs describe the evolution of the thermodynamic irreversibility of a system from completely reversible at short times to irreversible at infinitely long times; they relate the microscopic to the macroscopic equations, the time-reversible to the irreversible.

It was originally stated that these FTs gave the time evolving ratio of probabilities that a given particle trajectory would constitute a negative/positive entropy change in the system [169, 171] However, subsequent literature later pointed out that the 'dissipation function' in these FT, which was initially being equated to entropy in early experiments, was in some cases not the entropy at all but rather the total work done on the system; and that this connection to entropy could only be asserted if the work done on the system was purely dissipative [172]. In optical trapping experiments like those presented in this chapter, there is dissipative work done and heat generated as a result of the friction of moving a particle through a viscous fluid, but there is also a change in the potential energy of the particle as it is moved inside the harmonic trap, so some of the work is stored in the potential [173]. Nonetheless the validity of the fluctuation theorems can still be shown for the total work done on a system.

A Langevin FT derivation

In this section a derivation of a stochastic FT which is consistent with Langevin dynamics is presented, and will proceed as per Reid *et al.* [174]. The form of a FT is given by:

$$\frac{P(\Omega_t = -A)}{P(\Omega_t = A)} = \exp(-A), \tag{6.1}$$

where P represents a probability, Ω_t is a dissipation function, and A some constant. The main argument, then, in this fluctuation theorem is the dissipation function, Ω_t. This is the logarithm of the ratio of probability densities of observing a trajectory to that of its corresponding anti-trajectory as will be seen shortly, although as has just been mentioned the fluctuations of the total work done on the system could also be used here and the validity of a work based FT

could be shown.

Whereas the dissipation function directly gives a measure of a system's reversibility at a given trajectory duration, the FT describes the time evolution of the asymmetry of this measure. Many works exist where the dissipation function is found using deterministic, Newtonian equations of motion [170]. However, for large systems over long time periods, this method can become unsuitable and unwieldy with regard to molecular dynamics simulations, where the state of a system is given by the positions and momenta of all of its constituent molecules. Whilst this is not of particular concern for the relatively simple experiments in this thesis, the Langevin method of Reid *et al.* (2004), by use of stochastic equations, reduces the necessary computing power to simulate experiments and find the FT by only requiring the coordinates of the colloidal particle whose dynamics are being investigated, $\boldsymbol{r}(t) = \boldsymbol{r}_t = (x, y, z, t)$. A Langevin rather than Newtonian/deterministic derivation of the FT is therefore shown here in the background section to this chapter.

Consider a colloidal particle in the low Reynolds number regime (such that its motion can be described by the inertia-less Langevin equation (Equation 3.84). Unlike a Newtonian derivation of the dissipation function, here there are random forces acting which mean it is not possible to construct perfect, time-reversible conjugate pairs of trajectories. Additionally there are not unique combinations of position and momentum which only belong to one trajectory as in the Newtonian case, only particle coordinates which could belong to infinitely many trajectories. Instead it can be said that there are an infinite number of trajectories that begin at a coordinate $\boldsymbol{r}_0$, some of which arrive at a position $\boldsymbol{r}_t$ [174]. Therefore, $\{\boldsymbol{r}_0, \boldsymbol{r}_t\}$ is used to denote a set of forward trajectories which evolve from $\boldsymbol{r}_0$ to $\boldsymbol{r}_t$, and $\{\boldsymbol{r}_t, \boldsymbol{r}_0\}$ is used to denote the corresponding set of backward trajectories, evolving from $\boldsymbol{r}_t$ to $\boldsymbol{r}_0$.

To begin evaluating probabilities, an infinitesimal volume of trajectory sets is considered around $\{\boldsymbol{r}_0, \boldsymbol{r}_t\}$, as given by:

$$\delta V_{r,r}\left(\{\boldsymbol{r}_0, \boldsymbol{r}_t\}\right) \equiv \lim_{\delta \boldsymbol{r}_0, \delta \boldsymbol{r}_t \to 0} \delta \boldsymbol{r}_0 \delta \boldsymbol{r}_t. \tag{6.2}$$

The probability of observing a trajectory with the particle beginning in the volume element $\delta V_{\boldsymbol{r}}(\boldsymbol{r}_0)$ and finishing in the volume element $\delta V_{\boldsymbol{r}}(\boldsymbol{r}_t)$ is given by:

$$P\left[\delta V_{r,r}\left(\{\boldsymbol{r}_0, \boldsymbol{r}_t\}\right)\right] = p(\boldsymbol{r}_0, \boldsymbol{r}_t) \delta \boldsymbol{r}_0 \delta \boldsymbol{r}_t, \tag{6.3}$$

where the volume elements are of the same size ($|\delta \boldsymbol{r}_0| = |\delta \boldsymbol{r}_t|$), and $p(\boldsymbol{r}_0, \boldsymbol{r}_t)$ is some known normalised probability distribution (such as the Green's function which gives the probability of observing a particle at a position $\boldsymbol{r}_t$ in a harmonic trap of strength κ, given an initial position of $\boldsymbol{r}_0$ [175]). The dynamics used to model a system (Langevin or Newtonian) should not affect the reversibility of that system. It is fairly intuitive to see that one way to measure the reversibility of a system is to take the ratio of the likelihood of observing the forward trajectories to the likelihood of observing the reverse trajectories. The logarithm of this ratio is the dissipation function [176]:

$$\Omega_t(\boldsymbol{r}_0, \boldsymbol{r}_t) = \ln\left(\frac{P(\delta V_{\boldsymbol{r},\boldsymbol{r}}(\{\boldsymbol{r}_0, \boldsymbol{r}_t\}))}{P(\delta V_{\boldsymbol{r},\boldsymbol{r}}(\{\boldsymbol{r}_t, \boldsymbol{r}_0\}))}\right) = \ln\left(\frac{p(\boldsymbol{r}_0, \boldsymbol{r}_t)}{p(\boldsymbol{r}_t, \boldsymbol{r}_0)}\right). \tag{6.4}$$

Reid *et al.* show that, using this stochastic approach, the dissipation function obtained is not unique. It can vary depending upon the coordinate system they choose for a given problem. All dissipation functions found did, however, satisfy the fluctuation theorem [174]. The above derived Langevin dissipation function satisfying the FT can be seen by considering the probability density for observing

a given set of trajectories, duration t, with a dissipation function equal to some constant, A:

$$P(\Omega_t = A) = \int d\boldsymbol{r}_0 d\boldsymbol{r}_t \delta \left[\Omega_t(\boldsymbol{r}_0, \boldsymbol{r}_t) - A\right] p(\boldsymbol{r}_0, \boldsymbol{r}_t). \tag{6.5}$$

Similarly the probability density for some set of trajectories with the inverted ratio of trajectory probabilities ($\Omega_t = -A$) is given by:

$$\begin{aligned} P(\Omega_t = -A) &= \int d\boldsymbol{r}_0 d\boldsymbol{r}_t \delta \left[\Omega_t(\boldsymbol{r}_0, \boldsymbol{r}_t) + A\right] p(\boldsymbol{r}_0, \boldsymbol{r}_t) \\ &= \int d\boldsymbol{r}_0 d\boldsymbol{r}_t \delta \left[\Omega_t(\boldsymbol{r}_t, \boldsymbol{r}_0) - A\right] p(\boldsymbol{r}_0, \boldsymbol{r}_t), \end{aligned} \tag{6.6}$$

where $\Omega_t(\boldsymbol{r}_0, \boldsymbol{r}_t) = -\Omega_t(\boldsymbol{r}_t, \boldsymbol{r}_0)$ has been employed. Rearranging Equation 6.4 for $p(\boldsymbol{r}_0, \boldsymbol{r}_t)$ and substituting this into Equation 6.6 gives:

$$P(\Omega_t = -A) = \int d\boldsymbol{r}_0 d\boldsymbol{r}_t \delta \left[\Omega_t(\boldsymbol{r}_t, \boldsymbol{r}_0) - A\right] \times \exp\left[-\Omega_t(\boldsymbol{r}_t, \boldsymbol{r}_0)\right] p(\boldsymbol{r}_t, \boldsymbol{r}_0). \tag{6.7}$$

Finally, the ratio of the probability densities for the positive and negative dissipation function cases from Equations 6.5 and 6.7 can be found as:

$$\frac{P(\Omega_t = A)}{P(\Omega_t = -A)} = \frac{\int d\boldsymbol{r}_0 d\boldsymbol{r}_t \delta[\Omega_t(\boldsymbol{r}_0, \boldsymbol{r}_t) - A] p(\boldsymbol{r}_0, \boldsymbol{r}_t)}{\int d\boldsymbol{r}_0 d\boldsymbol{r}_t \delta[\Omega_t(\boldsymbol{r}_t, \boldsymbol{r}_0) - A] \exp[-\Omega_t(\boldsymbol{r}_t, \boldsymbol{r}_0)] p(\boldsymbol{r}_t, \boldsymbol{r}_0)}, \tag{6.8}$$

which simplifies to:

$$\frac{P(\Omega_t = -A)}{P(\Omega_t = A)} = \exp(-A). \tag{6.9}$$

Thus satisfying the form of the FT as seen in Equation 6.1 [170]. Often, in order to obtain better statistics, the FT is expressed instead as the integrated fluctuation theorem (IFT). This is the ratio of the total negative to positive dissipation function values at a given time along a trajectory. The form of the IFT is:

$$\frac{P(\Omega_t < 0)}{P(\Omega_t > 0)} = \langle \exp(-\Omega_t) \rangle_{\Omega_t > 0}, \tag{6.10}$$

where $\langle \ldots \rangle_{\Omega_t > 0}$ denotes the ensemble average over the trajectories for which $\Omega_t > 0$ [176].

6.1.2 Hydrodynamic Coupling

The experiments documented in this chapter concern the motion of more than just a single particle. As such it is pertinent to discuss the dynamics of a group of immersed, interacting particles. A given particle's motion will depend upon the forces exerted upon it by its neighbouring particles. A force on a neighbouring particle will cause this neighbour to move, thus leading to displacement of the fluid surrounding it. This, in turn via the motion of the fluid, will exert a small force upon the original particle and affect its motion. This interaction that occurs through the motion of the immersing fluid is known as hydrodynamic coupling.

A way to analyse the dynamics of a particle, or several particles, is to look at the auto-correlation and cross-correlations in their respective movements. Cross-correlation is a way to compare two different sets of data and assess whether they are similar at different delay, or 'lag' times. In the case of two trapped particles this could be used to identify if the motion of the second particle mimics or is affected by some change in the motion of the first particle at

some time previously. This cross-correlation at some lag time τ between two signals, a and b, can be written as [81]:

$$C_{ab}(\tau) = \langle a(t)b(t+\tau)\rangle, \tag{6.11}$$

where the angled brackets indicate a time average, which would then be evaluated for many time lag intervals. The auto-correlation is a measure of how, at different time intervals, a particle's trajectory correlates with itself. i.e. it is the cross-correlation of a signal with itself. As such it is useful for identifying periodic, repeating patterns in a signal, particularly if they might be obscured by random noise such as the Brownian fluctuations of optically trapped particles.

The first step on the route to identifying expressions for the correlations of optically trapped particles' position fluctuations is to write equations for the velocity of the fluid at the location of a particle n, $\boldsymbol{v}_n$, produced by forces, $\boldsymbol{F}_m$, acting at the locations of the other particles [175, 177]:

$$\boldsymbol{v}_n = \sum_{m=1}^{N} \boldsymbol{H}_{nm} \cdot \boldsymbol{F}_m, \tag{6.12}$$

which is similar to the form of the inertia-less Langevin equation (Equation 3.84), where the $1/\gamma$ term (sometimes referred to as the mobility) has been replaced by $\boldsymbol{H}_{nm}$. This term is known as a mobility matrix or the Oseen tensor, and is responsible for modelling the coupled motion of the interacting particles. This has the properties:

$$\boldsymbol{H}_{nn} = \frac{\mathbb{I}}{\gamma}, \qquad \text{and,} \qquad \boldsymbol{H}_{nm} = \frac{1}{\gamma}\frac{3\alpha}{4d_{nm}}\left(\mathbb{I} + \hat{\boldsymbol{d}}_{nm} \otimes \hat{\boldsymbol{d}}_{nm}\right) \quad \text{for } n \neq m, \tag{6.13}$$

where $\mathbb{I}$ is a 3×3 identity matrix, d_{nm} is the distance between optical traps n and m, $\boldsymbol{d}_{nm}$ is the vector which connects the centres of the two particles, and $\hat{\boldsymbol{d}}_{nm} \otimes \hat{\boldsymbol{d}}_{nm}$ is a tensor product of the unit vector parallel to $\boldsymbol{d}_{nm}$ with itself. If two spheres are tightly confined and held apart by separate optical traps then their average motion about the location of their traps due to Brownian fluctuations can be assumed small compared to their separation. If the Cartesian direction in which they are separated is x, and they sit in the same y and z planes, then following approximation can be written:

$$\boldsymbol{d}_{nm} \approx d_{nm}\hat{\boldsymbol{x}} + 0\hat{\boldsymbol{y}} + 0\hat{\boldsymbol{z}}. \tag{6.14}$$

Inserting this into the right hand expression in Equation 6.13 and utilising $\hat{\boldsymbol{d}}_{nm} \otimes \hat{\boldsymbol{d}}_{nm} = (\boldsymbol{d}_{nm} \otimes \boldsymbol{d}_{nm})/d_{nm}^2$ gives:

$$\boldsymbol{H}_{nm} = \frac{1}{\gamma}\frac{3\alpha}{4d_{nm}}\left(\mathbb{I} + \frac{1}{d_{nm}^2}\begin{bmatrix} d_{nm} \\ 0 \\ 0 \end{bmatrix}\begin{bmatrix} d_{nm} & 0 & 0 \end{bmatrix}\right) \tag{6.15}$$

$$= \frac{1}{\gamma}\frac{3\alpha}{4d_{nm}}\begin{bmatrix} 2 & 0 & 0 \\ 0 & 1 & 0 \\ 0 & 0 & 1 \end{bmatrix}. \tag{6.16}$$

Therefore:

$$\boldsymbol{H}_{nm} = \frac{\epsilon_i}{\gamma}, \qquad \epsilon_i = \begin{cases} \frac{3\alpha}{2d_{nm}} & \text{for } i = x \\ \frac{3\alpha}{4d_{nm}} & \text{for } i = y, z. \end{cases} \tag{6.17}$$

Consider now for the sake of simplicity, a system of just two coupled particles.

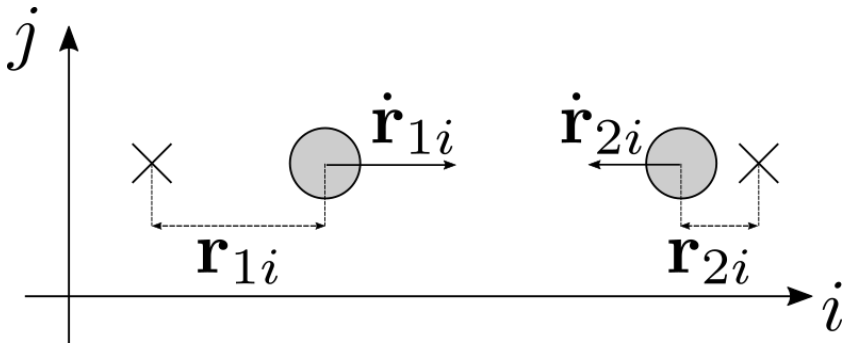

Figure 6.1: An illustration of two coupled particles (filled circles) displaced from their traps (crosses) with their displacements and velocities indicated.

Let $\boldsymbol{r}_{1i}$ denote the displacement of particle 1 from its trap in the i direction at time t, and $\dot{\boldsymbol{r}}_{1i}$ its velocity at this time (see Figure 6.1).

Equation 6.12, along with the forces from the inertia-less Langevin equation can then be used to write out the following:

$$\begin{aligned}\dot{\boldsymbol{r}}_{1i} &= \boldsymbol{H}_{11}\boldsymbol{F}_1 + \boldsymbol{H}_{12}\boldsymbol{F}_2 \\ &= \frac{1}{\gamma}(-\kappa_i \boldsymbol{r}_{1i} + \zeta_1) + \frac{\epsilon_i}{\gamma}(-\kappa_i \boldsymbol{r}_{2i}) \\ &= \frac{1}{\gamma}\left[-\kappa_i(\boldsymbol{r}_{1i} + \epsilon_i \boldsymbol{r}_{2i}) + \zeta_1\right], \end{aligned} \tag{6.18}$$

and similarly:

$$\dot{\boldsymbol{r}}_{2i} = \frac{1}{\gamma}\left[-\kappa_i(\epsilon_i \boldsymbol{r}_{1i} + \boldsymbol{r}_{2i}) + \zeta_2\right], \tag{6.19}$$

where the ζ_n are Gaussian noise terms with the properties already mentioned in Section 3.3, except here a slight modification is made that takes into account introduction of the mobility matrix such that: $\langle \zeta_1(t)\zeta_2(t+\tau)\rangle = 2\boldsymbol{H}_{12}^{-1} k_{\mathrm{B}} T \delta(\tau)$.

These are a pair of coupled differential equations of motion for the two particles. To reach the respective correlation functions for each particle it is prudent to first

introduce and work with the following normal modes of motion for the system:

$$q_{1i} = \frac{1}{\sqrt{2}}(\boldsymbol{r}_{1i} + \boldsymbol{r}_{2i}) \tag{6.20}$$

$$q_{2i} = \frac{1}{\sqrt{2}}(\boldsymbol{r}_{1i} - \boldsymbol{r}_{2i}), \tag{6.21}$$

such that working with the coupled expressions can be avoided. One dimensional illustrations of each of these modal motions is shown in Figure 6.2. The first of these modes, q_{1i}, corresponds to the centre-of-mass (COM) motion of the two particles in the i direction. The two cases of this can be seen in Figures 6.2a and 6.2b. Assuming that movement to the right of these illustrations is in the positive i direction, then these correspond to a positive and a negative change in the COM of these particles respectively in the i direction. The second normal mode, q_{2i}, corresponds to relative motion ('breathing mode') of the two particles in the i direction. The two cases of this motion can be seen in Figures 6.2c and 6.2d. These correspond to an increase and a decrease respectively in the relative/breathing modal coordinate (the relative separation), of these two particles in the i direction.

Considering the auto-correlation of the first mode (Equation 6.20) gives:

$$C_{q_{1i}q_{1i}}(\tau) = \langle q_{1i}(t)q_{1i}(t+\tau)\rangle, \tag{6.22}$$

where the (t) has been explicitly stated to differentiate the function at the lag time, τ, later than t. The first step to finding an equation for the

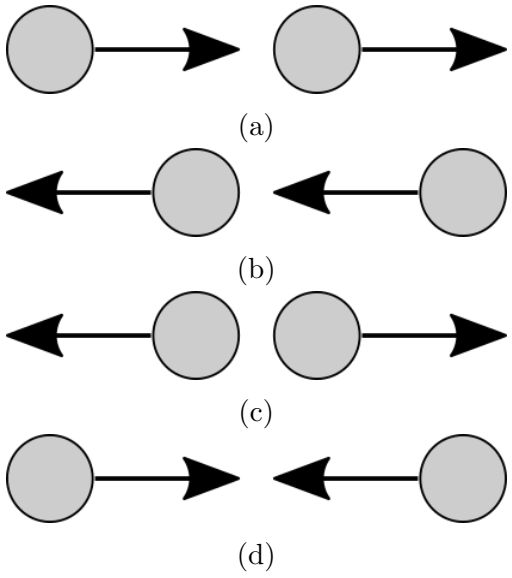

Figure 6.2: An illustration of the possible modal motions of two particles in one coordinate direction for the centre-of-mass, a) and b), and relative/breathing modes, c) and d).

auto-correlation involves differentiating this with respect to the lag time:

$$\frac{\partial C_{q_{1i}q_{1i}}(\tau)}{\partial \tau} = \left\langle q_{1i}(t)\frac{\partial q_{1i}(t+\tau)}{\partial \tau} \right\rangle. \tag{6.23}$$

An expression for the derivatives of the modes is thus needed. Looking at just the first mode initially, using Equation 6.20, it can be said that:

$$\dot{q}_{1i} = \frac{1}{\sqrt{2}}(\dot{\boldsymbol{r}}_{1i} + \dot{\boldsymbol{r}}_{2i}). \tag{6.24}$$

Substituting into this the expressions for the particles' velocities from Equations 6.18 and 6.19, and then simplifying yields a final expression for the time derivative of the modes' motion:

$$\begin{aligned}\dot{q}_{1i} &= \frac{1}{\sqrt{2}}\Bigg[\frac{1}{\gamma}\big(-\kappa_i(\boldsymbol{r}_{1i}+\epsilon_i\boldsymbol{r}_{2i})+\zeta_1\big) \\ &\qquad\qquad -\kappa_i(\epsilon_i\boldsymbol{r}_{1i}+\boldsymbol{r}_{2i})+\zeta_2)\Bigg] \\ &= \frac{1}{\gamma}\left[-\frac{\kappa_i(1+\epsilon_i)}{\sqrt{2}}(\boldsymbol{r}_{1i}+\boldsymbol{r}_{2i})+\frac{1}{\sqrt{2}}(\zeta_1+\zeta_2)\right] \\ &= \frac{1}{\gamma}\left[-\kappa_i(1+\epsilon_i)q_{1i}+\frac{1}{\sqrt{2}}(\zeta_1+\zeta_2)\right], \end{aligned} \tag{6.25}$$

and similarly it can be shown that:

$$\dot{q}_{2i} = \frac{1}{\gamma}\left[-\kappa_i(1-\epsilon_i)q_{2i}+\frac{1}{\sqrt{2}}(\zeta_1-\zeta_2)\right]. \tag{6.26}$$

Comparing these to the velocity of an individual particle as seen in the Langevin equation previously (Equation 3.84), it can be seen that the form of the mobility term associated with the restoring force has developed in the case of coupled particles and modal motion from: $1/\gamma \rightarrow (1 \pm \epsilon_i)/\gamma$. Using this, it can also be asserted therefore that the time constant or the relaxation time, τ_r of this motion has also developed from the single particle case of, $\tau_r = \gamma/\kappa_i$, to the coupled modal coordinate form: $\tau_r = \gamma/(1 \pm \epsilon_i)\kappa_i$. Inserting Equation 6.25 back into the expression for the lag-time derivative of the auto-correlation gives:

$$\begin{aligned}\frac{\partial C_{q_{1i}q_{1i}}(\tau)}{\partial\tau} &= \left\langle q_{1i}(t)\frac{1}{\gamma}\left[-\kappa_i(1+\epsilon_i)q_{1i}(t+\tau)+\frac{1}{\sqrt{2}}(\zeta_1(t+\tau)+\zeta_2(t+\tau))\right]\right\rangle \\ &= \frac{1}{\gamma}\Bigg[-\kappa_i(1+\epsilon_i)\left\langle q_{1i}(t)q_{1i}(t+\tau)\right\rangle \\ &\qquad +\frac{1}{\sqrt{2}}\Big(\left\langle q_{1i}(t)\zeta_1(t+\tau)\right\rangle+\left\langle q_{1i}(t)\zeta_2(t+\tau)\right\rangle\Big)\Bigg]. \end{aligned} \tag{6.27}$$

The second and third time averaged terms in the above expression will equal 0. This is because the Brownian fluctuation, ζ, terms are by their very definition and nature random forces that should not have any correlation with the particles' positions or trajectories. This only leaves the first term which, upon inspection, is proportional to the autocorrelation of this mode. Stating this:

$$\frac{\partial C_{q_{1i}q_{1i}}(\tau)}{\partial \tau} = -\kappa_i \frac{(1+\epsilon_i)}{\gamma} C_{q_{1i}q_{1i}}(\tau), \tag{6.28}$$

makes it clear that this is now just a simple differential equation, the solution to which is as follows:

$$C_{q_{1i}q_{1i}}(\tau) = C_{q_{1i}q_{1i}}(0) \exp\left(-\frac{\kappa_i(1+\epsilon_i)}{\gamma}\tau\right). \tag{6.29}$$

The expression $C_{q_{1i}q_{1i}}(0)$ corresponds to the auto-correlation function at zero lag time, i.e.:

$$\begin{aligned} C_{q_{1i}q_{1i}}(0) &= \langle q_{1i}(t) q_{1i}(t+0) \rangle \\ &= \langle q_{1i}^2(t) \rangle, \end{aligned} \tag{6.30}$$

the variance of the mode. From the equipartition theorem, the energy associated with each harmonic degree of freedom is $\frac{1}{2}k_{\mathrm{B}}T$ [178]. i.e.:

$$\langle U(x) \rangle = \frac{1}{2}\kappa \langle x^2(t) \rangle = \frac{1}{2}k_{\mathrm{B}}T. \tag{6.31}$$

Applying this to Equation 6.30 it can be seen that:

$$C_{q_{1i}q_{1i}}(0) = \frac{k_{\mathrm{B}}T}{\kappa_i}, \tag{6.32}$$

which finally leads to the completed equation for the auto-correlation of this mode:

$$C_{q_{1i}q_{1i}}(\tau) = \frac{k_{\mathrm{B}}T}{\kappa_i} \exp\left(-\frac{\kappa_i(1+\epsilon_i)}{\gamma}\tau\right), \tag{6.33}$$

and similarly,

$$C_{q_{2i}q_{2i}}(\tau) = \frac{k_{\mathrm{B}}T}{\kappa_i} \exp\left(-\frac{\kappa_i(1-\epsilon_i)}{\gamma}\tau\right), \tag{6.34}$$

Both modal correlation functions therefore exhibit decay according to a single exponential whose decay time is linked to the time constant/relaxation time of their respective modal motions. Now that these correlation functions for the modes of the motion have been obtained, it is possible to work back and find the auto and cross-correlations for the individual coordinates. From the definition of the modes in Equations 6.20 and 6.21 it can be seen that:

$$\boldsymbol{r}_{1i} = \frac{1}{\sqrt{2}}\left(q_{1i} + q_{2i}\right) \tag{6.35}$$

$$\boldsymbol{r}_{2i} = \frac{1}{\sqrt{2}}\left(q_{1i} - q_{2i}\right). \tag{6.36}$$

It can therefore be written that:

$$
\begin{aligned}
C_{\boldsymbol{r}_{1i}\boldsymbol{r}_{1i}}(\tau) &= \langle \boldsymbol{r}_{1i}(t)\boldsymbol{r}_{1i}(t+\tau)\rangle \\
&= \left\langle \frac{1}{\sqrt{2}}\big(q_{1i}(t)+q_{2i}(t)\big)\frac{1}{\sqrt{2}}\big(q_{1i}(t+\tau)+q_{2i}(t+\tau)\big)\right\rangle \\
&= \frac{1}{2}\Big(\langle q_{1i}(t)q_{1i}(t+\tau)\rangle + \langle q_{2i}(t)q_{1i}(t+\tau)\rangle \ldots \\
&\quad \ldots + \langle q_{1i}(t)q_{2i}(t+\tau)\rangle + \langle q_{2i}(t)q_{2i}(t+\tau)\rangle\Big) \\
&= \frac{1}{2}\Big(C_{q_{1i}q_{1i}}(\tau) + C_{q_{2i}q_{1i}}(\tau) + C_{q_{1i}q_{2i}}(\tau) + C_{q_{2i}q_{2i}}(\tau)\Big). \qquad (6.37)
\end{aligned}
$$

Owing to the fact that they are the two normal modes of the system, the cross-correlation terms of q_{1i} and q_{2i} must be identically zero. Equation 6.37 therefore reduces to:

$$
\begin{aligned}
C_{\boldsymbol{r}_{1i}\boldsymbol{r}_{1i}}(\tau) &= \frac{1}{2}\Big(C_{q_{1i}q_{1i}}(\tau) + C_{q_{2i}q_{2i}}(\tau)\Big) \\
&= \frac{k_{\mathrm{B}}T}{2\kappa_i}\left[\exp\left(-\frac{\kappa_i(1+\epsilon_i)}{\gamma}\tau\right) + \exp\left(-\frac{\kappa_i(1-\epsilon_i)}{\gamma}\tau\right)\right] \\
&= C_{\boldsymbol{r}_{2i}\boldsymbol{r}_{2i}}(\tau) \qquad (6.38)
\end{aligned}
$$

The cross-correlation of the particles' coordinate motions can also be found in a similar way:

$$
\begin{aligned}
C_{\boldsymbol{r}_{1i}\boldsymbol{r}_{2i}}(\tau) &= \langle \boldsymbol{r}_{1i}(t)\boldsymbol{r}_{2i}(t+\tau)\rangle \\
&= \left\langle \frac{1}{\sqrt{2}}\big(q_{1i}(t)+q_{2i}(t)\big)\frac{1}{\sqrt{2}}\big(q_{1i}(t+\tau)-q_{2i}(t+\tau)\big)\right\rangle \\
&= \frac{1}{2}\Big(C_{q_{1i}q_{1i}}(\tau) + C_{q_{2i}q_{1i}}(\tau) - C_{q_{1i}q_{2i}}(\tau) - C_{q_{2i}q_{2i}}(\tau)\Big). \qquad (6.39)
\end{aligned}
$$

The two modal cross-correlation terms are, again, identically zero and so this reduces to:

$$\begin{aligned} C_{\boldsymbol{r}_{1i}\boldsymbol{r}_{2i}}(\tau) &= \frac{1}{2}\Big(C_{q_{1i}q_{1i}}(\tau) - C_{q_{2i}q_{2i}}(\tau)\Big) \\ &= \frac{k_{\mathrm{B}}T}{2\kappa_i}\left[\exp\left(-\frac{\kappa_i(1+\epsilon_i)}{\gamma}\tau\right) - \exp\left(-\frac{\kappa_i(1-\epsilon_i)}{\gamma}\tau\right)\right] \\ &= C_{\boldsymbol{r}_{2i}\boldsymbol{r}_{1i}}(\tau) \end{aligned} \tag{6.40}$$

The forms of the individual particles auto and cross-correlations therefore feature the sum and the difference respectively of two exponentials whose decay times are linked to the relaxation times of the two modal motions. Upon the derivation of these correlation equations a method has now been shown for theoretically obtaining both the fluctuation theorem for a system to quantify the evolution of its time irreversibility [174, 176], and the auto and cross-correlations of a pair of optically trapped particles in order to assess their coupling and dynamics [179].

6.2 Literature Review

The fluctuation theorem measure was first proposed by Evans *et al.* in 1993 [169]. They looked at a fluid under an external shear, analysing the non-equilibrium steady state of particles moving in the fluid and finding the ratio of probabilities of finding trajectory segments that were in the direction of, or opposite to, the externally imposed shear. Their theoretical calculations were supported by molecular dynamics simulations, and showed that for finite amounts of time it was possible to see second law violations. Since this paper there has been a good deal of interest in this subject and refinement of the ideas originally presented.

In 1994 Evans and Searles questioned why it is difficult to identify initial microstates that would lead to these second law violations over long time scales [170]. They showed that the number of anti-trajectory generating initial states vanishes exponentially with the duration of the trajectory length/time, and were able to corroborate this with numerical simulations which showed the ratio of probabilities of observing negative trajectories to probabilities of observing positive trajectories decreases to zero at long times.

Reid *et al.* further analysed the dissipation function, the main argument at the heart of the FT, in 2004 [174]. They discussed how until that point, even studies which had considered the FT in stochastic systems had done so via a derivation of the dissipation function which was based in deterministic Newtonian equations of motion [180, 181]. They demonstrated how the dissipation function, Ω_t, can be derived through the use of stochastic equations. They further showed how this Ω_t could differ in the two frameworks, and indeed vary within the stochastic framework depending upon the coordinate system chosen, however that all of the different expressions for Ω_t ultimately satisfy the FT.

Numerous experiments have been conducted to verify the FT. These have taken on different forms although frequently adopt optical tweezers as their principal tool. This is because they exert very small forces and so only represent a small amount of work done on trapped objects, work which can therefore be comparable to the thermal motion of the objects and so reverse trajectories on short time scales are more likely to be observed than in macroscopic systems with larger forces involved. Wang *et al.* (2002) investigated the transient fluctuation theorem (TFT) by holding a particle fixed in an optical trap and dragging it through water by moving a microscope stage relative to it [171]. The TFT is the name given to the FT when considering a system which undergoes some change at its beginning, such that there is an initial transient phase before

some non-equilibrium steady-state is reached. They were unable to demonstrate the TFT this way but were able to for the integrated transient fluctuation theorem (ITFT) (see Equation 6.10). Then in 2004 Carberry *et al.* did successfully demonstrate this TFT with an experiment that observed the relaxation of a particle held fixed in an optical trap as the strength of the trap was modulated and reduced [182].

In 2005 Wang *et al.* studied the FT for non-equilibrium steady states, i.e. for scenarios that don't have the initial transient phase [167]. This is referred to as the steady-state fluctuation theorem (SSFT). It had been thought that the FT theorem would only hold in long time limits for these steady-state scenarios, yielding the form of the SSFT:

$$\lim_{t\to\infty} \frac{P(\Omega_t = -A)}{P(\Omega_t = A)} = \exp(-A). \tag{6.41}$$

However Wang *et al.* showed that the assumption of this limit arises due to approximations made in the derivation of the dissipation function, and that, if the dissipation function can be derived exactly then the 'regular' FT holds over all time and not just in the long time limit. This was demonstrated via both the integrated [167] and non-integrated forms [183] of the FT, utilising a particle dragging/stage moving experiment similar to that mentioned earlier.

Carberry *et al.* repeated their 2004 experiment [182] where the trap power was modulated in order to study the FT, but this time by trapping particles immersed in a viscoelastic solvent [184]. In so doing they were able to experimentally confirm the FT in an environment with more complicated dynamics than one just obeying the Langevin equation with white noise.

Meiners and Quake analysed the correlation functions for two optically trapped

hydrodynamically coupled particles [179]. Experiments were conducted and the correlations were measured with two fixed traps, the results of which supported their theoretical calculations. The form of the auto-correlation that they found (Equation 6.38) contains the sum of two exponentials, both with equal amplitudes and time constants that are similar to the relaxation time of the traps (γ/κ_i), assuming large trap separation relative to particle radius. A single trapped particle without hydrodynamic coupling with neighbours would have an auto-correlation with twice the amplitude and the characteristic relaxation time ($\frac{k_\mathrm{B}T}{\kappa_i}\exp\left(-\frac{\kappa_i}{\gamma}\tau\right)$). The change to the auto-correlation of an individual particle is therefore very minimal. For the cross-correlations however, a marked difference was observed. A minimum was seen to emerge on short time scales owing to the difference in time constants in the exponential terms (see Figure 6.3). Their explanation for this points to the asymmetry of the hydrodynamic interaction. They state that as the general motion of the particles is such that one is dragged in the wake of the other, it therefore takes longer for anti-correlated fluctuations to relax, as they rely on the displacement of fluid between the spheres, than it does for correlated fluctuations [179].

Bridging the gap between the FTs and coupled particles, more recent studies have sought to consider the energy exchanges in non-equilibrium systems of viscously coupled particles and to observe the resulting correlations and agreement with FTs. A prominent method of driving these systems out of equilibrium is to have two optically trapped particles held at different 'effective temperatures'; realised by deliberate random-forcing of one trap via a Gaussian white noise signal [185] that is sufficiently small that it does not affect the stiffness of the trap [186]. Experimentally it has been shown that these show a short-term negative cross-correlation [186] not dissimilar to that seen in Figure 6.3 for the two coupled particles held with the same temperature [179].

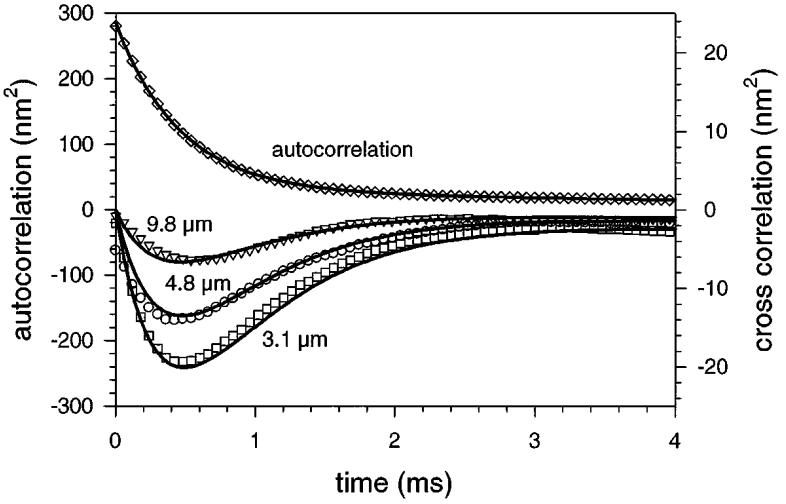

Figure 6.3: Correlation functions of the positions of two optically trapped beads. The upper data set of crosses shows the auto-correlation function of the positions of one of the beads, along with a theoretical line. The lower data sets (squares, circles, and triangles) show the cross-correlation functions of the two beads at different separation distances, along with theoretical prediction lines. Reprinted figure with permission from J. C. Meiners and S. R. Quake, Phys. Rev. Lett., 82, 2211 (1999). Copyright 2017 by the American Physical Society. http://dx.doi.org/10.1103/PhysRevLett.82.2211

Comparison of the dissipative, viscous particle coupling in this system to conservative coupling (via an electric circuit) has been made experimentally and certain similarities have been established between the two - the heat flux and the work performed by one component of the system on the other have been isolated separately and shown to both satisfy the fluctuation theorem [187]. It has also been detailed that in the case of two symmetric traps with exactly equal stiffness, then all the effective extra heat is dissipated through the coupling to the colder particle and the system is indistinguishable from one with conservative coupling [187, 188]. Experimentally, effective heat fluxes between these particles have been identified and it has been shown that they satisfy a steady state exchange fluctuation theorem [188]. Finally, sudden temperature gradients between the particles have been introduced to this system and it has been shown experimentally [188] and explained theoretically [189] that statistical properties of the heat flow differ depending upon the flow direction. The hot to cold

particle flow follows a transient exchange fluctuation theorem for all time, whereas in the reverse direction this is only the case for asymptotically long time, which is something which had previously been predicted but for conservative coupling system [190].

6.3 Objectives

The aim of this research is to conduct preliminary simulations and experiments to extend the current body of experimental work on fluctuation theorems in the literature by looking at systems where work is performed upon hydrodynamically coupled colloids by deliberate directional movement of them. That is, movement over and above an increased effective temperature from forced noisy perturbations seen previously in the literature. This will be carried out by monitoring two particles in distinct optical traps as work is done on them via stage or trap translation. The correlations (auto and cross) of these particles will be calculated and the fluctuation theorems evaluated in order to ascertain whether these are fulfilled and valid for this more complicated work.

6.4 Contributions

Here I will detail the contributions of those involved in the research in this chapter. The theoretical background for this project, the calculation of fluctuation theorems for a particle in one dimensional fluid flow or with a trap moving in one direction and the calculation of modal correlations of coupled particles, was already established in the literature. What is novel is the use of two coupled particles when considering the fluctuation theorems, and using the centre-of-mass and relative motions of these two particles in order to work out

their total work fluctuation theorems and predict how this evolves. Thomas Smart (U.C.L) and myself worked together on these theoretical calculations with assistance from our supervisor (Philip Jones, U.C.L). Again, we both worked on the experiments together and collected all of the data, together. Where our contributions differ is that Thomas worked on the simulations (modifying those from the Kapitza experiment to move the trap in different ways and model 2 random particles), whilst I modified the MATLAB tracking code to track n particles, rather than just two. I also worked in Labview, to record the mirror positions synchronously, as well to drive them and record the video and stage positions as mentioned before. In addition to this I wrote MATLAB software to process the tracked data and calculate the correlations and fluctuation theorems from these.

6.5 Theoretical Calculations

Before beginning the theoretical calculations for these coupled experiments, a labelling convention will be established here. Since systems of two trapped particles will be extensively discussed throughout this chapter, let the following definitions preside. Particle 1 and trap 1 refer to the particle that was held with a fixed optical tweezers trap in these experiments (which was always the leftmost trap), whilst particle 2 and trap 2 refer to the particle held in the steerable optical trap whose beam path includes the galvanometer mirrors (which was always the rightmost trap).

6.5.1 Fluid Drag Calculations

The first method of performing work on this system that was attempted was introducing fluid drag. That is, translating the immersing fluid relative to the optical traps such that the particles in the traps experience a viscous drag force.

This fluid drag should affect both particles equally, forcing them both to displace in the same direction from their original positions. It is fairly intuitive to see that this is the same scenario that is illustrated with regards the modal motions in Figures 6.2a and 6.2b (depending upon the direction of the fluid motion). In terms of the modes then, this method of working on the system only drives the centre-of-mass mode, and should not affect the breathing mode since the particle separation remains constant. This is a very similar experiment to the one performed by Wang *et al.* [171], but with the addition of an extra particle and the resultant modification of their hydrodynamics.

Total Work FT

The simplest way, and the way which will be employed in this thesis, of forming a FT for this experiment is to use the total work FT that Wang *et al.* unknowingly initially used [171, 172], and to study the time evolution fluctuations of the total work done on the system. The total work done moving an object at a constant velocity, $\boldsymbol{v}$, with a force, $\boldsymbol{F}$, is given by: [43]

$$W = \int_{t_1}^{t_2} \boldsymbol{F} \cdot \boldsymbol{v} dt, \tag{6.42}$$

where t_2 and t_1 are two arbitrary times with $t_2 > t_1$. For this system of moving the immersing fluid relative to the traps then, the total work during a trajectory

time τ is given by:

$$W_{\tau}^{\mathrm{tot}} = \frac{1}{k_{\mathrm{B}}T}\int_{0}^{\tau} \boldsymbol{F}(\boldsymbol{r}, \boldsymbol{r}_{\mathrm{Trap}}) \cdot \boldsymbol{v}_{\mathrm{Opt}} dt, \tag{6.43}$$

where:

$$\boldsymbol{F}(\boldsymbol{r}, \boldsymbol{r}_{\mathrm{Trap}}) = -\kappa(\boldsymbol{r} - \boldsymbol{r}_{\mathrm{Trap}}) \tag{6.44}$$

is the harmonic trapping force exerted upon the particle based on its position, $\boldsymbol{r}$, and the position of the trap, $\boldsymbol{r}_{\mathrm{Trap}}$, at a given time, $\boldsymbol{v}_{\mathrm{Opt}}$ is the constant velocity of the fluid, and the convention of Wang *et al.* [171] of dividing through by the Boltzmann constant and temperature, $k_{\mathrm{B}}T$, in order to give a dimensionless work has been followed.

Forming the FT from this total work then gives:

$$\frac{P(-W^{\mathrm{tot}})}{P(W^{\mathrm{tot}})} = \exp^{-W^{\mathrm{tot}}}. \tag{6.45}$$

In order to obtain better statistics in these experiments, the previously mentioned integrated form of the FT will be used in order to find the ratio of the total number of negative to positive work fluctuations along a trajectory. What will be calculated and plotted from the experimental data is therefore:

$$\frac{P(W^{\mathrm{tot}} < 0)}{P(W^{\mathrm{tot}} > 0)} = \langle \exp^{-W^{\mathrm{tot}}} \rangle_{W^{\mathrm{tot}}>0}. \tag{6.46}$$

An expression for the probability distribution of this dimensionless energy has been derived by Wang *et al.* [167], and from this an expected analytical form of

the integrated FT was found as:

$$\frac{P(W^{\mathrm{tot}}<0)}{P(W^{\mathrm{tot}}>0)}=\frac{1-\mathrm{erf}\left(\frac{1}{2}\sqrt{\omega(t)}\right)}{1+\mathrm{erf}\left(\frac{1}{2}\sqrt{\omega(t)}\right)} \tag{6.47}$$

where:

$$\omega(t)=\mathcal{F}^2\left(\frac{t}{\tau_r}-(1-\exp^{-t/\tau_r})\right), \tag{6.48}$$

and erf() is the error function, given by:

$$\mathrm{erf}(x)=\frac{2}{\pi}\int_0^x e^{-t^2}dt. \tag{6.49}$$

$\tau_r=\gamma/\kappa$ is the characteristic relaxation time, and $\mathcal{F}^2=\gamma^2\boldsymbol{v}_{\mathrm{Opt}}^2/(\kappa k_BT)$ is a dimensionless quantity that characterises the opposing forces on the trapped particle, found as the ratio of the squares of lag distance, $\gamma\boldsymbol{v}_{\mathrm{Opt}}/\kappa$, and the typical particle position within the trap from equipartition, $\sqrt{k_BT/\kappa}$ [167]. This theoretical, analytical expression will be used to compare to experimental values for the integrated FT found from Equation 6.46.

Finally, a few factors must be remembered and implemented in these equations to account for this being a coupled particle experiment. The centre-of-mass mode is being driven, so the mobility in these equations must be changed to suit this (i.e. $\gamma\rightarrow\gamma/(1+\epsilon)$). When it comes to performing these calculations for the modal motion, the COM trap position must be used in Equation 6.43 and the COM velocity must be used throughout as this will be equal to $\sqrt{2}\boldsymbol{v}_{\mathrm{Opt}}$ - on account of the velocity of the fluid moving relative to both traps and not just one.

The expectation was that, just as in the literature where this experiment is performed on one particle [171, 174], the fluctuation theorem would hold for these

coupled particle experiments and that an exponential curve tending towards zero would emerge as the theorem was evaluated for longer and longer trajectory times. This was expected because this system must obey the second law of thermodynamics and so as long as the FT holds for coupled particles, which effective temperature experiments suggest it does [187], it must tend towards thermodynamic irreversibility at long times.

Probability Densities FT

An alternative way of checking the validity of the FT would be to use the dissipation function seen in Section 6.1.1, the ratio of the probabilities of observing trajectories and anti-trajectories. A brief derivation using this method will be given here. Reid *et al.* [174] can be leant upon for the initial theoretical calculations towards a FT for this scenario, as they employ a useful reference frame when discussing the single particle case. Consider again the Langevin equation for a single immersed particle, located in an optical trap, in a low Reynolds number regime (Equation 3.84). This time though, let the trap be translated with a constant velocity relative to the fluid:

$$\gamma \dot{\boldsymbol{r}} = -\kappa(\boldsymbol{r} - \boldsymbol{v}_{\mathrm{Opt}} t) + \zeta(t). \tag{6.50}$$

Now this Langevin equation is transformed into a new coordinate system with the particle position denoted, $\boldsymbol{x}$. This new system utilises a reference frame that translates with the relative velocity of the trap motion, $\boldsymbol{v}_{\mathrm{Opt}}$, but also has its origin displaced backwards from this by $\gamma \boldsymbol{v}_{\mathrm{Opt}}/\kappa$, i.e. compensating for the viscous drag upon the particle making it lag behind the translating trap. This

can be written as: $\boldsymbol{r} = \boldsymbol{x} + \boldsymbol{v}_{\mathrm{Opt}}t - \gamma\boldsymbol{v}_{\mathrm{Opt}}/\kappa$, which transforms equation 6.50 into:

$$\gamma\dot{\boldsymbol{x}} = -\kappa\boldsymbol{x} + \zeta(t), \tag{6.51}$$

which is just the Langevin equation for a particle in a static trap (Equation 3.84).

The initial distribution of possible positions of a particle in a static 2-D optical trap follows a Boltzmann distribution [175]:

$$P_B(\boldsymbol{r}_0, \kappa) = \left(\frac{\kappa}{2\pi k_B T}\right) \exp\left(-\frac{\kappa \boldsymbol{r}_0^2}{2k_B T}\right), \tag{6.52}$$

and the Green's function gives the probability of finding a trapped particle at a location, $\boldsymbol{r}_t$, given its position at $\boldsymbol{r}_0$ some time, t, earlier [175]:

$$G(\boldsymbol{r}_t; \boldsymbol{r}_0, \kappa, t) = \left(\frac{\kappa}{2\pi k_B T[1 - \exp\left(-\frac{2t}{\tau_r}\right)]}\right) \exp\left(\frac{-\kappa[\boldsymbol{r}_t - \boldsymbol{r}_0 \exp\left(-\frac{t}{\tau_r}\right)]^2}{2k_B T[1 - \exp\left(-\frac{2t}{\tau_r}\right)]}\right). \tag{6.53}$$

N.B. At long times (as $t \to \infty$) this becomes equivalent to the Boltzmann distribution seen above it, as would be expected. Thus at long times, in the steady state, the distribution of the particle's position in a translating trap would be the same as for a static trap, only lagging behind the trap position by $\gamma\boldsymbol{v}_{\mathrm{Opt}}/\kappa$. (This is of course not the case for short time scales of $t \ll \tau_r$).

Consider a set of conjugate trajectories in this new reference frame: $\{\boldsymbol{x}_0, \boldsymbol{x}_t\}$ and $\{\boldsymbol{x}_t, \boldsymbol{x}_0\}$. The probability density of the set of forward trajectories $p(\boldsymbol{x}_0, \boldsymbol{x}_t)$ can be found from the product of the probability that the particle started at position $\boldsymbol{x}_0$ at time $t = 0$, and the probability of the particle being located at position $\boldsymbol{x}_t$ some time t later. As a result of the simple Langevin equation of motion in this

new coordinate system, the latter of these multiplying terms is simply the Green's function: $G(\boldsymbol{x}_t; \boldsymbol{x}_0, \kappa, t)$. The probability distribution of the initial position comes from the Boltzmann distribution (Equation 6.52), where the $\boldsymbol{r}_0$ term is written in terms of the new coordinate system at time $t = 0$, i.e. $\boldsymbol{r}_0 = \boldsymbol{x}_0 - \gamma \boldsymbol{v}_{\mathrm{Opt}}/\kappa$. For the complete probability density of the set of forward trajectories this gives:

$$p(\boldsymbol{x}_0, \boldsymbol{x}_t) = P_B(\boldsymbol{x}_0 - \gamma \boldsymbol{v}_{\mathrm{Opt}}/\kappa, \kappa) G(\boldsymbol{x}_t; \boldsymbol{x}_0, \kappa, t). \tag{6.54}$$

The same reasoning can be followed for the probability of the backwards trajectories, yielding the same result with the $\boldsymbol{x}_t$ and $\boldsymbol{x}_0$ terms swapped. Since it is known from Equation 6.4 that the dissipation function is just the ratio of these backwards to forwards trajectories, it can be written that:

$$\Omega_t(\boldsymbol{x}_t, \boldsymbol{x}_0) = \frac{p(\boldsymbol{x}_t, \boldsymbol{x}_0)}{p(\boldsymbol{x}_0, \boldsymbol{x}_t)} = \ln \left(\frac{P_B(\boldsymbol{x}_t - \gamma \boldsymbol{v}_{\mathrm{Opt}}/\kappa, \kappa) G(\boldsymbol{x}_0, \boldsymbol{x}_t, \kappa, t)}{P_B(\boldsymbol{x}_0 - \gamma \boldsymbol{v}_{\mathrm{Opt}}/\kappa, \kappa) G(\boldsymbol{x}_t, \boldsymbol{x}_0, \kappa, t)} \right). \tag{6.55}$$

There are a couple of observations and simplifications that can be made immediately. The first multiplying bracket in each of these expressions (Equations 6.52 and 6.53) is not dependent on the coordinate. Therefore these will be equivalent for the forward and backward trajectories and so will cancel out due to the division in the dissipation function. This will leave an expression of the form: $\Omega_t(\boldsymbol{x}_t, \boldsymbol{x}_0) = \ln[(\mathrm{e}^a \mathrm{e}^b)/(\mathrm{e}^c \mathrm{e}^d)]$. The four exponential expressions can be combined into one by adding or subtracting their powers and this single natural exponential will cancel with the natural logarithm to give: $a + b - c - d$. Finally, from the definitions of the Boltzmann distribution and Green's function it can be seen that these terms all have a common factor of $-\kappa/2k_BT$. Factorising this out and taking into account the other simplifications, the

dissipation function can be written as:

$$\Omega_t(\boldsymbol{x}_t, \boldsymbol{x}_0) = -\frac{\kappa}{2k_BT}\left((\boldsymbol{x}_t - \gamma\boldsymbol{v}_{\mathrm{Opt}}/\kappa)^2 + \frac{\left(\boldsymbol{x}_0 - \boldsymbol{x}_t\mathrm{e}^{-t/\tau_r}\right)^2}{(1-\mathrm{e}^{-2t/\tau_r})}\ldots \right.$$
$$\left. \ldots - (\boldsymbol{x}_0 - \gamma\boldsymbol{v}_{\mathrm{Opt}}/\kappa)^2 - \frac{\left(\boldsymbol{x}_t - \boldsymbol{x}_0\mathrm{e}^{-t/\tau_r}\right)^2}{(1-\mathrm{e}^{-2t/\tau_r})}\right). \tag{6.56}$$

Expanding out the squared terms and factorising where possible before performing a small amount of cancelling and rearrangement yields:

$$\Omega_t(\boldsymbol{x}_t, \boldsymbol{x}_0) = -\frac{\gamma\boldsymbol{v}_{\mathrm{Opt}}}{k_BT}(\boldsymbol{x}_0 - \boldsymbol{x}_t). \tag{6.57}$$

Converting this into an equation for the dissipation function of the COM, which is being driven here, requires changing the $\boldsymbol{x}$ to the modal coordinates in this reference frame, q, but it must also be remembered that the mobility and velocity are different for the case of the modal motion. For the centre-of-mass motion this gives:

$$\Omega_t(q_{1t}, q_{10}) = -\frac{\gamma\sqrt{2}\boldsymbol{v}_{\mathrm{Opt}}}{k_BT(1+\epsilon)}(q_{10} - q_{1t}), \tag{6.58}$$

6.5.2 Trap Translation Calculations

The second method of working upon the system was performed by translating the galvanometer-steerable optical trap relative to the fixed trap and the surrounding fluid. In this way the work performed on the system was only directed at one particle, but would also affect the other particle via the hydrodynamic coupling. The steerable trap was rotated through a given angle, θ,

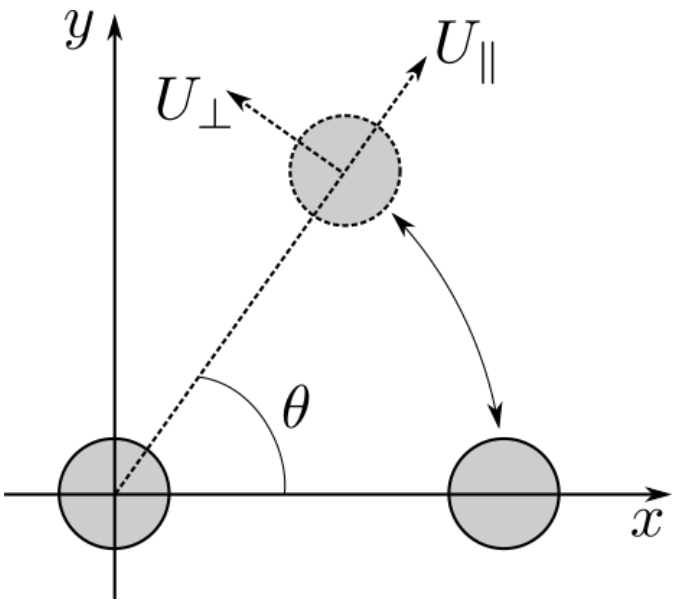

Figure 6.4: A schematic of the rotation of the galvanometer trap about the fixed trap in the trap translation experiment, along with the new rotated coordinate directions.

in an anti-clockwise direction about the fixed trap. The absolute, radial separation of the traps is therefore kept constant, thus simplifying calculations of the mobility matrix. An illustration of this experiment can be seen in Figure 6.4.

To work on the theory behind this experiment and get at the form of the correlation functions and fluctuation theorem, it is helpful to consider a new set of basis vectors, to express the position of the particles, one that rotates with trap 2. These are simply the basis vectors of a polar coordinate system (radial distance and angle), but slightly different labels are adopted here. Coordinates in this system are given by:

$$\begin{pmatrix} U_\parallel \\ U_\perp \end{pmatrix} = \begin{pmatrix} \cos(\theta) & \sin(\theta) \\ -\sin(\theta) & \cos(\theta) \end{pmatrix} \begin{pmatrix} x \\ y \end{pmatrix} = R_\theta \begin{pmatrix} x \\ y \end{pmatrix}, \tag{6.59}$$

where $U_\parallel$ and $U_\perp$ represent the parallel (along a line joining the two traps), and perpendicular (in the direction of increasing θ, perpendicular to $U_\parallel$), coordinates, respectively in the new basis. R_θ is the rotation matrix (see Figure 6.4). The unit

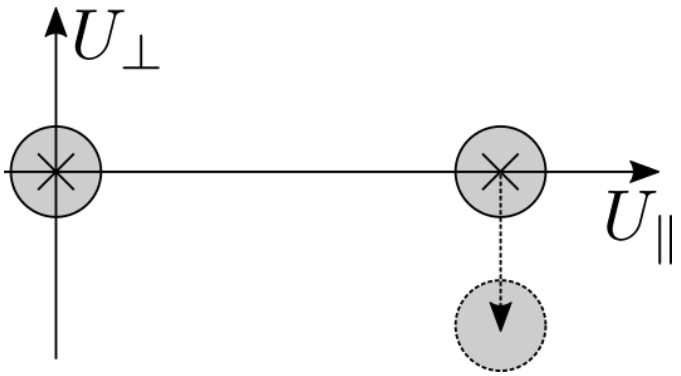

Figure 6.5: A plot of the expected motion of the two optically trapped particles in the new system of basis vectors. Crosses signify the location of the traps.

vectors in the new basis, relative to the old basis of $\begin{pmatrix}\hat{x}\\ \hat{y}\end{pmatrix}$ are therefore given by:

$$\hat{U}_\parallel = \begin{pmatrix}\cos(\theta)\\ \sin(\theta)\end{pmatrix}, \qquad \text{and,} \qquad \hat{U}_\perp = \begin{pmatrix}-\sin(\theta)\\ \cos(\theta)\end{pmatrix}. \tag{6.60}$$

To aid in understanding and visualising the particles' movements in this new basis, it can be used to provide the axes for a 2-D plot (see Figure 6.5). It was expected, since trap 2 moves in an arc of fixed radius about trap 1, that throughout trap 2's rotation $U_\parallel$ would stay constant at a value equal to the initial separation of the particles (barring any Brownian motion of course). The velocity of an object undergoing circular motion is tangential to the line connecting the object to its centre of rotation. This is the direction $U_\perp$. Just as in the fluid drag case it was expected that once there is relative motion of the trap and the surrounding fluid, the particle position will exponentially equilibrate towards a position displaced slightly behind the trap. Assuming this displacement is relatively small, it will be in the opposite direction to the trap's motion, i.e. $-U_\perp$. The $U_\perp$ coordinate of particle 2 can therefore be thought of as the distance behind trap 2 that it lags. Figure 6.5 illustrates these predictions.

In terms of the modal motions in Figure 6.2, this trap translation scenario is not

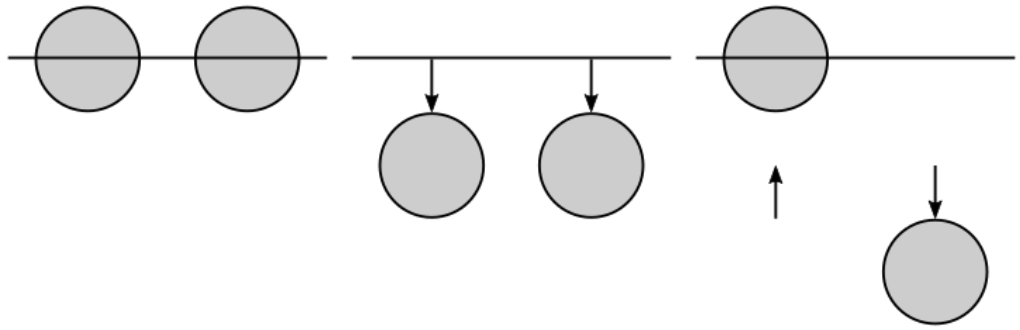

(a) (b) (c)

Figure 6.6: An illustration of two particles on an axis, a), undergoing a COM, b), and relative, c), modal motion in order to achieve the predicted configuration of displacement in the trap translation experiment (as seen in Figure 6.5)

quite as simple as the fluid drag one. In order to achieve the displaced particle 2 position seen in Figure 6.5 there must be a combination of two modal motions, a COM shift and a relative separation increase. These can occur in any order. An example of this is shown in Figure 6.6. This trap translation method of working on the system therefore drives both the COM and breathing modes in this perpendicular direction.

Total Work FT

The total work done method of attempting to verify the FT for coupled particles will again be adopted in this experiment. This method doesn't benefit from any special reference frame and the equations seen previously in Section 6.5.1 all still apply here, although the parallel and perpendicular coordinate system will be used as it makes it simpler to intuit the particles' motions, as has been described above.

A few small modifications to these equations will need to be made for this trap translation experiment. As has been explained, both the centre-of-mass and the relative/breathing modes are being driven in this scenario, so the mobility will

need to be adjusted to account for a combination of these two:

$$\gamma \to \left(\frac{\gamma}{1+\epsilon} + \frac{\gamma}{1-\epsilon} \right) = \frac{2\gamma}{1-\epsilon^2}. \tag{6.61}$$

When the modal FTs are evaluated, care must again be taken to use the correct COM or relative modal trap positions in the calculations. Finally it must be noted that the magnitude of the modal velocity in this experiment is $\boldsymbol{v}_{\text{Opt}}/\sqrt{2}$ - on account of only trap 2 moving through the fluid.

Probability Densities FT

Using the new basis vectors and a new reference frame, it is again possible to formulate a dissipation function that could be used to verify the FT for this experiment, as was seen in Section 6.5.2. Particle 2 is being considered here since this is the particle being worked upon. This will be explained briefly here for completeness.

First consider an equation of motion for the particle in the $\boldsymbol{r}$ coordinate system similar to one seen previously in Equation 6.50:

$$\gamma \dot{\boldsymbol{r}} = -\kappa(\boldsymbol{r} - \boldsymbol{r}_{\text{Trap}}) + \zeta(t), \tag{6.62}$$

where the $\boldsymbol{v}_{\text{Opt}}t$ term has been replaced by $\boldsymbol{r}_{\text{Trap}}$ to indicate the position of the trap because it no longer moves with a constant linear velocity relative to the fluid. If the distance between the traps is: r (a scalar quantity, not to be confused with the bold typeface coordinate position $\binom{x}{y} = \boldsymbol{r}$), then inspection of Figure 6.4 shows that this trap position is given by: $\boldsymbol{r}_{\text{Trap}} = r \begin{pmatrix} \cos(\boldsymbol{\omega}t) \\ \sin(\boldsymbol{\omega}t) \end{pmatrix}$. Here the angular velocity $\boldsymbol{\omega} = \frac{\partial \theta}{\partial t}$ has been introduced to give a similar form (velocity

multiplied by time) to the trap position across both experiments. This could also be written in terms of the new basis vectors, $\boldsymbol{r}_{\text{Trap}} = r\hat{U}_{\parallel}$, as would be expected intuitively.

The velocity of an object undergoing circular motion is given by, $\boldsymbol{v} = r\boldsymbol{\omega}$. This is directed tangentially to the object's position vector along the circle of motion, in the direction of increasing θ. From Figure 6.4 it can be seen therefore that this velocity could also be written simply in terms of the new basis vectors: $\boldsymbol{v}_{\text{Opt}} = v\begin{pmatrix} -\sin(\theta) \\ \cos(\theta) \end{pmatrix} = v\hat{U}_{\perp}$, where the non-bold, v, is the speed of the motion.

Now a new reference frame, $\boldsymbol{y}$, for the particle's motion will be introduced. The origin of this frame will be fixed at trap 1's static location and it will rotate with constant angular velocity $\boldsymbol{\omega}$, mimicking the motion of trap 2. Additionally it will be displaced backwards from trap 2's angle by $\gamma\boldsymbol{v}_{\text{Opt}}/\kappa$. This is the same approach that was utilised for frame $\boldsymbol{x}$ in Section 6.5.1. This frame moves with the trap but lags behind such that it follows the position of a particle in dynamic equilibrium rather than the position of the trap exactly. Combining the particle position and velocity that were found earlier, an equation for this translation between the frames can be written:

$$\begin{aligned} \boldsymbol{r} &= \boldsymbol{y} + \boldsymbol{r}_{\text{Trap}} - \frac{\gamma}{\kappa}\boldsymbol{v}_{\text{Opt}} \\ &= \boldsymbol{y} + r\hat{U}_{\parallel} - \frac{\gamma}{\kappa}v\hat{U}_{\perp}. \end{aligned} \tag{6.63}$$

In order to find the equation of motion of the particle in this reference frame it is necessary to find the time derivative of this expression. Since the basis vectors of the $\boldsymbol{U}$ basis are time dependent, unlike Cartesian unit vectors, they change under

differentiation with respect to time according to:

$$\frac{\partial \hat{U}_{\parallel}}{\partial t} = \frac{\partial}{\partial t}\begin{pmatrix}\cos(\boldsymbol{\omega} t)\\ \sin(\boldsymbol{\omega} t)\end{pmatrix} = \boldsymbol{\omega}\begin{pmatrix}-\sin(\boldsymbol{\omega} t)\\ \cos(\boldsymbol{\omega} t)\end{pmatrix} = \boldsymbol{\omega}\hat{U}_{\perp}, \tag{6.64}$$

and similarly,

$$\frac{\partial \hat{U}_{\perp}}{\partial t} = -\boldsymbol{\omega}\hat{U}_{\parallel}. \tag{6.65}$$

The derivative of Equation 6.63 therefore becomes:

$$\dot{\boldsymbol{r}} = \dot{\boldsymbol{y}} + v\hat{U}_{\perp} + \frac{\gamma}{\kappa} v\boldsymbol{\omega}\hat{U}_{\parallel}. \tag{6.66}$$

Substituting $\boldsymbol{r}$ and $\dot{\boldsymbol{r}}$ from Equations 6.63 and 6.66 back into Equation 6.62 and remembering the form of $\boldsymbol{r}_{\text{Trap}}$ yields:

$$\begin{aligned}\gamma\left(\dot{\boldsymbol{y}} + v\hat{U}_{\perp} + \frac{\gamma}{\kappa} v\boldsymbol{\omega}\hat{U}_{\parallel}\right) &= -\kappa\left(\boldsymbol{y} + r\hat{U}_{\parallel} - \frac{\gamma}{\kappa} v\hat{U}_{\perp} - r\hat{U}_{\parallel}\right)\\ \Rightarrow \gamma\dot{\boldsymbol{y}} &= -\kappa\boldsymbol{y} - \frac{\gamma^2}{\kappa} v\boldsymbol{\omega}\hat{U}_{\parallel} + \zeta(t).\end{aligned} \tag{6.67}$$

This is very nearly a simple inertia-less Langevin equation as was seen for $\boldsymbol{x}$ in Equation 6.51. However there is an additional $\frac{\gamma^2}{\kappa} v\boldsymbol{\omega}\hat{U}_{\parallel}$ term on the right hand side. This term only acts in the parallel coordinate direction. It would therefore be possible to write an equation of motion in exactly the form of the Langevin equation if it were written for only the perpendicular coordinate (the direction that displacement from the trap was predicted for), however inspection of the relative size of this term compared to the term for the restoring force of the trap

can show that this short-cut is unnecessary. Let the particle displacement from the trap, trapping strength, particle size and particle separation all be set to the order of 10^{-6}. The previous Kaptiza experiment gave the insight that relative speeds of the trap compared to the fluid of greater than approximately 5×10^{-6} μms^{-1} would cause the particle to be lost from the weak traps. Taking this as a maximum value then yields a maximum angular velocity on the order of approximately 5 rads^{-1}. Using these values (which are for the most part generously skewed towards increasing the size of this extra term within the realms of experimental possibility) gives the following values: $\kappa \boldsymbol{y} \approx 10^{-12}$, and $\frac{\gamma^2}{\kappa} v\boldsymbol{\omega} \approx 10^{-15}$. This is three orders of magnitude difference. It therefore seems reasonable to discard this term as it will have a much smaller, to the point of being negligible, effect upon the parallel coordinate than the restoring force and noise terms. Making this change gives a final form of:

$$\gamma \dot{\boldsymbol{y}} = -\kappa \boldsymbol{y} + \zeta(t), \tag{6.68}$$

which shows the particle in this new reference frame following a simple inertia-less Langevin equation of motion. Since this is an equation of the same form as the one for the $\boldsymbol{x}$ coordinate frame seen previously (Equation 6.51), it is possible to follow the same analytical path as in Section 6.5.1 to get to a dissipation function for the coordinates of particle 2 in this frame:

$$\Omega_t(\boldsymbol{y}_t, \boldsymbol{y}_0) = -\frac{\gamma \boldsymbol{v}_{\mathrm{Opt}}}{k_B T}(\boldsymbol{y}_0 - \boldsymbol{y}_t). \tag{6.69}$$

This is just a dissipation function for a particle moving in an arc. In this experiment there are two particles. The other, particle 1, sits at trap 2's centre of rotation and its trap does not translate. To get the modal dissipation functions

for the motion of the two particles the changes to the mobility and velocity for the cases of the COM and relative modes must be utilised, giving:

$$\Omega_t(q_{1t}, q_{10}) = -\frac{\gamma \boldsymbol{v}_{\mathrm{Opt}}}{\sqrt{2}k_B T(1+\epsilon)}(q_{10} - q_{1t}), \tag{6.70}$$

for the centre-of-mass motion, and:

$$\Omega_t(q_{2t}, q_{20}) = -\frac{\gamma \boldsymbol{v}_{\mathrm{Opt}}}{\sqrt{2}k_B T(1-\epsilon)}(q_{20} - q_{2t}), \tag{6.71}$$

for the relative motion.

6.6 Simulations

As in Chapter 3, simulations of particles residing within Brownian traps have been carried out in order to verify and complement these analytical results. These have again been done in the style of the finite difference equations discussed in Volpe and Volpe [86], and with parameters (such as particle size and trap strength) having values consistent with those achievable in the experimental set-up. As such, the information contained within Section 3.4 on how the simulations were carried out is still relevant here. Any important new detail will be stated.

This simulation section and the following experimental sections will contain many graphs with data relating to these two particles and the modes of their motion. A convention/key will be described here for the data within these graphs, such that the significance of colours and marker shapes need not be restated many times over. First let the distinction be made between non-modal, and modal graphs. Non-modal graphs will contain data based on the individual

particle positions, rather than their modes of motion. This data may be a position in any coordinate system (x, y / $U_\perp, U_\parallel$ / r, θ), or it may be auto-correlations and cross-correlations. Modal graphs will show similar quantities in similar coordinate systems, but for the modal motions of the two particles. The following colour and/or shape combinations will be used throughout the remainder of this chapter.

Non-modal plots: Light blue will correspond to particle 1. Circles will be used for this data when a marker shape is required. Grey will signify particle 2, with the corresponding marker shape being crosses. Light magenta will be used for quantities based on both particles (cross-correlations) and the corresponding shape will be diamonds. Where exponential fits are plotted alongside the data for comparison these are in the same colour as the data they correspond to, but are a darker/bolder shade (e.g. dark blue, black, or dark magenta).

Modal plots: These follow the same colour and shape scheme as the non-modal plots (since they never appear on the same axis), but here blue will correspond to the centre-of-mass motion, grey/black to the relative or breathing modal motion, and magenta will correspond to the cross-correlation of the two. Fits will again be in darker shades of the same base colours.

Finally, in some plots the angle of trap 2, or positions of the microscope stage will be shown alongside particle position. When featured these will be in orange.

6.6.1 Fixed Traps Simulations

The first simulated scenario explored involved two particles being held fixed in their respective traps with no other external work being performed on the system. This is therefore a simulation of the experiments carried out by Meiners and Quake [179]. Attempting this scenario first enabled a direct comparison of the

results with those already published, and so gave the opportunity to verify that the simulations were working as expected in this simple arrangement before any extra work was introduced to the system. Finite difference forms of the coupled equations 6.18 and 6.19 were used to perform the simulations. For example:

$$\boldsymbol{r}_{1,t} = \boldsymbol{r}_{1,t-1} + \boldsymbol{H}_{11}\left(\boldsymbol{F}_{\mathrm{Opt},1,t-1} + \sqrt{\frac{2k_{\mathrm{B}}T\gamma}{\Delta t}}\zeta_{1,t}\right)\Delta t + \boldsymbol{H}_{12}\boldsymbol{F}_{\mathrm{Opt},2,t-1}\Delta t, \qquad (6.72)$$

where $\boldsymbol{F}_{\mathrm{Opt},1}$ represents the optical confining force from trap 1 and is derived from a circularly symmetric potential that has a Gaussian intensity profile, decreasing with distance from the trap. The correlation results for the longitudinal (x-direction) motion of the particles in this simulation can be seen in Figure 6.7. These simulations were carried out with a particle separation of 3 μm in the x direction, and trap stiffnesses of 0.5 pNμm^{-1}.

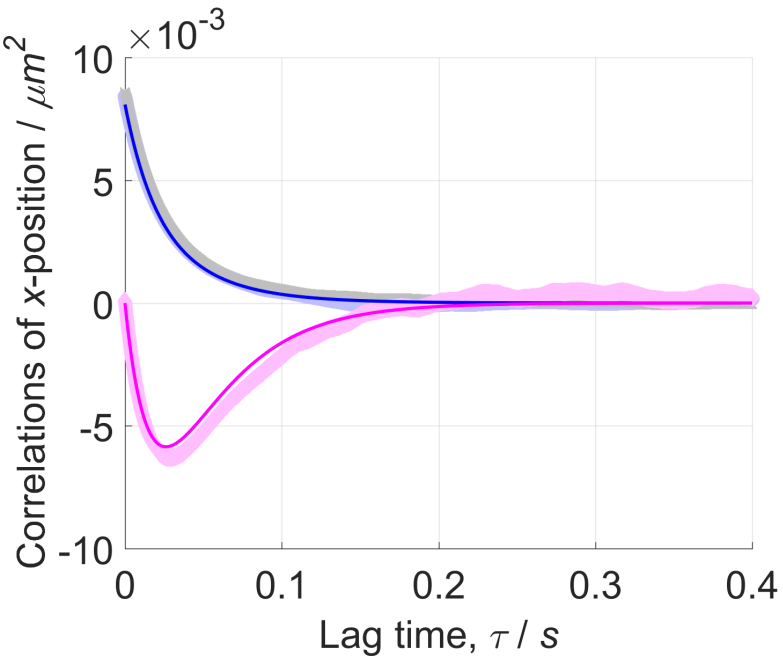

Figure 6.7: Correlation functions of the positions of two optically trapped beads in a Brownian simulation. To facilitate easier viewing via the same, single y-axis, the cross-correlations have been multiplied by five.

The results seen in this correlation plot are in line with the expectations of this simulation. They show that the auto-correlation functions for these particles' positions decay towards zero with good agreement with a predicted theoretical line plotted according to the additive double exponential expression derived earlier (Equation 6.38). There is a dip in the cross-correlation, indicating an anti-correlation of the particles' positions at approximately 50 ms, which again agrees with the predicted theoretical line plotted (Equation 6.40). These results echo and show good agreement with the form of those presented by Meiners and Quake (see Figure 6.3). All of the above strongly suggested that the simulation was performing as expected and that the two particles were indeed behaving in a fashion consistent with them being hydrodynamically coupled.

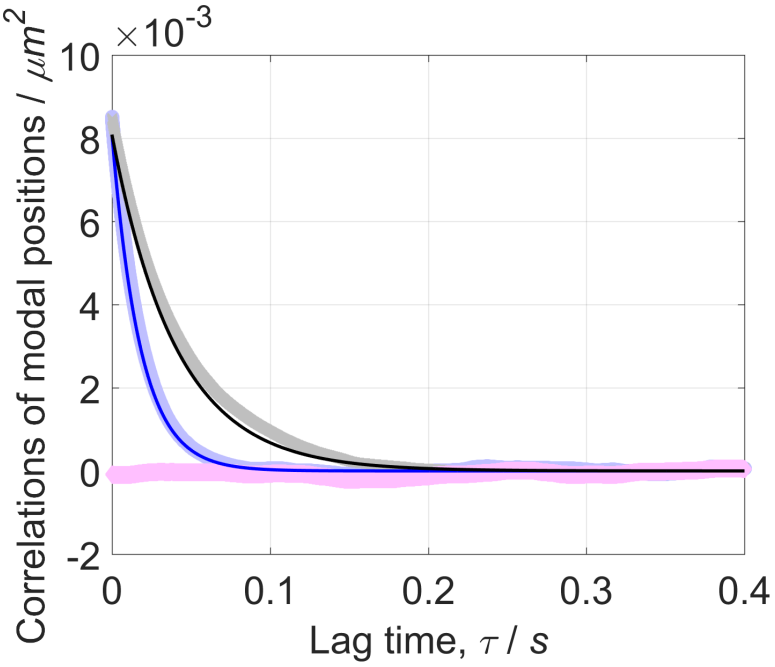

Figure 6.8: Correlation functions of the modal positions of two optically trapped beads in a fixed traps Brownian simulation.

The centre of mass and breathing mode motions were obtained from these individual particle coordinates using Equations 6.20 and 6.21. The correlations of these modal coordinates were also found and are plotted in Figure 6.8. This plot shows the differing exponential time scales at which the modal motions decay.

Auto-correlations of the centre-of-mass motion decay faster than those of the breathing mode. The difference in these time scales arises from the $(1 \pm \epsilon)$ factors in the mobilities of each of the modes, and physically from the time required to move fluid between the particles. Both of the modal auto-correlations agree very well with their respective theoretical predictions (found via Equations 6.33 and 6.33). The cross-correlation of these two modes is seen to stay at zero throughout, which is as expected since they are normal modes of the system.

This modal correlation plot is useful in understanding the correlations seen in Figure 6.7 for the individual coordinates of the hydrodynamically coupled particles. The particle auto-correlations behave as per Equation 6.38. The form of this decay is the sum of two exponentials, which are the exponentials seen for the centre-of-mass and relative correlations in Figure 6.8. Similarly the particle cross-correlations decay form is given by the difference between these two modal decay exponentials in Figure 6.8. Visual inspection of the two plots in this section can quickly confirm this is the case for the forms of these curves.

6.6.2 Fluid Drag Simulations

After confirming the validity of the static simulations, these were then modified to account for the first method of doing work on the two particle system. These simulations worked in much the same way as those seen previously for the static traps, but an additional term was added to the iterative step of the simulations, $\boldsymbol{v}_{\mathrm{Opt}}\Delta t$, in order to account for the displacement produced by the force on each of the particles from the motion of the stage and the ensuing fluid drag. The particle separation in these simulations was maintained at 3 μm, and the weak strength of the traps was kept at 0.5 pNμm^{-1} in order to exaggerate the dragging effect of the stage movement. The stage velocity was chosen to be 5 μms^{-1} such

that the weakly trapped particles were not lost from the traps due to this being too large. The stage begins moving at zero seconds and continues at this speed for 2.5 seconds, after which the simulation cycle ends. One hundred runs of this simulation cycle were undertaken for both parallel and perpendicular driving directions. Representative results of these simulations are presented in this section.

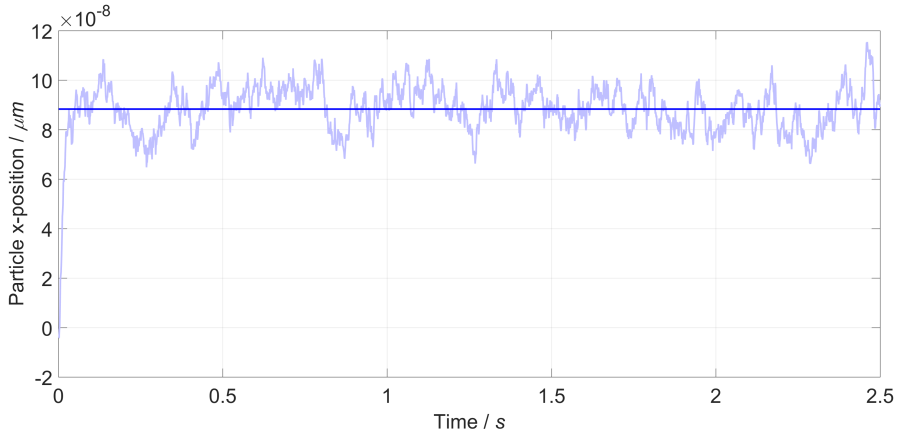

(a)

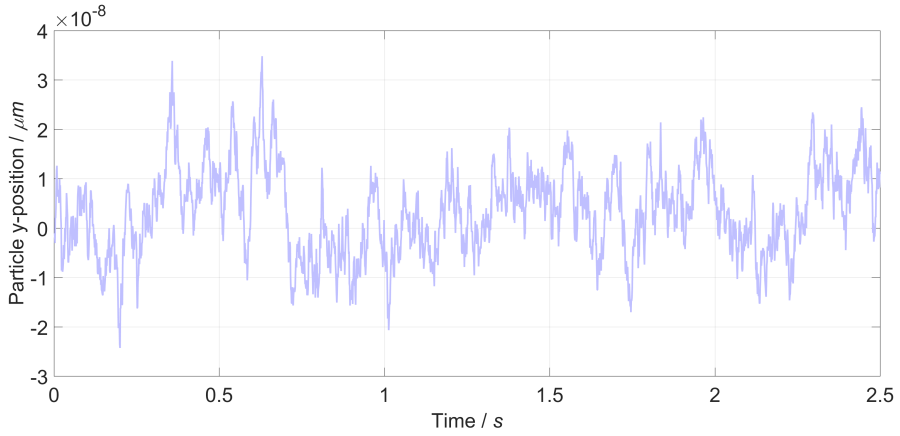

(b)

Figure 6.9: The averaged x and y displacements of particle 1 from its trap in the case of parallel stage driving are shown in a) and b) respectively. For the x displacement, a predicted line for the dynamic equilibrium position is also shown.

Figure 6.9 shows the averaged (over the 100 cycles) x and y position displacements of particle 1 from its trap in the cases of parallel stage driving (N.B. Only particle 1's and the parallel driving simulation's results are plotted in

this section as the motion for particle 2, and for the perpendicular driving simulation both show very similar forms and equally good levels of agreement to theoretical predictions). Figure 6.9a also features a solid line indicating the predicted equilibrium position of the particle away from the trap, given by $\gamma \boldsymbol{v}_{\mathrm{Opt}}/(1+\epsilon)\kappa$. These results show the particle behaving as would intuitively be expected, and in line with theoretical predictions. That is, the particle is displaced from the trap in the direction of stage driving and exponentially arrives at a predicted equilibrium plateau displacement value at which it remains thereafter. In the direction perpendicular to driving (Figure 6.9b), the particle remains at its initial coordinate and simply exhibits Brownian motion here for the duration of the simulation.

The x and y positions from these simulations were converted into modal coordinates. The averages of the centre-of-mass and breathing modes in the x direction for parallel driving are shown in Figure 6.10. The centre-of-mass motion evolves exponentially until it arrives at a plateau value away from the trap, just as was seen for the individual particle coordinates in Figure 6.9. This exponential curve agrees very well with the predicted theoretical line shown. The form of the equation used to generate this line was:

$$a(1-\exp(-t/b))+c. \tag{6.73}$$

The first variable, a, dictates the plateau value and was given by, $a = \sqrt{2}\gamma \boldsymbol{v}_{\mathrm{Opt}}/(1+\epsilon)\kappa$, corresponding to the predicted lag distance of the particle behind the trap, with an extra $\sqrt{2}$ factor added due to both particles experiencing equal displacement (Equation 6.20). The second variable corresponds to how quickly the exponential curve levels off and was given by, $b = \gamma/(\kappa(1+\epsilon))$, the relaxation time of the centre-of-mass motion. The final

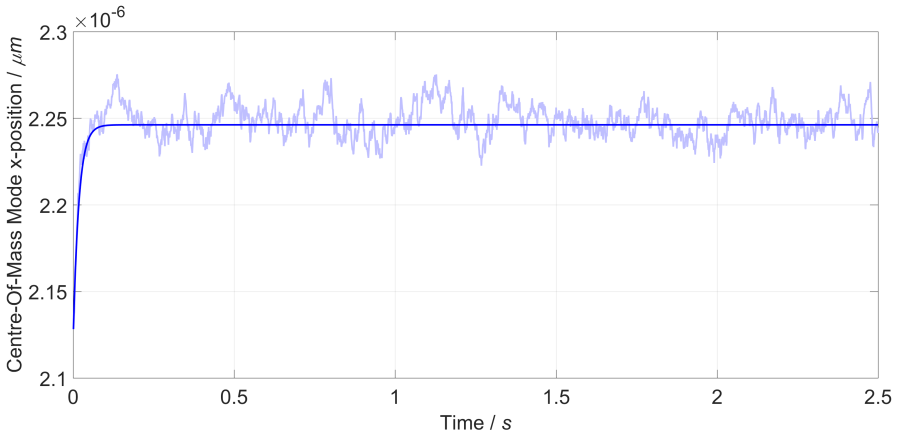

(a)

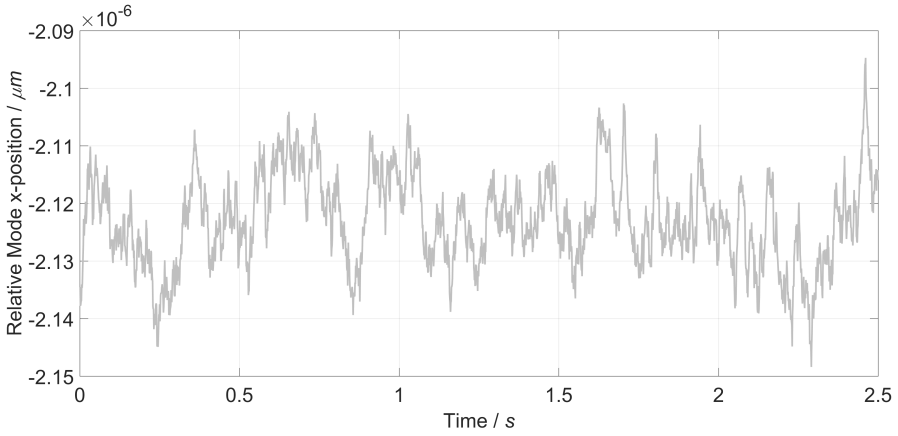

(b)

Figure 6.10: The averaged centre-of-mass mode and breathing mode motions, a) and b) respectively, of the particles in the x direction for the case of parallel stage driving. a) Also features a predicted exponential line for this modal motion.

variable, c, shifts the position of the curve such that it starts at the right position, it is given by the initial COM coordinate of the two traps. The relative motion also behaves as expected, in that it simply fluctuates around its initial value (both particles displace at once so work is only done upon the centre-of-mass mode and the relative mode remains unchanged). N.B. The y coordinates are not plotted here as parallel (x) driving is the case being considered, so these would change only due to Brownian motion and thus are not the coordinate of most interest.

Correlation plots for the individual particles and their modal motions in these

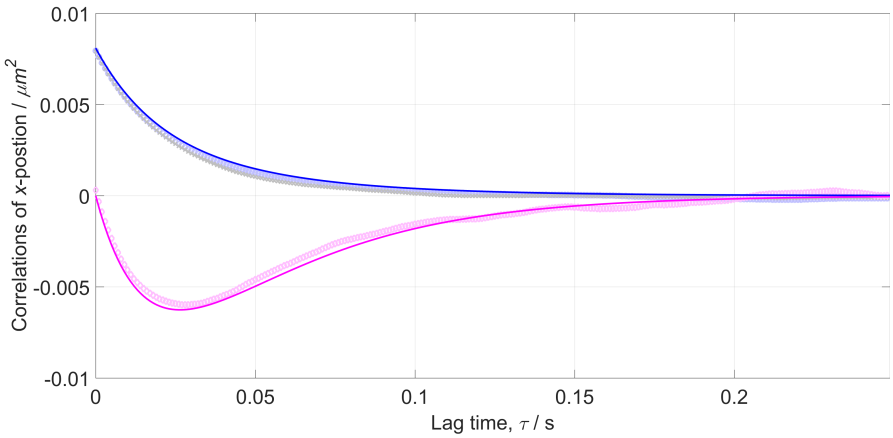

(a)

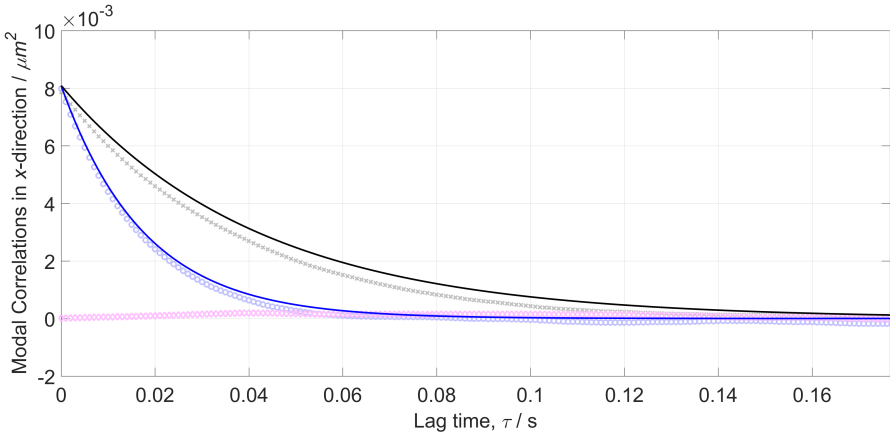

(b)

Figure 6.11: Position and modal correlations, a) and b) respectively, in the x-direction for the case of parallel stage driving, complete with predicted curves. The cross-correlation data in a) has been multiplied by 5 to make it more clearly visible upon the same plot as the auto-correlations.

simulations were calculated and can be seen in Figure 6.11. Figure 6.11a shows the individual particle correlations. The auto-correlations of each particle decay exponentially towards 0, showing that over long times their position is not self-correlated. The cross-correlation data for the two particles shows a pronounced dip, an anti-correlation, early on as it falls from zero at approximately 0.035 seconds, before then rising again to indicate no long-term cross-correlation. All of these correlations agree well with the form of the predicted lines, which are given by the equations at the end of Section 6.1.2.

Figure 6.11b shows the modal motion correlations, and that these behave generally in agreement with the theoretical predictions. The auto-correlations both decay exponentially towards 0. They do so at different rates, with the centre-of-mass motion being the faster decay of the two. The difference between these decay rates arises from the $(1 \pm \epsilon)$ terms in the form of the correlations seen in Equations 6.33 and 6.34. The cross-correlation of the two modal coordinates is seen to remain at zero throughout, as per expectations mentioned earlier in Section 6.6.1 since these are normal modes of the system.

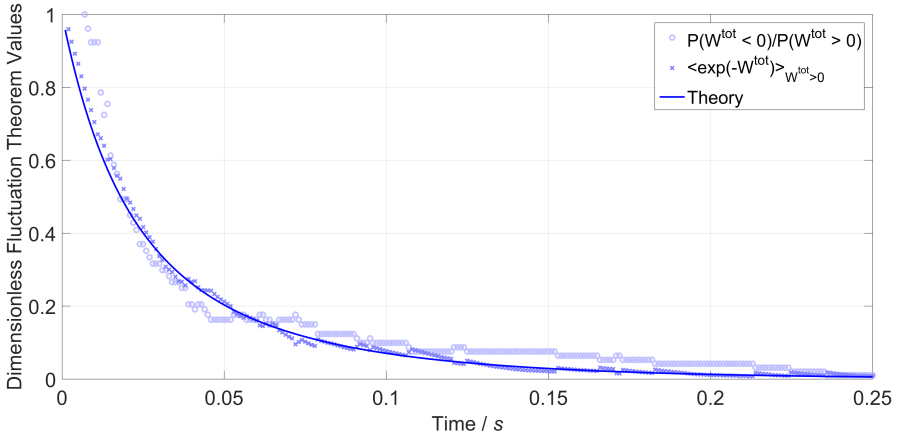

(a)

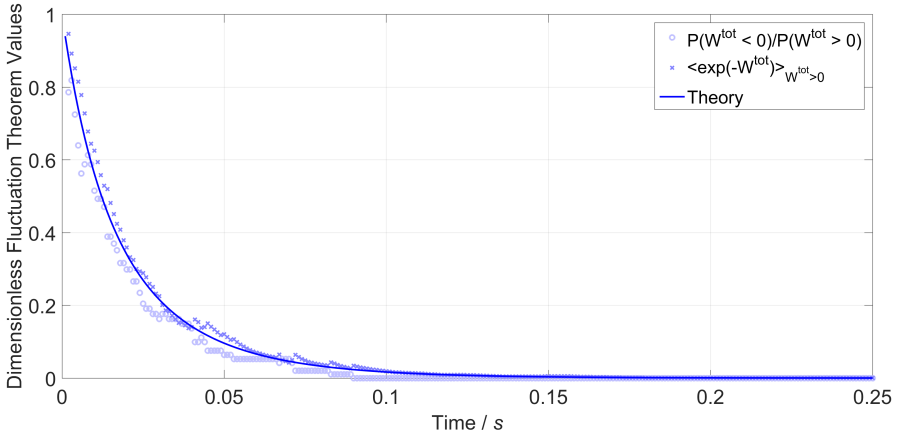

(b)

Figure 6.12: Position and modal integrated FTs, a) and b) respectively, in the x-direction for the case of parallel stage driving, complete with predicted curves. Circles and crosses denote the left and right hand sides respectively of Equation 6.46, the solid lines represent the theoretical prediction from Equation 6.47.

Finally the integrated total work fluctuation theorems, and predicted theoretical

values were calculated for these fluid drag simulations in accordance with the formulae in Section 6.5.1. These are presented in Figure 6.12. Figure 6.12a shows the total work IFT for particle 1 in the x direction during parallel stage driving. The derived quantities from the simulated experiment, the left and right hand sides of the IFT (the ratio of the probabilities of positive and negative dissipation functions, and the ensemble average of the exponentials of the positive trajectories respectively), behave as expected. That is, they decay to zero with increasing simulation time/trajectory length, and show reasonable agreement with the theoretically predicted curve (Equation 6.47). Figure 6.12b shows the same total work IFT for the COM motion of the particles in the parallel fluid drag simulation. Relative motion is not shown since this is not being driven in this experiment. In this plot it is again seen that the derived IFTs from the simulated data decay to zero over long times, showing the expected behaviour and agreeing well with the predicted curve, found from the same theoretical equation but modified in ways previously described to account for the modal mobility and velocity. Comparison of the two plots shows that the fluctuations for the COM motion die out and reach zero first, this is to be expected given the greater modal velocity, which becomes a factor in Equation 6.48.

It is noteworthy for both of the FT plots, and the modal correlations plot, that whilst the general forms of the data behave as theoretically predicted, the exact values often differ slightly from the predictions. A few contributing factors are suspected as the cause of this. The first two are the time interval between points in the simulations, and the number of repeats performed. In order to avoid prohibitively long computing times in the preliminary investigations presented in this chapter, the simulation time interval was set at 1 ms. The centre-of-mass motion relaxation time in the parallel direction is approximately 18 ms. Even with the 100 simulation cycles that were performed, this does not correspond to

an especially large data set for the pre-relaxation time motion of the particles. In the literature, simulations of the single particle fluid drag experiment have been done as many as 500,000 times, which would obviously yield much better statistics [174]. In addition to this there is a consideration of the relative sizes of the fluctuations, $\sqrt{k_B T/\kappa}$, and the driving movement, $\gamma \boldsymbol{v}_{\mathrm{Opt}}/(1+\epsilon)\kappa$, that should be taken into account. For the parameter values used in these simulations, the two quantities are approximately equal. Therefore, whilst the particle will move in the expected direction to the predicted equilibrium spot because the driving movement always acts in this direction unlike the Brownian motion, there will be significant fluctuations upon approach to, and around this position. The relative size of the fluctuations may very probably be the reason for some of the discrepancies seen in the the above plots. It is therefore the expectation of the author, based upon viewing the improvement in the agreement between the averages and the predicted lines as more and more repeat cycles are included, that having a larger number of repeats, smaller time intervals, and a greater stage driving speed would improve the fit of the data to the predictions in these plots and shrink the discrepancies. This issue likely did not arise for the fixed trap simulations because these used a much smaller time interval, $dt = 5 \times 10^{-5}$ s, since there was no issue of completing a certain amount of stage or trap motion, and so a shorter total simulation time was needed.

6.6.3 Trap Translation Simulations

After completing simulations for these first two scenarios, an attempt at simulating the case of a translating second trap (as discussed in Section 6.5.2) was made. This was done with a very simple modification to the simulations of the two static traps. It involved simply changing trap 2's position coordinates in the Matlab code to an array of values corresponding to the cosine and sine of

some increasing angle about the origin/trap 1, rather than just a single fixed value. After this change, the rest of the simulation could be run in the same way as before.

The trap separation was once more maintained at 3 μm. The strength of the traps was kept at 0.5 pNμm^{-1} (as in the fluid drag simulations) such that any displacement away from these weak traps would be more obvious. In the simulations trap 2 begins moving at zero seconds and translates through $\pi/2$ rads. Its initial position lies along the positive x axis (where the origin of the axes is the location of trap 1). From here it moves to a final position on the positive y axis in 2 seconds. Thus the trap moves with an angular velocity of ≈ 0.785 rads^{-1}, or a tangential linear velocity of ≈ 2.36 μms^{-1}. One hundred runs of this simulation cycle were completed and the outcomes were averaged. Results from these simulations are presented in this section.

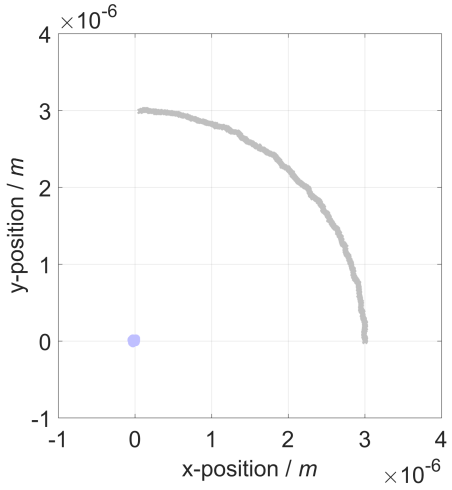

Figure 6.13: A plot of the position data of the two optically trapped particles in the translating trap Brownian simulation.

Figure 6.13 is an x-y plot of the position data of the two particles in this simulation. This served as a quick and simple check that the changes made to the simulation to move the location of trap 2 worked as expected. Particle 2 clearly traces out an arc of $\pi/2$rad about the origin (trap 1 location). Other than

small noisy motions due to Brownian motion, which both particles exhibit, particle 1 remains static at the origin within its trap.

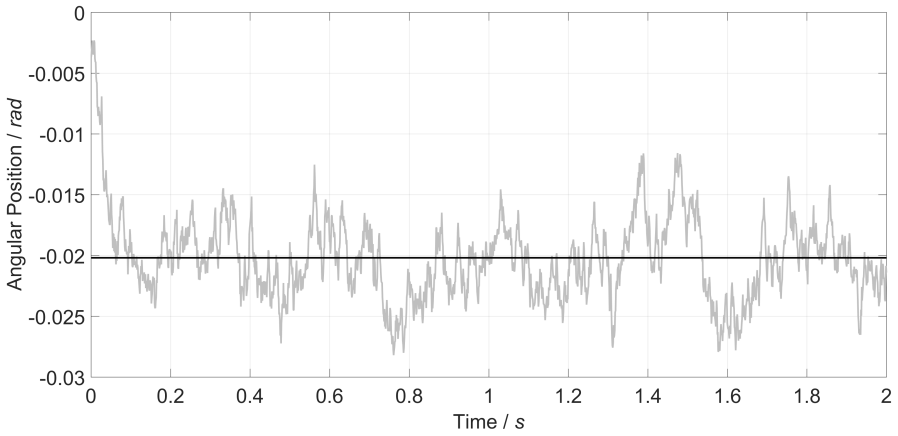

Figure 6.14: The angle of particle 2 relative to trap 2 in the translating trap simulations, featuring a predicted line for the equilibrium displacement angle of the particle from the trap.

The raw x and y positions of the translating trap and particle 2 were used to find their angular coordinates about trap 1. The angle of particle 2 relative to trap 2 was found by subtracting these from each other, and this is plotted in Figure 6.14. The angular difference between these two quickly exponentially decreases to some negative plateau value, indicating that the particle starts at the same angle as the trap (on the x axis) but very quickly begins to lag behind it until it reaches some equilibrium displacement value. This displacement agrees with the predicted line shown on the graph. The value of this line is given by $\gamma\boldsymbol{\omega}/(1-\epsilon^2)\kappa$, in a similar way to how the predicted linear displacement of the particle was found in the earlier fluid drag simulations.

As discussed in the theoretical calculations in Section 6.5.2, knowledge of the angular position of trap 2 allows for the rotation of the coordinate system to give the new basis vectors $\hat{U}_{\parallel}$ and $\hat{U}_{\perp}$ and the particle coordinates in this new system. This conversion was performed for the simulated data and the resulting parallel and perpendicular positions of particle 2 are shown in Figure 6.15. Figure 6.15a

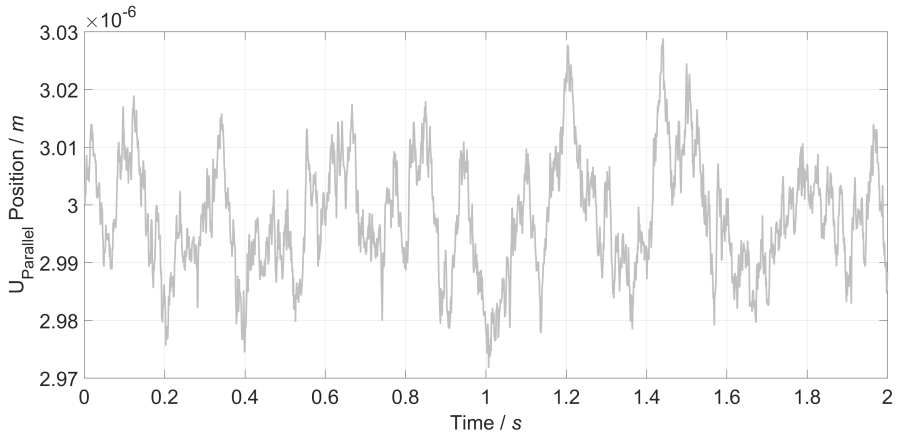

(a)

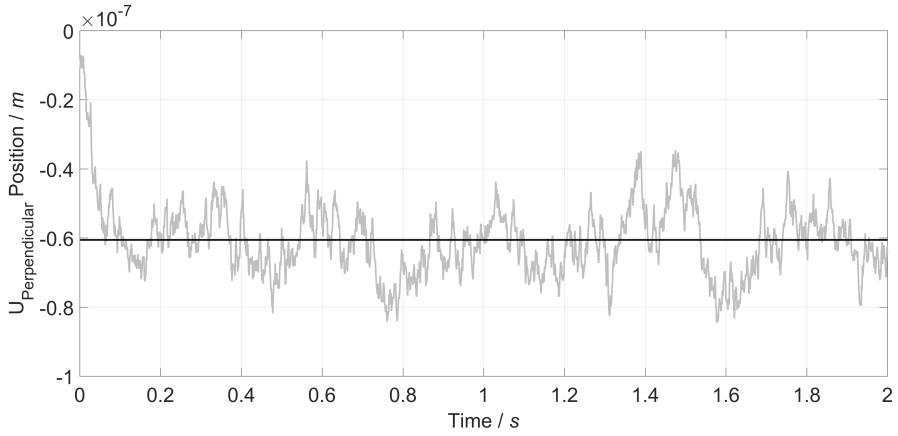

(b)

Figure 6.15: The parallel, $U_{\parallel}$, and perpendicular, $U_{\perp}$, coordinates, a) and b) respectively, of particle 2 against time in the trap translation simulation. b) Also features a line for the predicted equilibrium displacement of particle 2.

shows the $U_{\parallel}$ coordinate of particle 2 against time. This maintains a value of 3 μm (with Brownian motion) during the trap translation, as would be expected since the radial separation of the two traps is kept constant throughout. Figure 6.15b shows the $U_{\perp}$ coordinate of particle 2 against time. This reinforces the result of the angular displacement of particle 2 from its trap seen in Figure 6.14. In this coordinate direction, the particle's position undergoes an exponential decay to an equilibrium plateau value. This value agrees well with the theoretical prediction of $\gamma r\boldsymbol{\omega}/(1-\epsilon^2)\kappa$, the linear/tangential lag of the particle behind the trap.

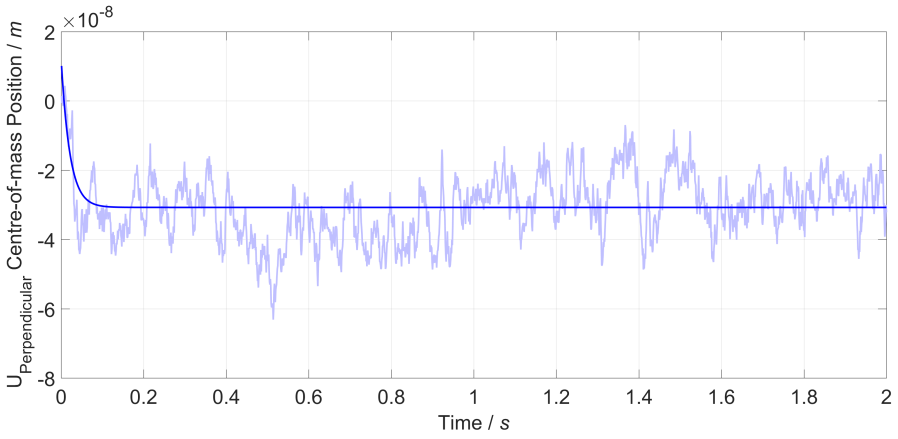

(a)

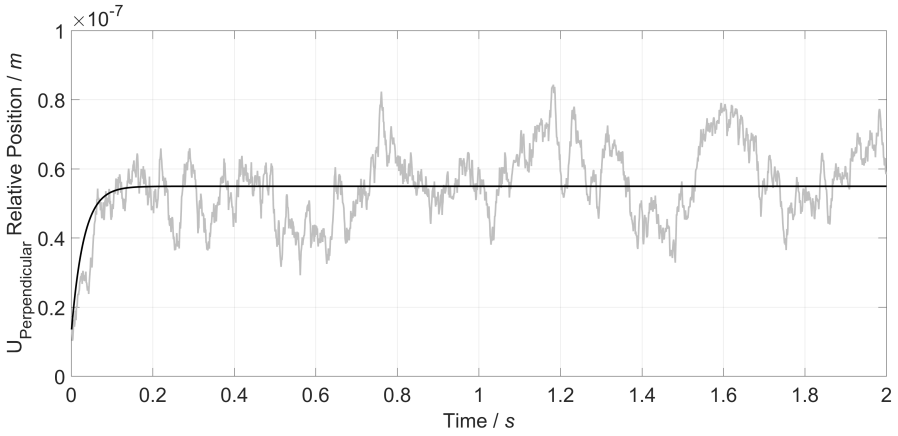

(b)

Figure 6.16: The perpendicular centre-of-mass and relative modal coordinates, a) and b) respectively, for the translating trap simulation, featuring predicted exponential curves.

Furthermore, modal coordinates (both centre-of-mass and relative) for the particles in both the parallel and perpendicular directions to trap motion were calculated. These are shown in Figure 6.16 for the perpendicular direction. The parallel direction is not plotted since these stay approximately constant, exhibiting only Brownian motion about their initial values, as would be expected. Figure 6.16a shows the centre-of-mass motion for the perpendicular direction. This decreases exponentially to a plateau value. This shift towards the negative was in line with intuitive expectations, and can be very easily justified and understood by inspection of Figure 6.5. This motion also shows very good agreement with a plotted theoretical prediction. The predictions for both of

these modal plots followed the form already seen for a previous exponential prediction line in Equation 6.73, with the obvious changes made to correspond to the relaxation time of the modal motions in question and the decreased modal displacements in this experiment owing to only one of the two particles translating, as has been discussed previosly. The relative motion, in Figure 6.16b, in this direction is seen to shift exponentially towards a plateau in the positive direction. A change in the relative motion coordinate was expected as this method of working upon the system drives both the breathing and the centre-of-mass modes. This specific change of the shift towards positive rather than negative values is because this relative motion is calculated as: $\frac{1}{\sqrt{2}}(p_1 - p_2)$. So as particle 2 shifts towards the negative, this quantity and the position of particle 1 relative to particle 2 shifts into the positive. This plot also shows very good agreement with the theoretically predicted line.

Once these modal coordinates were obtained, their correlations could then be calculated. These are plotted in Figure 6.17, along with the correlations of the individual particles' $U_\perp$ coordinates. Figure 6.17a shows the individual particle position correlations for the perpendicular coordinate direction. The two auto-correlation data sets in this plot show the expected shape, an exponential decay to zero starting from some initial positive correlation. They agree well with the predicted line added to the plot, the form of which originates from Equation 6.38. The cross-correlation of the two particles' positions exhibits the expected general shape. That is, it has a pronounced dip, or anti-correlation, at the relaxation time of the motion $\tau_r = \gamma/\kappa = 0.0249$ s, before rising again back up to approximately zero. It does however exhibit noticeable, albeit relatively small compared to the size of the anti-correlation dip, fluctuations about zero after this. Although the general shape is as expected, this data does differ in amplitude from the predicted line during the anti-correlation dip (found from

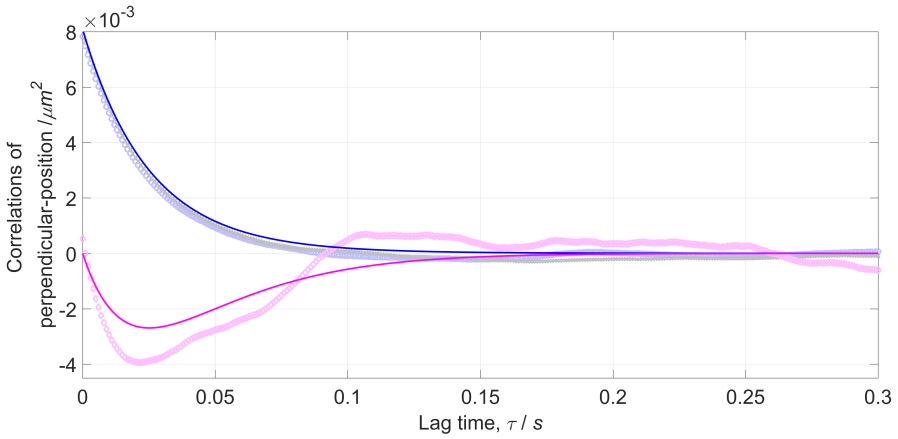

(a)

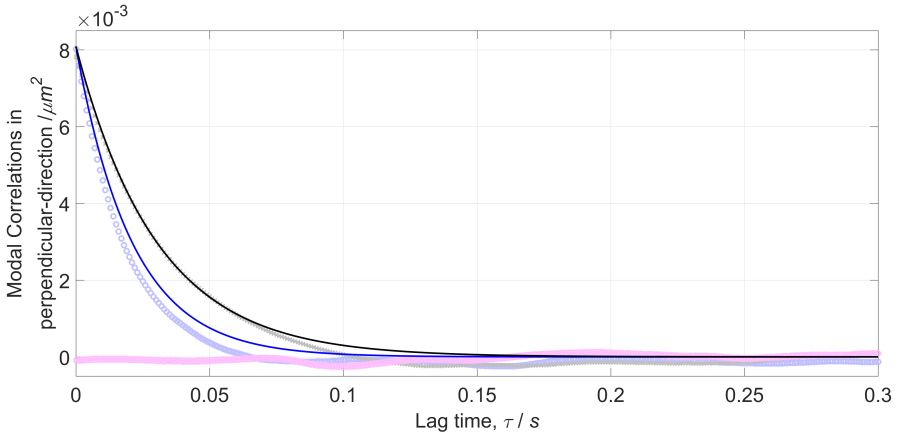

(b)

Figure 6.17: Individual particle position, a), and modal position, b), correlation plots in the $U_\perp$ direction for the trap translation simulations. The cross-correlation data in a) has been multiplied by 5 for ease of viewing on the same axes.

Equation 6.40).

The modal auto-correlations seen in Figure 6.17b agree with the form of predicted lines (found from Equations 6.33 and 6.34), showing an exponential decay towards zero that is faster for the case of the centre-of-mass motion than it is for the relative motion. Whilst these exhibit generally stronger agreement than the individual particle cross correlations, they do still unfortunately show some discrepancy when compared to the exact values of the predictions. The cross-correlation, as expected, remains at zero throughout since these are normal modes of the system.

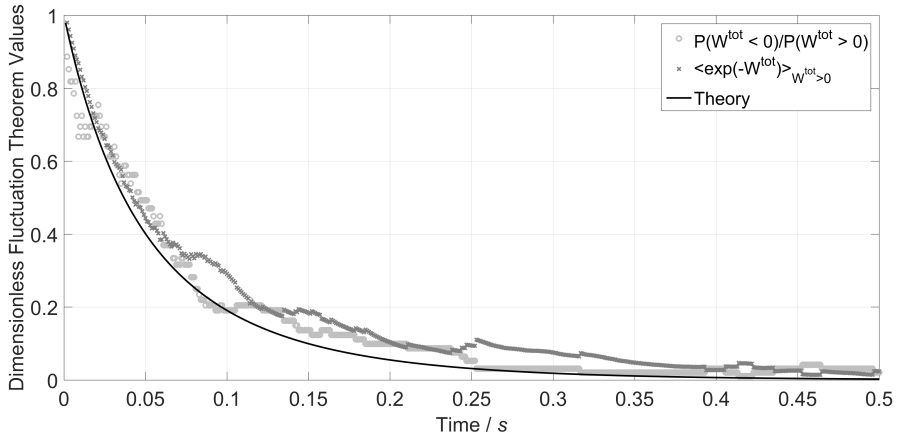

(a)

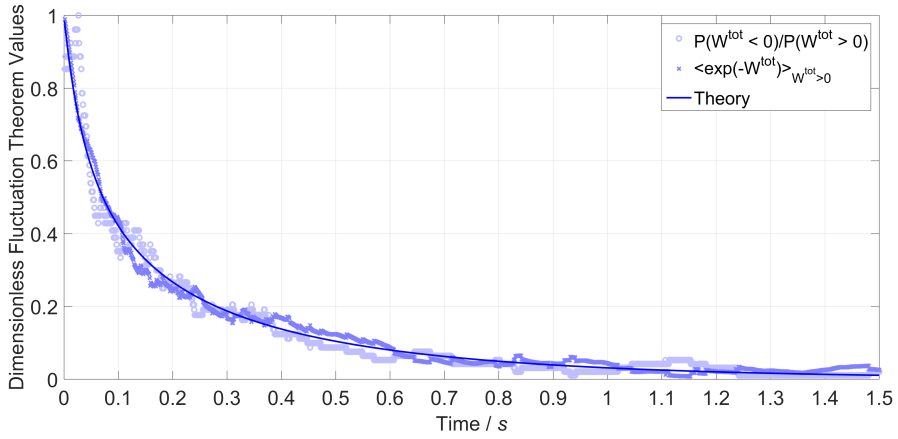

(b)

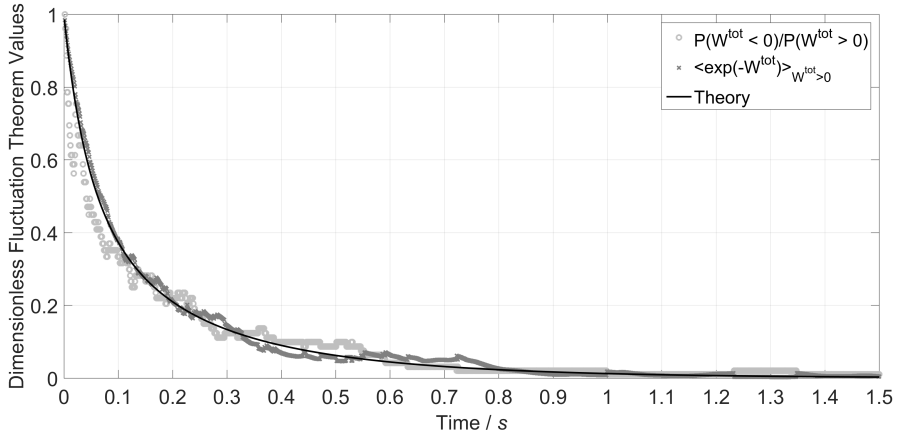

(c)

Figure 6.18: Position, a), COM, b), and relative mode, c) integrated IFTs, in the $U_{\perp}$-direction for the trap translation simulations, complete with predicted curves. Circles and crosses denote the left and right hand sides respectively of Equation 6.46, the solid lines represent the theoretical prediction from Equation 6.47.

The integrated total work fluctuation theorems, and predicted theoretical values were calculated for the trap translation simulations in accordance with Sections 6.5.1 and 6.5.2. These are presented in Figure 6.18. Figure 6.18a shows the total work IFT for particle 2 in the perpendicular direction. The derived IFTs from the simulated experiment behave as expected, decaying to zero with increasing simulation time/trajectory length, and show reasonable agreement with the theoretically predicted curve. Figures 6.18b and 6.18c show the total work IFT for the COM and relative modal motion of the particles respectively in the simulations. In these plots the derived IFTs show very good agreement with their predicted curves, decaying from one to zero with increasing trajectory time. The predicted curves for all three of these plots are found from Equation 6.47 with the relevant modifications made to take into account the decreased modal velocity and the mobilities in this simulation. Comparison of all three of these plots to each other shows that particle 2's fluctuations decrease faster than those of the modal motions. This is to be expected because the modal velocity is less than the individual particle velocity in this experiment and that will affect equation 6.48 and so the theoretical prediction. Moreover, within the modal IFTs, there is a slight difference in this time and the COM is seen to take longer to reach zero. This is also expected behaviour which can be justified and followed through from the effect of the $(1 \pm \epsilon)$ term in the mobilities of the two modal motions in equation 6.48.

It is again noteworthy that in the correlations and the IFT plots, there are times when the general form of the predicted lines is adhered to by the data but the exact values do not match. These simulations were done with the same number of repeats and with the same step intervals as those for the fluid drag experiment. It is therefore believed that all of the same comments made about inaccuracies seen in those results apply here, and that smaller simulation time intervals and a

larger number of repeats would decrease any discrepancies. Furthermore the size of the fluctuations in these trap translation simulations is slightly larger, relative to the desired motion due to trap or stage translation, than it was in the fluid drag simulations. It is perhaps to be expected therefore that larger fluctuations and deviations from theory are seen in some of these plots.

6.7 Experiment

6.7.1 Experimental Set-up

Many aspects of the set-up, calibration, and execution of these experiments were the same as those previously described in earlier chapters. What follows is an account of the similarities and differences between this and the previous experiments, and other notable information pertaining to this study.

The experimental set-up used for these fluctuations experiments was the same as that previously described for the red blood cell stretching experiments in Section 5.5.2. That is, a dual beam optical tweezers, created by splitting the beam from a single laser, was used. In this instance though, this was utilised to trap silica microparticles of the same kind, and contained within a slide prepared in the same fashion, as in Section 4.2.1. Additionally, the translating microscope stage mentioned previously in the Kapitza experiment was also utilised here to create an external fluid flow force (Section 4.1).

Video microscopy was again used for obtaining data from these experiments. Videos were recorded and then tracked using the custom Matlab script previously discussed. To process these recordings however, the software was modified such that it could locate multiple particles in a given frame and then correctly identify which previously seen particles each newly found particle

position in this frame belonged to.

Calibration of this experiment and the two traps was performed in the same way as the first step of the calibration discussed in the RBC chapter 5.5.3. That is, a particle was held in each trap independently and its fluctuations recorded and trapping strength obtained for a range of HWP angles. The HWP setting that gave the smallest difference in spring constant across both traps and in both directions was selected for use in this experiment.

6.7.2 Fixed Traps Experiment

The three experiments seen in the simulations section of this chapter were attempted experimentally for this area of research. The first of these simply employed two stationary trapped particles and recorded them to assess their motion. This was therefore a recreation of the experiment of Meiners and Quake [179], just as was done first in the simulations. Repeating this study from the literature provided a useful first port of call as it enabled verification, through the correlation functions, that the experiment was behaving as expected.

The fixed and galvanometer mirror steerable traps were positioned approximately 3 μm apart in the x-direction, and sitting in the same y and z planes. The strength of the traps was calibrated and they were balanced by adjusting the HWP before the beam splitter cube and recording a particle in each trap respectively (whilst the other trap was blocked). After this procedure, the trapping strengths measured for the fixed and galvanometer controlled traps in the x and y directions respectively were: $\kappa_{\mathrm{Fix,x}} = 0.309 \pm 0.003$ pNμm^{-1}, $\kappa_{\mathrm{Fix,y}} = 0.317 \pm 0.006$ pNμm^{-1}, $\kappa_{\mathrm{Galv,x}} = 0.328 \pm 0.006$ pNμm^{-1}, and $\kappa_{\mathrm{Galv,y}} = 0.298 \pm 0.004$ pNμm^{-1}. A reasonably good balance of trapping strengths across traps and in both directions was therefore obtained.

Two particles were then isolated from all others on the slide and one was positioned inside of each trap. Recording of these two took place at 200 fps for ∼100,000 frames. From these recordings the particles were tracked, and their modal positions and correlations were calculated. An example of these individual particle and modal correlations can be seen in Figure 6.19.

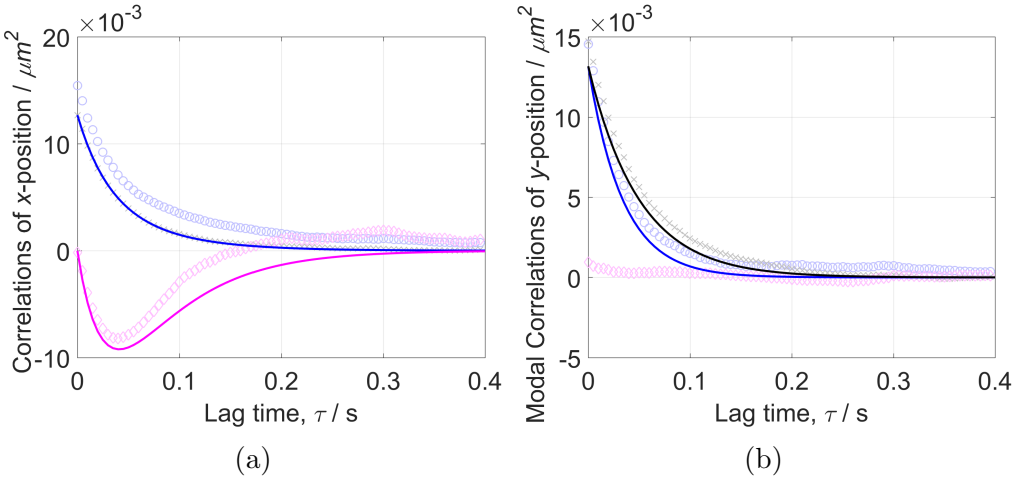

Figure 6.19: a) Auto and cross-correlation data and theoretical predictions for the x positions of two particles in static optical traps. b) Auto and cross-correlation data and theoretical predictions for the modal y positions of two particles in static optical traps.

The results of this experiment are consistent with those of both the simulation performed and the experiments of Meiners and Quake [179]. The modal correlations of the y-direction motion of the particles is seen in Figure 6.19b. The auto-correlations of the two modes both decay exponentially towards zero. They do so with different time constants, the centre-of-mass motion decaying faster, and agree reasonably well with the form of the predicted lines, given by Equations 6.33 and 6.34. The cross-correlation of these two modes stays at approximately zero throughout. This was expected since these are the two normal modes of the system.

The individual particle's x-position correlations are shown in Figure 6.19a, along with predicted theoretical lines given by Equations 6.38 and 6.40. The

auto-correlations decay towards zero with increasing lag time, as a sum of the two exponentials seen in the modal auto-correlations. Only one predicted line is shown since, although each trap has a slightly different trapping constant (κ), switching between these throughout the equations of the theoretical lines makes so little difference that the two are almost indistinguishable on these graphs. It is very noteworthy at this point that whilst one of these auto-correlations agrees very well with the predicted line, the other does not. This was not seen in the simulations and that fact alone may be crucial. In the simulations it was possible to make the two traps identical, experimentally however this was not possible. It has already been shown that there are small (albeit seemingly insignificant in terms of these predictions) differences in the trapping constants in x and y for both traps. There are other quantities that were not compared and balanced between these two traps, for example the axial trapping constants or perhaps more interestingly the depth of the wells that the traps make in the potential energy landscape. It therefore seems plausible that these differences in auto-correlation are due to the traps not being completely identical. This could, and rightly so, call into question the significance of the difference between the modal auto-correlations and their decay time constants. A point of note here though is as follows: throughout all of the experiments undertaken in this last chapter the particle whose auto-correlation has decayed fastest has varied (consistent with small differences in balancing the traps etc. as the experiments have been revisited and the apparatus tweaked); the mode which decays fastest however has remained constant throughout, and has always been the expected centre-of-mass mode. This hopefully returns some credence to observations of the modal correlations behaving broadly as expected.

The cross-correlation is zero initially and evolves to a pronounced dip at a lag time of approximately 50 ms, thus indicating an anti-correlation in the particles'

motion. This also agrees reasonably well with the form of the predicted line (the dips are at approximately the same lag time giving the same shape although the magnitudes do differ slightly).

Although the forms of the predicted lines are seen in the data, there are often discrepancies in the exact values of the two. These are, as was seen in the simulations, likely due to not having a large enough sample rate to produce enough data at small (sub relaxation time) time scales. In the experimental set-up, this sample rate was limited by the acquisition rate of the camera for a given AOI. In the case of these fixed trap experiments this was 200 fps, corresponding to the acquisition of one frame every 5 ms. Calculating the smallest relaxation time for the motions of the particles in this system (which corresponds to the centre-of-mass motion in the x-direction) gives $\tau_r \approx 30$ ms. This means that only 6 frames could be acquired before this shortest relaxation time. This is obviously only a very small amount of data. In order to obtain any substantial amount of data in this region a faster particle position detection method/equipment must be employed/obtained. For the sake of the following preliminary investigations into coupled particle fluctuation theorems, the decision was therefore made to collect a reasonably large amount of data by having the following experiments run through cycles of backwards and forwards motion; but it was decided not to expend too much time fixating on conducting hundreds of repetitions of each experimental run. An attempt was made, after the preliminary experiments that follow in this chapter were completed, to set-up a system of two quadrant photo diodes (QPDs) for this purpose, but interruptions and setbacks along the way consumed too much time and so results were never obtained using this set-up.

Nonetheless, the results from this initial experiment were encouraging. They implied that the two particles in their respective traps were behaving as would be

expected if they were coupled via the surrounding fluid and that correlations in their motion were indeed being detected, even if there were doubts about the detection method being fast enough to accurately and precisely measure these.

6.7.3 Fluid Drag Experiment

After establishing that the experiment was working as expected (that correlated behaviour was being exhibited by the particles) external forces were then introduced to the system with increasing complexity. In the first instance the fluid drag method discussed in Section 6.5.1 was used to work on the centre-of-mass mode by translating the fluid, and so both particles, relative to the traps despite only one of the trapping beam paths being incident upon the movable galvanometer mirrors. Experimentally, this relative fluid flow was achieved by moving the microscope stage (as seen in the Kapitza experiment previously). Stage motion was attempted in directions both parallel and perpendicular to the line connecting the two traps (illustrated in Figure 6.20)

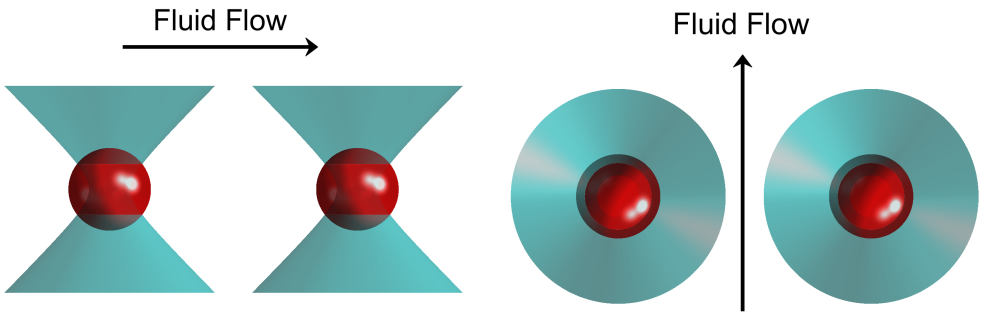

Figure 6.20: An illustration of the particles in their individual traps, along with the two directions, a) parallel and b) perpendicular, of fluid flow used in the fluid drag fluctuations experiment.

A quick initial test was performed to check that motion of a particle within a trap would be significantly and detectably altered by moving the stage. A single

particle was trapped in a relatively weak trap and the stage was then translated back and forth in the x-direction with a triangle wave at a speed of 10 μms^{-1}. The particle's position was monitored via the back scatter of the HeNe laser from the particle which was then incident upon a battery powered QPD. Results from this test can be seen in Figure 6.21.

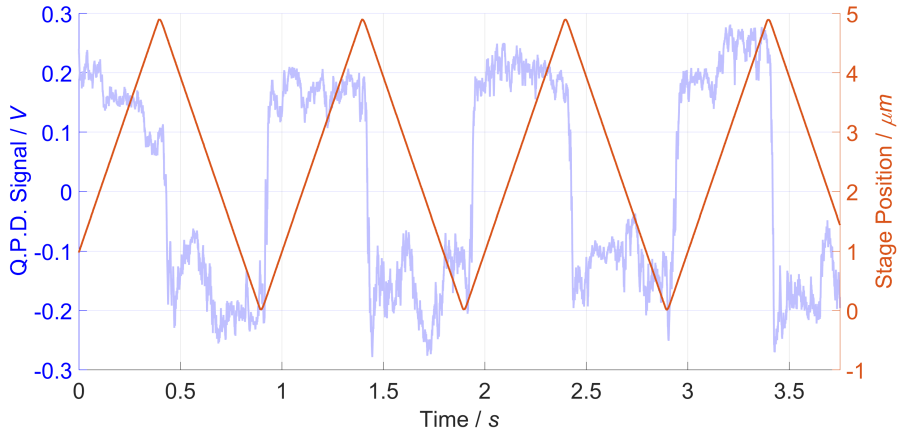

Figure 6.21: A plot of a trapped particle's tracking signal relative to the centre of the optical trap as the microscope stage is ramped back and forth at 10 μms^{-1} in the x-direction.

It can clearly be seen that the particle moves in response to the stage motion, residing either side of the centre of the trap depending upon which way it is being pushed by the fluid flow.

Following this, both traps were unblocked and their x separation set to ~ 3 μm. A particle was held in each and these were isolated from the rest of the beads present in the slide by moving them sufficiently far away that there would be no coupling effects. The traps were set with only very weak strengths ~ 0.5 pNμm^{-1} such that the particles would be sufficiently displaced by the stage motion as to be detectable, but not so weak as to lose the particles during stage motion, and also so that the relaxation time, $\tau_r = \gamma/\kappa$, would be longer (and thus allow as many pre-relaxation time data points to be collected as possible). The stage was programmed to move far slower than in the initial test,

such that the drag force was not overbearingly large compared to the coupling or the trapping. It was driven at 1 μms^{-1} for 2 seconds, then paused for 2 seconds, allowing the particle significantly longer than its characteristic relaxation time to forget its previous dragged displacement from the centre of the trap. This motion was then run in reverse, such that the trap ended up in its original position and paused here for two seconds also. This entire sequence was repeated 49 times (a total of 50 runs) per video, and 5 videos were made for each of the parallel and perpendicular driving motions. An example of just a couple of these stage runs for motion in the parallel driving direction, as recorded from the monitor output of the stage control box, is shown in Figure 6.22.

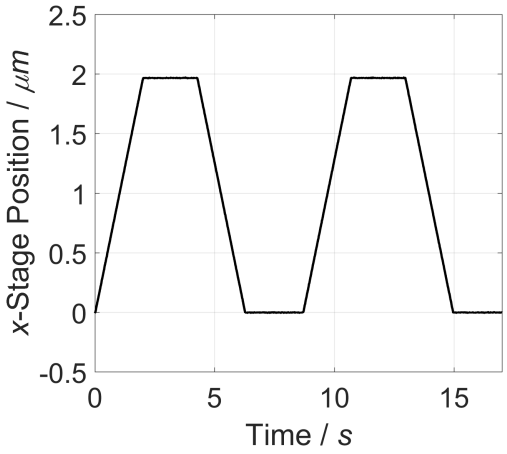

Figure 6.22: A plot of stage position against time for a couple of example runs of the stage driving routine that occurred 50 times per video in the coupled fluid drag experiment.

Matlab code was then written to identify and extract the particle positions for the 50 repeats of each of the 4 stages: 1) positive stage driving, 2) the first relaxation stage, 3) negative driving, and 4) the second relaxation stage of each video. The displacement of the particles from their traps was found and averaged across all 50 repeats. Figure 6.23 shows the individual particle and modal displacements for the positive driving stage of the parallel stage movement experiment.

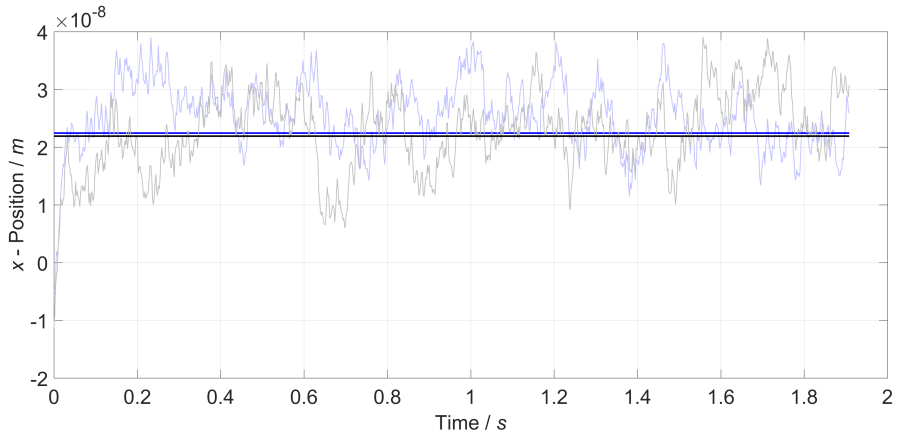

(a)

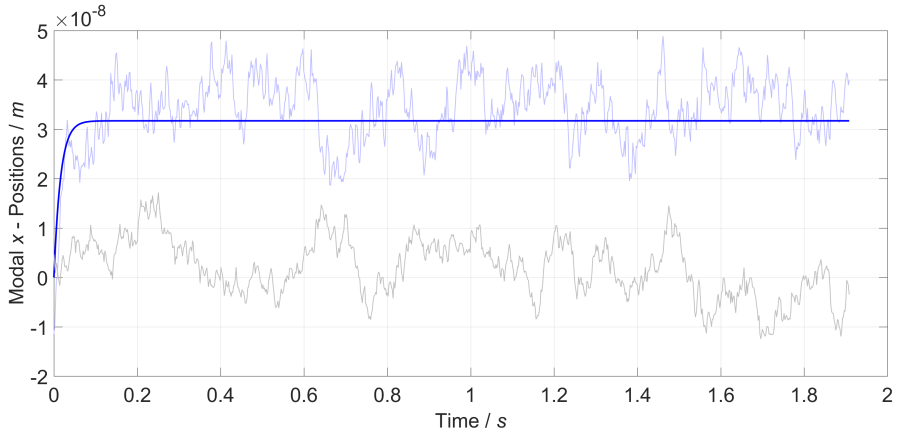

(b)

Figure 6.23: a) The displacement of particles 1 and 2 from their respective traps during positive parallel stage motion in the fluid drag experiment, complete with predicted lines. b) The modal displacements for the same driving case, also with a predicted line.

The individual particle motions in Figure 6.23a showcase the expected behaviour of a short exponential curve to some plateau value of displacement beyond the trap in the direction of the stage motion. These agree well with the theoretical predictions for their displacement found in the same way as for Figure 6.9a (two separate but very close prediction lines are shown as, in the experimental case, the two traps do not have exactly the same strengths). The modal displacements in Figure 6.23b also behave as expected. The centre-of-mass motion is being driven in this experiment and this shows in this graph. This motion, like the individual motions, rises exponentially to some equilibrium displacement value as

both particles are shifted away from their traps by the fluid drag. The experimental data shows very good agreement with the theoretical line (this was found in the same way as the previous discussion around Equation 6.73). Finally the relative motion remains at zero, exhibiting Brownian motion here. This is as expected since both particles are displaced equally from their traps so their separation does not change.

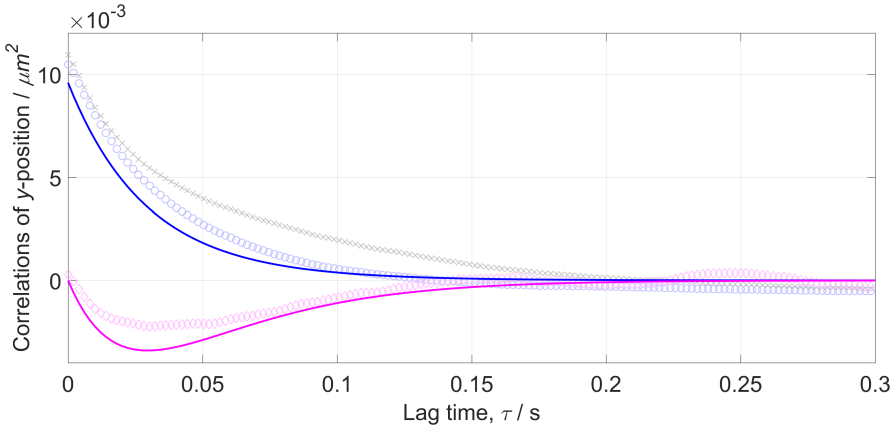

(a)

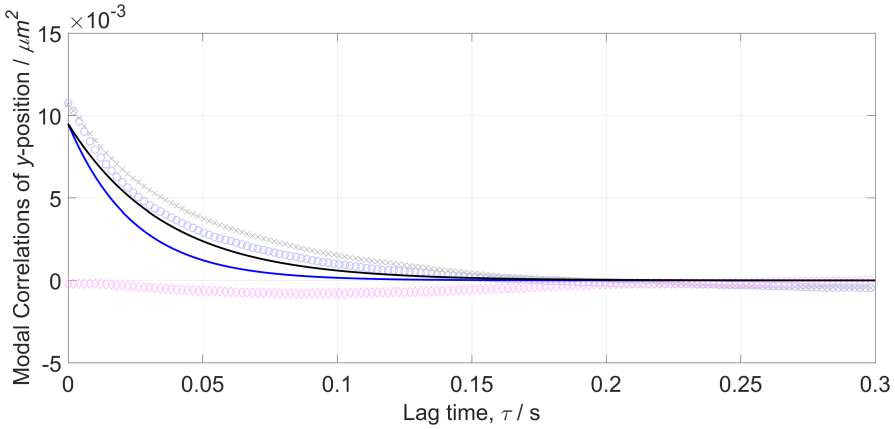

(b)

Figure 6.24: a) The correlations of particles 1 and 2 during the first relaxation stage of the perpendicular stage movement fluid drag experiment, complete with predicted lines. b) The modal correlations for the same driving case, also with predicted lines.

Correlations (both auto, and cross) were determined from the particle positions of the fluid drag experiment. These were calculated for each of the four driving stages. Theoretical predictions for these correlations were calculated in line with the calculations at the end of Section 6.1.2. The behaviour of the individual

particle correlations in Figure 6.24a is broadly as expected. The auto-correlations both decay exponentially to zero, albeit with different rates (a reason for which has been suggested previously), and the cross-correlation has an initial anti-correlated dip at the predicted time before rising again to approximately zero. The agreement with the predicted lines before the relaxation time is not good. It is believed that the reasons for this are as discussed before, and that there is too little data being taken in this time period. The modal correlations also behave as expected. The auto-correlations both decay at different rates with the relative motion being the slower decay of the two. These are again in line with the general form of the predictions although the exact values differ slightly. The modal cross-correlation remains around 0 throughout, as expected for these normal modes of the system.

6.7.4 Trap Translation Experiment

After the fluid drag scenario had been attempted, finally the galvanometer mirrors were employed to translate just one particle in a fixed radius arc around the other, as per the scenario in Section 6.5.2.

The separation distance of the two particles is key to the coupling terms from the mobility matrix. It was therefore important to establish that the amplitude and phase corrections found earlier for circular galvanometer mirror movement at given speeds/frequencies were still accurate. Doing so would enable the movement of the second particle through an arc about the first particle with a precisely maintained radius. The galvanometer trap was translated until its cover slip reflection was overlapping with the fixed trap in order to find a mirror voltage value for the arc's centre. Both traps were then occupied with particles and particle 2 was made to move in circles of fixed radii (3, 5, and 8 μm) around

particle 1 by moving the galvanometer mirrors. This calibration step's results can be seen in Figure 6.25.

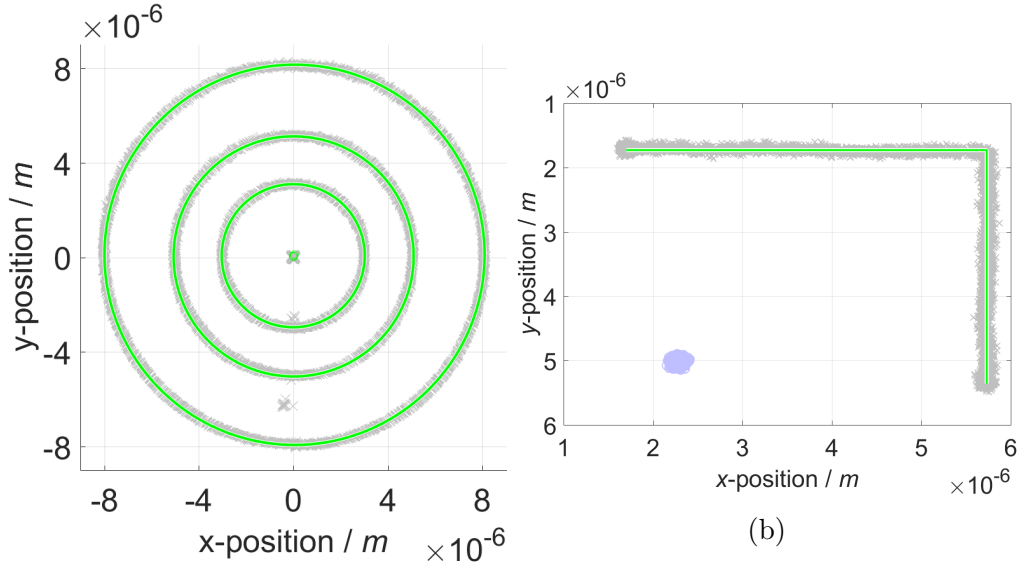

Figure 6.25: a) Circular trajectories of radii 3, 5, and 8 μm of particle 2 about particle 1 to check the accuracy of the trap translation. The green lines denote fitted circles in Matlab, and the central green data points are the fitted centres of these circles. b) Results from the mirror voltage/position calibration step. The green line shows the conversion made from mirror voltages to trap 2 position.

As can be seen from this figure, this calibration step seemed to confirm that the executed movement of the galvanometer trap still appeared to be a fairly precise circle. N.B. the few data points which fall outside of the circles of given radii are caused by either a loss of the particle momentarily from the trap or by a failing of the tracking software to accurately detect the particle (often due to a larger axial movement of the particle which causes a difference in the intensity of its centre).

In order to obtain the $U_{\parallel}$ and $U_{\perp}$ coordinates in this experiment it was necessary to know the angle of trap 2 relative to trap 1, and therefore the position of the two traps, at any given time during the recording. In case of any misalignment in the imaging path between trap reflections and trapped particle positions (as was reckoned to have been seen previously), this was achieved using only trapped

particle positions. Particles were held in the two traps, which were made as strong as possible, at a separation distance of approximately 3 μm. Trap 2 was then translated very slowly (0.8 μms^{-1}) in a straight line in x, and then y-directions. The associated galvanometer mirror voltages were recorded along with the times at which they were outputted and the times at which the video frames were recorded (the same AOI was used for this and the final experiments such that the mean of the tightly confined position of particle 1 here could be taken as the location of trap 1). After tracking the videos it was then possible to identify a linear relationship between the outputted galvanometer mirror voltages and the trap coordinates in the experiment. This relationship was used to find the position of the galvanometer mirror trap, from the voltages sent to the mirrors, as it translated through its arc in the final experiment. This mirror calibration can be seen in Figure 6.25b.

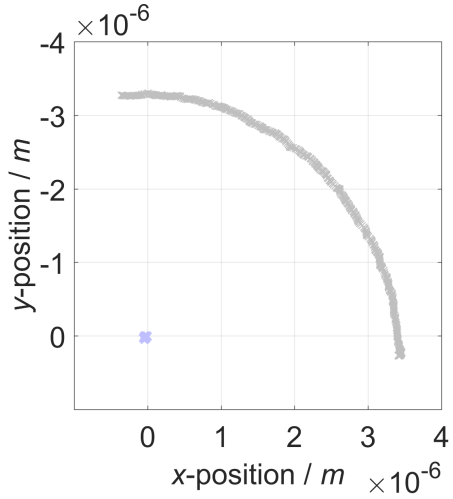

Figure 6.26: A plot of the averaged position data of the two optically trapped particles in the translating trap experiment.

The traps were again balanced (both in x and y directions within a given trap, and between the two traps) using HWP adjustments, and recordings were made of particles in each trap individually whilst the other trap was blocked. Their trapping strengths were recorded as: $\kappa_{1,x} = 0.34 \pm 0.04$ pNμm^{-1},

$\kappa_{1,y} = 0.361 \pm 0.009$ pNμm^{-1}, $\kappa_{2,x} = 0.35 \pm 0.01$ pNμm^{-1}, and $\kappa_{2,y} = 0.295 \pm 0.007$ pNμm^{-1}. The errors were found as 95% confidence bounds on a fit of the energy landscape of the traps.

For the arc trajectory experiments, trap 2 was initially placed at a separation distance of 3.5 μm from trap 1 along the x-axis. It was then translated in an anti-clockwise arc, about trap 1, through an angle just larger than a quarter of a circle, ~ 1.8 rad, in 2 seconds. The trap remained at this new position for 4 seconds (far longer than the characteristic relaxation time), before translating back through the same arc at the same speed to its original position, and then pausing here for a further 4 seconds. This arc can be seen via the positions of the two particles in Figure 6.26. This equates to an angular velocity of ~ 0.9 rads^{-1} or a linear velocity of ~ 3 μms^{-1}. If this is defined as one cycle, then a single recorded video consisted of 20 cycles, and 5 videos of this experiment were taken. Due to the size of AOI needed to capture the whole of trap 2's arc, it was only possible to record videos at 200 Hz.

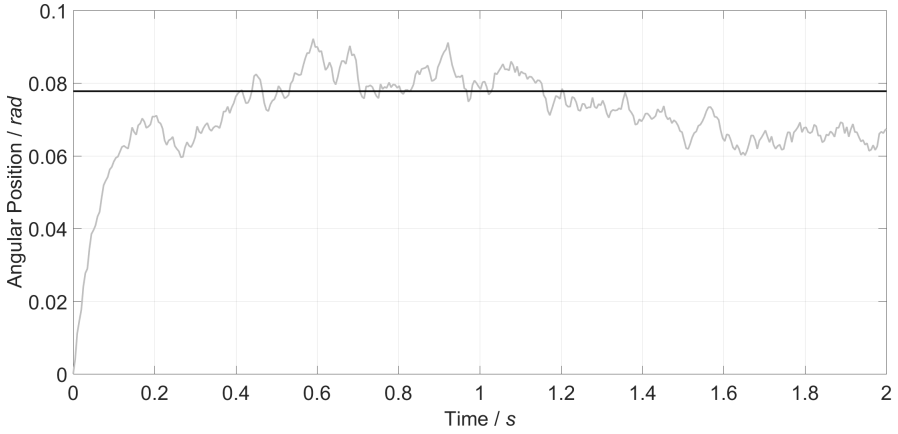

Figure 6.27: The averaged result for the angle of particle 2 relative to trap 2 during clockwise trap motion in the translating trap experiment, featuring a predicted line for the equilibrium displacement angle of the particle from the trap.

Angular positions of the particles and trap 2 were calculated from the known origin position of trap 1. The angular displacement of particle 2 from its

translating trap was calculated. This was averaged across all 100 cycles and is shown in Figure 6.27 for the anti-clockwise trap motion segment of the experiment. It can be seen in this plot that the particle's angular displacement from its trap behaves in the expected fashion. It initially starts at zero angular displacement whilst at rest, and this very quickly and exponentially increases before settling at some plateau value. A predicted line for this displacement value is featured on this graph and was found as discussed previously for Figure 6.14 in Section 6.6.3. The data and the theoretical line show a considerable amount of agreement which suggests that the particle and the experiment were behaving as expected. It could perhaps be suggested from this plot that there is a small discrepancy between the plateau value and the prediction line. Indeed, the mean of the data after $t = 0.2$ s (when the exponential rise seems to halt) is $\theta_{\text{disp}} = 0.074$ and the prediction line is at $\theta_{\text{disp}} = 0.078$. However, there are significant fluctuations of the particle's displacement angle. This is not unexpected, given that in this experiment the relative size of the motion expected at each time step from the trap translation is only just over twice that of the fluctuations. These fluctuations make it difficult to perceive what is the actual equilibrium angle of the particle and what is just a noisy fluctuation in one direction or the other. This is something which more experimental repeats could help to atone for. A possible reason for a discrepancy here might be that the arc the mirrors, and so the particle, were being driven in was imperfect. An eccentric or incorrectly centred arc would affect the particle 2's coordinate and so may make it deviate slightly from the expected position. The check of the driving circle that was conducted and displayed in Figure 6.25a is presented on a graph that spans 16 μm in either axis direction. The displacement differences seen here, when converted to the perpendicular coordinate, are fractions of a micrometre. Very small variations such as these in the centre position of the translating trap

or eccentricity of the translation arcs would therefore not be very easy to spot in this Figure, so it is possible they exist and were missed. In addition to this, both of the calibration graphs at the beginning of this section have a finite width/spread in the experimental data points owing to Brownian motion. This was minimised by using strong traps but is inevitably still present and visible in small amounts either side of the fit lines. It is therefore also possible that the mirror voltage to trap position calibration contains some inaccuracies.

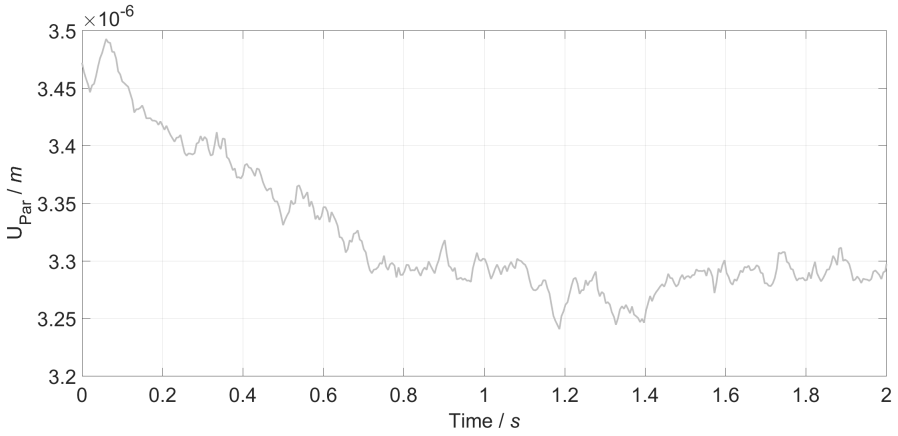

(a)

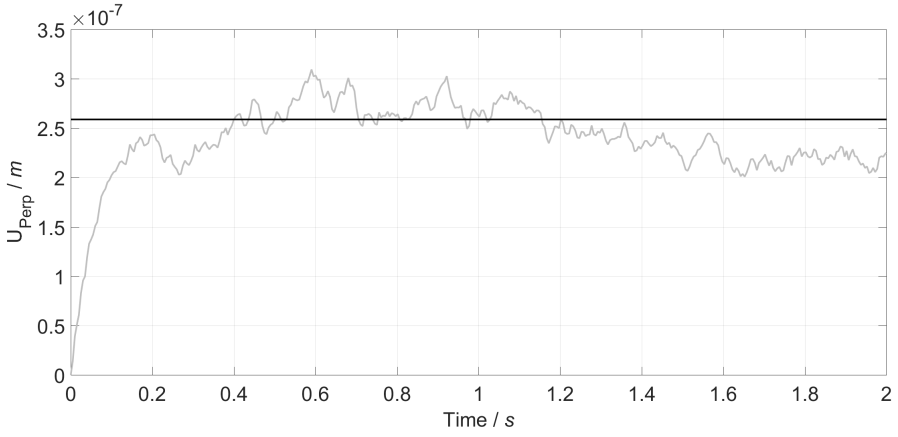

(b)

Figure 6.28: The averaged parallel and perpendicular coordinates, a) $U_{\parallel}$ and b) $U_{\perp}$ respectively, of particle 2 against time in the anti-clockwise segment of the trap translation experiment. b) Also features a line for the predicted equilibrium displacement of particle 2.

Once these angular positions were found, it was possible to rotate the coordinate frame and calculate the $U_{\parallel}$ and $U_{\perp}$ coordinates of the particles, as discussed

previously. These are seen in Figure 6.28 for the same anti-clockwise trap motion segment. Figure 6.28a shows the parallel coordinate of particle 2 during trap 2's motion. The expectation was that this would remain at the initial trap separation value of 3.5 μm, exhibiting only Brownian motion. It can clearly be seen that this was not the case, and that the particle's parallel/radial coordinate actually decreases slightly to 3.3 μm. The opposite was true for the clockwise trap movement segment when it was analysed, and the stationary trap segments saw the parallel coordinate remain at either end of this shift. This lends strength to the notion mentioned earlier that the arc of trap 2 was not perfectly centred on trap 1 and/or was slight eccentric. The perpendicular coordinate for this segment, seen in Figure 6.28b, behaved as expected; exhibiting the now very familiar exponential shift to some plateau value of equilibrium displacement behind the trap. The data shows reasonably good agreement with the predicted value for this displacement, as was to be expected after the result seen from the angular displacement. It is noteworthy that whilst the parallel coordinate does change throughout the trap translation, it does not exhibit a quick exponential curve and then a long plateau like the perpendicular motion. It is a much more gradual change which is indicative of the aforementioned translation arc faults, rather than some significant particle dynamics.

Following the same pattern of data analysis as in the other experiments, the modal coordinates for both $U_{\parallel}$ and $U_{\perp}$ directions were then calculated. These are shown in Figure 6.29 for the perpendicular coordinate during anti-clockwise trap translation (comparable results were seen for both directions of trap translation). The parallel coordinate modes are not plotted here for the sake of brevity, but showed the gradual increases and decreases during the translations that were expected after having seen the individual coordinates for this direction of motion. Figure 6.29a shows the centre-of-mass mode for the perpendicular coordinate.

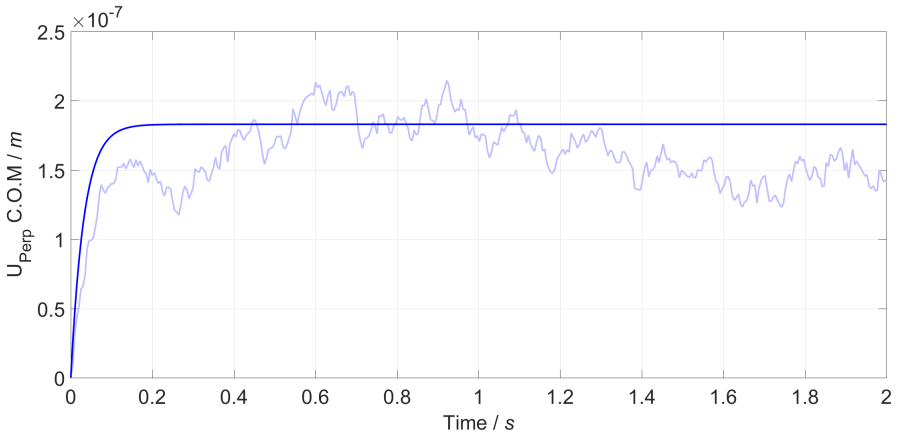

(a)

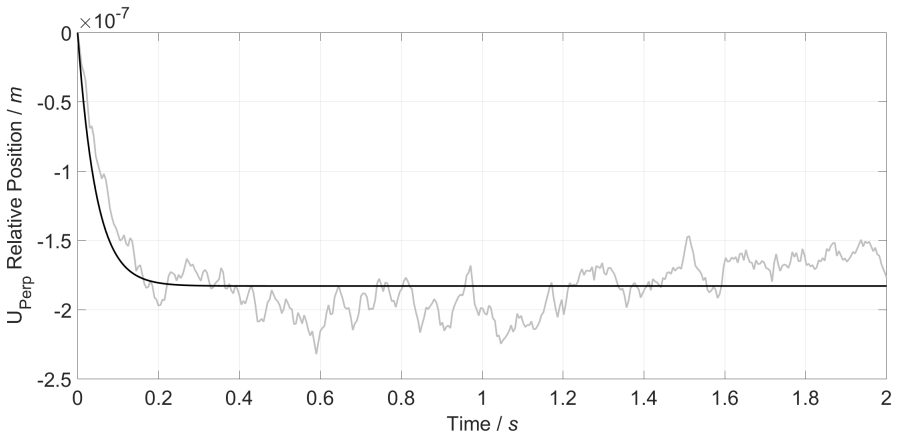

(b)

Figure 6.29: The averaged perpendicular centre-of-mass and relative modal coordinates, a) and b) respectively, for the anti-clockwise stage of the translating trap experiment, featuring predicted exponential curves.

This displays the expected exponential shift to a plateau where both the rise time and the plateau displacement value seem to agree well with the predicted curve. It is once more possible that there is a slight discrepancy between the experimental and theoretical plateau values, but as before the fluctuations make it hard to assert this strongly and possible reasons for this relating to the arc and calibrations have already been stated. The relative modal motion in Figure 6.29b exhibits many of the same characteristics. The data shows a short exponential that levels off to a plateau, that was expected because this type of working on the experiment drives both modes. The direction of change of the relative

coordinate, decreasing rather than increasing, is simply due to the way this mode is calculated, as has been mentioned previously. There is good agreement with both the exponential decay constant, the time at which the exponential levels off, and the plateau value at which the relative position equilibrates. The predicted lines for both modes were found in the same way as was detailed earlier when discussing Figure 6.16 in Section 6.6.3.

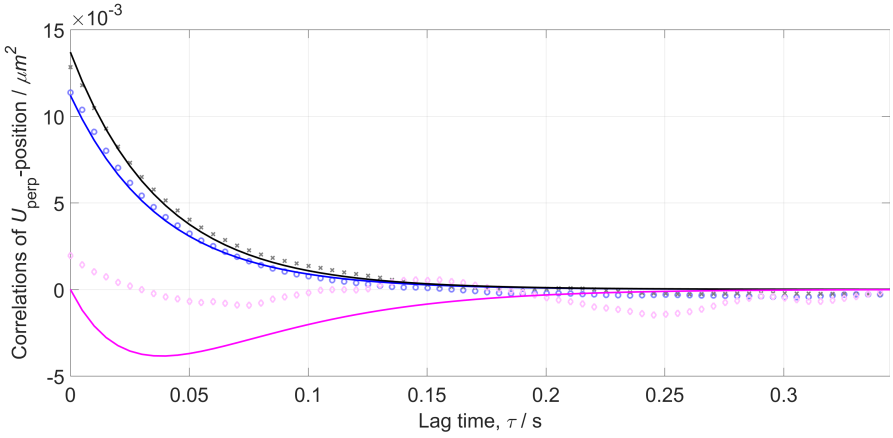

(a)

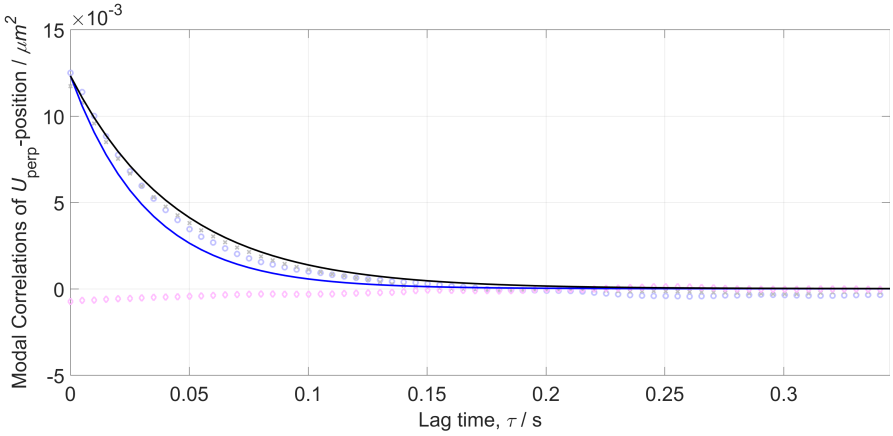

(b)

Figure 6.30: Individual particle position, a), and modal position, b), correlation plots in the $U_\perp$ direction for the anti-clockwise trap translation experiment. The cross-correlation data in a) has been multiplied by 5 for ease of viewing on the same axes.

After calculating the modal positions, these were used to obtain the correlations for each movement section. Correlations in the $U_\perp$ direction are shown for the same anti-clockwise translation phase in Figure 6.30. Figure 6.30a shows the

correlations for the individual particles. The forms of the predicted lines are given by Equations 6.38 and 6.40 for the auto and cross-correlations respectively. The auto-correlations in this plot both behave as expected with a decay to zero from some initial value. They do so at different rates due to their different trapping strengths, and in this instance the perpendicular trapping strengths were sufficiently different that plotting separate prediction lines for the two sets of data was warranted. Good agreement is shown between the predictions and the data for these auto-correlations. The cross-correlation however is another matter. Here the data starts above zero, suggesting some small initial positive cross-correlation. It does show an anti-correlated dip at approximately the same time as the prediction line but, perhaps due to its initial start point, this is nowhere near as large as predicted. Whilst the data does then rise to zero again as expected, it exhibits some small fluctuations thereafter and a noticeable anti-correlation dip at $t = 0.25$ s. The question then becomes what the cause of this poor cross-correlation data is. It is unlikely to be the imperfect arc that seems to have been in place. Even with a suspected imperfect arc it has been seen that particle 2 still reaches an equilibrium perpendicular coordinate behind the trap, which remains fixed apart from Brownian motion. Particle 1's $U_{\perp}$ coordinate was inspected for this translation phase and it was seen that there is an initial sharp change in this coordinate at about the relaxation time, which must be the cause of this initial cross-correlation behaviour (N.B. this motion was readily detectable when plotted on its own but was actually an order of magnitude smaller than the displacement motion of particle 2 from its moving trap). Why this initial jump should be present is unclear, since intuition would suggest that this particle should simply remain at approximately zero in both coordinates. The best explanation that can be offered for this behaviour at present again pertains to the fluctuations and the small amount of data. As was

mentioned earlier in this chapter, the relative size of the fluctuations is still a significantly large fraction of the size of the expected motion due to the trap translation in this experiment. There are still, at best, only around 10 frames before the relaxation time of the motion with the longest characteristic time in this experiment. That coupled with the low number of repeats (even fewer in this experiment as some had to be excluded due to tracking anomalies) means that there is very little data to rely on in the time scale of the lag times of the correlation plots, and a relatively large amount of Brownian noise to contend with.

The modal correlations for this motion are shown in Figure 6.30b. These generally look better, in terms of agreement with their predicted lines, than the individual particle coordinates' correlations did. The predictions for the COM and breathing mode lines are given by Equations 6.33 and 6.34 respectively. The auto-correlations both decay to zero, with the COM mode doing so faster as explained previously. These two are closer together than on previous modal correlation plots. This is almost certainly due to the smaller ϵ term in the perpendicular direction - it is fairly straightforward to see how this would then make the difference between the two theoretical equations smaller. The cross-correlation generally behaves as expected, remaining around zero the whole time; although it does show a small initial negative value which is likely due to the observations already made about the unexpected behaviour seen in the average of particle 1's perpendicular trajectory.

Finally the perpendicular position and trap data were used to generate the total work done IFTs for the individual particle and modal coordinates, these are shown in Figure 6.31. Figure 6.31a show an example of particle 2's IFT during trap translation. As expected, this decays towards zero from an initial value of one. The experimentally derived left and right hand sides of the IFT (Equation

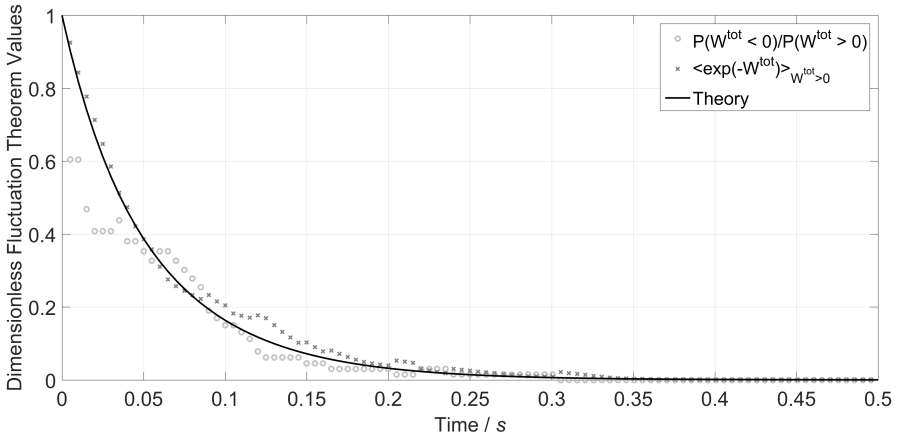

(a)

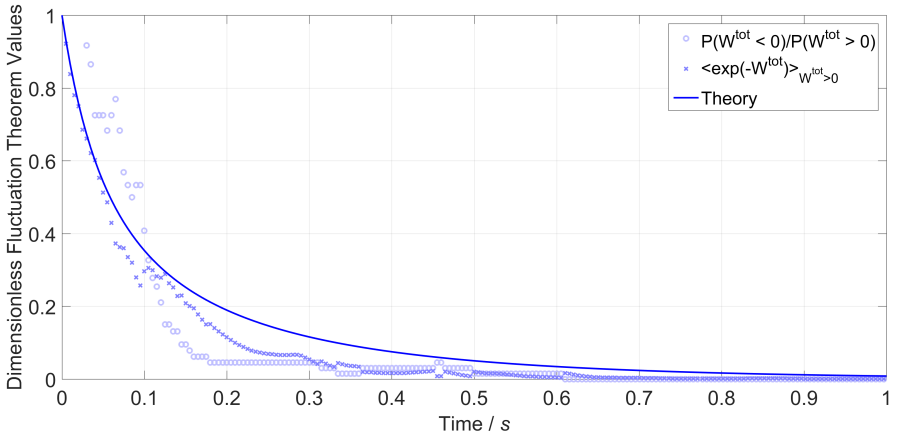

(b)

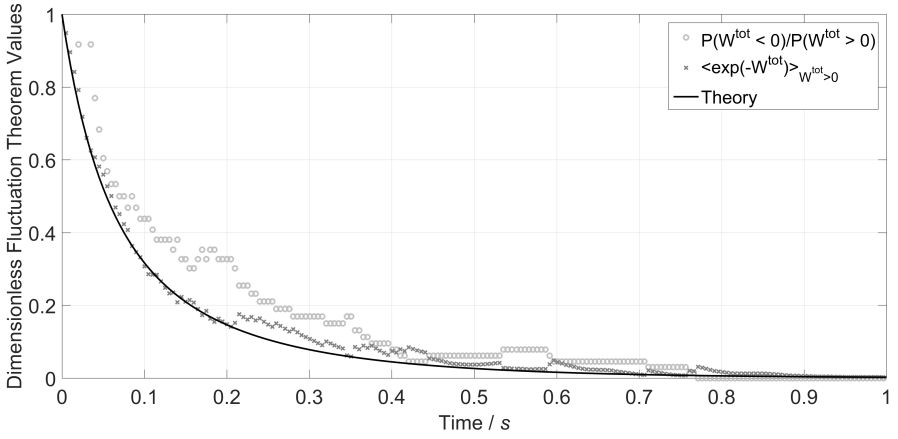

(c)

Figure 6.31: Individual particle, a), COM, b), and breathing, c), mode IFT plots in the $U_\perp$ direction for the trap translation experiment.

6.46) agree reasonably well with the theoretical prediction given by Equation 6.47; although the LHS does start a little lower than one, most likely due to the

random nature of the fluctuations and less of the trajectory having been integrated along at this point, so individual starting fluctuations are more significant. Figures 6.31b and 6.31c show examples of the COM and breathing mode total work IFTs respectively. These both have greater discrepancies when compared to their theoretical lines than the individual particle 2 IFT did. This is likely due to reasons already discussed; the unexpected motion of particle one now having an effect because the modes are being considered, and the small amount of data and relatively large random fluctuations. Despite all the limitations of these preliminary forays into coupled particle FTs, it is nonetheless encouraging to see that both of these follow the general form of their theoretical lines and decay from one to zero within roughly the same time period as them. This suggests that with a faster detection method, more repeats, and perhaps a stronger trap translation to lessen the effect of the fluctuations, even better results and agreement should be possible for these plots.

6.8 Summary and Outlook

6.8.1 Summary

In this chapter the correlated motions of two hydrodynamically coupled particles have been investigated as work was performed upon them in various ways, with a view to analysing their adherence to fluctuation theorems.

A pilot study was conducted using a dual-beam optical tweezers set-up to confine two silica particles in separate optical traps, separated by a few micrometres. Initially the two trap positions were fixed, whilst the motions of the particles in them were recorded. This yielded results for comparison with previous studies in the literature and so verification that the experiment was behaving as expected.

Two methods of performing work upon this system of coupled particles were then undertaken. In the first of these the microscope stage was translated back and forth at a fixed speed such that both particles would be subjected to a fluid drag force (in addition to Brownian motion and their coupling). In the second of these, trap 2 was translated through an arc about trap 1 using galvanometer mirrors such that only particle 2 was actively worked upon.

Theoretical calculations have been presented, using the Oseen tensor to account for the coupling, in order to predict the motion of the particles, their correlations and their IFTs in each of these arrangements. These calculations have been supplemented with Brownian motion simulations, completed via a finite difference equation method, and using parameters akin to those achievable experimentally. These simulations show generally good agreement with the theory.

Experimental data was acquired using Labview, a ThorLabs CMOS camera (for imaging the particles and video microscopy), and a National Instruments Data Acquisition Board (for acquiring the galvanometer mirror positions and microscope stage position). This data was processed in Matlab in order to acquire the positions of the particles and of the translating trap or stage. The relative displacement of the particles from their traps was calculated and in the stage translation experiment seemed to show good agreement with the theory and simulations. The agreement was marginally less good in the trap translation experiment, but by no means poor, where it was suspected that a non-perfect translation arc was to blame.

Modal coordinates, both centre-of-mass and relative motion of the two particles were also extracted from this data, and in the translating trap experiment, data was also processed to extract particle positions in a coordinate system whose unit vectors lie parallel and perpendicular to the line joining the two traps.

These too showed good agreement between the theory and simulations in most cases, despite some unexpected small motion of particle 1 being discovered.

These positions, both modal and non-modal, were then used to calculate the auto and cross-correlations of the particles' coordinates. For the initial fixed trap experiment, as well as the stage and trap translating experiments these showed fair agreement to the predictions and expectations from the theoretical calculations and simulations. In general the form of the data for these correlations was good, rising and falling exponentially and showing the predicted features at the expected times. The precise values for these however sometimes disagreed with those in the predictions. A reason for this was ventured. It was suggested that these inaccuracies may stem from the relatively large (compared to the relaxation times of the particle motions involved) acquisition time/low frame rate of the camera used to collect the video microscopy data. These acquisition times were sufficiently large that only approximately 10 frames were captured before the relaxation times, and so even with many repeats there was not a statistically large amount of data available to average and more accurately determine the shape of the correlations in these early time periods. The trap translation experiment's non-modal cross-correlation had a poor fit to the theoretical prediction. As well as the reasons mentioned already a suggestion as to why this was particularly poor was ventured as being related to the unexpected initial perpendicular behaviour of particle one.

Finally total work IFTs were calculated and plotted for the two experiments where work was performed upon the system. In both the simulations and the experiments these showed reasonable agreement with the theoretical predictions, for modal and non-modal cases. There were deviations from the theoretical prediction lines at times, and it was suggested that the reason for these was the same as those given for the correlations and indeed stated throughout this

chapter as being a fault of the set-up. These deviations aside, the results seem to strongly suggest that the motion of these worked upon, coupled particles was indeed in-line with predictions made based upon a fluctuation theorem. Harking back to the objectives of this chapter it can be said that these were fulfilled and that, yes, the behaviour of these coupled particles does indeed fulfil the predictions of the FTs and suggest that they are valid when considering these set-ups.

6.8.2 Outlook

It is by now abundantly clear that the main limitation of the study undertaken was the particle position recording method. Video microscopy with the ThorLabs camera utilised was limited in data acquisition rate to the maximum frame rate of the camera for the area of interest being recorded. Generally speaking this meant a frame rate of 200 Hz. Inspection of the correlation plots reveals that the predicted initial anti-correlation dip takes place at a lag time somewhere in the range of approximately $0.025 - 0.05$ s. With the available maximum frame rate this only allows for a handful of points (10 at most) to map out this crucial area of the correlations plots.

A hope for future experimentation would therefore be to use a much faster method of position data collection for the particles. One such method could be the use of two QPDs, with forward scatter of some detection laser from the particles. This could record much faster, at rates in the order of kHz. This would immediately yield orders of magnitude more data points and so would offer much better resolution at low lag times, even if only one run of the experiment is conducted. Work on this method was undertaken, but a source of noise persisted in the readings and within the research time available it was not identified and

eliminated. Obviously this method would not be applicable, or at least would be much harder to implement, in the case of the trap translation experiment where particle 2 moves across relative large distances, but it could prove very effective for any experiments where the traps remain fixed and the displacement of the particles is sufficiently small that they still encounter the detection laser (as in the fluid drag experiment).

This field remains one of interest and importance, and the evolution of microscopic fluctuations over time will only become more relevant as technological devices shrink and micro-scale motors / molecular motors are studied and utilised ever more. To that end, a suggestion for a further investigation would be an experiment, similar to the fluid drag one here undertaken, but featuring chains of coupled particles, rather than two. If a relation for the FT of a chain of N particles could be established it may have significance to more complicated micro-motor systems. Rapid, kHz detection of the positions of these chains of many particles may present a significant challenge. The method attempted for two particle QPD detection was to use a beam splitter and direct the two resulting beams to overlap with the particles. Obviously, as the number of particles increases, so does the number of optical elements required for this and it would very quickly take up too much space on an optical bench. One suggestion to overcome this would be to use spatial light modulators (SLMs) in order to make an array of trapping and detecting spots that could be filled by particles. Separation of the scattering beams after the microscope would still be difficult though and would require many QPDs which would again take up a lot of real estate on an optical bench. Perhaps a better solution would be to stick with a video microscopy method, but to utilise a faster camera and analyse more carefully the trade off between motion relaxation time and size of displacement when picking a trapping strength value. Optical

binding [191], where particles can spontaneously self-arrange in potentially large numbers as a result of their multiple optical scattering interaction, could potentially be a simpler way of trapping large chains of particles than using an SLM for this experiment.

Chapter 7

Conclusion

This thesis has presented and discussed research undertaken into the use of optical tweezers to probe the dynamics and properties of microscopic systems. Naturally, all of the experimental studies in this thesis therefore exploited optical tweezers as their primary tool. Thus, in Chapter 1, background information was given concerning the history and development of the optical tweezers apparatus, as well as a brief overview of the physics behind optical trapping.

In Chapter 2 the classical mechanical phenomenon of the Kapitza pendulum was introduced. This background information was presented via a complete theoretical description of this pendulum, starting from a simple pendulum before adding in the base oscillations that typify this set-up. Derivations were presented for inequalities that are necessarily satisfied in order to observe the non-standard/inverted pendulum stability. This chapter served as a foundation for the subsequent chapter, the first of novel work, to build upon.

Chapter 3 sought to go beyond the traditional Kapitza Pendulum and extend current understanding of its equilibrium by introducing damping into the system. Equations of motion for the pendulum in the presence of a viscous drag coefficient (given by Stokes' Law) and in the presence of Brownian noise were used as the starting point for this theoretical work. A quartic model was considered for the pendulum potential as it encompassed the significant desired features and was fairly amenable to calculations. Kapitza's method of separation of fast and slow variables was utilised to identify an effective potential which could be analysed for its stability. Through this analysis and consideration of the variable parameters in the set-up, it was found that two new regimes of stabilisation emerged. The first of these emerged at very high driving frequencies (or high friction coefficients). The stabilisation angle in this regime was found to depend upon the amplitude of the base modulation as well as the stiffness of the pendulum in relation to its natural oscillation frequency. Once this high driving

frequency regime had been entered, the stabilisation angle was not dependent upon the modulation/driving frequency. As such this regime was termed the 'driving dominated' regime. In this new regime neither the inverted position, nor the standard position were stable equilibrium points, instead two new bifurcated equilibrium positions emerged which tend towards stability in a direction perpendicular to the modulation rather than being completely inverted. The other regime identified occurred when this driving frequency was lowered greatly, such that the pendulum was once again very rigid compared to this frequency. In this regime the stabilisation angle was found to be additionally dependent upon the friction coefficient and the driving frequency. This regime was therefore termed the 'friction filter' regime. Expressions were derived in this theoretical chapter for both the expected stabilisation angles in both regimes as well as the threshold driving amplitude required to see non-standard stabilisation.

In the interests of verifying these theoretical calculations, simulations were performed using a finite difference method. These were undertaken for both the driving dominated and the friction filter regimes. Good agreement was shown, for the chosen parameter values chosen, between the simulated experiments and the accompanying theoretical predictions in both of these regimes.

Chapter 4 gave an account of thorough experimental tests of this new theory. A single optical tweezers set-up was utilised where the beam was incident upon two galvanometer mirrors. An optical pendulum analogue was established by scanning these mirrors in a high frequency circle whilst translating the microscope stage, and the extra modulation/driving was supplied by oscillating the centre position of the scanned trapping circle. Individual silica beads were trapped and used as the microscopic analogue to a pendulum bob. Their movements were recorded and tracked using video microscopy. The available range of experimental system frequencies was determined in order to confirm

that it would be possible to enter both of the new stability regimes. The high frequency, driving dominated regime was explored by systematically increasing the modulation amplitude and observing the corresponding stability angles. This returned results with very good levels of agreement to both theoretical and simulated values, for both the stabilisation angles and threshold modulation amplitude. Additional explorations of this regime were conducted. The trap stiffness was altered in order to shift the data and its threshold modulation frequency, thus testing the proper frequency dependency in the stabilisation angle formula. Experiments were also conducted at two frequencies, an order of magnitude apart, in order to test the driving frequency invariant nature of the angular stability positions. Both of these tests were very successful, with the former clearly showing a shift of the data and a lower threshold value for the larger proper frequency experiment, and the latter showing two sets of data whose stability angles and threshold driving amplitudes agreed well with each other at vastly different frequencies. The friction filter regime was also explored, this time by systematically increasing the modulation frequency and observing the stability angles. This was performed for a range of trap stiffness values. The stability angles and threshold modulation frequencies in all of these cases agreed well with the theoretical predictions.

A comparison of the dynamics of the particle in the two regimes was also made. It was seen that in the low frequency regime, there was a peak in the power spectral density plot at about the corner frequency and the driving frequency. This, along with plotted experimental trajectories indicated radial oscillations occurring about the equilibrium stabilisation angle. No such peaks were present in the high frequency regime where the detection method was far slower than the trap driving. The particle's radial coordinate was insensitive to the high driving frequency and the trap acted as a low-pass filter. Future experiments were

proposed whereby it might be possible to utilise this system with specific oscillation amplitudes and rates in order to achieve filtering/separation of different particle sizes.

In Chapter 5 a brief introduction was given into diabetes mellitus and the suspected pathogenesis of diabetic retinopathy (microaneurysms, macular oedema, vascular occlusion, retinal ischaemia and ultimately retinopathy/blindness), the occurrence rates, and the treatment options available. These were used to inform a pilot study that was conducted in order to investigate a possible link between red blood cell deformability and diabetic retinopathy (DR). In this experiment the trapping beam was split and a dual-beam optical tweezers set-up was used, applied directly to the RBCs, in order to perform stretching cycles upon them. RBCs from a healthy control group, a DM group, and a DR group were all stretched through the same routine. In addition to this several haematological and biochemical tests were performed upon the blood. Video microscopy was once again used in order to track the RBCs as they were stretched and to establish their lengths throughout the stretching cycles. From these measurements a simple fractional elongation measure, the deformability index, was calculated. The deformability index found for the two diabetes groups was significantly lower than that found for the control group, and of these two the DR group was the lowest. An inverse correlation was also observed for the first time between initial cell size and reduced cell deformability. Upon multivariate analysis of the biochemical tests, there was found to be no significant link between any of the tested parameters and initial cell size or deformability. A pilot attempt to identify morphological properties of the cells and connect these to deformabilities was also made in this chapter. Cell images were taken at different heights and from these 3-D images of the cells were constructed. Insufficient data was obtained from this method in

this study to be able to begin to make any meaningful comparisons using this, and the sample size was very small to begin with. It remains, however, a topic of interest and it would be desirable to conduct a larger study to identify any possible correlation between haematological/biochemical/morphological (e.g. sphericity) factors and RBC deformability.

Finally, Chapter 6 began with an introduction to the fluctuation theorem, the evolution of the distributions of probabilities of observing forward and backward particle trajectories in a system, as well as to the correlations of coupled particles. This chapter then proceeded to discuss a preliminary investigation into the FTs of a system of coupled particles that were being worked upon, but in ways other than simply adding noise to them and so changing their effective temperature. Two systems of working were discussed, one of which worked only the centre-of-mass mode of the two particles (stage translation), and the other which worked both this and the breathing/relative mode (trap translation). An analytical evaluation of these scenarios was made, via a reworking of the coordinate system found in research on similar single particle systems, in order to arrive at a total work done dissipation function for them both (which could be used in a fluctuation theorem). Initial simulations and experiments of two fixed traps containing hydrodynamically coupled particles were conducted. These both showed good agreement with their intuitively expected behaviour and with the theoretical correlation functions from the literature. These were used as an initial check and stepping stone before the two discussed methods of performing work on the system were put in to practice. The particle motions in both of these were extracted and averaged over many cycles and were found to be behaving as expected, both for individual particle and for system mode coordinates, and generally agreed well with theoretically predicted values and curves. The motions were also analysed for their correlations. These showed good agreement with the

forms of the theoretical predictions, but they often disagreed on the exact values. It was thought that this was most likely due to a lack of data before the characteristic relaxation time of the coupled motion, which in turn was due to the relatively slow detection rate of the camera equipment being used. Finally the total work done IFTs were calculated for the simulations and experiments. These showed a reasonable level of agreement for both the modal and non-modal cases and where discrepancies to theoretical predictions did occur they were generally small and were reckoned to be for the same reasons of a general lack of data and relatively large Brownian fluctuations. Thus it was asserted that the total work FTs held valid and were fulfilled for these coupled particle modal motions. Suggestions for future experiments, and crucially a faster detection method to obtain more data were made at the end of this chapter.

The experiments in this thesis, hearteningly, are not isolated in using optical tweezers for scientific research. They add to the wealth of experimental work present in the literature, just a small fraction of which has been referenced in this paper, which has made use of this tool in many widely varied fields. It is the opinion of the author that the work presented in this thesis has demonstrated the continuing importance of optical tweezers as a tool for probing the properties and micro-dynamics of soft-matter systems - for manipulating the microscopic. This is shown here through their utilisation in the fields of statistical physics and biophysics; aiding the discovery of new regimes of dynamic equilibrium in a damped pendulum, performing the first dual-trap, no bead handles stretching experiments to assess the deformability of RBCs, and investigating the FTs and correlations of coupled particle systems being worked upon.

Bibliography

[1] J. Kepler, *De Cometis Libelli Tres* (Augustae Vindelicorum, 1619).

[2] K. R. Lang, *The Cambridge Guide To The Solar System*, 2 ed. (Cambridge University Press, 2011), Chap. 14.5, p. 422.

[3] J. Clerk Maxwell, Philosophical Transactions of the Royal Society of London Series I **155**, 459 (1865).

[4] J. Clerk Maxwell, *A Treatise on Electricity and Magnetism* (Clarendon Press, 1873).

[5] E. F. Nichols and G. F. Hull, The Astrophysical Journal **17**, 315 (1903).

[6] T. H. Maiman, Nature **187**, 493 (1960).

[7] A. Ashkin, Selected Topics in Quantum Electronics, IEEE Journal of **6**, 841 (2000).

[8] A. Ashkin, Proceedings of the National Academy of Sciences **94**, 4853 (1997).

[9] A. Ashkin, Phys. Rev. Lett. **24**, 156 (1970).

[10] C. Fury *et al.*, Proc. SPIE **9126**, 91263L (2014).

[11] A. Ashkin, Phys. Rev. Lett. **40**, 729 (1978).

[12] A. Ashkin and J. P. Gordon, Opt. Lett. **4**, 161 (1979).

[13] A. Ashkin and J. M. Dziedzic, Applied Physics Letters **19**, 283 (1971).

[14] A. Ashkin and J. M. Dziedzic, Applied Physics Letters **24**, 586 (1974).

[15] A. Ashkin and J. M. Dziedzic, Appl. Opt. **19**, 660 (1980).

[16] A. Ashkin, J. M. Dziedzic, J. E. Bjorkholm, and S. Chu, Opt. Lett. **11**, 288 (1986).

[17] A. Ashkin, Biophysical Journal **61**, 569 (1992).

[18] A. Ashkin and J. M. Dziedzic, Science **235**, 1517 (1987).

[19] A. Ashkin, J. M. Dziedzic, and T. Yamane, Nature **330**, 769 (1987).

[20] P. H. Jones, O. M. Maragò, and G. Volpe, *Optical Tweezers Principles and Applications*, 1 ed. (Cambridge University Press, 2015).

[21] H. Minkowski, Mathematische Annalen **68**, 472 (1908).

[22] M. Abraham, Rendiconti del Circolo Matematico di Palermo (1884-1940) **28**, 1 (1909).

[23] R. N. C. Pfeifer, T. A. Nieminen, N. R. Heckenberg, and H. Rubinsztein-Dunlop, Rev. Mod. Phys. **79**, 1197 (2007).

[24] S. M. Barnett, Phys. Rev. Lett. **104**, 070401 (2010).

[25] F. Pedrotti, L. Pedrotti, and L. Pedrotti, *Introduction To Optics*, 3 ed. (Pearson, 2007), Chap. 23, pp. 491–509.

[26] Y. Harada and T. Asakura, Optics Communications **124**, 529 (1996).

[27] H. Kogelnik and T. Li, Appl. Opt. **5**, 1550 (1966).

[28] D. Marcuse, *Light Transmission Optics*, 2 ed. (Van Nostrand Reinhold, New York, 1972), Chap. 6.

[29] L. W. Davis, Phys. Rev. A **19**, 1177 (1979).

[30] J. P. Barton and D. R. Alexander, Journal of Applied Physics **66**, 2800 (1989).

[31] J. A. Stratton, *Electromagnetic Theory* (McGraw-Hill, New York, 1941), pp. 175–176, 205–207.

[32] M. Kerker, *The Scattering of Light and Other Electromagnetic Radiation* (Academic, New York, 1969), Chap. 3.

[33] K. N. Liou, Appl. Math. Comput. **3**, 331 (1977).

[34] G. Mie, Annalen der Physik **330**, 377 (1908).

[35] P. C. Waterman, Phys. Rev. D **3**, 825 (1971).

[36] M. I. Mishchenko, L. D. Travis, and A. A. Lacis, *Scattering, Absorption, and Emission of Light by Small Particles* (Cambridge University Press, 2002).

[37] F. Borghese, P. Denti, and R. Saija, *Scattering from Model Nonspherical Particles: Theory and Applications to Environmental Physics* (Springer-Verlag, Berlin, 2007).

[38] G. Gouesbet and G. Gréhan, *Generalized Lorenz-Mie Theories* (Springer, 2011).

[39] G. Gouesbet, Optics Communications **283**, 517 (2010).

[40] A. Stephenson, Phil. Mag. **15**, 233 (1908).

[41] P. L. Kapitza, Soviet Phys. JETP **21**, 588 (1951).

[42] P. L. Kapitza, Usp. Fiz. Nauk **44**, 7 (1951).

[43] J. W. Jewett and R. A. Serway, *Physics for Scientists and Engineers with Modern Physics*, 7 ed. (Brooks/Cole, 2008).

[44] M. G. Calkin, *Lagrangian and Hamiltonian Mechanics* (World Scientific Publishing Co Pte Ltd, 1996), Chap. 3.

[45] C. Fox, *An Introduction to the Calculus of Variations* (Dover Publications Inc, 1987), Chap. 1, p. 8.

[46] E. I. Butikov, American Journal of Physics **69**, 755 (2001).

[47] P. S. Landa, *Nonlinear Oscillations and Waves in Dynamical Systems* (Springer, 1996).

[48] P. S. Landa and P. V. E. McClintock, Journal of Physics A: Mathematical and General **33**, L433 (2000).

[49] I. I. Blekhman, *Vibrational Mechanics: Nonlinear Dynamic Eects, General Approach, Applications* (World Scientific Publishing Company, 2000).

[50] P. L. Kapitza, in *Collected Papers Of P. L. Kapitza*, 1 ed., edited by D. ter Haar (Pergamon, 1965), Vol. 2, Chap. 45, pp. 714–726.

[51] L. D. Landau and E. M. Lifshitz, *Mechanics*, Vol. 1 of *Course of Theoretical Physics*, 1 ed. (Pergamon, 1960).

[52] W. T. Grandy Jr. and M. Schöck, American Journal of Physics **65**, 376 (1997).

[53] I. I. Blekhman, *Selected Topics in Vibrational Mechanics*, Vol. 11 of *Series on Stability, Vibration & Control of Systems: Series A* (World Scientific Publishing Co Pte Ltd, 2003), Chap. 15, pp. 363–386.

[54] M. Borromeo and F. Marchesoni, Phys. Rev. Lett. **99**, 150605 (2007).

[55] M. Grifoni and P. Hänggi, Phys. Rev. Lett. **76**, 1611 (1996).

[56] V. N. Chizhevsky, E. Smeu, and G. Giacomelli, Phys. Rev. Lett. **91**, 220602 (2003).

[57] A. Wickenbrock *et al.*, Phys. Rev. Lett. **108**, 020603 (2012).

[58] V. N. Chizhevsky, Phys. Rev. E **89**, 062914 (2014).

[59] D. Cubero, J. P. Baltanás, and J. Casado-Pascual, Phys. Rev. E **73**, 061102 (2006).

[60] S. H. Weinberg, Chaos **24**, 043104 (2014).

[61] N. I. Vaganova and E. N. Rumanov, Journal of Experimental and Theoretical Physics **115**, 346 (2012).

[62] J. A. Hołyst and W. Wojciechowski, Physica A: Statistical Mechanics and its Applications **324**, 388 (2003), proceedings of the International Econophysics Conference.

[63] I. P. M. Wickramasinghe and J. M. Berg, 2013 IEEE/ASME International Conference on Advanced Intelligent Mechatronics: Mechatronics for Human Wellbeing, AIM 2013 686 (2013).

[64] M. M. Michaelis, American Journal of Physics **53**, 1079 (1985).

[65] J. A. Blackburn, H. J. T. Smith, and N. Grønbech-Jensen, American Journal of Physics **60**, 903 (1992).

[66] H. J. T. Smith and J. A. Blackburn, American Journal of Physics **60**, 909 (1992).

[67] E. I. Butikov, Journal of Physics A: Mathematical and Theoretical **44**, (2011).

[68] B. Ahmad and S. Borisenok, Physics Letters, Section A: General, Atomic and Solid State Physics **373**, 701 (2009).

[69] J. Tellez and J. Collado, 2013 10th International Conference on Electrical

Engineering, Computing Science and Automatic Control, CCE 2013 87 (2013).

[70] S. Michalowsky and C. Ebenbauer, Proceedings of the IEEE Conference on Decision and Control 3981 (2013).

[71] I. V. Miroshnik and N. M. Odinets, IFAC Proceedings Volumes (IFAC-PapersOnline) **16**, 625 (2005).

[72] R. Citro *et al.*, Annals of Physics **360**, 694 (2015).

[73] R. Chacón and L. Marcheggiani, Physical Review E - Statistical, Nonlinear, and Soft Matter Physics **82**, (2010).

[74] F. V. Lisovskii and E. G. Mansvetova, Bulletin of the Russian Academy of Sciences: Physics **71**, 1500 (2007).

[75] V. S. Bagnato, N. P. Bigelow, G. I. Surdutovich, and S. C. Zílio, Optics Letters **19**, 1568 (1994).

[76] V. A. Vladimirov, Journal of Mathematical Fluid Mechanics **7**, S397 (2005).

[77] R. M. Carbo, R. W. M. Smith, and M. E. Poese, The Journal of the Acoustical Society of America **128**, 1623 (2010).

[78] T. Leiber and H. Risken, Physics Letters A **129**, 214 (1988).

[79] M. V. Bartuccelli, G. Gentile, and K. V. Georgiou, Proceedings: Mathematical, Physical and Engineering Sciences **457**, 3007 (2001).

[80] G. K. Batchelor, *An Introduction to Fluid Dynamics* (Cambridge University Press, 2000), Chap. 4, p. 233.

[81] K. F. Riley, M. P. Hobson, and S. J. Bence, *Mathematical Methods for Physics and Engineering*, 2 ed. (Cambridge University Press, 2002).

[82] P. H. Jones, T. J. Smart, C. J. Richards, and D. Cubero, Proc. SPIE **9922**, 992202 (2016).

[83] C. J. Richards, T. J. Smart, P. H. Jones, and D. Cubero, Proc. SPIE **9548**, 954820 (2015).

[84] N. Rott, Annual Review of Fluid Mechanics **22**, 1 (1990).

[85] E. M. Purcell, American Journal of Physics **45**, 3 (1977).

[86] G. Volpe and G. Volpe, American Journal of Physics **81**, 224 (2013).

[87] D. S. Lemons and A. Gythiel, American Journal of Physics **65**, 1079 (1997).

[88] R. Kubo, M. Toda, and N. Hashitsume, *Statistical Physics*, Vol. 2 of *Springer Series in Solid-State Science*, 1 ed. (Springer-Verlag Berlin Heidelberg, 1985).

[89] P. H. Jones, C. J. Richards, T. J. Smart, and D. Cubero, Proc. SPIE **9379**, 93790L (2015).

[90] P. H. Jones, O. M. Maragò, and E. P. J. Stride, Journal of Optics A: Pure and Applied Optics **9**, S278 (2007).

[91] http://www.npl.co.uk/measurement-services/dimensional/npl-reference-stage-graticules.

[92] K. Berg-Sørensen and H. Flyvbjerg, Review of Scientific Instruments **75**, 594 (2004).

[93] W. Singer, S. Bernet, N. Hecker, and M. Ritsch-Marte, Journal of Modern Optics **47**, 2921 (2000).

[94] M. P. MacDonald, G. C. Spalding, and K. Dholakia, Nature **426**, 421 (2003).

[95] C. F. Chou *et al.*, Proceedings of the National Academy of Sciences **96**, 13762 (1999).

[96] A. van Oudenaarden and S. G. Boxer, Science **285**, 1046 (1999).

[97] S. Matthias and F. Muller, Nature **424**, 53 (2003).

[98] D. G. Gardner and D. M. Shoback, *Greenspan's Basic and Clinical Endocrinology*, 9 ed. (McGraw-Hill Education, 2011), Chap. 17.

[99] L. Stryer, *Biochemistry* (W.H. Freeman & Company, 1995), pp. 773–774.

[100] R. Ross, Nature **362**, 801 (1993).

[101] P. T. O'Gara *et al.*, Circulation **127**, e362 (2013).

[102] D. L. Kasper *et al.*, *Harrison's Principles of Internal Medicine*, 18 ed. (McGraw-Hil, 2011), p. 2982.

[103] M. D. Abràmoff, M. K. Garvin, and M. Sonka, IEEE transactions on medical imaging **3**, 169 (2010).

[104] M. Yanoff and J. W. Sassani, *Ocular Pathology*, 6 ed. (Mosby Elsevier, 2009), pp. 393–394.

[105] M. Brownlee, Nature **414**, 813 (2001).

[106] D. M. Nathan, New England Journal of Medicine **328**, 1676 (1993), pMID: 8487827.

[107] N. Cheung, P. Mitchell, and T. Y. Wong, The Lancet **376**, 124 (2010).

[108] R. L. Engerman, Diabetes **38**, 1203 (1989).

[109] T. Smart *et al.*, Proc. SPIE **9548**, (2015).

[110] NCD Risk Factor Collaboration (NCD-RisC), The Lancet **387**, 1513 (2016).

[111] J. W. Y. Yau *et al.*, **35**, 556 (2012).

[112] Q. Mohamed, M. C. Gillies, and T. Y. Wong, JAMA **298**, 902 (2007).

[113] J. H. Kempen *et al.*, Archives of Ophthalmology **122**, 552 (2004).

[114] M. S. Roy *et al.*, Archives of Ophthalmology **122**, 546 (2004).

[115] R. J. Tapp *et al.*, Diabetes Care **26**, 1731 (2003).

[116] P. J. Kertes and T. M. Johnson, *Evidence-Based Eye Care* (Wolters Kluwer Health, 2013).

[117] P. G. O'Malley, Archives of Internal Medicine **172**, 1014 (2012).

[118] J. Penn, *Retinal and Choroidal Angiogenesis* (Springer Netherlands, 2008), Chap. 6, p. 119.

[119] R. Machemer, Graefes Arch. Clin. Exp. Ophthalmol. **233**, 453 (1995).

[120] C. C. T. Wang and S. Charles, Journal of Clinical Engineering **9**, (1984).

[121] M. Rendell *et al.*, J. Lab. Clin. Med. **117**, 500 (1991).

[122] R. Agrawal *et al.*, Sci Rep **6**, 15873 (2016).

[123] J. A. Rhodin, Microvasc. Res. **5**, 313 (1973).

[124] M. Bessis and N. Mohandas, Schweiz Med Wochenschr **105**, 1568 (1975).

[125] J. Stuart, J. Clin. Pathol. **38**, 965 (1985).

[126] Y. C. Fung, *Biomechanics: Circulation*, *Plant Gene Research: Basic Knowledge* (Springer New York, 1996).

[127] J. H. Jeong, Y. Sugii, M. Minamiyama, and K. Okamoto, Microvasc. Res. **71**, 212 (2006).

[128] E. J. Diamantopoulos, S. A. Raptis, and S. D. Moulopoulos, Horm. Metab. Res. **19**, 569 (1987).

[129] Y. Suzuki, N. Tateishi, M. Soutani, and N. Maeda, Microcirculation **3**, 49 (1996).

[130] M. Rendell *et al.*, Biochim. Biophys. Acta **1133**, 293 (1992).

[131] S. Shin, J. X. Hou, J. S. Suh, and M. Singh, Clin. Hemorheol. Microcirc. **37**, 319 (2007).

[132] P. J. Bronkhorst *et al.*, Biophys. J. **69**, 1666 (1995).

[133] S. Henon, G. Lenormand, A. Richert, and F. Gallet, Biophys. J. **76**, 1145 (1999).

[134] S. Rancourt-Grenier *et al.*, Opt Express **18**, 10462 (2010).

[135] J. Guck *et al.*, Biophys. J. **81**, 767 (2001).

[136] M. Dao, C. T. Lim, and S. Suresh, Journal of the Mechanics and Physics of Solids **51**, 2259 (2003).

[137] G. B. Liao, P. B. Bareil, Y. Sheng, and A. Chiou, Opt Express **16**, 1996 (2008).

[138] N. Babu and M. Singh, Clin. Hemorheol. Microcirc. **31**, 273 (2004).

[139] P. Vague and I. Juhan, Diabetes **32 Suppl 2**, 88 (1983).

[140] S. Keymel *et al.*, Horm. Metab. Res. **43**, 760 (2011).

[141] D. E. McMillan, N. G. Utterback, and J. La Puma, Diabetes **27**, 895 (1978).

[142] C. D. Brown *et al.*, Kidney Int. **67**, 295 (2005).

[143] K. M. Amoussou-Guenou *et al.*, Technol Health Care **5**, 347 (1997).

[144] World Medical Association, JAMA **310**, 2191 (2013).

[145] T. Deutschbein *et al.*, Clin. Endocrinol. (Oxf) **73**, 153 (2010).

[146] R. Hoffman *et al.*, *Hematology: Diagnosis and Treatment* (Elsevier Health Sciences, 2012).

[147] I. Krasnikov, A. Seteikin, and I. Bernhardt, Optical Memory and Neural Networks (Information Optics) **19**, 330 (2010), cited By 2.

[148] J. Hirsch *et al.*, Clinical Chemistry **49**, 792 (2003), cited By 15.

[149] R. A. Fisher, Journal of the Royal Statistical Society **85**, 87 (1922).

[150] R. A. Fisher, *Statistical Methods For Research Workers*, *Cosmo study guides* (Cosmo Publications, 1925).

[151] S. Siegel, *Nonparametric statistics for the behavioral sciences*, *McGraw-Hill series in psychology* (McGraw-Hill, 1956).

[152] V. A. Epanechnikov, Theory of Probability & Its Applications **14**, 153 (1969).

[153] B. U. Park and J. S. Marron, Journal of the American Statistical Association **85**, 66 (1990).

[154] B. W. Silverman, *Density Estimation for Statistics and Data Analysis*, *Chapman & Hall/CRC Monographs on Statistics & Applied Probability* (Taylor & Francis, 1986), p. 48.

[155] S. M. MacRury and G. D. Lowe, Diabet. Med. **7**, 285 (1990).

[156] E. Ernst and A. Matrai, Diabetes **35**, 1412 (1986).

[157] C. J. Magri and S. Fava, Diabetes Metab Syndr **8**, 13 (2014).

[158] A. V. Buys *et al.*, Cardiovasc Diabetol **12**, 25 (2013).

[159] M. Born, E. Wolf, and A. B. Bhatia, *Principles of Optics: Electromagnetic Theory of Propagation, Interference and Diffraction of Light* (Cambridge University Press, 1999).

[160] J. W. Goodman, *Introduction to Fourier Optics*, *McGraw-Hill physical and quantum electronics series* (W. H. Freeman, 2005).

[161] P. M. S. Roma *et al.*, Applied Physics Letters **104**, (2014).

[162] S. Blundell and K. M. Blundell, *Concepts in Thermal Physics* (OUP Oxford, 2010).

[163] C. Bustamante, J. Liphardt, and F. Ritort, Physics Today **58**, 43 (2005).

[164] A. M. Fennimore *et al.*, Nature **424**, 408 (2003).

[165] J. Howard, *Mechanics of Motor Proteins and the Cytoskeleton* (Sinauer Associates, Publishers, 2001).

[166] E. M. Sevick, R. Prabhakar, S. R. Williams, and D. J. Searles, Annual Review of Physical Chemistry **59**, 603 (2008), pMID: 18393680.

[167] G. M. Wang *et al.*, Phys. Rev. E **71**, 046142 (2005).

[168] J. Loschmidt, *Über den Zustand des Wärmegleichgewichtes eines Systems von Körpern mit Rücksicht auf die Schwerkraft: I [-IV].* (aus der KK Hof-und Staatsdruckerei, 1876).

[169] D. J. Evans, E. G. D. Cohen, and G. P. Morriss, Phys. Rev. Lett. **71**, 2401 (1993).

[170] D. J. Evans and D. J. Searles, Phys. Rev. E **50**, 1645 (1994).

[171] G. M. Wang *et al.*, Phys. Rev. Lett. **89**, 050601 (2002).

[172] R. van Zon and E. G. D. Cohen, Phys. Rev. E **67**, 046102 (2003).

[173] R. van Zon and E. G. D. Cohen, Phys. Rev. Lett. **91**, 110601 (2003).

[174] J. C. Reid *et al.*, Phys. Rev. E **70**, 016111 (2004).

[175] M. Doi and S. F. Edwards, *The Theory of Polymer Dynamics*, *International series of monographs on physics* (Clarendon Press, 1988), Chap. 2, p. 17.

[176] D. J. Evans and D. J. Searles, Advances in Physics **51**, 1529 (2002).

[177] M. Polin, D. G. Grier, and S. R. Quake, Phys. Rev. Lett. **96**, 088101 (2006).

[178] P. H. Jones, in *Encyclopedia of Optical and Photonic Engineering, Second Edition (Print) - Five Volume Set*, edited by C. Hoffman and R. Driggers (Taylor & Francis, 2015), Chap. Optical Tweezers, pp. 5–7.

[179] J. C. Meiners and S. R. Quake, Phys. Rev. Lett. **82**, 2211 (1999).

[180] J. Kurchan, Journal of Physics A: Mathematical and General **31**, 3719 (1998).

[181] J. Farago, Journal of Statistical Physics **107**, 781 (2002).

[182] D. M. Carberry *et al.*, Phys. Rev. Lett. **92**, 140601 (2004).

[183] G. M. Wang *et al.*, Journal of Physics: Condensed Matter **17**, S3239 (2005).

[184] D. M. Carberry *et al.*, Journal of Optics A: Pure and Applied Optics **9**, S204 (2007).

[185] J. R. Gomez-Solano, L. Bellon, A. Petrosyan, and S. Ciliberto, EPL (Europhysics Letters) **89**, 60003 (2010).

[186] A. Bérut, A. Petrosyan, and S. Ciliberto, EPL (Europhysics Letters) **107**, 60004 (2014).

[187] A. Bérut, A. Imparato, A. Petrosyan, and S. Ciliberto, Journal of Statistical Mechanics: Theory and Experiment **2016**, 054002 (2016).

[188] A. Bérut, A. Imparato, A. Petrosyan, and S. Ciliberto, Phys. Rev. Lett. **116**, 068301 (2016).

[189] A. Bérut, A. Imparato, A. Petrosyan, and S. Ciliberto, Phys. Rev. E **94**, 052148 (2016).

[190] G. Bulnes Cuetara, M. Esposito, and A. Imparato, Phys. Rev. E **89**, 052119 (2014).

[191] X. Han and P. H. Jones, Opt. Lett. **40**, 4042 (2015).